Microstructures and Corrosion of Intermediate Level Wasteforms Fabricated Using Novel Thermal Techniques

Charles Allan Hutchison

Doctor of Philosophy

Imperial College London, Materials

Abstract

Simulant intermediate level waste materials received from Sellafield, 3 produced using Joule heating techniques, and 3 from plasma furnace methods, were characterised and subjected to leaching tests for up to 14 weeks to assess their potential as a waste matrix. Each wasteform was used to simulate a combination of waste surrogates such as plutonium contaminated material, site ion exchange plant waste, high metal content waste, Magnox sludge, asbestos, or pile fuel cladding.

Five samples were characterised as glass composite materials, containing a crystalline and glassy portion, with the sixth being characterised as a glass. XRD and EDX analysis were used to identify the crystalline components, revealing a wide array of phases over the six samples such as pigeonite, anorthite, diopside, Cerium-Lanthanum silicate, proto and clino hypersthene, augite, and two glasses from liquid-liquid phase separation. ICP-OES analysis and pH were used to analyse the leachant, and SEM-EDX surface scans and depth profiles for analysis of the wasteform, post corrosion. Results revealed several of the wasteforms to be more than adequate for safe disposal, showing protective corrosion layers or durable crystalline components. However, not all wasteforms were suitable; in particular glass encapsulated metals should not be used as a waste matrix due to the susceptibility of the metal/metal oxide portion to chemical attack.

Acknowledgements

First and foremost, I would like to thank my supervisor, Professor William Lee for his continued patience and guidance thought my doctorate. I am immensely grateful for his unusual methods for motivating me, which were nonetheless very effective, without which this thesis would not be possible.

Secondly, I would like to thank my parents, Charles and Gillian Hutchison, and my fiancée, Alix de Laportalière for their support for the entirety of my time at Imperial College London.

I would like to thank Sellafield LtD, for supplying the samples used, and for their funding, in addition to their help in successfully finding the relevant background documents on the samples they supplied.

I am grateful to all those at Imperial College London Materials department, and the Centre for Nuclear Engineering for continually providing me with support, guidance, advice, and for taking time to show me how to use the various instruments that were critical to this thesis. In particular I would like to thank the scanning electron microscopy suite technicians; Dr. Mahmoud Ardakini, and Mrs Ecaterina Ware who opened up a whole new world of electron microscopy to me. Mr. Richard Sweeney for showing me the subtleties of the XRD lab and its software, and a lab technician known only as Ben, who provided access to the grinding and polishing lab too regularly.

Declaration of originality

I hereby declare that this document is entirely my own work, and any additional sources of information from published/unpublished papers, internet sources, books, or other sources have been properly cited.

Copyright declaration

Contents

List of tables and figures

Acronyms

ACM	Asbestos Contaminated Material
ATM	Approved Testing Materials
BEI	Backscattered Electron Imaging
BSE	Back Scattered Electrons
CMAS	Calcium Magnesium Alumino-Silicate
DTA/TGA	Differential Thermal Analysis and ThermoGravimetric Analysis
EDX	Energy Dispersive X-ray Spectroscopy
FEG	Field Emission Gun
GCM	Glass Composite Materials
GDF	Geological Disposal Facility
HLW	High Level Waste
HMS	High Metal Surrogate
ICP-MS	Inductively Coupled Plasma-Mass Spectrometry
ICP-OES	Inductively Coupled Plasma Optical Emission Spectrometry
ILW	Intermediate Level Waste
JH-CM	Joule Heated Ceramic Melter
JH-HMS	Joule Heated High Metal Surrogate
JH-ICV	Joule Heated In-Container Vitrification
JH-PCM	Joule Heated Plutonium Contaminated Material
JH-SIXEP	Joule Heated Site Ion Exchange Plant
LLW	Low Level Waste
Magnox	Magnesium Non-Oxidising
MCC	Materials Characterisation Centre
M/MO	Metal/Metal Oxide
NBO	Non Bridging Oxygens
Nlpm	Normalised litres per minute
OPC	Ordinary Portland Cement

PCM	Plutonium Contaminated Material
PF-Asb	Plasma Furnace Asbestos
PFC	Pile Fuel Cladding
PF-HMS	Plasma Furnace High Metal Surrogate
PF-HMS2	Plasma Furnace High Metal Surrogate 2
PNNL	Pacific Northwest National Laboratory
PVC	PolyVinyl Chloride
SA/V	Surface Area to Volume Ratio
SEI	Secondary Electron Imaging
SEM	Scanning Electron Microscope
SIXEP	Site Ion Exchange Plant
Synroc	Synthetic Rock
ToF-SIMS	Time of Flight Secondary Ion Mass Spectrometry
WCS	Worst Case Scenario
XRD	X-Ray Diffraction

1.0 Introduction

The continued use of nuclear power in the UK for the last 60 years without a final disposal option has resulted in a stockpile of diverse wastes created by the variety of reactors used (Windscale piles, Magnox, Pressurized Water and Advanced Gas cooled Reactors). Most prominent among these are the UK legacy wastes held at Sellafield Ltd consisting of 4 key silos and ponds containing several waste types. The silos and ponds have been documented as containing the following wastes [1]:

1) Pile fuel storage pond: This was used for the decanning and storage of spent fuel from the Windscale piles, it has additionally been used to store Magnox and other oxide fuel, with miscellaneous irradiated materials. The contents of this pond have been cited as oxide fuel, sludges, metal fuel, ILW isotopes, ILW Magnox swarf, ILW zircalloy containers, and low level waste.
2) First Magnox pond: This pond was constructed in 1959 for the storage and decanning of irradiated spent Magnox fuel. The fuel was stored underwater, and was left underwater for "abnormally long periods of time". The result it a slurry comprising of corrosion products at the bottom of the pond. Radiologically, the pond has been cited as containing spent fuel debris, sludges, loose miscellaneous beta/gamma emitters, zeolites, and wet bay intermediate level waste (ILW) [1].
3) Magnox fuel cladding silo: Originally this silo comprised of 6 concrete compartments containing Magnox fuel cladding submerged underwater for cooling purposes. The issues associated with this pond are more related to the build-up of hydrogen that occurs because of magnesium corroding.
4) Pile fuel cladding silo: This silo is known only to contain "miscellaneous ILW" generated from the Windscale and Chapelcross sites from 1951-1964. However, continued tipping of additional waste up to 1968 combined with the length of time of the storage, has led to an uncertainty into the exact composition of this silo.

Although strategies have been put in place for waste removal, treatment, and storage, there are still issues for each of these steps. Information on what was originally placed in these silos/ponds is mostly known as described above, however up to 60 years in a wet silo and open to the environment has resulted in corrosion products (fuel skip, concrete) and organic wastes from animal remains and bird guano [2]. The extensive and complex uncharacterised Intermediate Level Wastes contained in these ponds are a major safety threat. In addition, the engineering hurdles to successfully deal with this waste are not trivial, the waste needs to be characterised, segregated when needed, and then immobilised in a wasteform made to last hundreds (ILW) if not tens of thousands of years in the case of High Level Waste (HLW). One of the strategies being looked at is the use of alternate waste matrices to dispose of these complicated wastes, however it is still not agreed upon as to what category these wastes fall under (LLW, ILW, HLW) or whether the remnant fuel should be classified as fuel (and so reprocessed) or be classified as ILW/HLW and disposed of as such. This poses an even greater problem as any wasteform chosen may eventually be discarded as an option, as characterisation of these ponds reveals the extent of their radioactivity. Further, the diverse, reactive, metal waste content poses technical issues with current disposal methods in addition to the radioactivity of the other wastes. Due to these issues, any potential wasteform must not only meet the current (and somewhat arbitrary) safety standards imposed for these waste streams, but

must anticipate that the classification of these wastes may change and so also meet the higher requirements that may be decided. It is for this reason that the final fate of these hypothetical wasteforms is unresolved, as it is not certain as to whether it will be categorised as ILW and stored on a surface repository, or HLW and stored deep underground.

Currently, vitrification is seen as the ideal method for final disposal of HLW and certain ILW, owing to high water corrosion and irradiation resistance [3] and a high tolerance for incorporation of a large number of elements into its structure. It also helps that it has been widely used in many countries for many decades, so it is an industrially mature technology.

However, one of the issues with current waste glasses is the opportunity for crystallisation which is not desirable unless it does not impair the chemical durability of the final wasteform [4,5]. This may mean limited ability to incorporate certain waste elements due to their limited solubility in the glass. A good example is molybdenum, which has a solubility of 1wt% in nuclear glasses [6] before crystallizing into the infamous yellow phase: a water soluble molybdate/sulphate which is deleterious to the durability of the wasteform. This avoidance of crystalline phases in glasses for the final wasteform may be unnecessary, certain polycrystalline ceramics have a higher chemical durability and radiation resistance than borosilicate glasses under storage conditions [7] although this is balanced by the relatively difficult mode of manufacture for ceramic wasteforms [8]. It is also of note that a glass matrix with a ceramic phase could accommodate waste composition fluctuations and impurities to a higher degree than an equivalent wasteform composed of a multi-phase ceramic which is found to develop low durability phases containing radioactive elements [9] and these phases can make long term prediction of ceramics durability difficult [**Error! Bookmark not defined.**].

The combination of a ceramic and glassy phase, in addition to providing a double barrier to radionuclide release, can incorporate the best properties of each material without compromising the durability, corrosion resistance, and radiation resistance of the final wasteform. To this end Glass Composite Materials (GCM) are being studied. GCMs contain at least one crystalline and one amorphous component, either of which can be the major phase [10,11]. GCMs are currently being investigated to immobilize all categories of nuclear waste due to their flexibility as their properties can be tailored by altering the composition and manufacturing method [12,13]. GCMs can be subcategorised as:

- Glass ceramics: where a separate heat treatment is intentionally used to crystalise a part of the glass.
- Crystal containing glasses: the main wasteform, where crystals are unintentionally formed.
- Glass containing crystals: where the amorphous phase encapsulates a core like refractory crystalline phase.

The methods for production of GCMs investigated in this study are the same as those for glasses, namely plasma vitrification and Joule heating (In-container). Joule heating makes use of ohmic heating; an electric current passed through a conductor will generate heat. For joule heated melters, several variations based on this effect are used, with most using a conductive starter path between 2 or more electrodes. The heat produced by this conductive pathway provides the energy to melt the surrounding material which, in its liquid form, becomes the conducting material, continuing this

process until all the necessary material is melted. This is in contrast with plasma furnaces which make use of the high temperatures of plasma torches to directly melt the waste. Each thermal treatment has benefits and drawbacks when compared to each other; the exact details of these production methods and pros/cons are described in later chapters. Examples of the use of each of these treatments include: destruction of asbestos [14,15], an alternative to conventional HLW vitrification [16,17], or for difficult LLW/ILW [18].

Several trials using these thermal techniques have already been performed (see section 3.1), each with a goal, but usually designed for an extreme such as having an excessive amount of waste, or with disproportionately high temperatures. The idea in these tests was to gather information regarding how each furnace reacted to the excessive circumstances to calibrate the conditions for the "real" tests resulting in the materials studied here.

In this thesis, the following will be examined:

- Characterisation of the microstructure, chemical composition and all phases present in 6 GCM simulant wasteforms supplied by Sellafield.
- Leaching tests to assess the chemical durability of the simulant wasteforms
- Determination of the viability of each material as a suitable ILW disposal matrix.

2.0 Literature Survey

2.1 Historical Background

Glasses have been of interest to man since we first took obsidian and crafted it into weapons for hunting, up to more complex modern glasses, such as the use of phase separated micro porous glass for reverse osmosis of seawater [19].

With the start of the Manhattan project it was only time before we would have to deal with the environmental impact of the radioactive waste produced, waste that could remain dangerous to the biosphere for 10,000 years, if not longer, and this would need to be contained, isolated, and safeguarded from the biosphere for at least that time. Any material we picked to surround our waste needed to be resistant to as many envisioned methods of attack, such as chemical corrosion from water, mechanical from earthquakes, and radioactive deterioration from the waste itself. There is one material we have studied that has stood the test of time with little change.

Studies into borosilicate glass have shown it to have good radiation resistance [20], good durability [21], reasonable mechanical strength [22], and thermal resistance (important due to self-irradiation) [23]. Whilst these are the most important characteristics of any wasteform, other properties led to glass becoming the preferred matrix:

- The ability to incorporate a variety of elements into its structure without much change to the properties.
- Ease of production as glass manufacturing was already a mature technology.
- The manufacturing process resulted in a wasteform volume reduction.

2.2 Theory of Amorphous Solids

The definition of an amorphous material is described as a material where no medium or long range order exists, only short range order is present i.e. one bond length. While super cooled liquids can display similar properties, and fit the description, glasses are amorphous solids, displaying a second order phase transition whilst liquids do not.

In silicates for example, the basic structural unit of any silicate, be it amorphous, liquid or crystalline, is that of a silicate tetrahedron with oxygens at the points of the tetrahedron whilst silicon sits at the centre [24]. Although angles between the central silicon and the oxygens are fixed at 109^{o} in all directions, for amorphous materials it is the angles between these tetrahedra which lead to no long-range order as there is no fixed angle (see Figure 1).

The basis for formation of glasses from oxides was first described by Zachariasen in 1932 [25] the four rules he described enable prediction of glass forming potential for a given material:

1) An oxygen atom is linked to no more than two glass-forming atoms.

2) The coordination number of the glass forming atoms is small.

3) The oxygen polyhedra share corners with each other, not edges nor faces.

4) The polyhedra are linked in a three-dimensional network.

Several other additions have been suggested [26] mainly due to the formation of glasses outside of the Zachariasen rules (vanadium, molybdenum, technetium, and tungsten oxides).

In a pure network oxide glass, the network would be an infinite, random arrangement of tetrahedra (the most common structural unit) however the network nearly always contains additional elements which change the network in some form or another; two modifications can be distinguished. The first are known as network modifiers, these elements disrupt Si-O-Si bonds reducing them to Si-O-Na+ ion pairs (Na as an example- can be replaced by similar ions). These types of linkage, where the oxygen no longer connects to another network former are more commonly termed Non-Bridging Oxygens (NBO), the alkaline and alkaline earth ions are the most common i.e. sodium, potassium, magnesium, and calcium. In a hypothetical pure silicate glass all tetrahedra are undisrupted but with the addition of one modifier ion the tetrahedron only has 3 oxygens associated with it. A terminology was developed for describing this in terms of "Q units" or Q^x where x is the number of Si-O-Si bonds associated with one tetrahedron [25].

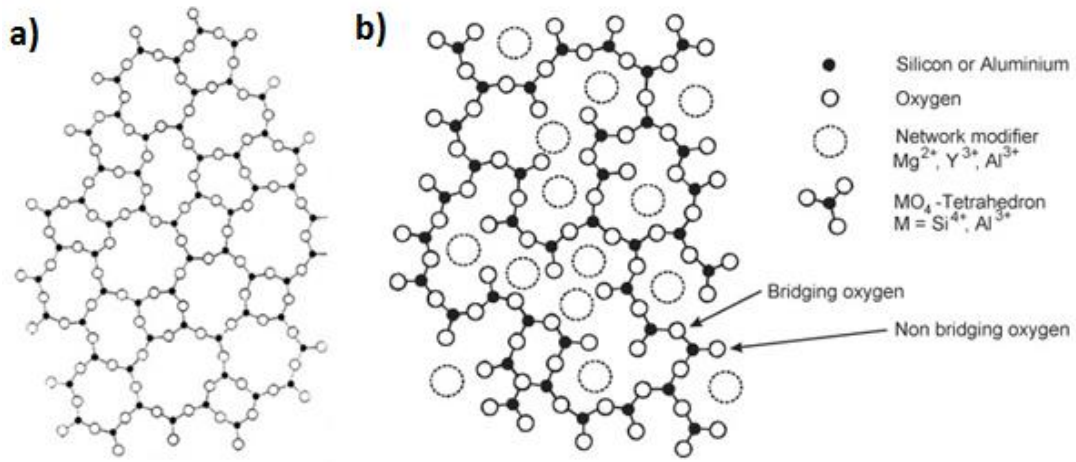

Figure 1: Representative two-dimensional structure of a) a pure glass and b) with network modifiers. Adapted from Zachariasen [25] and Schilm [27], for a) and b) respectively.This shows the change that occurs in the network as a result of adding modifying ions.

The second method for altering the network is via network formers, they form as part of the network and generally work to mitigate, or completely negate, the effect of network modifiers usually resulting in increased corrosion resistance amongst other properties. Using aluminium as an example, after forming a tetrahedron with 4 oxygens, it has one negative charge left over, allowing it to accommodate one positively charged network modifier that would otherwise have disrupted the

network. They can also form separate glasses in their own right. Some elements can take on both these roles and are termed intermediates; the best example of which is aluminium which plays an important role in nuclear glasses (see section 2.3.2).

2.3 Nuclear Glasses

2.3.1 Borosilicates

To get the right properties for a potential nuclear waste glass, specific glass formulations are required to moderate certain properties and augment others; using silicate glasses as the starting material several additions were made. Volatilisation of certain elements led to the addition of boron to reduce processing temperatures, aluminium added for higher chemical durability and after several iterations led to the waste glass used today, such as the French R7/T7 or the Approved Testing Materials (ATM) 10 defence waste glass for the Savannah river processing facility (USA) [28].

Several disadvantages to this wasteform have been found, such as the limited solubility of some elements such as sulphates [29], molybdates [30], and chromates [31] (and to some lesser extent the halogenides [32]) in borosilicate glasses. In high enough concentration they form a water soluble phase termed yellow phase. The formation of this deleterious phase, and similarly behaving phases, led to the general rule of thumb of “no crystallisation”. This resulted in strict limitations on waste loadings, and in the exclusion of certain wastes which has ultimately caused the nuclear community to look outward for alternative waste matrices for unsuitable wastes.

The research into the right composition of borosilicate glasses alongside the relatively few problems associated with its ability to immobilise HLW has led them to become the matrix of choice in most nuclear nations, with only the Russians considering an alternative, the sodium alumino-phosphate type glasses [33].

2.3.2 Aluminosilicates

Alumina is well known as taking an intermediate role when introduced into the structure of glasses [34], whether it takes the role of former or modifier depends on the presence and concentration of other ions [35].

Whilst the co-ordination of Al in crystalline materials varies from 3,4,5 in glasses it is generally found in 4-fold thus leading to an Al tetrahedron, this arrangement is not charge neutral, needing +1 to balance. As was mentioned previously, additions of modifiers reduce the number of Q^4 units, resulting in lower stability of the network, as the silica is more easily hydrolysed forming Silanol ($Si(OH)_4$). However, the unbalanced Al tetrahedron counteracts the effects of modifiers. Instead of breaking oxygen bonds, the modifiers instead charge compensate the Al [36,37], Boron also has the same effect, Bunker [37] noted that the Al-Na+ (and also B-Na+) bond was over 5 times stronger than the equivalent NBO.

The effects that Al has on the properties of the glass when either all modifier’s extra charge is accounted for, or when none are present is not in the scope of this review, but information on this was reported in references 20,21, and 22. It is for this reason that aluminosilicate glasses and variations including alumina show an increased durability [24] among other properties (hardness, tensile and compressive strengths, and thermal endurance [24]). It is also of interest to note that for

alkali silicate melts, the presence of even small amounts of Al_2O_3 (5 mol %) can reduce the chance of liquid-liquid phase separation during cooling [38].

2.3.3 Calcium and magnesium alumino-silicate glasses

Ca-Al-Si oxide and Mg-Al-Si oxide glasses have been well studied in geological circles due to their importance in cooled silicate magmas, however, the structural role these elements play and by extension, the properties of the resulting glass are still applicable to the glasses discussed in this review. These compositions often easily crystallised into similarly composed polycrystalline materials such as enstatite ($MgSiO_3$), wollastonite ($CaSiO_3$), diopside ($MgCaSi_2O_6$), and various spinel's ($MgAl_2O_4$) [13]making these glasses of particular interest for GCMs.

The structural role aluminium plays in a silicate network, both network modifier and former, can have several effects on the final properties of the glass containing Al as a major component, such as melt viscosity, T_g, durability [39], and various physical properties such as hardness. For this study, the effects on durability is of importance.

The oxidation state of Al as a network former, specifically $Al^{4+,}$ results in an oxygen co-ordinated aluminium tetrahedron (AlO_4^-) with excess negative charge. This excess charge allows the incorporation of alkali and alkali earth cations without the creation of NBOs should enough Al be present, and the very least reduces the number of NBOs. Mg and Ca importance in glasses stems from their ability to create twice as many NBOs as their alkaline metal cousins, this of course means that twice as many Al/B tetrahedra are needed to prevent this [40]. Although this would suggest a reduced chemical durability, making them unsuitable for nuclear waste glasses the opposite can be true. Paul found that the addition of calcium and magnesium improved the durability of the parent glass [41] although it has been noted that silica extraction increased when the CaO content was greater than 10 mol%. It was suggested that this was due to micro phase separation [42] however the co-ordination of these elements, and thus the resulting glass properties (durability), is dependent on the presence of other elements; Na (20 mol%) and large amounts of Al (50 mol%) were found to alter these [43,44,45]. Thus, it is inadvisable to extrapolate properties for calcium magnesium aluminosilicate (CMAS) glasses to those of other glasses with different compositions, rather use them as guides as to the potential properties these elements might impart.

It has also been seen that Calcium-Aluminosilicate glass compositions have formed GCMs with properties such as high hardness, good abrasion, and a low thermal expansion co-efficient [46], however glasses with low Ca/Al ratio and low SiO_2 were observed to have poor corrosion resistance in alkaline media [47]. CMAS compositions have been seen to devitrify easily forming a diopside and anorthite GCM [48], which was found to have good durability, especially in acidic regimes [48].

The thermodynamic effect of CMAS and CAS glasses are well known to be related to the atomic structure of the glass, and relate to the melt viscosity, diffusivity, and density [49, 50, 51] however the exact nature of how these properties are effected is still being researched. Al has been shown to affect the melt properties much more than that of silicon [52] causing an increase in the melt viscosity with the addition of Al, up to a maximum when the CaO: Al_2O_3 reaches 1:1 [53] and originates from the conversion of NBOs to BOs. The substitution of Mg in place of Ca can have a large effect on the properties of both the melt, and the final glass [54] due to the smaller ionic radii

and larger field strength of the ion. Comparative thermochemical studies on Magnesium-Aluminosilicate glass versus CAS glass have shown that former stabilises at a lower temperature [55].

2.3.4 Iron silicate glasses

The role iron plays in the structure of glass is not simple, it can act as a modifier or network former and can often do so at the same time [56] due to the variation in the ratio of Fe(II) and Fe(III) which leads to differently co-ordinated Fe. Various studies have been performed to assess the role and effect it plays and it has been shown that many variables effect its role such as preparation, oxidation state, concentration of iron and concentration of certain elements [56, 57, 58]. It is due to the oxidation state that in most cases it will change its role. Fe^{3+} will act in an almost identical method to that of aluminium bringing the same benefits [56]. However, Fe^{2+} can lead to 6 co-ordinated Fe which leads to weaker bonds and does not integrate into the network as strongly as that as AlO_4^- and FeO_4^- [56]. The lower durability for Fe(II) can be partly related to the bond strength, with Fe(II) having an ionic field strength of 32.8, compared to 54.5 for Fe(III), for reference, Na is 9.8 and Si ,100 [59]. It has been seen in iron phosphate glasses that the relative durability of these glasses increased as the amount of Fe(III) in the glass increased where a direct relation between the bond strength and Fe coordination was observed using XPS and Mössbauer spectroscopy [60]. The increase in durability was seen to occur due to less 6 co-ordinated iron in favour of a Fe-O tetrahedron creating the stronger Fe-O-P bonds, instead of P-O-P bonds (where P is a phosphate tetrahedron). However, it was noted that small amounts of Fe(II) in the phosphate glass could be beneficial, but from a glass forming perspective rather than for durability. The removal of iron from silicate glasses has previously been shown to be low in alkaline solutions with no known anionic species of hydrated Fe_2O_3 until a pH of 13 is reached, lower than most leaching experiments [61]. In fact the main reason attributed to the apparent increase of Fe removal as a function of ph was due to the removal of the silica network. In general, small amounts of Fe in glasses (>5 mol%) will have a negative impact on the durability due to a high amount of Fe(II) whilst amounts larger than this will increase the durability due to an increased ratio of Fe(III): Fe(II) [56].

Similar to Fe(III), Al(III) also has a detrimental effect on the durability of the glass. The formation of Al(III) is different from that of Fe, in that it has only been seen to occur when the sum of the alkaline and alkaline earths is insufficient to provide charge balance of the AlO_4^- tetrahedron, where it forms 5, and 6 co-ordinated Al [62]. The decrease in durability is the same as that of Fe(III) in that it stops becoming a network former and starts modifying the network creating NBOs and weakening the network. However, as the mechanisms of formation between Fe(III) and Al(III) are different, the formation of Al(III) is less of an issue due to the requirements necessary for its formation.

Evidence shows that iron can have a nucleating effect, instigating iron crystalline phases such as maghemite and magnetite, further, it was seen that when added to glasses that had seen previous crystalline products, that those products were replaced with iron oxides such as franklinite ($ZnFe_2O_4$) [63]. This aspect of iron, alongside other nucleating elements (titanium, chromium, vanadium) is of great importance for formulations of GCMs.

2.4 Corrosion in Glasses

Corrosion of glasses in pure water has been well studied [64,65,66]. For neutral conditions (such as in near surface repositories) diffusion controlled ion exchange reactions between the water and network modifiers occurs first, either H^+ or H_3O^+ exchanges with network modifiers, the order of which can usually be determined by bond strengths and ionic radii, the alkaline metals are usually the first to go (sodium for example). This process leads to an increase in pH (in a static environment) of around pH 9 and above (composition dependant). At this alkalinity network hydrolysis occurs [67] leading to breakdown of the silica network. Hench et al. [68] described the 5 dissolution mechanisms of glasses in aqueous environment, illustrated in Figure 2 and summarised below:

1) Type 1 dissolution is where the ratios of elements in the leachate are the same as those in the bulk glass. This results in an extremely thin (>50Å), hydrated layer of glass which is considered stable. Whether this stability extends to geological time scales has not been established. This layer forms through crystallisation or silica network dissolution leading to a surface similar to that of the bulk [69].

2) Type 2 surfaces develop a silica rich film from alkali ion removal. This layer protects the bulk glass from further dissolution and network hydrolysis. Ménard et al. [70] found that kinetics for this type are based on $Q = kt^{1/2}$ where Q is a rate (s) "k" is a rate constant "t" is time due to diffusion controlled alkali loss.

3) Type 3 dissolution leaves a surface that is also protective but the protection mechanism originates from dual surface layers such as an alumino-silicate on top of a silica-rich layer; this imparts enhanced durability. Kinetics for this type is also diffusion controlled with a $t^{1/2}$ relationship.

4) Type 4 dissolution starts similar to type 2: a silica rich film begins to develop. However, this is not sufficient to prevent de-alkalisation or network dissolution.

5) Type 5 dissolution is the most detrimental and glasses undergoing this type of attack show congruent dissolution; the composition at the surface is nearly identical to the bulk. Kinetics are linear with a Q=kt dependency making this the most undesirable corrosion mechanism for nuclear glasses.

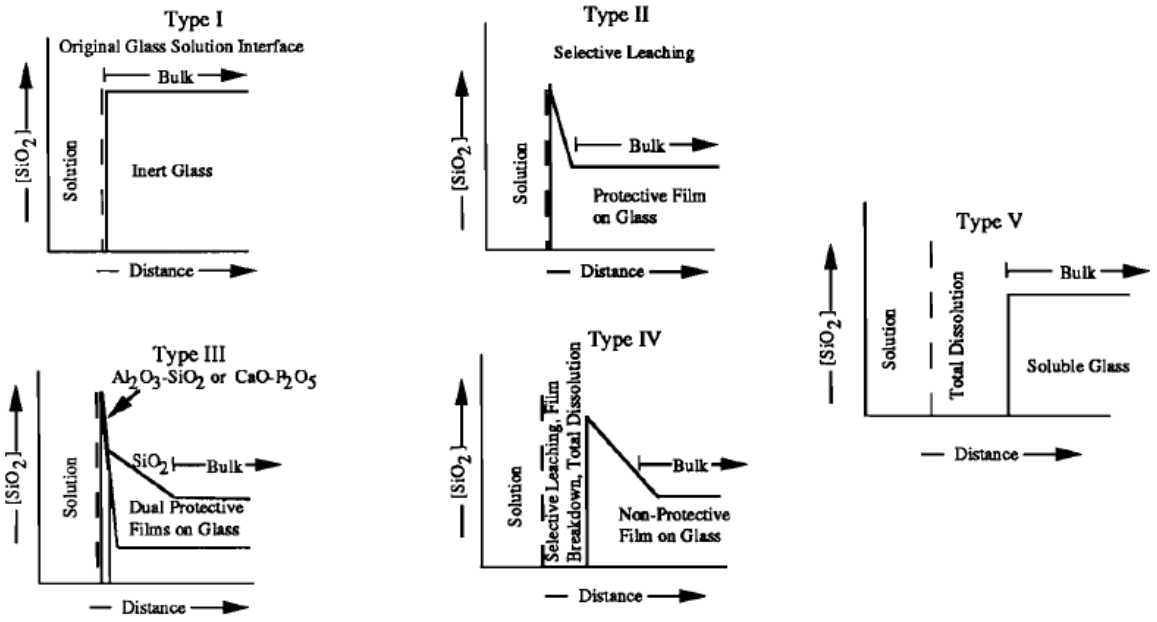

Figure 2: The 5 types of corrosion of glass in aqueous environments shown graphically as Silica content versus depth from the original glass surface, as outlined by Hench et al. [68]. Additions to this model have since been made

Continued work on glass corrosion presents new advances in our knowledge of how glass reacts under aqueous corrosion conditions. Work on the concentration of ions in solution during corrosion glass studies led to the conclusion that 5 subsequent rate regimes are possible during glass corrosion: initial corrosion rate (diffusion/inter-diffusion), the initial or forward rate, a slowing of the initial rate, the residual rate, and optionally a renewed increase in the corrosion rate [71]. As was mentioned by Frugier et al. the underlying mechanism attached to these rates are often complex and unfortunately open to multiple interpretations [72]. As these rate regimes form the basis for modern corrosion glass models, each stage will be discussed in turn.

The initial regime is a result of inter-diffusion of the mobile cations in the glass network (network modifiers) with the highly mobile protons in the attacking solution. This ion exchange was already revealed by Doremus [73], and has been more than satisfactory to describe the initial rate observed in all glass corrosion experiments since its publication in 1975. However, this initial regime has been altered slightly since; only network modifiers were thought to diffuse through the matrix in this regime, but research since has shown this is not the case [74], where boron (a network former) was also released into solution. These seemingly contradictory results show that although the model of ion exchange has proven well for predictions, the actual mechanism was more complex. Geneste et al. reconciled this by showing that ion exchange causes a major “shuffling” in the network forming ions around the ion exchange site due to the inability of the H^+ to fully compensate for the alkali ion removal, which resulted in the removal of network formers from the matrix [75].

The second regime, the forward rate, signifies the beginning of network attack, causing disruption to bridging bonds causing network hydrolysis and depolymerisation of the silica network. The result of this hydrolysis leads to the formation of 2Si-OH bonds at the glass surface, and the release of

orthosilicate acid (H_4SiO_4) into solution. A model describing process this was developed by Boksay et al. [76], however other models have been developed around various relations such as the number of non-bridging oxygens [77], a thermodynamic model based on enthalpy of formation and structural role [78], and a thermodynamic model based on free enthalpy of glass hydration [79]. However as was pointed out by Frugier et al. these explain trends seen only for a narrow range of compositions.

Following this regime, a rate drop is observed, two competing theories exist one centred on the chemical affinity of the initial glass [80], the other on the protective nature of the gel layer [81]. These competing theories were shown to not necessarily be mutually exclusive and their combination led to the current model of glass corrosion; a chemical different depolymerised surface layer (gel layer), and a leached zone from the mechanism already discussed.

Glass corrosion experiments observe a drop in the corrosion rate after a certain amount of time, reaching a plateau in pH and in ion concentrations in solution which has been termed the residual rate. This residual rate has been described by the difficulty in further removing ions from the glass due to the presence of an already hydrolysed layer between the attacking solution and the pristine glass, in which diffusion of ions is more difficult than in the pristine glass, and additionally, due to the precipitation of secondary phases due to a locally saturated solution [74]. No additional theories on this regime, to the authors knowledge, have been confirmed due to the success of these theories in accounting for observed experimental evidence, and in predictions.

A final rate regime has been observed, but not consistently, following the constant rate described previously, known as the “resumption of alteration” and describes a phenomenon whereby corrosion rates resume at similar, or even greater, rates than in stage II. In borosilicate glasses this has been described by the precipitation of zeolitic phases [82]. These phases cause the gel layer to no longer be protective, and have been postulated to occur when a specific pH is reached and when the precipitation itself is self-sustaining, although no kinetic model has been developed to describe this process [72].

Other theories have been developed; one such theory postulated that the corrosion mechanism is due to an interfacial-dissolution-reprecipitation [83], whereby the glass is stoichiometrically dissolved, and reprecipitates as an amorphous layer onto the newly formed glass surface without “inter-diffusion ion exchange controlling the glass reaction front” [84]. Work by Hellmann et al. used nano-scale analysis techniques and found this theory is not without merit, however further work is needed before 20 years of work towards our current glass corrosion is changed to include this new evidence.

2.4.1 Pitting corrosion in glasses

Pitting corrosion in metals is a well-known phenomenon, whereby a localised and accelerated form of corrosion occurs on the surface of the metal, due to localised increased concentrations of anionic species, in most cases, chlorine [85]. Whilst the underlying driving mechanism for this type of corrosion in metals is unlikely to apply in glasses (galvanic corrosion), the idea of an area that has accelerated, and localised, corrosion compared to the main surface of the material is of particular interest, especially in GCMs where crevice corrosion will be of more concern. Even without any chemical driving force for accelerated corrosion in cracks or pits, the driving force for localised

accelerated corrosion is readily apparent; these areas will increase the surface roughness, resulting in a potentially large increase to the SA/V ratio. It is well known that glass fines corrode at a much faster rate than an equivalent mass as one particle. However, it could not be readily established from current literature how damaging these pits can be to the glass in the long term, as most literature reviews how pits effect the optical properties of glass [86], or on the increased surface roughness [87].

Hench and Clark [88] found that scratches in the glass surface can eventually lead to pit formation in glass; the increased surface area resulting from scratches deeper than 0.2µm results in increased pH leading to faster degradation of the glass matrix in that area, leading to pit formation. Whilst this might appear as a chemical reaction, the driving force was kinetic; the increased surface area from the scratches/pits.

A study on the corrosion of a medieval composition glass revealed pitting [89], however they defined the pits that formed as spherical in nature, appearing as craters rather than the enclosed pits seen in metals. Further results revealed these pits favoured microbial attack, causing hairline fractures in the glass causing severe degradation of the glass structure. Whilst this type of corrosion is not within the scope of this review, there is little reason it does not apply to nuclear wasteforms following burial or surface storage (following failure of all other engineered barriers).

2.5 Effect of Fe on the corrosion of glass

Once the waste has been either immobilised or encapsulated in a GCM, it will then be placed in a carbon steel container, and from there into a GDF, where it will be backfilled with various materials designed to extend the lifetime of the waste before exposure to groundwater. The last barrier to fail is that of the carbon steel container, in which the glass or GCM will be. As this barrier is unlikely to corrode congruently, the GCM will first be exposed to a water enriched in iron. Whilst this thesis does not investigate the effect of simulated iron-containing water on the corrosion of GCMs, the effect that iron in solution has on the durability of these materials is of importance due to the presence of iron in some GCMs which will be leached into solution, possibly creating a locally iron saturated solution, not dissimilar to the water exposed to a corroding canister. To this end literature on the studies of simulated iron-containing water is reviewed.

Simple tests on all GCMs begin with the assumption that all other barriers have not only been breached but no longer affect the groundwater or environment, ignoring the possibility of additional elements in solution, precipitates from the corroded barriers, or pH changes (i.e. from alkaline cement). Following distilled water corrosion tests, the next logical step is to fully simulate the environment that the waste material will be subjected to. As the last barrier before the waste matrix will be the steel container, it is reasonable to assume that the characteristics of the resulting water will be significantly influenced by the corrosion of the canister.

Whilst one of the criteria for the nuclear waste canisters is a reasonable congruent corrosion [90] for whichever metal is selected, however it is realistic to assume that corrosion will not be fully

congruent and some areas will be fully exposed to the wasteform before others. The corrosion of a ferrous canister will lead to a local change in environment, and in the reducing conditions of a GDF will encourage the precipitation of iron oxides such as magnetite [91]. For the wasteform that is exposed, it will not be subject to deionised water, or even standard simulated water used in other studies but by a water with iron ions and corrosion products, not to mention the possibility of other barrier relics. There have been some studies on the effect that this may have on glass corrosion but no literature regarding the same effect on GCMs could be found.

Many different environmental conditions are possible for a GDF and all scenarios assume that the corrosion of the canister will be in an aqueous media. At its most basic the reduction of iron to iron oxide when in the presence of water is extremely well known and gives the simplest of equations:

$$Fe^{2+} + 2\,H_2O \rightleftharpoons Fe(OH)_2 + 2\,H^+ \quad (1)$$

$$Fe^{3+} + 3\,H_2O \rightleftharpoons Fe(OH)_3 + 3\,H^+ \quad (2)$$

The chemistry behind the corrosion and precipitation of iron and iron hydroxides in a GDF was reviewed by Biederman and Schindler [92] who cited the following reaction to occur:

$$Fe^{3+} + 2H_2O \rightleftharpoons FeOOH\ (s) + H^+ \quad (3)$$

Tests were performed at room temperature and in an acidic environment, however it has been reported that in an alkaline environment this phase still forms, along with several others, $FeCO_3$, α-FeOOH, β-FeOOH, γ-Fe_2O_3, Fe_3O_4 [93] the formation of these in GDF conditions was summarised by King and Padovani in Figure 3.

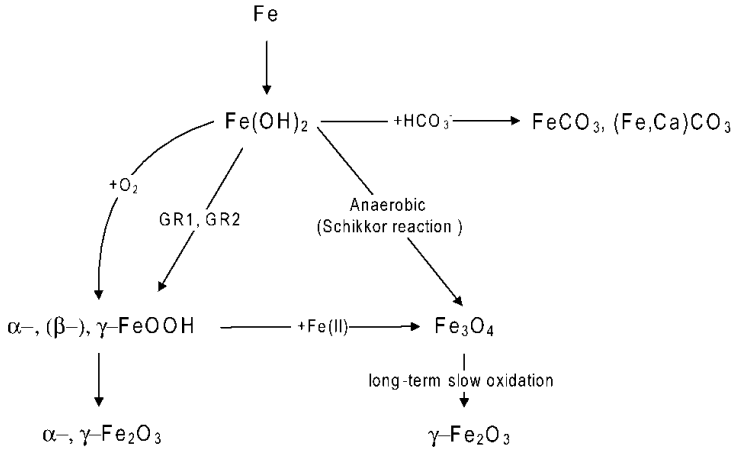

Figure 3: Progression of iron in anaerobic and carbonate conditions, showing which phases occur under what conditions. It is thought these are likely to occur in a GDF environment [90].

The effect on glass leaching of aluminium, copper, lead, tin and titanium was studied by Buckwalter and Pederson [94] who showed that only lead and aluminium had any meaningful effect on the leaching, with aluminium causing a reduction in leaching and lead was found to stop corrosion completely. It is clear from this study that neglecting the composition of the groundwater, both at the time the GDF is full and closed, and for future easily anticipated events, would be a mistake.

McVay and Buckwalter [95] used ductile iron in a 90 °C MCC-1 test with Pacific Northwest National Laboratory (PNNL) 76-68 glass to assess the effect it had during short term leach tests, several types of water were utilised to allow comparisons, the leach rates of which can be seen in Figure 4. The effect of iron in solution is clear, increasing the normalised leaching rate after a few days for all the waters. As might be expected from these results, the leached layer on all Fe-waters showed varying increases in the leached layers for the same leaching times. Gel thickness was 9, 5, and 1 µm for deionised, tuff and basaltic waters without iron, and 14, 13, and 13 µm for the Fe-enriched versions.

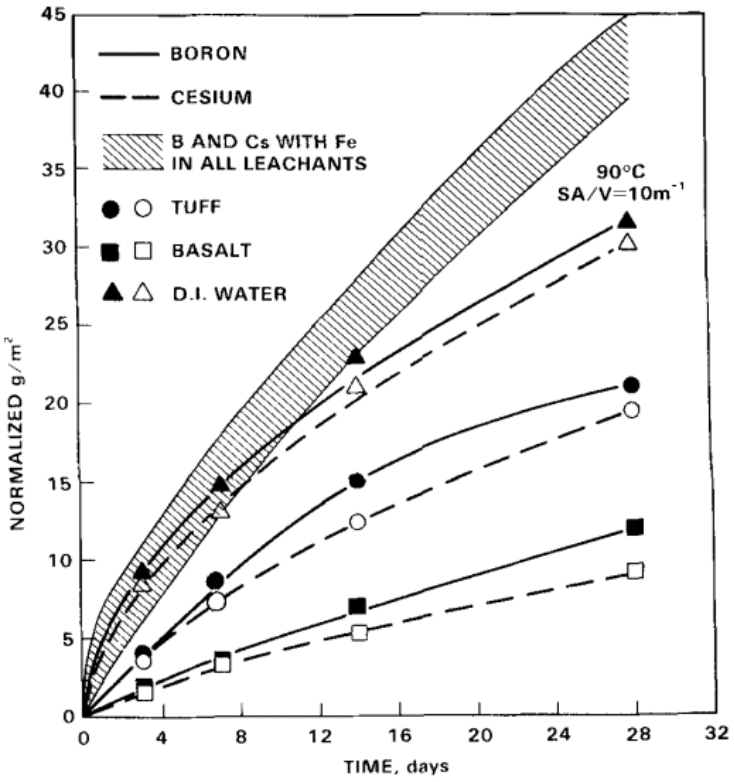

Figure 4: Normalised leaching rates of boron and cesium in various simulated ground waters as a function of time [95].

Investigation of these samples showed precipitation to occur, based on the particles forming only on the top of the sample (not the sides) and EDX study of the elements found silicon in addition to the iron. This was the main explanation for the increased leaching, higher pH (0.5 pH higher on average), and thicker gel layer; as silicon was removed from the glass it reacted with the iron forming iron silicates which helped remove further elements within the glass.

Detection of iron ions in solution was unlikely due to the formation of colloids and precipitation directly onto the glass and original iron block. Iron was expected to form variations of iron hydroxide and iron silicates once removed into solution, these particles were removed by the filters used for ICP analysis. These formed particles over not just the glass, but the iron block as well, this was found to accelerate the corrosion of the iron leading to a synergistic effect which could mean that once some glass is exposed to groundwater what is left of the canister could suffer increased corrosion, further reducing the life time of the canister.

2.6 Crystalline Wasteforms

Glasses have been the primary choice for nuclear waste immobilisation due to the aforementioned properties, and in addition have already been proven effective as a waste matrix with actual radionuclides. At the start of the nuclear era little thought was given to the use of polycrystalline or polyphasic materials as a wasteform however in the last 60 years, excepting novel wasteforms such as GCMs, only one ceramic was researched in any detail, that of Synroc. It is unsurprising that little thought has been given to other potential crystalline materials as no full-scale production method has been fully proven to be a viable alternative to borosilicate glass, or more effective a waste matrix. Whilst it is true that certain crystalline materials prove more effective at immobilising certain waste elements than glasses [96] or have shown similar leaching times but much higher waste loadings, no one crystalline wasteform has shown the durability, ease of production and overall waste loadings (over all elements) as that of glass.

Synroc, however, has shown great promise for the immobilisation of specific wastes and may be considered for widespread use in the future, should research show it is wiser to do so.

2.6.1 Synroc

Synroc polycrystalline ceramic was first researched in America (where it was called supercalcine) but was dropped early on as a wasteform after the success of borosilicate glass, Australia continued development eventually building a full-scale plant to immobilise wastes from medical isotope production. Following this, several other countries also invested research into various aspects of Synroc, such as Japan, China, UK, and Russia.

Synroc itself is a titanate based polyphasic ceramic and can be further subdivided into Synroc-A to Synroc-E. All contain hollandite ($Ba(Mn^{4+}_6Mn^{3+}_2)O_{16}$), perovskite ($CaTiO_3$), and zirconolite ($CaZrTi_2O_7$) but Synroc-A has Ba-feldspar kalsilite ($KAlSiO_4$), and leucite ($K[AlSi_2O_6]$) in addition. Other variations of Synroc exist (such as synroc-C, or D) but are less studied. Other phases have been reported, such as pyrochlores, aluminates, titanates, and noble metals [97]. Each phase is specialised for immobilising a specific set of elements allowing high waste loadings, but outside of this small number of elements, have little to no solubility.

The polyphasic nature of Synroc has led to certain difficulties in determining a dissolution rate for the wasteform as a whole. Ringwood et al. [98] performed a study showing that caesium was mostly retained in hollandite which was found to have extremely impressive retention of the element, apart from small areas at the extremities of the sample which turned into rutile losing all of the immobilised element. The nature of this retention was due to the strong bonding of barium (2+) in the crystal structure at susceptible areas effectively stopping the ingress of leaching elements. It was observed however by Lumpkin et al. [99] that of all the major phases present, hollandite was the most susceptible to dissolution. Further, the most susceptible phases were found to be the minor phases and relicts from processing such as beta alumina type phases, Al relicts, intermetallic alloys particles and perovskite [99]. This leads to a further complication when determining leach rates for such a multi-phasic matrix, as each phase will have its own leach rate (and possibly corrosion mechanism) thus it is either assumed all leach/dissolve at the rate of the most susceptible phase or,

as was assumed by Smith et al. [100], an average is taken based on the weight loss of the matrix as a whole. This issue is obviously applicable for GCMs as well, which may have even wider disparity in leaching and dissolution rates for the individual phases. In addition to this issue, was the rate at which each phase releases its constituent elements; Synroc usually has its waste elements in more than one phase, hollandite and caesium are an exception to this rule. Determining which of the phases is leaching a certain waste element more than the other can be challenging, not to mention the reason for the preferential release.

Lumpkin et al. [99] used the following formulae to determine the overall leach rate of the Synroc they investigated:

$$X = \frac{\Delta m}{\rho\,(SA)} \tag{4}$$

where X is the thickness of the material dissolved from the sample, Δm is the difference in mass before and after dissolution, ρ is the density, and SA is the surface area subject to attack.

Although the main result was the average over the whole sample, a "worst case scenario" (WCS) for the dissolution rate was also given based on the corroded depth of the most susceptible phase-beta alumina. The average was 0.1 nm a day whilst the WCS was 0.9 nm over a 552 day period. It is clear that there is a large disparity in these results and that both should be reported when working with multiphasic materials or glass composite materials.

2.7 Corrosion of Ceramics

Generally speaking, the corrosion behaviour of all materials can be divided into three groups: (1) electrochemical, (2) chemical, and (3) mechano-chemical corrosion.

Chemical corrosion of ceramics is the most studied case of corrosion in aqueous environments and includes several steps: (1) reaction (dissolution) of grain boundary phases; (2) water transport along grain boundaries into the bulk of ceramics, which is often accompanied by phase changes in the grain boundary phase; and (3) reaction (dissolution) of ceramic grains. The corrosion of ceramics and crystalline materials has been studied using simple reaction kinetics and the principle that the slowest of the steps involved for corrosion is the rate limiting step. The 5 steps given for this corrosion are transport to the surface, adsorption of the reactants, chemical reaction between adsorbed species and the crystal surface, desorption of the reactant products, and transport of the reaction products into solution.

Provided that the dissolving solid comes into equilibrium with the leachant, the following two equations were given by White [101]:

$$\frac{dC}{dt} = \left(\frac{V}{SA}\right)k_S(C_S - C)^n \tag{5}$$

$$Rate = \left(\frac{V}{SA}\right)\left(\frac{dC}{dt}\right) = k(1-\Omega)^n \tag{6}$$

$$\Omega = (ion\ activity\ product)/(solubility\ product\ constant) \tag{7}$$

Where Ω is the saturation ratio defined as Equation 7, “n” is the order of the reaction, and “k” is the reaction rate constant. V is the volume of leachant (l), SA the surface area exposed to attack (cm^2), C is the concentration of ions in solution (g/l) and C_s is the saturation concentration, and t is the time (days).

2.8 Production methods

Vitrification technologies for HLW have gone through several iterations and technologies as described by Ojovan and Lee [130] before we reached current technologies. Out of all the technologies researched, two were adopted on an industrial scale for use to immobilise nuclear waste. The first, developed in France (1978), later adopted and modified by the UK, was termed the AVM process (Atelier de Vitrification de Marcoule) and is a two-step process. First the liquid waste was fed into a rotary calciner, the resulting solid waste then fed into an induction heated melter where it was immobilised into glass. On the other hand, the USA (among others) adopted joule heated ceramic furnaces to treat its liquid waste in a one step process rather than two, negating the need for a calciner, but the melter in this process is required to deal with the off-gas. Whilst these describe HLW, certain UK ILW (such as wet wastes, high organic content wastes, and sand filters [102]) have been investigated for immobilisation in glass rather than encapsulation in cement, using either of these techniques.The technologies used in the following experiments, were those of plasma Vitrification (PV) (Tetronics International, Marston Gate, South Marston Park, Swindon, Wiltshire SN3 4DE UK) and Joule Heated Ceramic Melters using GeoMelt (Kurion, corporate headquarters, 2020 Main St., Suite 300, Irvine, CA 92614, USA). Both techniques are explained below.

2.8.1 Plasma Vitrification

An emerging technology for waste processing is the use of thermal plasmas in vitrification of hazardous waste from various fields including refractory processing, medical usage, and nuclear waste immobilisation.

Plasma is the fourth state of matter, and is similar to that of a gas in that it homogeneously fills the container it is in. The plasma itself is electrically neutral but the electrons have been dissociated with their atoms becoming an electron/ion pair, and can be further divided into cold and hot/thermal plasmas, only thermal plasmas being of interest. The interest in plasma has risen lately in fields such as coal fly ash [103,104], medical [105], for pyrolysis of various liquid and solid wastes [106], and for various nuclear waste materials.

The primary reason for the industry looking towards plasma based solutions for waste treatment arises from several unique advantages plasma offers [106]:

1) The plasma high temperature offers higher operating temperatures allowing for certain wastes that normally would need to be encapsulated, to be vitrified.

2) Plasma can destroy volatile organic gases that would otherwise need filtered and adsorbed to water or filters causing additional waste.

3) ILW or LLW typically need pre-treatment to separate wastes; chemical, combustible, and metallic, mostly due to the incapability of normal incinerators to process all of these, however plasma vitrification can successfully vitrify all of these simultaneously.

4) Relatively simple to run, no calciner or other components are needed.

5) Offers waste size reduction.

6) Furnace is generally smaller than other melters for the same throughput.

Downsides to plasma include the large amount of electricity consumed (0.57kWh/kg for typical coal incinerator [107] versus 1.5kWh/kg for a DC double arc argon plasma melter [103]) and the perceived unreliability of the technology [106].

Current technology revolves around a plasma torch, a continuous input of electricity is used to create an electrical arc between two electrodes the high resistivity of the surrounding gas causes it to heat up and with the continued input of gas and electricity temperatures exceeding 20,000K have been reported [106]. Three different types of torch exist, however the most thermally efficient is the one currently being considered to destroy nuclear related waste [108,109] termed a direct current transferred plasma torch.

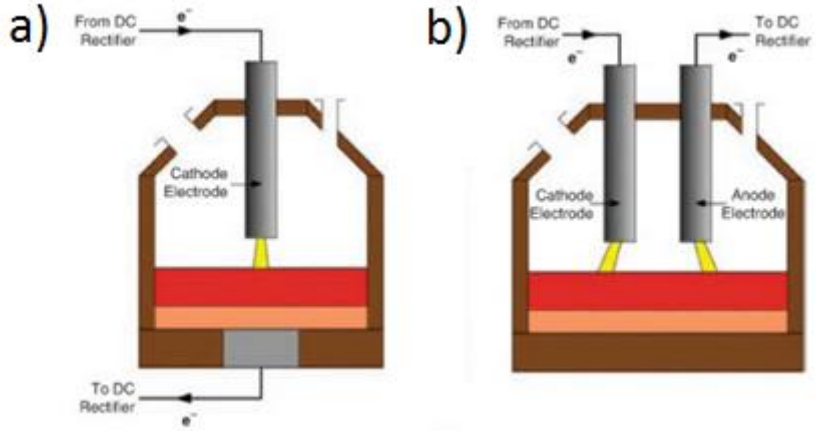

Figure 5: Principles of two types of plasma furnace, using either a) single electrode where the second electrode is placed at the base of the furnace creating a conductive pathway through the melt, or b) a dual electrode configuration [110].

Several companies are working towards plasma based hazardous waste disposal, one of which is Tetronics; they use a twin electrode skull plasma reactor to destroy a wide variety of wastes. Their reactor consists of two graphite plasma torches, one the cathode and the other the anode. The input of electricity between the electrodes ionises the argon gas which is constantly fed into the reactor, this results in a zone of plasma as seen in Figure 5. Waste is continuously fed into the reactor whilst the skull melting technique is used to avoid the various issues associated with a refractory container such as secondary waste and monetary cost from removal and replacement of the refractory tiles.

The ability to control the parameters of the reactor (heat and chemistry) can allow for a more flexible method of waste disposal, allowing optimisation of the final wasteform.

2.8.2 Joule Heated In Container Vitrification

The main principle of this type of vitrification is that of resistive/ohmic heating, whereby any conductive material with resistance produces heat when subject to an electrical current dependent on the resistance of the material and as a function of the square of the current.

Melters based on this technology use the high electrical resistance of glass frit and its waste (either liquid or solid) to produce a high temperature (1000-1800 ^{o}C) environment. The general principle is that containers have two electrodes submerged in waste and glass frit. A high electrical current is passed through the solid glass and Joule heating is dissipated as heat into the surrounding glass/waste eventually turning the entire batch into a liquid.

The whole process can be used in a continuous or semi-continuous fashion, and in addition offers the benefit of being a one-step procedure which allows it to be applied in-situ to wastes that are not suitable for transport; one such example is the in-situ trials done at Hanford of contaminated soil [111].

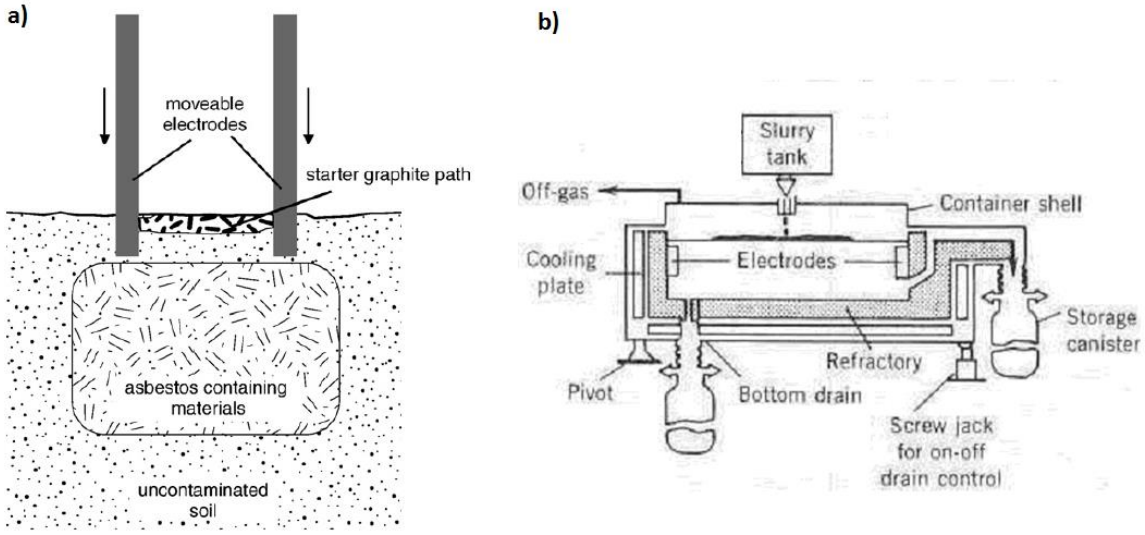

Figure 6: Showing two common methods for treating waste using joule heating methods, either a) in-situ treatment, processing waste material in the ground common for disposal of legacy hazardous landfill sites and b) in-container for the treatment of silo stored wastes [112].

The process used in the in-situ method uses a “top down” strategy; here the electrodes are gradually lowered into the waste (Figure 6a). They start at the surface melting the starter graphite path into a liquid, which provides the conductive path necessary for it to continue heating its surroundings, the electrodes then melt the surrounding soil/waste and sink into the liquid waste. This process continues until the waste is fully vitrified. GeoMelt uses the in-situ technology for its in-container waste processing, and for the samples used here a batch experimental run was used.

2.9 Glass Composite Materials

The benefits of both glasses and ceramics as wasteforms have been summarised earlier, each have their own strengths and weaknesses. The idea of combining these two materials in such a way that we could acquire both their strengths and use one material to cover the weakness of the other is appealing. Lee et al. have made an excellent review of nuclear wasteforms, including GCMs [5].

GCMs must be separated into three distinct sub categories: glass ceramics, glass encapsulated crystal waste, and crystal containing glasses from the processing. These are discussed in the following sections.

2.9.1 Glass ceramics

Glass ceramics are defined by the method of production; these materials are produced intentionally by using a second heat treatment on a glassy wasteform to encourage nucleation and crystallisation. Of all the three categories, these are the most studied as they have many applications outside of the nuclear industry such as dental (fillings and coatings), ceramic glazes, cooker tops [113], and even as mirrors for space applications [114].

2.9.1.1 Phosphates

Except for the Russian sodium-aluminium phosphate glass, nuclear glasses for HLW can only cope with small phosphate loadings (max solubility 2-3 wt% for P_2O_3 [115]) however often these loadings are much less than the solubility limit to dilute the element and its negative effects on the glass properties. The disadvantage of dilution is an increased waste volume, which in turn will make production and final disposal in a GDF more expensive, making such a disposal route undesirable.

Sengupta et al. (2012) established that although several ideas had been proposed, no research has been directed to solving the problem of stability of phosphate glasses, and any phosphorous containing waste, mainly due to a complete lack of understanding of the difficulties associated with this waste. Sengupta et al. summarized others work [116, 117, 118] to demonstrate that even small amounts (1-2wt%) of phosphate wastes in borosilicate glasses caused liquid immiscibility, trace element partitioning, reduction of melt viscosity, depressed solidus and a shift in the liquidus boundaries towards a silica deficient domains with variably polymerised silicate melts.

Whilst glasses cannot immobilise large amounts of phosphate wastes (3wt% maximum), ceramics based on phosphates have good long term behaviour and a high incorporation capacity [119,120] making their feasibility as a GCM relatively appealing. The use of a nuclear GCM based on a phosphate ceramic above laboratory use has not been addressed to date and remains an area of research [115], although uses have been found outside this field including biomedical applications and electronic packaging [121].

2.9.1.2 Titanates

Zirconolite ($CaZrTi_2O_7$) has long been studied as a waste matrix for the immobilisation of various actinides and lanthanides and was in designed to be the most durable phase in Synroc for the immobilisation of plutonium having a good leach resistance and resistance to radiation-induced amorphisation [122].

Experiments on the SiO_2–Al_2O_3–CaO–ZrO_2–TiO_2 system incorporating lanthanides and actinides and processed into a zirconolite-glass ceramic via a two-stage heat treatment have been performed to assess the material as a wasteform [123]. With a variety of surrogate oxides (Ce_2O_3, Nd_2O_3 ,Eu_2O_3, Yb_2O_3, ThO_2) only zirconolite formed in the bulk at 1050 and 1200 ^oC. Loiseau et al. [122] showed surface crystallisation of several other phases. The phases observed were titanate ($CaTiSiO_5$), anorthite ($CaAl_2Si_2O_8$) , baddeleyite (ZrO_2) and small crystals of thorium dioxide (ThO_2). The thickness of these crystals was dependant on the heat treatment, at 1200 ^oC they were up to 1000 μm thick [122]. These results agree with Caurant et al. [124] who found the same phases with the exception of thorium dioxide (as their samples contained no thorium). Further, it was discovered that zirconolite was replaced with titanate crystals for long heat treatment times (4 h+) making it appear that zirconolite is not a thermodynamically stable phase [124] although it is assumed that like glasses, decomposition kinetics are greater than the expected life time of the waste.

Study of sphene ($CaTiSiO_5$) as a waste matrix has mostly been done in Canada for safe disposal of HLW produced from their CANDU reactors as sphene has been shown to be particularly stable under the saline ground-water conditions present at GDF depth. Research on sphene, and sphene glass ceramics has been going on since 1984 [125], it shows promise as a wasteform being thermally stable in the envisaged Canadian environment (T<423K) and it has been found to have a better leach resistance than that of borosilicate glass [126]. However, study on the radiation resistance of sphene found that its structure does not cope well under irradiation, and was 2-3 times more susceptible to alpha recoil damage than zircon, but interestingly, does not seem to undergo amorphisation [127] although results on this are not fully agreed upon [125].

Formation of sphene glass ceramics varies from composition to composition but generally the expected melting temperature for the material is around 1300-1350 ^oC [128] and along with reasonable viscosity leads to compatibility with a Joule Heated Ceramic Melter (JH-CM). However, it was noted that the high temperatures, whilst capable for a JH-CM, are not conducive towards limiting volatilisation. Hayward et al. [128] used two compositions and studied their progression under XRD as a function of temperature. Fluorite structure (believed to be $Ca[U,Ce]Ti_2O_7$) formed in the first composition and wollastonite ($CaSiO_3$) formed in the second, and that both these phases recrystallised into sphene at around 1000-1150 ^oC.

A leaching study performed on a sphene glass ceramic showed that waste elements leached out of the glass much more so than the sphene, and additionally the ICP-OES results indicated that the glass suffered more structural corrosion than the sphene [128]. Other studies on sphene, and similar titanates, have shown that they are prone to forming a thin film of TiO_2 over the surface preventing further corrosion. Hayward et al. demonstrated, quantitatively that sphene glass ceramics have a leach rate an order of magnitude lower than that of borosilicate glass.

Many GCMs based on a pyrochlore structure ($(U,Pu,Hf,Gd)_2Ti_2O_7$) encapsulated in a lead glass matrix have been investigated for possible use as wasteform [129,130,131] and it was demonstrated that these wasteforms showed a good tendency for Pu retention, good mechanical strength, good thermal properties (close co-efficient of thermal expansion), and >90% theoretical density's. However, little to no information has been provided on the leaching characteristics of such a wasteform. Leaching characteristics on just the pyrochlore structure, such as zirconolite, have been found to be susceptible to amorphisation under alpha radiation which substantially reduces

the chemical durability. Pace et al. [132] Reported that the transition to a glassy phase occurs in all repository conditions and is predicted to be fully complete after 1000 years. Tests demonstrated that the amorphous form had leaching rates 50 times higher than the crystalline form [23]. It can only be inferred that a glass encapsulated form of this waste would have a higher durability if the two phases did not interact. This GCM serves as a prime example of where a less durable wasteform, with a high waste loading capability, can be safely protected by the relatively superior durability of the glassy matrix.

2.8.1.3 Ca-Mg-Si Glass ceramics

Various waste forms based on calcium magnesium silicates glasses have been used containing various crystalline phases such as diopside ($CaMgSi_2O_6$), powellite ($CaMoO_4$), perovskite [133] (unsuitable due to temperature instability),wollastonite ($CaSiO_3$) and mellite ($Al_2C_6(COO)_6{\cdot}16H_2O$), dependent on the nucleating agent added [134].

Diopside has been examined as a chemically durable phase, however most work has been in the areas of matte glazes [135], dental fillings/coverings and for immobilisation of non-nuclear wastes [136]. This material is highly resistant to aqueous corrosion in the respective fields although the formation of diopside is often accompanied by crystallisation of a relatively less durable phase; anorthite and/or wollastonite [137]. The literature on the use of this material to safely encapsulate/immobilise coal and fly ash waste reported mainly on the mechanical strength and general stability of the glass; Barbieri et al. found that the glass was particularly stable and resulted in a material with higher thermal and strength properties than that of the parent glass [138]. Reports on the durability were reported by Fröberg et al. over 4 days to be below detection limits (ICP-OES) and gave no observable corrosion in the pH range 1.5-13.4 [135]. In contrast, the corrosion of wollastonite (dendritic and columnar), pseudo-wollastonite, and plagioclase showed signs of corrosion up to pH 9.1 after which only dendritic wollastonite demonstrated signs of corrosion. This disagrees with the findings of Barbieri et al. [139] who found that wollastonite had a reasonable durability.

One of the issues with glass ceramics with this composition is the formation of other phases that may not necessarily be wanted. As previously mentioned, some phases are known to form, their durability depending on the author and their definition of a “durable” material. In addition to the aforementioned phases, several other phases have been shown to form such as various iron oxides (haematite, magnetite, and Fe_3O_4), augite, and franklinite. The original diopside/wollastonite glass ceramic bulk crystallised, believed due to the presence of titanium and iron which act as nucleating agents. The iron can also stimulate the production of other phases thus restricting the iron content of these glass ceramics, should those phases not be wanted. Alizadeh and Marghussian [140] highlighted that various elements can affect the nucleation of different phases and how the morphology of the various phases could be altered by slightly altering the composition.

The naturally occurring zeolite, clinoptilolite is used as an inorganic ion exchanger to clean elements such as 90-strontium or 137-Cs from radioactive aqueous solutions. Whilst it proves very effective for cleaning these elements out of solutions containing them, it becomes a secondary waste that must be disposed of. One envisaged disposal route is encapsulation in glass. A 137 caesium clinoptilolite encapsulated in glass was studied by Juoi and Ojovan [141], the leaching rates of the

resulting GCM showed this wasteform to be reasonable, having leaching rates below that of similar waste encapsulated in both Portland and alumina cement. The glass proved effective as a corrosion resistant encapsulate for clinoptilolite and wollastonite, although an issue was formation of percolating clusters for high waste loadings leading to high leaching rates.

A similar study was performed by Bosch et al. [142] however the clinoptilolite was heat treated to attain a glassy phase (where none existed before) in comparison to the study by Juoi and Ojovan [141] where glass frit was added. Contrary to the findings of Juoi and Ojovan, Bosch et al. found that retention for Cs decreased the higher the proportion of glass, achieved by heat treatments of up to 1000^{o}C, however such a heat treatment produced secondary phases (K-feldspar and possibly pollucite($(Cs,Na)_2(Al_2Si_4O_{12})2H_2O$)) although the effect these had on the leaching was not determined. This method of producing a GCM may be preferable if the resulting wasteform is chemically durable, the temperatures are similar to what would be needed for Juoi and Ojovan's method but without the need for glass frit. During heat treatment, little migration of Cs occurred between the clinoptilolite and the glass, Cappelletti et al. [143] on a similarly formed waste showed that Cs was retained in the glassy phase and leaching tests showed low release rates however they also demonstrated the variability of the resulting wasteform based on minor composition fluctuations or heat treatment times/temperatures.

2.9.2 Glass encapsulated waste crystal waste

It is inevitable that certain wastes will require unrealistic processing temperatures to be immobilised in polyphasic ceramics or standard borosilicate glasses, the most prominent example being refractories. If such materials are added to glass frit and fired the result is a glass encapsulated waste, a crystalline waste in a glass matrix. This type of GCM is already being researched [144] and experimental wastes, originally designed to be fully amorphous but did not fully melt, are being found to have a reasonable leach rates suitable for ILW disposal [142].

The formation of water soluble complex molybdates in standard borosilicate nuclear waste glass when present in compositions over 1 wt% has meant the disposal of high-molybdenum content wastes has been problematic. Thus, research is being conducted in other methods to safely dispose of this waste, one such example is the calcium enriched waste glass encapsulated wasteform, which encourages the formation of powellite ($CaMoO_4$) to attain waste loadings of up to 12 wt% [144] a vast improvement over immobilisation in glass. One issue with this wasteform is the formation of secondary crystalline products as a direct consequence of the encapsulated waste; these may compromise the formation of a durable glass (liquid-liquid phase separation) or the sequestration of other waste elements into the less durable phase.

Other elements pose a similar problem, and have also been assessed for encapsulation such as phosphates or halide species. Donald and Metcalfe [145] used such a phosphate ceramic (for halide waste) encapsulated in a ternary aluminium-sodium-phosphorous glass, production of this glass encapsulated waste was by "pressure-less consolidation route or alternatively by cold pressing and sintering of ceramic/glass mixtures" [145].

Perhaps the best example is that of the aforementioned yellow phase, a complex molybdate formation in borosilicate glasses. Under normal conditions the solubility is about 1wt % and above

this it acts as a nucleating agent for various molybdates, chromates, and sulphates. When formed, it depletes the nearby glass of waste constituents, mainly molybdenum and caesium, the resulting phase is water soluble making it extremely undesirable for a wasteform that is supposed to last millennia [146].

2.9.3 Crystal Containing Glasses from processing

When looking into literature of glass composite materials in the context of nuclear waste, you will be sorely disappointed at the results; not much research has been put into this wasteform, and for good reason. Of all the wasteforms metal is by far the worst choice, undergoing electrochemical corrosion, a form that out-paces both chemical and mechano-chemical corrosion. In fact, the only literature on the subject that could be found was that of a patent for such a glass that used the glass a sort of sacrificial phase [147].

A possible scenario for low processing temperature wasteforms is that some metallic species will not fully integrate with the glass matrix and thus leave solid particles of metal waste encapsulated in glass. At the time of writing, no literature on the corrosion of such a composite material could be found, most likely due to the quick corrosion times of nearly all metals used in the nuclear industry; such materials are either fully melted to achieve dissolution and immobilisation into the glass matrix or, for LLW, encapsulation in cement is preferred. As such, it may be necessary to look outside the constraints of the nuclear industry to better understand how such a composite material would react under repository or near repository (ILW disposal site) conditions.

Metals in general corrode via galvanic corrosion, the less noble of the metallic species is corroded preferentially; the scientific theory on this subject is well known and not discussed further [148]. Several ways to reduce or galvanic corrosion is to isolate the metals in an insulating material, such as glass or non-conducting ceramic. Some work has been carried on out on aqueous corrosion of metal-ceramic joints [149] however this was with a ceramic assumed to be a semi-conductor. Perhaps the best idea of such a material is in reinforced concrete, whereby metallic rods are placed in a cement matrix. The steel and concrete have a synergistic relationship; the metal improves the strength whilst the cement helps to reduce corrosion of the steel bars by keeping any pore water at a high pH. Research performed by Gouda [150] demonstrated that the overall picture was not as simple as this, and that several other factors came into play. Solutions saturated with calcium had a passivating effect on the metal whilst solutions with small amounts of chlorine and sulphur ions had a large negative effect on the corrosion of the metal. For reinforced cement, the general idea is that the high pH causes a thin passivating layer of gamma iron oxide to form [151]. Some parallels with glass encapsulated metallic waste can be made, such as the pH environment the exposed metals will be subject to, or the reaction with ions in solution to form a passivating layer. In addition, the drawbacks of such a material should not be ignored, that small concentrations of ions such as Cl or S can have disastrous effects and as some nuclear wastes and GDF environments contain these elements it would be wise to have more studies performed on this material.

2.10 GCM Microstructures

The various microstructures that can develop during processing for glass ceramics only, were discussed in depth by Holand and Beall [**Error! Bookmark not defined.**] and are summarised here.

Figure 7a shows an ultrafine grained microstructure in what would now be termed nanoscale. Figure 7b shows a cellular membrane structure resembling an organic cell. The microstructure itself comprises the crystalline portion as the "cell" and the membrane as residual glass. Using silicate glass as an example, the formation of this structure occurs when the silica content of the crystal forming entity contains less than that of the surrounding glass. Normally, crystallisation would continue until all the glass has been consumed, or until the rejected elements formed their own separate crystal phase in a similar way to eutectic formation in metals. However, for glasses with certain compositions, the rejected elements may themselves form a stable glass (relative to the crystal) as reported by Chyung et al. for a LiO_2-Al_2O_3-SiO_2-TiO_2 glass crystallising to beta spodumene. They reported that the remnant glass was roughly 95% SiO_2 and 5% Al_2O_3 which is an extremely stable glass [152].

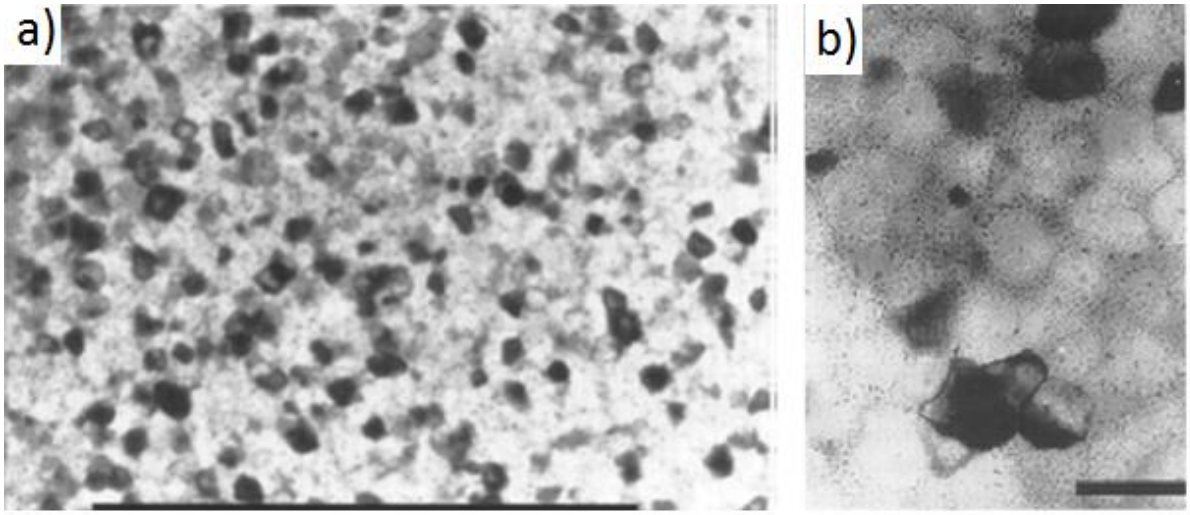

Figure 7:a) an ultrafine grained microstructure. The black bar represents 1 µm. B) Cellular membrane structure [153].

Dendrites are often defined as "branching tree like structures" (Figure 8, Figure 9). However, the standard definition is insufficient to fully describe the dendritic structures that can form. Whilst it is true that if you isolate one strand it will indeed appear to look similar to that of a Christmas tree. However, at the point at which it crystallised, whether it was due to large undercooling, nucleating agent, or through surface nucleation, the average angle, length, and spacing between branches will be different. For instance, Wang et al. [154] observed a small (200-500nm) surface-like dendritic crystallisation in between two different areas of composition. This is in contrast to Trivedi and Laorchan [155] who found a variety of bulk-dendrites (Figure 9).

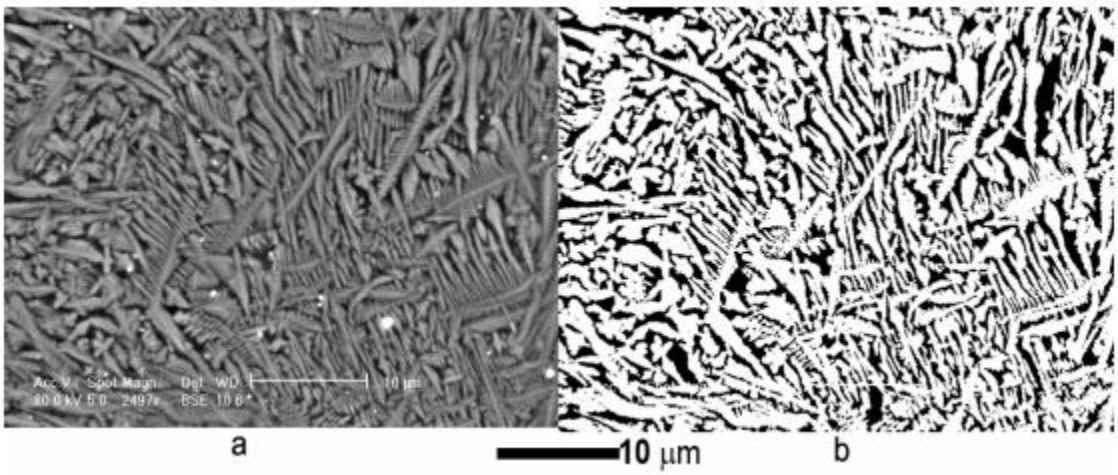

Figure 8: dendritic structure of a glass ceramic (a) and a computer simulated dendritic structure in a glass (b) [156].

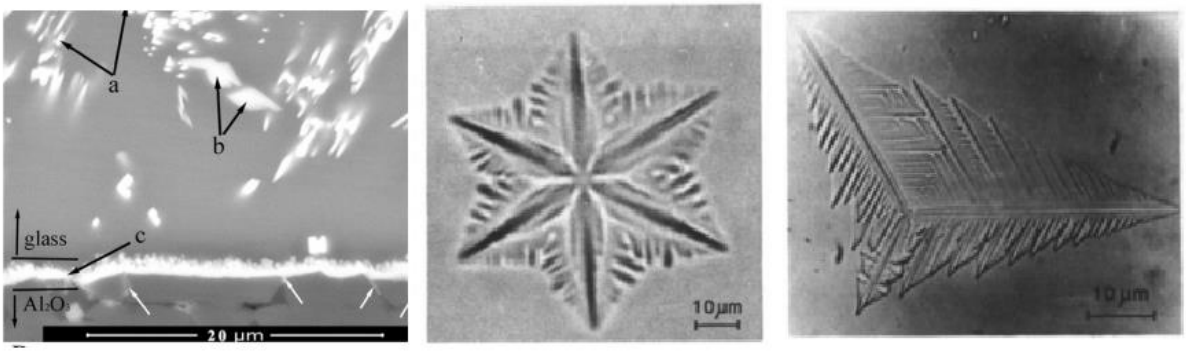

Figure 9: Various dendritic structures observed by Wang et al. (left) and Trivedi (middle,right).

In the case of a nuclear waste matrix, the formation of dendrites could be beneficial, for instance should closely packed surface dendrites that are superior to the waste underneath form, the lifetime of the wasteform would be increased. Dendritic microstructure formation during cooling for glass is much the same as it is in metallurgy, a reasonable degree of undercooling is preferred for the formation of a dendritic microstructure, however a heat treatment may be required to grow them [157].

The house of cards microstructure is not as ordered as the name might suggest, rather, consisting of randomly orientated crystalline flakes (Figure 10). This type of microstructure is sought after for certain applications as the flakes act to stop or redirect cracks such that they cause only local damage [153] and not catastrophic failure, although this is dependent on the nature of the crystal (flake versus spherulitic) [158]. The chemical durability of these types of microstructure have not been studied from a nuclear wasteform perspective but from a dental one, glass ceramics have been looked at for dental applications since 1968 and was finally made a reality with a tetra-silicate mica crystal in a glassy matrix and was found to hold up well to the biological environment [159].

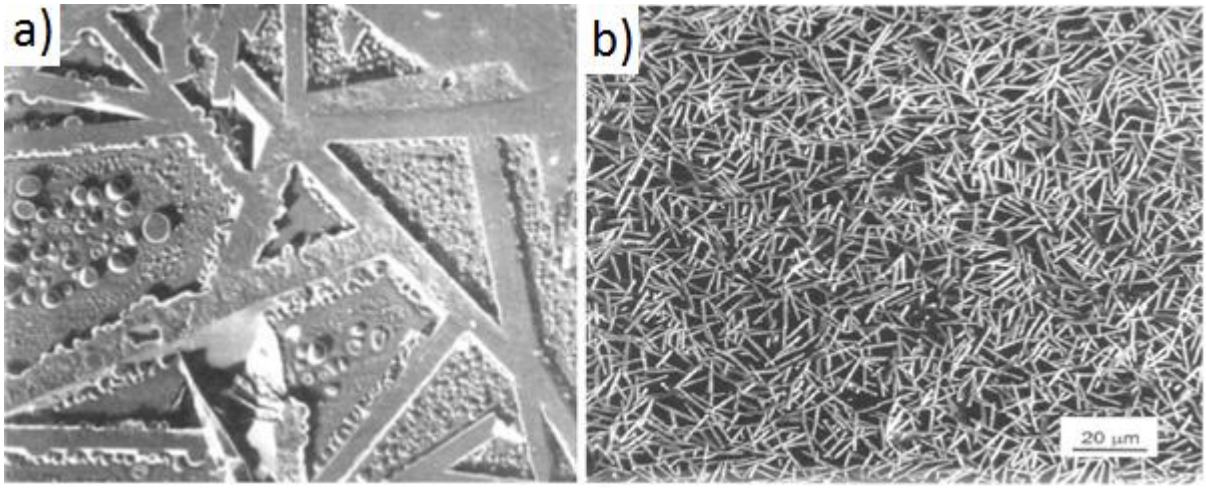

Figure 10:House of Card microstructure. a) Illustrating the orientation of this microstructure (no scale bar was found), b) House of card microstructure at the scale shown (20 µm scale bar) [160].

Glass encapsulated crystal GCMs display a microstructure of a glassy matrix, along with either an altered form of the crystal waste from thermal processing, or the original crystal dispersed in the matrix. The main difference between glass ceramics and glass encapsulated crystal waste forms is from the origin of the crystal, in glass ceramics the pre-treated materials naturally form a crystal component during processing leading to the microstructures previously shown. Glass encapsulated crystals will however result in crystals with differing microstructures dependant on waste loading, pre-treatment of the waste, and thermal treatment [161]. Figure 11 shows how the waste loading of a sintered borosilicate glass with Cs containing clinoptilolite resulted in different microstructures. When the clinoptilolite was sintered (Figure 11b) there was insufficient glass to fully encapsulate the waste allowing for Cs migration during leaching studies [162]. Further, with different waste loadings additional phases formed, such as sodalite ($Na_4Al_3Si_3O_{12}Cl$) which occurred due to a reaction between the clino and the glass. Overall, the effect this will have on the durability of the wasteform will be dependent on both the type of crystal that has formed, and its microstructure. Juoi et al. [162] found that increased waste loadings of a Cs-clinoptilolite GCM, the formation of wollastonite with different microstructures occurred; higher waste loadings resulted in a more rounded morphology with better durability than the angular ones that formed at lower waste loadings.

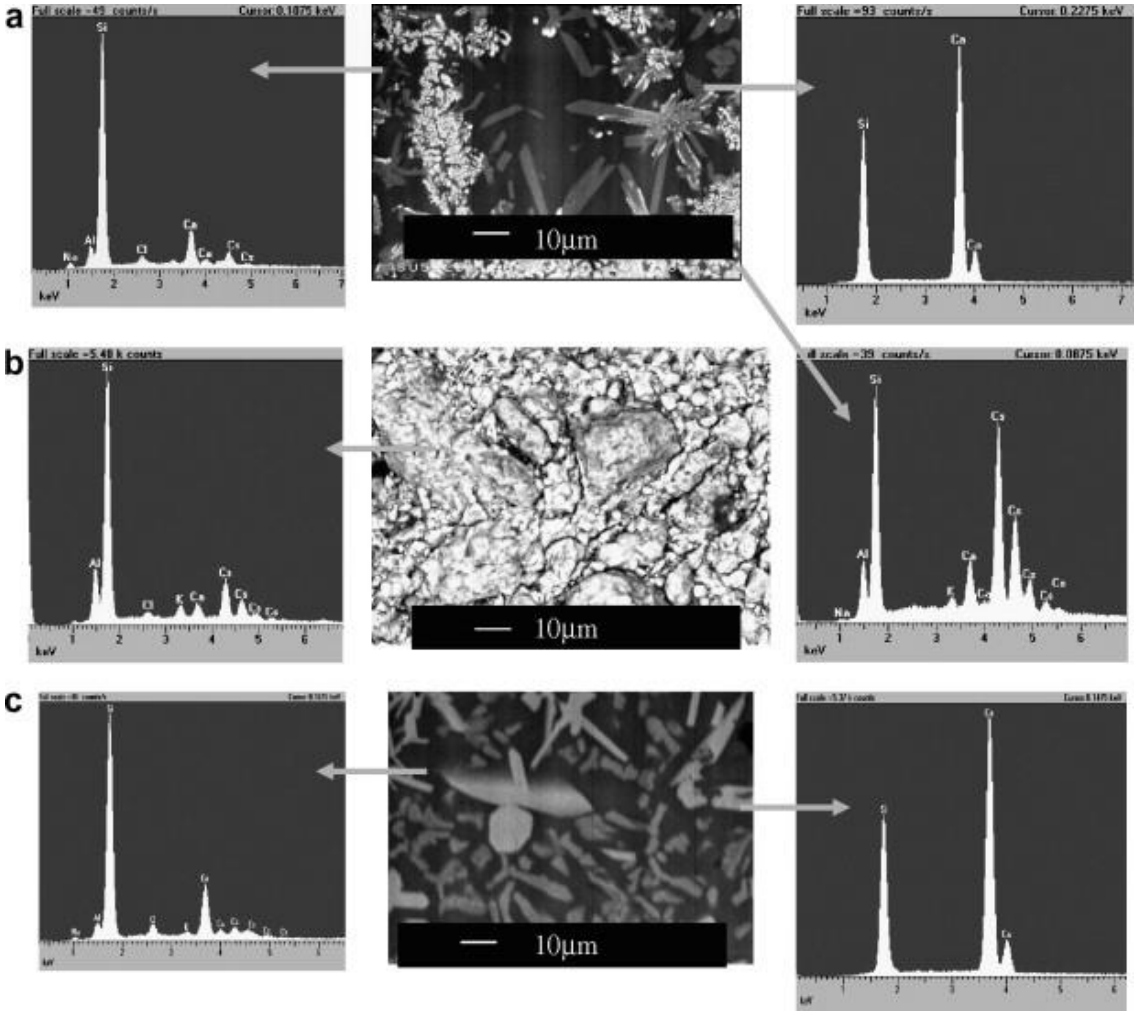

Figure 11: BSE image of 3 GCMs (a) GCM wasteform with 1:1 glass to Cs-clino volume ratio (b) sintered Cs-clino only and (c) sintered borosilicate only, accompanied are the EDX graphs for the glass and crystal phases present in each image; energy (keV) versus count rate (A.U) [162].

Another issues that arises from glass encapsulation is incomplete bonding between the crystalline and glassy phase, when encapsulating a crystalline phase it must be chosen such that the thermal expansion co-efficient are similar to avoid this [163].An example where such choices were made by Pace et al., resulted in good bonding between the encapsulated crystal and host glass can be observed (Figure 12); cracks propagated through the material with little deflection when encountering the crystal phase.

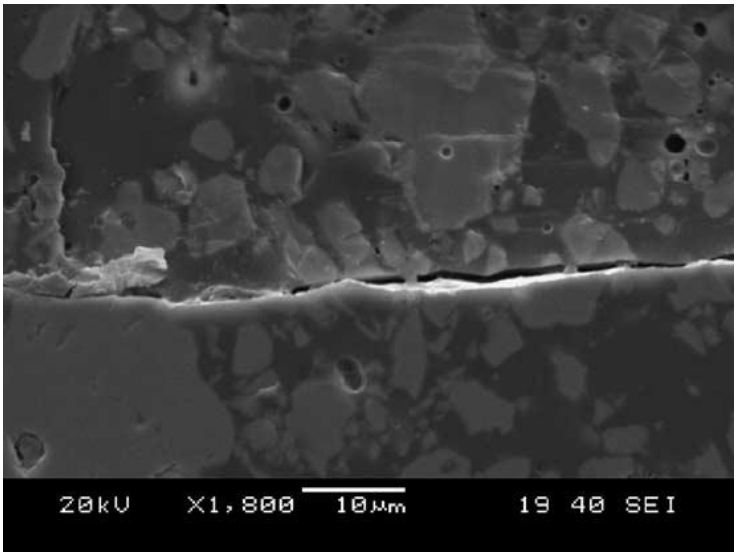

Figure 12: A glass encapsulated lanthanum zirconate material, where cracks propagated through the crystals, with little deflection, signifying strong bonding between the two [163].

2.11 GCM Macrostructure

Whilst it is important to control the microstructure of the GCM to give the best wasteform, if possible, the macrostructure is just important.

Ojovan et al. [164] demonstrated the importance of macrostructure in the case of a glass encapsulated clinoptilolite formed by pressure-less sintering for 2 h at 750 °C, various waste loadings were studied and leaching tests performed for each sample. Large increases in leaching rates for small increase in waste loadings were explained by the formation of interconnecting clinoptilolite particles (Figure 13).

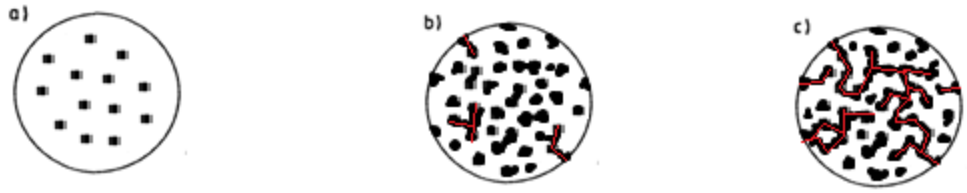

Figure 13:showing the importance of the distribution of crystals in a matrix on corrosion. (a) Showing that equally dispersed and isolated particles are ideal should one crystal be exposed only that crystal will be corrode, (b) and (c) show increasingly large amounts of crystals can lead to pathways for water ingress (pathway of leaching shown in red). As the weaker phase % is increased, so too is the depth from which ions can be leached due to intersecting crystals. Adapted from [164].

As the waste loading increased, it reaches a threshold whereby the clinoptilolite particles had produced a complex interconnecting network that allowed waste elements to bypass the protective glass (Figure 13c). The formation of these percolation clusters in highly undesirable for phases that may be designed to carry the waste (regardless of durability) or for phases that may be less durable.

Therefore, care must be taken to find a maximum waste loading with the avoidance of percolation clusters; clusters of particles that provide highways for leaching through the glass.

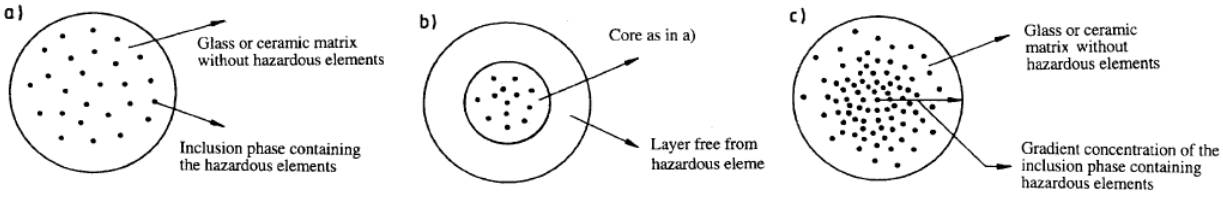

Figure 14: Various methods of encapsulating waste-containing crystals [164].a) isolated crystals dispersed homogenously in a glass/ceramic matrix b) showing a core of crystals dispersed in a glass/ceramic matrix, which is encapsulated in a waste free phase c) showing crystals dispersed inhomogeneously thought a more durable matrix leading to a gradient concentration of hazardous elements versus depth.

Assuming the GCM is devoid of percolation clusters, the positioning and partition of waste elements must be considered. Figure 14(a) shows a homogeneous distribution of a phase containing waste particles, embedded in a matrix of either glass or ceramic devoid of any waste elements. The durability of such a wasteform will be less than that shown in Figure 14(b) which has an additional layer, free of waste elements however it can be envisaged that the processing route would be problematic and costly.

Not included in Figure 14 is a fourth possibility, whereby a more corrosion resistant crystal forms at the surface, effectively encapsulating the more vulnerable glass. This mechanism, provided the crystal is more durable, is far easier to induce than any of the microstructures in Figure 14. Little literature exists for the kinetics of such systems, most likely due to the complexity. Some models have been constructed [163,165,166,167,168], for instance Pinet et al. [168] constructed a model using the simple principle that the crystalline phase consisted of variously sized perfect spheres encapsulated in the glass matrix (Figure 15).

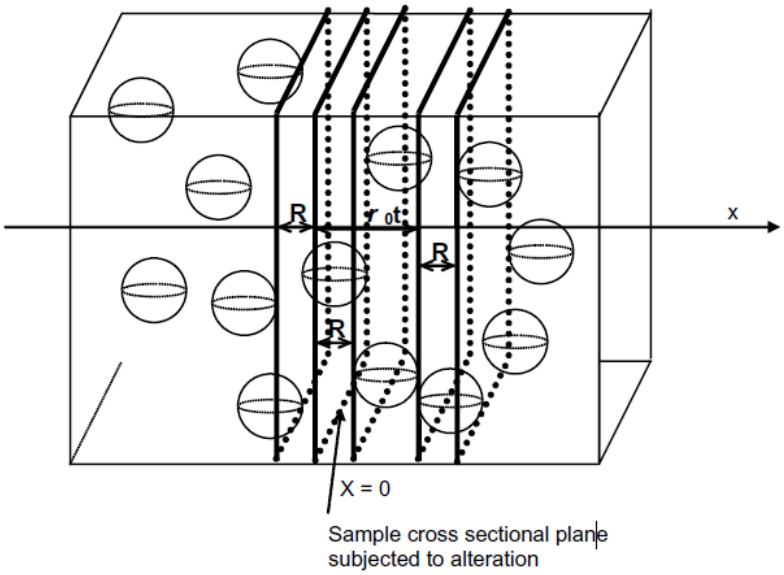

Figure 15: showing the principle of the model constructed by [168] where spherical crystals containing wastes are dispersed homogenously throughout a more durable matrix, 2D slices of this 3D wasteform were then taken to model alteration when attacked by water

The various equations used to verify this model for the glass composition used are not discussed here. Rushton et al. [167] used molecular dynamic simulations to investigate how the concentration of alkali ions varies at the boundary of different crystals and found that the alkali ions moved into positions above the crystal where the cations would have been had the crystal continued. This led to higher concentrations of certain elements (dependant on the crystal and orientation), and a small semi-crystalline layer; this layer will have important effects on the properties of the GCM though ion transport along the interface and interface strength [165, 167].

2.12 Expanded aims

Based on the literature survey preformed, the initial aims can be expanded:

- Characterisation of the specimens will play an important role in predicting corrosion behaviour, reliance on literature to assist in this regard is paramount, in a wide array of fields and not just in the nuclear sector.
- The wasteforms must be held to a higher standard than typical ILW, due to the historical background and the uncertainty of the classification of the waste involved in the future, therefore a worst-case scenario should be established and discussed. The likelihood of this scenario should be decided.
- Comparison with current, conventional waste matrices should be performed.
- Looking at how a purely glassy or purely ceramic phase corrodes will be useful for comparison, but cannot be used on its own to assess the durability of the entire wasteform as other factors will come into play not relevant to those wasteforms, such as less durable

phases providing an easy path of water ingress into the sample, leading to accelerated corrosion.

- The macro and micro structure will play an important role in the durability, with different arrangements leading to either better or worse durability. When deciding the life time of the wasteform, this should be considered.
- Glass corrosion is still an ongoing area of study; discussion on corrosion should look outside current theories if it does not agree with the evidence present.
- The thermal treatments used are different, and could lead to large difference in the wasteform for the same waste stream. This should be discussed when appropriate; the best thermal treatment for the relevant waste should be chosen.

3.0 Experimental Procedures

This chapter outlines the various techniques and instruments used throughout this thesis containing brief theory and technical details about the instruments, and information surrounding the materials preparation.

Each material supplied by Sellafield (Table 1) was subjected to the same regime; the sample was first prepared and characterised using the techniques explained below, this was then followed by leaching for set amounts of time. Following this the leachant was removed for analysis and the sample was subject to the same tests carried out pre-leaching to observe the changes.

3.1 Sample Background

Joule Heated In-Container Vitrification (JH-ICV) thermal treatment is being investigated by Sellafield Ltd with services provided by Impact Services incorporated (1952 E. Allegheny Avenue, Philadelphia, PA 19134, (215) 739-1600) using GeoMelt technology, on a proof of concept basis to establish an alternative method to dispose of difficult wastes, where the current method of disposal is typically cement encapsulation. One of the benefits provided by JH-ICV is the ability to directly convert an already contaminated vessel into a potential wasteform suitable for disposal; this completely avoids the intermediate procedure of handling/separation of wastes before intermediate steps prior to heating which can be hazardous and expensive. Three samples were investigated; a summary of the waste type and short hand name is outlined in Table 1, along with the samples produced using plasma technology, discussed later.

JH-PCM was developed to examine the possibility of converting a waste container, such as a skip or drums of untreated waste into an immobilised ILW. The process was aimed at treating ion exchange media, sand Plutonium Contaminated Material (PCM), concrete, uranium, pile fuel cladding, soils, and metals, all of which are categorised as having a high metal content in the form of containers, plant equipment, structural materials, and swarf. The “Joule Heated-High Metal Surrogate” (JH-HMS) sample in contrast was used to determine the feasibility of converting diverse size and shape high metal content waste, directly to a waste from. The wastes being treated were from the Site Ion Exchange Plant (SIXEP) at Sellafield (specifically sand and clinoptilolite mix) and pile fuel cladding. The JH-SIXEP material had the general objective of immobilisation of high metal content waste only, minimisation of non-active additives, volume reduction, and minimisation of secondary wastes produced during process, using the GeoMelt hybrid method (see section 3.1.1). The simulant wastes were that of plutonium contaminated metals and organics, but also SIXEP waste (Magnox sludge). Should the thermal treatments of the various issues that each of these samples address (high metal content, diverse shapes, in-container treatment) be successful in producing a wasteform capable of meeting the strict criteria placed for GDF wastes/ILW, the benefits would be great. Little pre-treatment would be required; such as sorting of wastes known to produce unsuitable wasteforms, the cutting of large or awkwardly shaped wastes, and the removal of wastes from a skip into the vessel used to thermally process it. This would accelerate the processing of legacy/difficult wastes, and reduce the hazards present in their treatment.

Direct current plasma furnaces are being considered for the thermal processing of various wastes in an effort to produce an inert and stable wasteform suitable for use on both hazardous and non-hazardous waste. It has many advantages over conventional nuclear thermal treatment systems and is discussed in more detail in section 2.8.1. Sellafield Ltd performed several trials using such a treatment method via the company Tetronics (Tetronics International, Marston Gate, South Marston Park, Swindon, Wiltshire SN3 4DE UK) who specialise in use of plasma technology for various hazardous waste disposal (asbestos, nuclear, chemical, organic etc.), to show the viability of using such a furnace for the treatment of hazardous radioactive waste, the ones discussed in this section are all categorised as ILW but are to be placed in GDF for long term disposal. Of the three samples discussed, a separation can be made between the "Plasma Furnace High Metal Surrogate" (PF-HMS) and "Plasma Furnace High Metal Surrogate 2" (PF-HMS2) materials, and the "Plasma Furnace Asbestos" (PF-Asb) material. PF-HMS and PF-HMS2 were part of the same set of trials used to assess the viability of using a DC plasma furnace to safely immobilise metal wastes comprising of containers, plant equipment, structural materials, and swarf in use in nuclear facilities. 5 trials were performed, with a final demonstration trial; the first 5 trials had the objective of investigating the possibility of integrating ferrous wastes into a molten bath with a temperature lower than the expected melting point of the waste metals. The information gathered from these trials was then used in trial 6 to help produce an ideal final wasteform that could meet the criteria for safe disposal. Whilst trials 1-5 investigated a particular treatment condition, or specific set of wastes, the demonstration trial used the full waste simulant for Pile Fuel Cladding (PFC), pond solids, and plutonium contaminated material.

Trial 3 had the main objective of destroying asbestos contaminated material (ACM), this trial was applicable to both asbestos within the nuclear industry and out, using the most commonly used asbestos material for insulating purposes. This type of waste is not commonly dealt with due to its relatively safe nature in comparison to more dangerous radioactive wastes, but still possesses a considerable health hazard. Any nuclear facility built before the 1985 ban on certain asbestos materials (amosite and crocidolite), and a few built before the 1999 outright ban on all identified asbestos, will contain asbestos and will need to be disposed of in compliance with both nuclear and ACM health regulations. The use of a plasma furnace to meet this criterion was tested in this sample, with the main objective of rendering the relevant asbestos inert as to allow disposal in landfill (for non-nuclear waste), and to a lesser extent, achieve higher waste loadings and waste volume reduction than other thermal techniques.

Radioactive isotope simulants were added to some of the waste streams, chosen to emulate as closely as possible the chemical nature of the actual elements thought to be present in the waste stream, where this has been done the elements being simulated are noted. Where information was supplied on these surrogates, the minimum mass needed to simulate them is given as estimated/calculated to be in the actual waste stream itself. The most prominent of these surrogates (and used in the largest amount) is that of cerium, a surrogate for plutonium. Cerium has been proven to be one of the best chemical surrogates for plutonium, and suffices in this role in many fields [169], however limitations exist on cerium as a surrogate, such as the role of calcium reacting between uranium and plutonium, versus cerium [169]. The inadequacy of cerium as a chemical surrogate are beyond the scope of this work, and can be found elsewhere [170,171]. Similarly, none of the surrogates used here can fully simulate the chemical nature of the actual

elements and will require repeat trials using the real elements to confirm similar behaviour. A list of chemical surrogates for a range of radioactive isotopes can be found here [172].

Table 1: Samples received from Sellafield produced by JH-ICV and plasma technology showing the waste type used and the abbreviation for them: JH-PCM, JH-HMS, JH-SIXEP, PF-HMS, PF-Asb, and PF-HMS2.

Production method	Waste	Short hand name
JH-ICV	Magnox sludge surrogate and Plutonium Contaminated Material	JH-PCM
JH-ICV	High Metal Surrogate, including SIXEP and PFC	JH-HMS
JH-ICV	SIXEP sand/Clinoptilolite mix and PFC silo waste	JH-SIXEP
Plasma furnace	High metal surrogate	PF-HMS
Plasma furnace	Asbestos	PF-Asb
Plasma furnace	High metal surrogate	PF-HMS2

3.1.1 Joule Heated-Plutonium Contaminated Material

The standard JH-ICV waste treatment involves placing the waste in a cubic container, with 4 graphite rods in each corner acting as electrodes to supply the heat. The treatment of these particular wastes involves a GeoMelt hybrid method which uses 2 stages to treat the wastes:

1) Simulant waste was first placed in the container without sorting and as is needed with such technology a starter path was added between the electrodes, the arrangement of this is schematically shown in Figure 16. The starter path is used to allow a conductive pathway between the electrodes to initiate heating in an otherwise non-conductive waste media. In addition, a combination of glass forming/waste material was placed on top of the starter path. Power was then supplied to the electrodes which cause the starter path/waste/glass forming material to form an electrically conductive melt. It must be noted that the entire container was not filled, a portion was left empty.
2) Following stage one additional waste was fed into the ICV container, while power was supplied to the electrodes (continuing the process), this continued until the level of waste reached a satisfactory height for the container allowing the container to be completely filled.

The main advantage of this technique is its ability to maximise the amount of waste in the container, as the anticipated glassy wasteform results in a significant waste volume reduction. If all the waste had been added at the beginning the container would not have been completely full at the end of the process. The alternative treatment used is when the container is completely full, and the starter path placed on top of the waste, as the heat propagates downwards and out, rather than upwards and out, the result is a far more efficient treatment process. The maximum temperature achievable with this JH-ICV is 1800 ^{o}C and can be controlled to match the wasteform being treated.

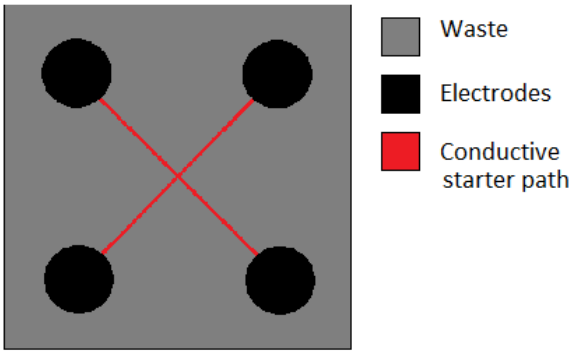

Figure 16: Sketch of the GeoMelt hybrid method from above looking down. Black circles show the location of the graphite electrodes with the starter path shown in red/orange [prepared by author].

Two unique waste streams; PCMs and SIXEP Magnox sludge were used. 334 kg of a variety of simulated PCM and glass forming materials were added in stage 1 followed by 425 kg of simulated Magnox sludge, no interruption of power occurred during the entire process. The compositions of the simulant wastes are shown in Table 2.

The steel, PolyVinyl Chloride (PVC) gloves, rubber, cellulose, and polyethylene were partially packed into 48 carbon steel tin coated cans and compacted. The cans were then placed in a separate small container and filled with Ordinary Portland Cement (OPC); these were then placed into the melter. The reason behind this methodology was to simulate a scaled 200 litre carbon steel waste drum loaded with PCM debris which has been compacted inside a 500 litre stainless steel over-pack drum.

Non-radioactive surrogates were used to simulate their radioactive isotopes Ce, Cs, Sr, Co,and Eu being used to simulate, specifically, ^{144}Ce, ^{137}Cs, ^{90}Sr, ^{60}Co, ^{241}Am, and $^{154/155}$Eu. Cerium, in addition to being used to simulate Ce^{144} was also used to simulate plutonium, and rhenium was used to simulate ^{99}Tc. Note the cerium was added in the form of misch-metal, whilst the composition of the misch metal was not given, it is assumed to be of similar composition to those used in other trials using this method (66.6% Ce, 33.3% La). The various amounts of these elements added are outlined in Table 3, which also displays the minimum amounts of these elements necessary to be detected in sample analysis, specifically ICP-MS and ICP-OES.

*Table 2: Composition of simulant wastes elements. *no information was supplied on the chemical content of these materials, other than they were included as glass forming additives. ^ Flux is added material to lower the glass transition temperature, no compositional data was given. No error ranges were given in the supplied information [173]. Note; the local soil composition by elements was estimated using British geological survey data of the soil composition in the area around Sellafield.*

Stage 1: PCM simulant waste			
Component	Mass of feed (kg)	Elements	wt%
Carbon steel drum fragments	78.9		
Stainless steel drum	7.1	Carbon	0.04
		Chromium	18.1
		Nickel	8.1
		Iron	73.76
Misch metal*	0.49	Lanthanum	33.68
		Cerium	66.11
		Praseodymium	0.11
		Neodymium	0.11
PVC gloves	24.1		
Rubber	9.7		
Polyethylene as grocery bags	5.4		
Portland cement*	27	Silica	22.45
		Alumina	5.1
		Iron Oxide	4.08
		Calcia	64.29
		Magnesia	2.04
		Potash	1.02
		Soda	1.02
Local soil and flux*^	163	Silicon	65
		Aluminium	20
		Iron	7
		Magnesium	2.3
		Calcium	6
Total	334		
Stage 2: SIXEP waste			
Demineralised water	63.96		
Misch metal*	2.93		
Brucite ($Mg(OH)_2$)	82.26		
Local soil*	276.25		
Total	425.4		

Table 3: Mass of waste surrogate elements added in g [173].

	Staged portion		SIXEP portion	
Material	Minimum mass needed (g)	Actual amount (g)	Minimum mass needed (g)	Actual amount (g)
Cerium	16	490.4	10	2928.7
$SrCO_3$	0	0	15	15
Cs_2CO_3	8	8	5	5
Re_2O_7	0	0	10	10
Eu_2O_3	8	8	5	5
Co_3O_4	7	7	5	5

The final wasteform as received is shown in Figure 17.

Figure 17: An image of the as received wasteform.

Table 4 reveals the calculated final composition of the wasteform, however due to partitioning this may not be representative of the composition of the phase(s) present.

Table 4: Calculated global elemental composition of the sample JH-PCM, calculated based on waste content, along with additions to promote glass forming.

Element	Wt%	Element	Wt%
Si	35.712	Pr	0.001
Al	13.184	Ny	0.001
Ca	5.557	Cr	0.187
Fe	22.193	Cs	0.007
Mg	13.491	Eu	0.007
La	0.168	Co	0.022
Ce	0.329	Re	0.015
Na	1.357	Sr	0.022
K	1.958	Ni	0.084
C	5.706		

3.1.2 Joule Heated-High Metal Surrogate

Trials producing the JH-HMS wasteform were to determine how the JH-ICV process could cope with diverse high metal content wastes categorised as ILW consisting of various shapes and sizes and those that may be considered difficult to process via conventional means. A summary of the various waste simulant is shown in Table 5 and Table 6. In addition to the 41 kg of surrogate waste material added, it was reported that 69 kg of glass/silica frit was added, and 28 kg of Fe_2O_3 was added as an oxidising agent.

This trial used a refractory (monolithic cast, aluminosilicate) lined 500 litre stainless steel ICV container, the inner refractory was separated from the rest of the container by a layer of silica sand.

Similar to sample JH-PCM, non-radioactive surrogates were used to simulate their radioactive isotopes Ce, Cs, Sr, Re, Ru, and Eu being used to simulate, respectively, ^{144}Ce, ^{137}Cs, ^{90}Sr, ^{99}Tc, ^{103}Ru (can additionally act as a surrogate for ^{99}Tc), and $^{154/155}Eu$.

Table 5: Waste composition in wt%, mass, and volume [173]

Material	Form	Mass (kg)	Element	wt%
Stainless steel	Plate of bars	9.55	Carbon	0.04
			Chromium	18.1
			Nickel	8.1
			Iron	73.76
Mild steel	Skip vessel	10.5	Carbon	0.3
			Silicon	0.25
			Manganese	0.8
			Sulphur	0.02
			Phosphorus	0.02
			Iron	98.62
Al	Plate or bars	3.8		
MgO/cement/organics	Round bars	1.85	Silica	22.45
			Alumina	5.1
			Iron Oxide	4.08
			Calcia	64.29
			Magnesia	2.04
			Potash	1.02
			Soda	1.02
Misch Metal	Square bars	11.45	Lanthanum	33.68
			Cerium	66.11
			Praseodymium	0.11
			Neodymium	0.11
MgO/cement/organics	Powder/pieces	3.9	Silica	22.45
			Alumina	5.1
			Iron Oxide	4.08
			Calcia	64.29
			Magnesia	2.04
			Potash	1.02
			Soda	1.02
Total		41.05		

Table 6: Composition of radioactive surrogate elements added to JH-HMS waste [173].

Item	*Mass (g)*
Eu_2O_3	5
Cs_2CO_3	5
Re_2O_7	6
SrO	5
RuO_2	5

A steady treatment of 16 h produced the final wasteform, the temperature in the furnace varied between 1200-1250 ^oC however a melt temperature of 1415 ^oC was determined to be the necessary temperature to achieve full dissolution of all waste elements. Once the reactive elements were treated this temperature was employed for the remainder of the processing, however the time at which this temperature was achieved throughout the waste was difficult to state accurately due to the location of the thermocouples used to determine the temperature of the mix. These were placed at strategic locations from the bottom up; the first thermocouple to show temperatures above the nominal 1200 ^oC was 360 mm above the bottom (highest elevated thermocouple) after 6 h treatment. In addition, reduction and increase to the power supplied to the furnace, and thus the temperatures, allowed for varying temperatures throughout the processing. The exact temperature of the melt was further convoluted by the migration of molten waste with differing thermal properties towards a thermocouple.

No mixing was employed; this was due to the low viscosity of the waste melt at the temperatures involved; it was predicted that sufficient convective mixing would occur to mix the sample.

Hot air was used to cool the waste during processing under pressure to ensure that the air leaving would not form water in the off-gas filters.

The final wasteform following thermal processing is shown in Figure 18.

Figure 18: Image of the wasteform as received.

Table 7 reveals the total composition of the wasteform by elements, but due to partitioning of elements in various phase(s) may not be representative of the composition of any one phase. Additionally, only a small portion of the final wasteform (138 kg) was received, and may not be representative of the entire wasteform.

Table 7:Calculated global elemental composition of the sample JH-HMS, calculated based on waste content, along with additions to promote glass forming. Note; these values may not be representative of the wasteform received, as only a small portion of the final material was sent for analysis.

Element	Wt%	Element	Wt%
Si	54.81	C	0.03
Al	3.16	Mn	0.06
Ca	2.85	S	0.00
Fe	28.69	P	0.00
Cr	1.33	Pr	0.01
La	2.98	Ny	0.01
Ce	5.84	Mg	0.09
Na	0.05	K	0.01
Ni	0.06		

3.1.3 Joule Heated-SIXEP

Further to JH-PCM which was the first of a two-part trial, this is a description of the second.

Trial 2 again involves two waste streams, that of sand and clinoptilolite (SIXEP) and PFC silo waste. As was described in the treatment of the wastes for JH-PCM the process involved two basic methods of initial melting. The first was used in JH-PCM the second in this case a top down approach method

was used. For this method, all the waste and glass forming material is added at once to fill the container, a starter path is then laid between the electrodes and power supplied. This causes the top layer of waste to become molten via Joule heating and with the continued input of electricity will eventually melt the entire container from the top down. This is illustrated in Figure 19.

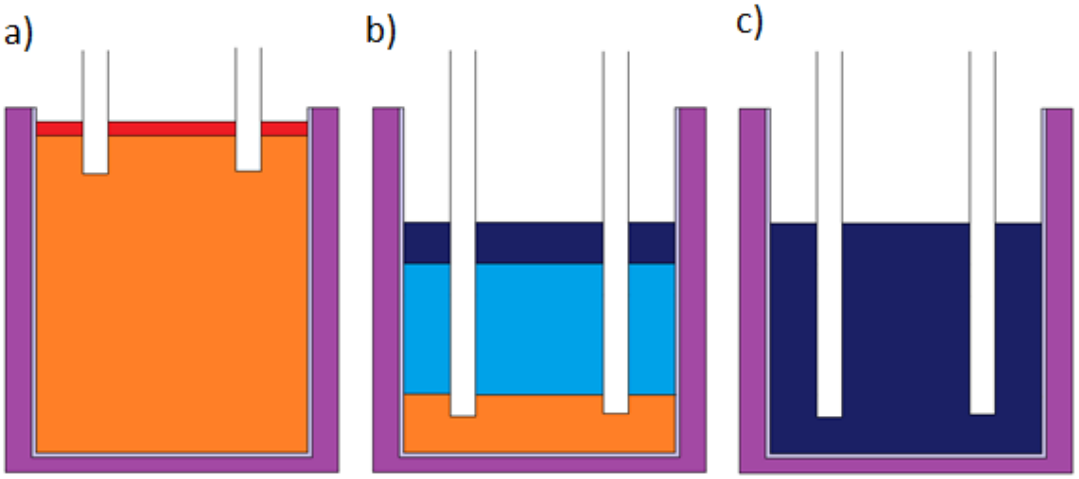

Figure 19: Schematic of how melting proceeds during JH-SIXEP waste treatment, (a) waste (orange) is added with a starter path layered on top (red).(b) the graphite electrodes are steadily lowered into the mixture of waste and molten waste (light blue) with the top solidifying (dark blue) and (c) the final wasteform is completely solidified [prepared by author] .

The container itself was an 80cm^2 x 100cm deep square box, stainless steel on the outside with a refractory lined interior; the refractory is pre-cast alumino-silicate panel and granular silica.

The addition of the waste streams/glass former was performed in stages, initially a 2.54 cm deep layer of glass former was placed on the base silica and inner surface, the pile fuel cladding silo waste was then continuously loaded whilst at different elevations 2.54 cm diameter by 15.24 cm long magnesium rods were placed in too. Following this sand/ clinoptilolite combination was added filling the remainder of the container dedicated to waste, the starter path layer was placed on top along with the graphite electrodes. The composition of the PFC, sand/ clinoptilolite combination, and mass of radioactive tracer elements is shown in Table 7and Table 8. Note, although the tracer elements were assembled along with the other wastes before being added to the other wastes, an error made by Sellafield resulted in the omission of all tracer elements.

Non-radioactive surrogates were used to simulate their radioactive isotopes Ce, Cs, Sr, Co,and Eu being used to simulate, specifically, ^{144}Ce, ^{137}Cs, ^{90}Sr, ^{60}Co, ^{241}Am and $^{154/155}$Eu

Table 8: Mass of simulant pile fuel cladding waste added and Composition of waste added to simulate sand/clinoptilolite mixture for JH-SIXEP. [173]

Pile Fuel Cladding Silo waste

	Mass (kg)	Element	Wt%
C - Graphite	13.5		
$CaCO_3$ -Limestone	5.5		
Fe- Steel	14.8		
Mg- Metal rods	16		
$Mg(OH)_2$ - Brucite	4.3		
Al_2O_3-Alumina	4.3		
Cellulose HEPA	2.2		
Hydraulic oil	0.3		
Total	60.9		
Sand/Clinoptilolite			
Demineralised water	34.1		
Clinoptilolite	42.4	Na	1.647
		K	2.802
		Ca	2.872
		Al	7.734
		Si	28.177
		O	55.034
		H	1.734
Silica sand	10.5		
Ce/La- Mish metal	0.8	La	33.68
		Ce	66.11
		Pr	0.11
		Ne	0.11
$Mg(OH)_2$ Brucite	4		
Al_2O_3-Alumina	0.1		
CaO-Quicklime	0.4		
Fe_2O_3- Hematite	0.1		
Na_2CO_3-Sodium carbonate	0.2		
K_2O - Potash	0.2		
Total	92.8		

Table 9: Mass of waste surrogate material added to simulate radioactive material, in g for sample JH-SIXEP. [173]

Radioactive tracer materials

	Minimum mass needed (g)	Mass added (g)		
		From trial 1 HEPA	Additional surrogates	**Total**
Ce (mischmetal)	420	0.2454	575.484	575.729
$SrCO_3$	6	0.9491	14.837	15.787
Cs_2CO_3	7	0.9673	16.317	17.284
Re_2O_7	8	0.1584	0	0.1574
Eu_2O_3	7	0.0173	10.367	10.3839
Co_3O_4	7	0.0101	17.068	17.0872

The final wasteform as receieved is shown in figure xx.

Figure 20: An image of the wasteform as received.

Table 10: Calculated global elemental composition of the sample JH-SIXEP, calculated based on waste content, along with additions to promote glass forming. Note; these values may not be representative of the wasteform received, as only a small portion of the final material was sent for analysis.

Element	Wt%	Element	Wt%
Si	16.260	Ny	0.001
Al	6.048	Pr	0.001
Ca	5.041	K	1.889
Fe	20.191	La	0.367
C	21.776	Ce	0.720
Mg	26.484	Na	1.223

3.1.4 Plasma Furnace-High Metal Surrogate

Tetronic's plasma furnace was used to melt various waste metals, consisting of stainless steel, mild steel, magnesium, and aluminium alloys with the objective to fully incorporate these metals into a low melting vitrified phase. The high melting point of some metals and the volatility of the magnesium made this challenging, leading to several trials to fully accomplish this goal. The plasma furnace can potentially reach temperatures of 1800 ^{o}C, however, the thermocouple used had a maximum temperature capability of 1200 ^{o}C making exact measurement impossible.

The waste metals used consisted of a hollow stainless steel block (unknown dimensions and thickness, composition shown in Table 11), mild steel rods (composition shown in Table 12), aluminum rods, and magnesium rods. The composition of the magnesium rods is only cited of being commercial quality, whilst the aluminum rods were sourced internally; no other information was given regarding the origins of the materials nor the amount added. These were used to simulate the wastes contained in the PFC silo specifically the PFC, a magnesium lithium alloy, and the aluminium nitride for decay to carbon 14. The magnesium and aluminium rods were placed inside the stainless steel block, which in turn was placed inside a copper crucible (600 mm inner diameter) together totaling 6 kg of metallic waste. An addition of 0.39 kg of slag maker (composition shown in Table 13) was added before thermal processing. A screw feeder connected to the furnace then fed the rest of the slag maker into the crucible when turned on at a rate of approximately 5.5 kg/hr, in total 9.1 kg of slag (including the initial slag) was present. This resulted in a 1.5:1 ratio of slag to metal waste.

Table 11: Composition of stainless steel used, as per ASTM 304 used as a waste simulant in sample PF-HMS. [173]

Stainless steel	**wt%**
Carbon	0.04
Chromium	18.1
Nickel	8.1
Iron	73.76
Total	**100**

Table 12: Mild steel composition used as a waste simulant in sample PF-HMS. [173]

Mild steel	wt%
Carbon	0.3
Silicon	0.25
Manganese	0.38
Sulphur	0.02
Phosphorus	0.02
Iron	98.62
total	**99.59**

Table 13: Composition of slag maker used in sample PF-HMS. [173]

Formula	Slag maker composition, trial 5	wt%
SiO_2	**Silica**	50
Al_2O_3	**Alumina**	20
CaO	**Lime**	30

Feed tubes supplied air to the furnace at 150 Normalised litres per minute (Nlpm) along with 20 Nlpm via the sparge ring. Due to pressure issues the feed tube air pressure was reduced to 75 Nlpm during the processing. The graphite electrodes used were used in a sacrificial method, thus becoming incorporated into the vitrification process. The recorded mass losses on the cathode and anode are shown in Table 14.

Table 14: Graphite anode/cathode initial, final and mass loss in g. [173]

Graphite electrode consumption	Anode	Cathode
Initial mass (g)	1865	2055
Final mass (g)	1695	1900
Mass loss (g)	170	155

One part of the wasteform as received is shown in Figure 21.

Figure 21: An image of one part of the wasteform as received.

3.1.5 Plasma Furnace-Asbestos

Simulant slag was added to the plasma furnace and heated at 1600 °C at atmospheric pressure until thermal equilibrium was reached, which occurred after 1.5 h, this was designed to give a glassy wasteform with a liquidus of approximately 1400°C. Overall, 70 kg of slag (composition in Table 15) was used over the course of 5 h. ACM waste was then added over 3 h involving a total of 42.5 kg of asbestos waste, a mix of amosite (~26.5 kg pure amosite ($Fe_7Si_8O_{22}(OH)_2$)).) and chrysotile (10 kg pure chrysotile ($Mg_3Si_2O_5(OH)_4$)Most of the amosite used was saturated with water (~26.5 kg), a 6 kg portion of material was an amosite/chrysotile mix and was wet; to the same extent as the pure amosite portion. No quantifiable information was supplied on how much water was contained in the "wet" amosite/chrysotile mixture.

Table 15: Composition of the glass forming mix added [173].

Formula	Name	Wt%
SiO_2	Silica Sand	33.7
CaO	Burnt Lime	58.8
Al_2O_3	Bauxite	3.2
Fe_2O_3	Iron Oxide	4.3

The arc was initiated by electrode contact with a voltage of 400 V and sustained until plasma current was detected. Typical arc voltages of 130 to 180 V were observed when the ACM was being processed and around 100 to 110 V during operational periods without ACM feed. Steady state operating currents were set at 1100 Amps through a balance of plasma stability and the process gross power requirement. The typical power input while processing ACM varied between 150-170 kW with occasional peaks at 250 kW (probably as a result of variations in the ACM water content). The gross energy requirement for handling wet ACM of different characteristics was calculated to be approximately 100 kWh $tonne^{-1}$ and, therefore, with a feed rate of 0.059 tonnes per hfrom an assumed hearth feed rate loading of 0.18 tonnes h^{-1} m^{-2}, the anticipated gross power requirement

was 150 kW. Argon was used as the plasma gas and the electrode gas flow rates were maintained 30 Nlpm during the heat to stabilise the plasma arc, with a typical 150 mm arc length.

The as received material is shown in Figure 22.

Figure 22: An image of the as received material.

Table 16 reveals the total composition of the wasteform based on the background composition provided. Note due to partitioning of elements amongst the phase(s) this may not be representative of the composition of any one phase.

Table 16: Calculated global elemental composition of the sample PF-Asb, calculated based on waste content, along with additions to promote glass forming. Note; these values may not be representative of the wasteform received, as only a small portion of the total wasteform was received.

Element	Si	Ca	Al	Fe	Mg
Wt%	31.217	46.093	0.929	9.599	12.162

3.1.6 Plasma Furnace-High Metal 2

The wasteform as received from Sellafield Ltd, comprised of a translucent green glassy material with approximately 0.5 g of a metallic and/or metal oxide mixture, separate from each other and easily separated by hand. The green portion of the sample is displayed in Figure 23, the brown tint was a thin powdery layer that fell off the sample upon further handling. The green portion of the material also had areas of black within it that were also translucent.

Figure 23: Picture of the bulk material as received from Sellafield of sample PF-HMS2, scale is shown in cm.

Simulant waste was designed to represent three key ILW; Pond solids, PFC and PCM wastes (exact compositions shown in Table 17). To further simulate the conditions of handling the actual active materials, no sorting was performed during preparation and processing. Simulant radioactive waste was used to mimic the chemical behaviour of PCM. The mischmetal used to simulate trans-uranic actinides, whilst specific elements were added to simulate their radioactive counterparts, namely crystalline caesium nitrate (99.8% pure, impurities composition not supplied) to simulate ^{137}Cs, europium oxide (99.999% pure) to simulate uranium, and rhenium pellets (<99.9% pure)to simulate technetium. Magnesium oxide powder (325 mesh) was used for the magnesium oxide outlined in Table 17and Empera polystyrene granules were used as a substitute for nitrile gloves and for other organics that may be present as ILW. OPC was also added, as a rough simulant for cement from decommissioned buildings that may be present in the waste silos.

The same initial waste set up as described in section 3.1.1 JH-PCM was used, waste components were added to the crucible before thermal processing. However, europium oxide, caesium nitrate, OPC, magnesium oxide, rhenium pellets, mischmetal, and polystyrene were added in addition to the hollow steel block (containing the aluminium and magnesium rods). This decision was made to fully simulate how an untreated waste container/skip would appear. In total, approximately 10 kg of the pre-thermally treated waste was added and ~0.3 kg of slag maker. A further 9.7 kg of slag maker was then added after establishing a plasma arc; via screw feeder at a rate of 5.5 kg/hr. The composition of the slag is shown in Table 18.

Table 17: Composition of the various wastes used as simulant, each waste is broken down into its elemental composition when appropriate. Error ranges were not given [173].

PF-HMS2 Wastes	Waste wt%	Elements	Wt%
Stainless steel	24.68	Carbon	0.04
		Chromium	18.1
		Nickel	8.1
		Iron	73.76
Mild steel	20.17	Carbon	0.3
		Silicon	0.25
		Manganese	0.8
		Sulphur	0.02
		Phosphorus	0.02
		Iron	98.62
Aluminium rods	9.96		
Magnesium rods	4.51		
Mischmetal	26.57	Lanthanum	33.68
		Cerium	66.11
		Praseodymium	0.11
		Neodymium	0.11
Europium oxide	1.04		
Caesium Nitrate	2.49		
Rhenium	0.67		
Polystyrene	3.30		
Magnesium oxide	3.30		
OPC	3.30	Silica	22.45
		Alumina	5.1
		Iron Oxide	4.08
		Calcia	64.29
		Magnesia	2.04
		Potash	1.02
		Soda	1.02
Total	100.00		

Table 18: Composition of the slag maker added [173].

Formula	Slag maker	wt%
SiO_2	**Silica**	50
Al_2O_3	**Alumina**	20
CaO	**Lime**	30

Table 19 reveals the overall composition of the wasteform, based on the background information received. Note that due to partitioning of elements in phase(s) this is not representative of the composition of any one phase. For instance, an issue documented in the processing of this wasteform was the formation of a metal rich phase at the bottom of the melter, as no such material was analysed, this would result in a depletion of these elements in the analysed wasteform, along with a corresponding increase in other elements.

Table 19: Calculated global elemental composition of the sample PF-HM2, calculated based on waste content, along with additions to promote glass forming. Note; these values may not be representative of the wasteform received, as only a small portion of the final material was sent for analysis.

Element	Wt%	Element	Wt%
Si	25.482	K	0.017
Al	15.115	Cs	1.249
Ca	16.115	Eu	0.522
Fe	19.180	S	0.002
Cr	2.241	P	0.002
La	4.490	Pr	0.015
Ce	8.812	Ny	0.015
C	1.691	Na	0.017
Mn	0.081	Ni	1.003
Mg	3.952		

3.2 General sample preparation

Unless stated otherwise, the term “ground” is used in the context of reducing surface roughness of bulk samples using an abrasive held fixed; the procedure involves using silicon carbide paper in six steps using 400, 600, 800, 1200, p2400, p4000 grit paper with 2 mins at each step, using the Buehler; 8” MetaServ 250 single grinder-polisher. Grit p4000 has a median particle size of 2.5 µm [174].

Similarly, the term “polishing” refers to a two-step polishing regime using loose abrasive particles; this is not in addition to the grinding regime; the two are not necessarily performed together. The sample is first polished using a 3 µm diamond suspension for 3 mins, after which it is washed in still water and then re-polished for 4 mins on a 1 µm diamond suspension. Polishing was performed on the Buehler; 8” Single Speed Grinder/Polisher.

Any powders mentioned refer to a sample that has been crushed using a pestle in a mortar such that it sits on top of a 38 µm sieve but fell through a 63 µm sieve unless stated otherwise. Following sieving the powder was washed in acetone.

3.3 Characterisation

3.3.1 Scanning Electron Microscope

Samples were ground and polished, and because of the non-conducting nature were coated with either gold or chromium using:

- Gold: EMITECH K550 at 25 milliamps for 1 min.
- Chromium: Quorum Q150TS ,pre-set program for 20 nm layer thick.

Gold or chromium were chosen to not interfere with elements known to be present in the samples for EDX analysis, based on the chemical composition as was determined from section 3.1. For instance, samples known to contain lanthanum, cerium, praseodymium, and neodymium were coated using gold rather than chromium, due to the K_α peak of Au overlapping with the minor actinide elements M_α. Carbon was not chosen to allow determination of the presence of carbon in the material, if any.

Following this they were then observed using Backscattered Electron Imaging (BEI), Secondary Electron Imaging (SEI), and Energy Dispersive X-Ray (EDX) results were collected. The Jeol JSM 6400 Scanning Electron Microscope (SEM) was used at an accelerating voltage of 20 keV and a working distance of 15 mm, unless stated otherwise. High resolution images were obtained using the LEO Gemini 1520 Field Emission Gun (FEG) SEM, both the working distance and acceleration voltage were varied.

Pre-corrosion tests were performed to allow comparison with the post corrosion SEM. Secondary electron and backscattered electron images were taken of areas of interest (such as a crystal or easily found feature) along with EDX results to allow a before and after comparison.

Post corrosion, samples were gold-coated and analysed using BEI, SEI and EDX. Following these results, the samples were mounted in epoxy, cut in half and gently polished to reveal a cross sectional view of the sample. This exposed cross section was then coated with gold and re-examined using SEM-EDX to gather chemical data as a function of depth from the original surface. The main focus of this test was EDX line scans. Whilst point scans give qualitative/quantitative information on the chemical content at the specific point selected, line scans give only a profile of how the elements are distributed along a line, showing any increases or decreases as a function of distance. This makes line scans a very useful tool for analysing how the chemical composition changes as a function of depth.

It is important to note that the interaction volume of X-rays under standard conditions is close to 1 μm^3, this is obviously undesirable for gel layers with thicknesses of <1 µm. To reduce the interaction volume as much as is possible, the acceleration voltage was lowered to 5 kV. The reduction was estimated to be approximately half, to 0.5 µm using the formula and basic assumptions shown in Equation 8.

Penetration depth equation:

$$x(\mu m) = \frac{0.1\, E_O^{1.5}}{\rho} \quad (8)$$

Where E_o is the accelerating voltage in kV and ρ the density of the sample in g/cm^3 [175].

Typically, borosilicate glass has a ρ around 2.23g/cm^3 giving a penetration depth of 0.501 µm using a 5 keV accelerating voltage.

The equation given for the width of the interaction volume is as follows:

$$y(\mu m) = \frac{0.077\, E_0^{1.5}}{\rho} \quad (9)$$

Where E_o is the accelerating voltage in kV and ρ the density of the sample in g/cm^3 [176].

The SEM principle is much the same as that of an optical microscope, however instead of light waves and an optical lens, electron and magnetic lenses are used, typically in a high vacuum to limit interference from dust particles however SEM's do exist that can operate without a vacuum [177]. The use of electrons is due to their potentially small wavelength. The spatial resolution of an image is directly proportional to the wavelength of the photon used to convey the image; electrons used in this manner can have very high theoretical resolution as their wavelengths are in the region of 10pm in comparison to a limit of 500 nm for visible light. One important difference is the mechanism of image formation; an SEM forms the image with each pixel being formed sequentially, by scanning each spot before moving onto the next.

Electrons are generated from an electron source; three sources currently exist for SEM applications however only two such sources were used in this study, a tungsten filament which produces electrons via thermionic emission, and a FEG, which as the name suggests, emits electrons through field emission; this provides a much higher image resolution than that of a tungsten gun. More information regarding the sources can be found in "Review of electron guns" by Christian Travier [178].

Electrons are then passed through a series of magnetic lenses and focused into a narrow beam and on to the sample. Several signals are emitted as a result of electronic interaction, the ones utilised in this thesis are secondary electrons, back scattered electrons and characteristic X-rays, and the zone from which they are generated is termed the interaction volume. This is summarised in Figure 24.

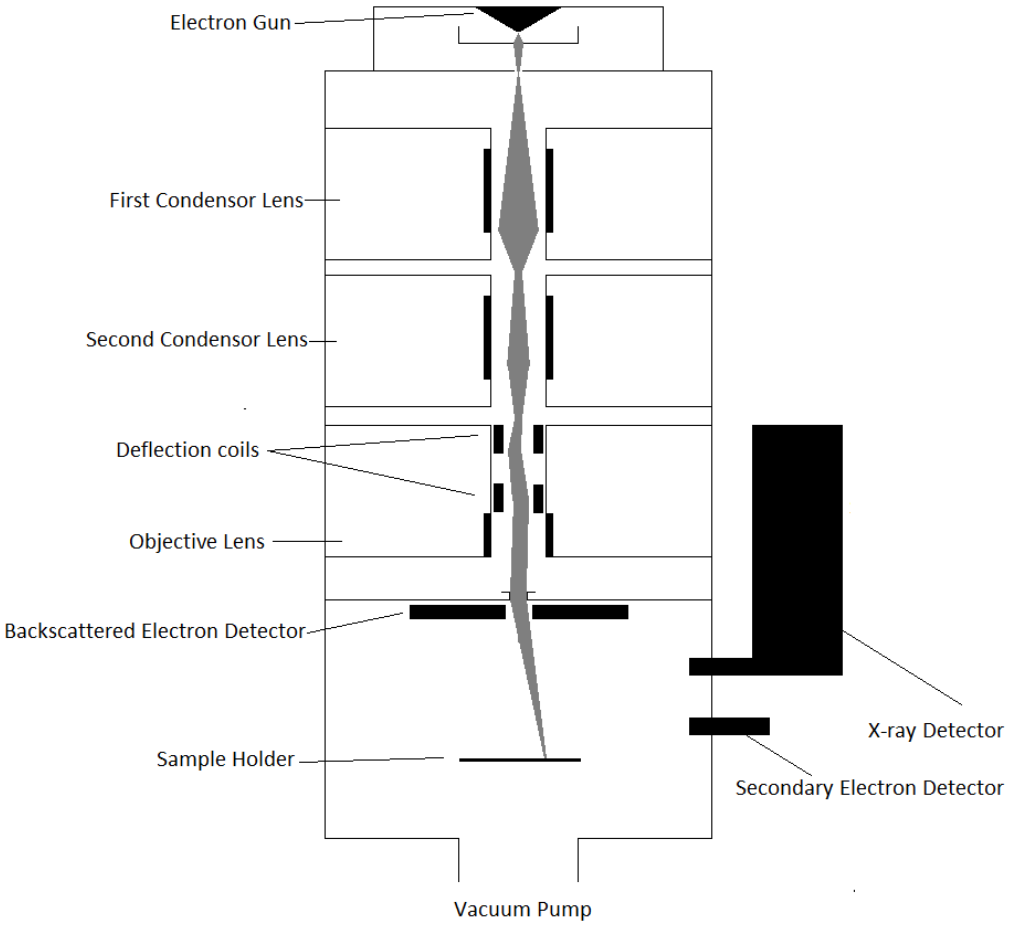

Figure 24: Cross sectional view of the generic set up of an SEM, showing how the electron beam is focused as it passes through several electromagnetic lens' before being directed onto the sample by a set of deflection coils. The relative position of the various detectors (BSE/X-ray, SE detector) and coils are shown. [prepared by author].

Although these signals are generated within the interaction volume, they originate from different portions of the interaction volume, the size of which is dependent on the density of the sample and the accelerating voltage applied to the electron source (and thus the energy of the electrons interacting with the sample) [179].

Each of the different signals is discussed in the following sections.

3.3.1.1 Secondary Electrons

Secondary electrons arise from the inelastic interaction of the primary electron with electrons in the sample, removing an electron from the atom it is bound to. The electrons produced are energetically weak, typically less than 50 eV and thus only those from the first new nanometres (~5 nm) escape the sample and are detected. The low energy nature and low penetration depth leads to a signal that primarily yields topographical features as crevices lead to reabsorption of electrons appearing dark, whilst raised surfaces and slopes allow more electrons to reach the detector appearing brighter. In addition, edges appear brighter due to enhanced emission at corners [180].

3.3.1.2 Backscattered electrons

Backscattered electrons (BSE) are electrons that have elastically interacted with the sample and have small sample escape angles, relatively to the electron beam. For this reason, the backscattered electron detector is usually a toroidal silicon solid state detector [181] placed directly above the sample, and such that the electron beam passes through the open centre. Production of BSE is dependent on the electron beam spot size, accelerating voltage, density of the material and chemical content of the investigated area. Heavier atoms and atomically denser areas will create more BSE as the nucleus will have a larger field of influence. It is for this reason that BSE imaging shows differences in composition with bright areas being atomically denser than darker areas. BSE originate from the lower half of the interaction volume, typically a depth of 1 µm, giving a similar spatial resolution. This can be influenced by the accelerating voltage and density of the sample.

3.3.1.3 Energy dispersive X-ray spectroscopy

The ejection of electrons in the sample atoms via inelastic primary electron collisions produces an unstable atom. This is instantaneously corrected by a high energy electron falling to the low energy position. By the law of conservation of energy, an X-ray is produced which is unique to that element. This allows for qualitative information regarding the chemical content of the specimen to be collected however quantitative data can also be obtained using standards calibrated by comparing their relative intensities. The resolution of EDX is similar to that of BSE and affected by the same factors.

3.3.2 Depth Profiles

Depth profiling features significantly in post corrosion sample analysis as a means to determine the concentration of elements as a function of depth. This involves mounting the sample in a nickel-epoxy mix to ensure the resin is conductive in such that the attacked surface is embedded in the resin and not visible. The mounted sample is then removed from the epoxy container and cut length wise, such that the attacked surface and pristine version of the sample are visible, along with the surrounding epoxy. The sample is then gold coated, or chrome coated (based on preliminary results of the sample composition) and placed in the SEM for analysis. This process is outlined in Figure 25.

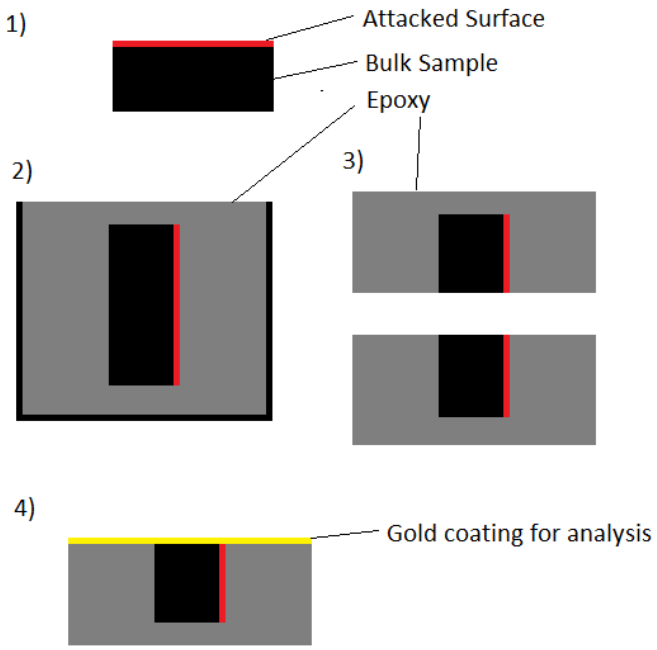

Figure 25: Process for sample preparation for depth profiling. 1) Sample attacked surface is determined 2) the attacked surface is placed at 90^{o} angle to the epoxy mould, and epoxy is poured in and allowed to set. 3) the solid epoxy is cut in half exposing the pristine sample, the attacked surface and the epoxy. 4) sample is then coated, and placed as seen in the SEM for observation [prepared by author].

The prepared sample is then analysed using EDX line scans. This analysis technique differs from usual EDX results in that the concentration is not provided in wt% or at% but in the number of X-rays associated with a particular element, and a plot of the X-ray count versus the length of the pre-determined line is formed. As already mentioned, EDX uses X-rays to determine the concentration of elements; it does so by plotting a graph of X-ray counts versus X-ray energies. Each energy is associated with a certain element, much like XRD peaks are associated with a certain crystal. The intensity of these peaks in comparison to each other allows qualitative analysis of the elements present. Line scans are made up with two steps, the first performs the normal EDX scan over the entire line analysed giving the elements present over the line. Step 2 involves narrowing the search by only analysing the energy associated with the elements found present in step 1, and counting the X-rays associated with that element. This function is not done 1 energy value at a time but over the entire spectrum as set out by the user, for all samples this was in the 0-20 keV range. The result of this technique is an X-ray count profile over the line investigated. The line was chosen such that it went through the bulk sample, attacked surface and any corrosion layer present, and into the epoxy. This is summarised in Figure 26.

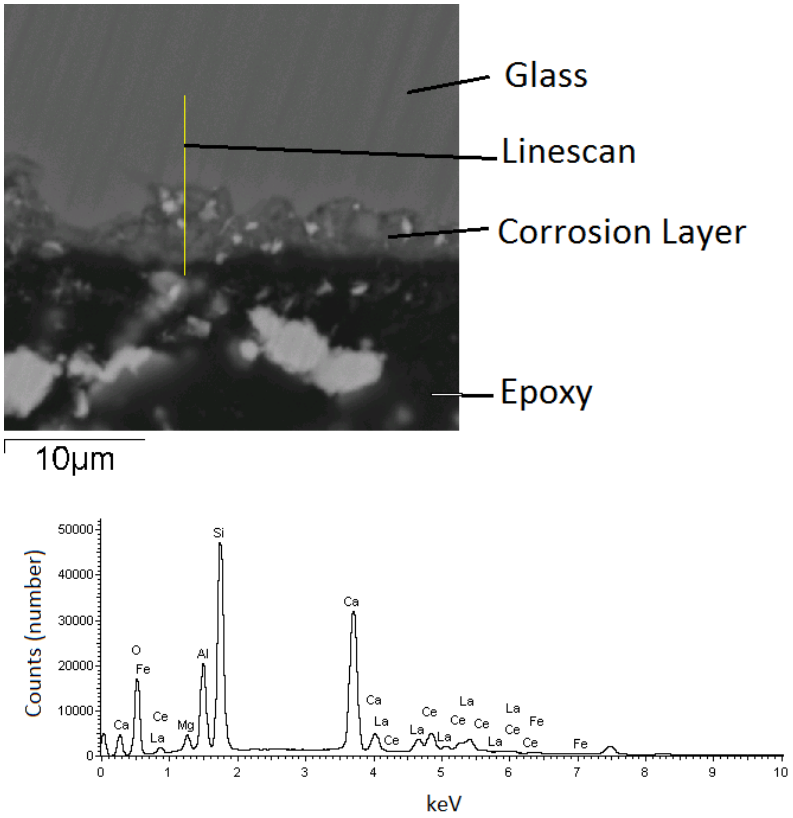

Figure 26: Example BSE image of a glass sample corroded for 10 weeks under MCC-2 conditions, superimposed on this image is the position of line-scan analysed (yellow line). The line scan, along with the sum of all X-ray counts over the line are illustrated in the spectrum; showing the total X-ray counts as a function of X-ray energy [prepared by author].

The results for this are plotted as X-ray counts versus length (µm) yielding a graph similar to that seen in Figure 27, however the scale relating to certain elements makes presenting these results on one graph impracticable. In this case the high counts for silicon would cause the other results to be dwarfed in comparison, and no information from the Na-Mg graph would be visible. The large scale of this technique used in this thesis made portraying the results as seen in Figure 27 also impracticable and so the results were normalised by the bulk values (100% is X-ray count in the pristine wasteform).

Normalising the results utilised the relatively constant number of X-ray counts in the pristine glass as the number of X-rays that would be detected in an uncorroded wasteform as it was not in direct contact with the attacking solution, and was too far away from the surface to have any elements leached as was found from long scans stretching over 100 µm; for most samples no leaching was found past 10 µm depth. For instance, the bulk X-ray counts for silicon in this example would be 4450 X-ray counts over the 10-15 µm range. Each point along the graph was then divided by this average, converting it to a percentage of the bulk X-ray count giving the more convenient graph shown in Figure 28. The final graph allows for any increase/decrease in the concentration of a particular element to be observed relative to the values that would be found in bulk.

It must be noted that these do not reflect the actual concentration of these elements, normal EDX software forces the composition to sum to 100, hence the qualitative nature of EDX. This technique only shows the X-ray counts for each element, thus results for each element are independent as

would not be the case for EDX point scan results where an increase in one element must have a corresponding decrease in another element, this does not occur here.

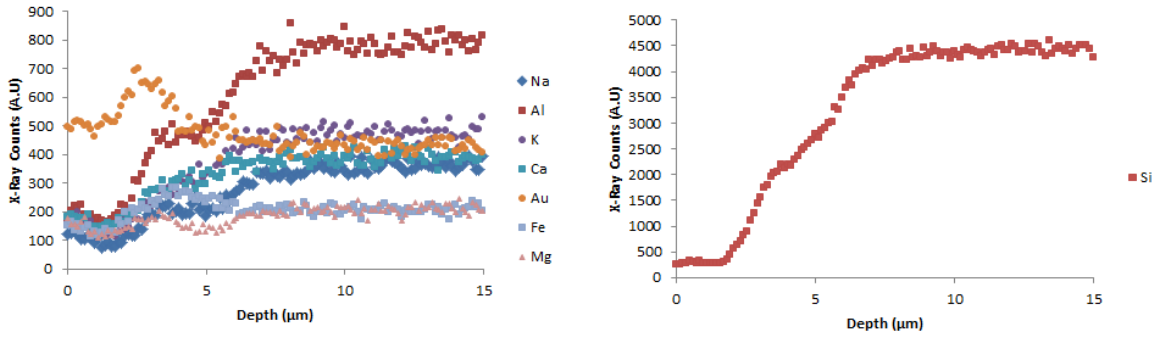

Figure 27: Example un-processed graph from an EDX line scan. The X-ray counts are plotted against length, the length is determined by the scale bar of the image used, the software extrapolates from the scale bar as to the length of the line chosen, in this case the length of the yellow line in Figure 26[prepared by author].

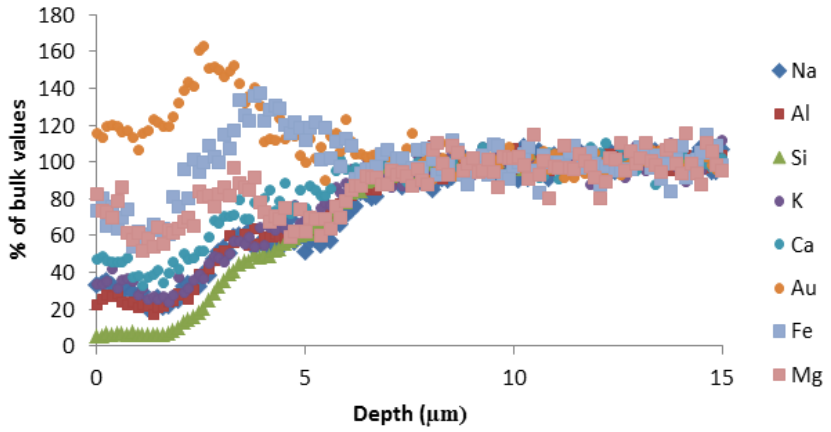

Figure 28: Example of a processed depth profile, by normaliing the results against the bulk values silicon is now easily observable on this graph as the green triangular points, retaining the profile observed in the previous graph, but allowing for quick comparison against the other elements [prepared by author].

This technique comes with both benefits and drawbacks. The benefits are numerous and include the following:

- In comparison to other techniques, this is a quick means of determining the elemental profile, whilst other techniques such as focused ion beam trenches and Time of Flight Secondary Ion Mass Spectrometry (ToF-SIMS) are often costly and very time consuming.
- Training time for this technique is minimal; a novice SEM-EDX user along with the correct software requires only modest training to properly use this technique.
- Cost. SEM and EDX are extremely common, and are relatively cheap to use. This is the cheapest method to show a depth profile.

The drawbacks are mostly based on the quality of the information received.

- The more expensive and time consuming techniques already discussed provide much more detailed information on the sample, including more accurate results, and include elements otherwise not detected by EDX.
- The spatial resolution is a limitation to this method. Under normal conditions this can be 2 μm but with adjustments to accelerating voltage, incidence angle of the electron beam, stage height, and the type of filament used this can be reduced to 0.5μm.
- The results collected show a profile, rather than a quantifiable concentration, whilst useful this may not be appropriate for other wasteforms.

This technique was chosen as a means to quickly determine whether a waste-form is worth more, in-depth analysis. Glass corrosion studies often jump to the more advanced techniques, when both money and time could be saved should this technique show the waste-form is unsuitable for disposal allowing more time and resources to be committed to the more promising wasteforms.

Error for this method was chosen to be no more than ±5% (of bulk values) for each data point, the error will be a function of the square root of the total X-ray count, longer scan times increased the total number of X-rays thus allowing for smaller error. Due to machine error, sample PF-Asb depth profiles are shown with error bars as longer scan times could not be employed resulting in a higher error for certain elements.

3.3.3 Scanning Electron Microscopy; Further Notes

SEM and EDX were first used to observe the presence and composition of the phase(s) present, for any material where a possible crystalline phase was present through visual inspection this was the first technique used. BEI was favoured over SEI for use in determining the location of the crystalline phase present in this sample. However not all samples produced an image where these phases were easily observable and distinguishable, thus further steps were taken to help detect these phases and analyse the differences between them. In addition, the inherent nature of EDX point scans make certain observations difficult, such as determining what element has increased/decreased in comparison to a previous scan as the results are forced to sum to zero, an increase in one element must have a corresponding decrease in another, or in all. The spatial resolution of EDX also makes determining the composition of small particles (diameters <2 μm) problematic as the scan will invariable include X-rays from the surrounding region, convoluting the results; this is better seen in Figure 29. To help with this problem, the settings of the SEM were adjusted to lower the width of the interaction volume, thereby decreasing the minimum width for accurate readings. The accelerating voltage was decreased from 20 keV to 15 keV to 10 keV and to 5 keV. This was expected to reduce the interaction volume width to around 1.5 μm (for 15 keV) and 0.3 μm (for 5 keV), and hence the spatial resolution was reduced to this width (see Equations 8 and 9, section 3.3.1). The spot size of the electron beam is dependent on several variables and cannot be calculated. However, the spot size was in the region of 10 nm (estimate 1-50 nm range), and therefore not the limiting factor for spatial resolution.

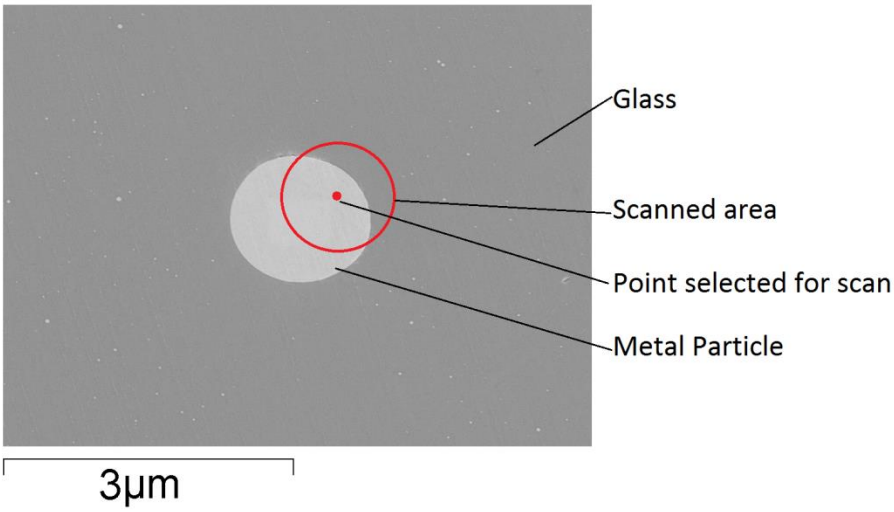

Figure 29: A mock example of how EDX scans cannot be representative of the actual composition. In this example the particle is ~2 µm wide. The region being scanned is shown as a red circle leading to results which include the surrounding regions composition. Typically, EDX point scans are shown as points (red dot) rather than the area being scanned (red circle) as the region scanned is influenced by a range of factors [prepared by author].

A second tool which helps with the issues surrounding the spatial resolution of EDX, is the use of EDX mapping, whilst these are still governed by the limitations on EDX spatial resolution, they can help by showing an increase/decrease in the number of X-ray counts associated with an element. This is not as noticeable in EDX point scans which forces the wt%/at% numbers to sum to 100, and might show an increase in one element, as a greater decrease in another element occurs and vice versa. Further, because the point scans are extremely close to one another (<1µm) they are much more sensitive to composition changes as they can show the increase/decrease of an element going into a small phase, such as the example one shown in Figure 29. If the mapping showed that, for instance, Fe increased in the sample region, before decreasing again to zero when leaving the sample then it is safe to assume that the particle consists of iron. Conversely if the amount of silicon decreased to zero going into the particle and rose again going out, then it is likely no silicon exists in the particle. If no other elements are detected then it can be said the particle consists of only iron, even though the particle may show signs of containing silicon. This of course can be accomplished by using multiple point scans instead of mapping, however this method is time consuming and the same conclusion can be reached in minutes using mapping in comparison to hours when using multiple individual point scans. This method is shown in Figure 30, the mock graph is linear, but this method is applied on a 2-dimensional scale making the process easier.

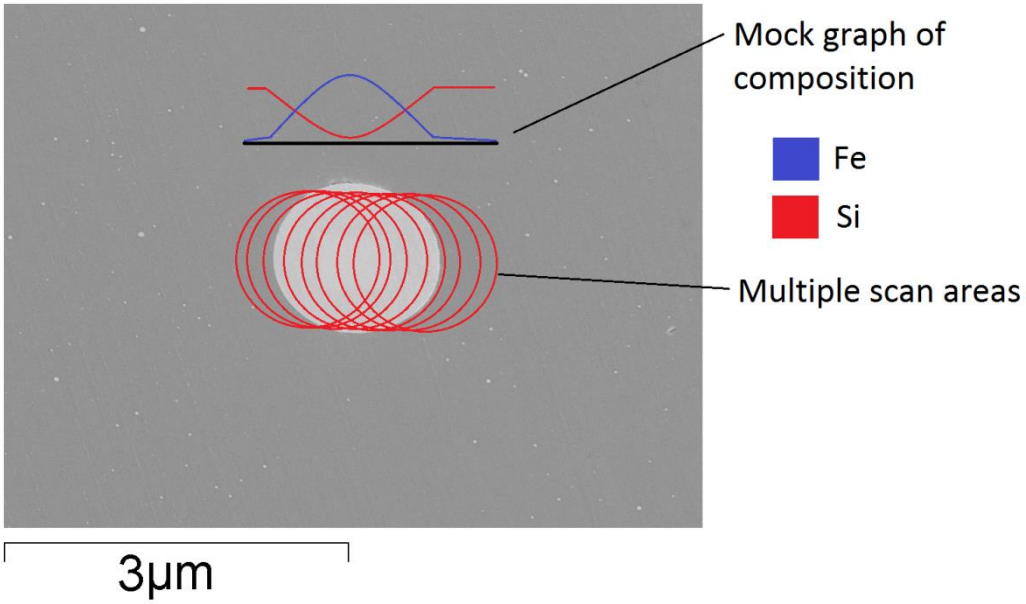

Figure 30: A mock example of how EDX mapping can help show the real composition of a particle, to some extent overcoming the spatial limitation. This will, to some degree, allow certain elements to be shown as either lower in composition than a single EDX point would show, or completely remove altogether. In this case the particle is pure Fe [prepared by author].

Where similarly composed phases were present in close proximity to each other, high contrast BEI was employed, whereby changing certain parameters results in better contrast but a "noisier" image. This technique is used due to the inability of BSE to distinguish between phases of similar composition, usually BSE can distinguish these phases but issues arise when the phase composition is close, and will vary from sample to sample. Generally, by altering the energy of the primary electrons the number of backscattered electrons produced by either atomically denser phases or by phases containing heavier elements, can be increased or decreased. This is done by lowering the accelerating voltage from 20 keV to 10 keV. The large decrease in accelerating voltage results in a large loss of total BSE production making a clear image harder to obtain. This was compensated for by using a longer scan time, typically the scan time was increased from a 2 mins to 5-10 mins, dependant on the resulting image.

The compositional accuracy of EDX (not based on spatial resolution) was checked by analysing against several known materials; the brass sample holder, and 4 standards used in calibration for wavelength dispersive X-ray spectroscopy (MgO, pure Si, $NaAlSi_3O_6$ (albite field), and CeAl). For this method, 10 EDX point scans were performed on each standard and averaged, this resulted in an accuracy of 0.1-2 wt% from the predicted stoichiometric wt%; the more complex the material (number of elements present) the greater the error. As the most complex material referenced for EDX was the $NaAlSi_3O_6$ and most of the GCMs analysed here were even more complex, it is difficult to establish an absolute upper error. As the albite material had an error of 2 wt%, this will be taken as the upper limit. Although 2 wt% is the established maximum error, error limits for EDX results will be presented as either the average from a series of EDX points, or the inherent error of EDX reported by the manufacture of 0.1 wt%, whichever is greater. The reason behind this choice is the method of calculating the error; although 2 wt% was found as a maximum this was a rare occurrence, and not the case for all the reference samples where on average, the error was approximately 1 wt%. Rather,

this should be noted as the upper error limit, with the presented error being representative of only the available information from the analysis.

Carbon and oxygen was observed as an impurity (in all samples) in amounts no greater than 0.5 wt% and 1 wt% respectively, and was present as organic surface contamination. This was repeated for when the standards were coated in gold, and again in chromium (on different dates). This resulted in a higher error for when the peaks of Au and Cr interfered with elements in the standards of approximately 5 wt%. This result led to the decision to first analyse each sample twice, once coated in gold, a second time in chromium to assess what elements were present and select the coating most appropriate for the material.

3.3.4 X-Ray Diffraction

Solid samples were held in place by plasticine to achieve a level surface. Powder samples (approximately 50 µm average particle diameter, ± 20µm) were placed on a single crystal; zero background substrate of silicon, the single crystal was cut such that the diffraction peaks would be at a large 2θ and so not appear on the trace. The powder was then flattened out using a glass slide.

Diffraction was carried out using a Bruker D2 Phaser, using a step size of 0.0249 2θ between 20-70 2θ. The total time for each analysis varied from 1 to 8 h. Following this, the program X-Pert HighScore Plus was used to identify the phases based on the detected diffraction lines. HighScore Plus uses the International Centre of Diffraction Data (ICDD) to do this.

X-ray diffraction (XRD) is a technique that utilises X-rays to probe the crystalline structure of a material, and provides unique information of its structure, allowing for identification of materials based on the measurements taken, by comparing to known crystalline XRD patterns. This analysis method works in an almost identical way to fingerprint analysis, and has the same drawbacks: it only works well for materials that are known and have been previously documented.

X-rays are electromagnetic radiation produced by electronic transitions in the atom and have wavelengths in the range of 0.02 Å -100 Å. Diffraction of these waves by regularly spaced atoms can then give information on the crystal. To achieve diffraction, the distance between the atomic slits, has to be comparable to that of the wavelength of the propagated radiation. X-rays meet these criteria, and as such are perfect for investigating the distances between atoms in any crystalline media. When the X-rays interact with the crystal, they are diffracted by a diffraction angle θ determined by the Bragg equation:

$$2d\ \sin\Theta = n\lambda \tag{10}$$

Where “d” is the spacing in the crystal, “θ” is the diffraction angle (between the beam and the lattice planes) “n” is an integer, “λ” is the wavelength of the radiation [182].

The interaction of X-rays for the same crystallographic plane produces constructive interference leading to an increase in detected X-rays for the incident angle used to achieve this. By plotting incident angle (measured in 2θ by Equation 10) versus X-ray counts, a set of peaks, representative of that particular crystal, gives the diagnostic “fingerprint”.

3.3.5 Differential Thermal Analysis/Thermo Gravimetric Analysis

About one g of powdered samples (~50 µm particle diameter, ±20 µm) were used in an inert alumina crucible, a heating regime of 5°C min^{-1} was used to a maximum temperature of 1600°C followed by a cooling rate of 20°C min^{-1}. This was performed in an argon atmosphere. The device used was the Netzsch STA 449 F1 Jupiter.

Differential Thermal Analysis (DTA) and Thermo Gravimetric Analysis (TGA) are two techniques, often used simultaneously, to help measure thermal attributes of a material e.g. melting temperature. The technique involves placing two inert crucibles in a sealed chamber, one containing the sample (powder or monolith) whilst the other one is empty and used as a reference. Both samples are then subject to a heating regime in a predetermined environment (argon or oxygen). A precise thermocouple and weighing scale detects differences in sample temperature, and any weight gain/loss [183].

3.4 Leach tests

3.4.1 Durability tests

The first step to understand how GCM degrade is to use ideal conditions, in this case de-ionised water, in a controlled temperature environment.

Several durability tests have been constructed to assess chemical resistance, mainly those devised by the Materials Characterisation Centre (MCC) at the PNNL in the USA. The MCC-2 (ASTM C1220-10) was selected, and comprises of a monolithic sample placed in a closed container with a volume of deionised water dependant on the surface area of the wasteform. For these tests the Surface Area to Volume ratio (SA/V) was 0.05 m^{-1}, on average this resulted in 10 ml of deionised water for every 0.5 g of wasteform. Once prepared the closed samples were placed in an oven at 90 ^{o}C for up to 14 weeks.

3.4.2 Sample preparation

Monolithic samples were first roughly cut into cuboids using a copper saw, and put through a grinding and polishing regime as discussed in section 3.2. The initial grinding regime (coarse) was performed in such a way so as to make a regularly shaped cuboid. The subsequent grinding stages were performed as usual apart from the final grinding stage where all sides were equally ground until the specimen weighed approximately 0.5 g (±0.0001) determined from a Sartorius mass balance. This process was repeated 5 times, resulting in 5 distinct cuboids of the same wasteform which were washed in acetone, allowed to dry, and were then collectively placed in one Teflon digestive vessel. A volume of de-ionised water was then added to the digestion vessel, the amount dependant on the surface area of the sample; the amount of water was calculated such that the SA/V ratio was the same across all wasteforms. The Teflon digestion vessel was then placed in an airtight oven set to maintain a temperature of 90°C ± 1°C.

The desired corrosion times were 2,4,6,10, and 14 weeks. At each time interval, the digestion vessel was removed from the oven (but not opened) and allowed to cool to room temperature in a water bath. A thermocouple was used to determine that the outside of the Teflon digestion vessel was within 1°C of room temperature (measured from the base), and then left to cool for an additional 1 h to ensure the entirety of the vessel was at room temperature. The vessel was then removed from

the water bath and opened. One specimen was removed from the vessel using sterilised plastic tweezers. A syringe was then used to remove a portion of the leachate, the amount removed was dependant on the intial SA/V ratio; the volume of water removed was such that it conserved the SA/V ratio throughout the experiment. The vessel was then resealed, and placed back into the oven. This procedure took no more than 2 h, the oven was noted to have dropped no more than 1 °C during the procedure, and recovered to 90 °C within 5-10 mins.

The whole procedure was repeated at each corrosion time until week 14 when the last specimen was removed along with the remaining water. The amount of water removed from the last specimen was measured to ensure that no excessive evaporation had occurred during the removal process for the entire corrosion time. For example, if 50 ml of water was the initial amount of water added, at each removal stage, 10 ml was removed; if less than 9 ml was present at week 14 then the results from the entire experiment was discarded.

The corroded specimen was immediately removed for electron-microscope analysis as described in section 3.3.3. The leachate was removed for both ICP-OES and pH analysis (on separate aliquots) as described in section 3.5.1 and 3.5.2.

Each wasteform had the above description preformed 7 times, resulting in 6 teflon digestion vessels, each containing 5 specimens for one wasteform. However, 3 of these were dedicated to pH analysis solely, and were removed much more frequently to measure the progression more accurately. The values were checked against those determined from the "main" experiment, as described above. Also of note, the pH analysis was performed after the main experiment, and did not interfere with the oven temperature.

At least one Teflon digestion vessel from each wasteform (30 samples across 6 wasteforms) failed the "test" on the leachate at week 14 and had all their results discarded, equating to a 84% success rate.

3.4.3 Surface areas

Various surface areas were calculated during the course of the experiments, most prominently for SA/V ratios, however other surface areas are given. All surface areas were measured using the same technique; a combination of high contrast SEM images, and pixel counting. Contrast on an SEM image was altered do make the desired shape appear as one colour (usually white), with everything else appearing as the opposite colour (usually black). The number of white pixels in the image was known (calculated by adobe photoshop) and compared with the scale bar to give a surface area. Error was limited to the contrast; this was performed manually and susceptible to human error, the contrast was altered until the operator was satisfied that the area only involving white/black pixels was associated with the desired area to be calculated.

When calculating the surface area occupied by a crystalline phase to determine total crystal%, BSE allowed for distinguishing the different phases, and using the above method the various surface areas calculated. The maximum error calculated for this method was ±5%, mostly due to the "grey" area at the crystal-glass boundaries. However, greater error is cited due to the size of the crystalline phases, and the size of the image; the inhomogeneity of some samples meant that certain SEM images contained more/less crystal % than the average. To lower the error associated with this, multiple sites were analysed.

Surface areas for SA/V ratio used this method, each side was imaged and the total surface area calculated. Error using this method was less than that for surfaces areas calculated elsewhere, as no boundary existed (these samples were not mounted in epoxy).

Average pore size utilised this method; one pore at a time was isolated and its pixel count calculated. Additionally, the software also allows for lines of known pixel length to be drawn, this allowed for the dimensions of the pores to be calculated when compared with the pixel length of the scale bar. A large number of pores were then analysed giving an average.

3.5 Solution Analysis

3.5.1 Inductively Coupled Plasma Optical Emission Spectroscopy

Inductively coupled plasma optical emission spectroscopy or ICP-OES was the used for determining leachant composition, this was used to analyse the elements released into solution during MCC-2 tests.

ICP-OES uses an argon based plasma torch, maintained at temperatures upwards of 7000K to completely ionise any element placed into the plasma chamber [184]. Liquids analysed using this technique must first be passed through a nebuliser, via a peristaltic pump; this aerosols the liquid changing it into a mist. This is then injected into the plasma chamber and “swirled” around by an electromagnetic field.

When the sample is passed through the plasma all compounds are broken down into their constituent elements, which are then further broken down to ions, however this de-ionisation process is continuous, with electrons joining the nucleus before being removed from it again. The plasma emits light based on the elements present due to recombination of electrons, the wavelengths of which are unique to that element. The light is passed through a spectrometer to help separate each wavelength before it reaches the main detector. Most modern detectors are a solid state type, based on charge coupled devices, thus removing the limitations on previous detectors which worked on a single wavelength basis requiring several detectors and were fixed once installed thus limiting the number of elements that can be to analysed.

Once the detector analyses the various wavelengths, a program compares the intensity of these wavelengths with known standards, thus allowing a high degree of accuracy on the order of ppm for analysed solutions. Some issues can arise from this such as an overlap of certain elements wavelengths; the intensities of certain elements can make it difficult for the computer software to accurately detect other elements with similar wavelengths. As each element produces more than one wavelength of emitted light, several wavelengths were selected to avoid these issues as far as possible.

Leachant samples were removed via a syringe and passed through a filter to remove any solid particulates which could damage the apparatus. These were then immediately moved to the instrument, an iCAP 6000 series ICP-OES and analysed. ICP multi-element standard solution VIII (24 elements in dilute nitric acid, 100ppm) was used to determine the presence of Al, B, Ba, Be, Bi, Ca, Cd, Co, Cr, Cu, Fe, Ga, K, Li, Mg, Mn, Na, Ni, Pb, Se, Sr, Te, Tl, Zn. A separate standard was used to determine the concentration of silicon (1000ppm in sodium hydroxide solution) due to

incompatibility between the two sets of standards. The standards were prepared at concentrations of: 5, 10, 20 and 40ppm. These were then double checked by placing a separately constructed sample of known concentration among the leachant samples analysed. Any deviation from the separately prepared standard would indicate a mistake in the reference standards preparation and it would be performed again with new standards.

3.5.2 pH tests

Long term pH tests were conducted using the MCC-2 test, after a fixed time a 10 ml (±2 ml based on SA/V ratio) portion of liquid was withdrawn and analysed. The vessels were removed from the oven (at 90 ^{o}C) and allowed to cool to room temperature without breaking the seal; this was to avoid any evaporation of the leachant. The vessels were then opened and the solution analysed using the Thermo Scientific Orion star A111 pH meter to an accuracy of 0.02. The results were run in triplicate and the vessel resealed and returned to the oven. Error was either the max difference from the average of 3 repeat results on each 10 ml of solution, totalling 9 results for one time, or the inherent error of pH (0.02) whichever was greater.

3.5.3 Normalised Leach Rates

Normalised elemental release rates (NL_r) are commonly used to calculate the rate loss of a material subject to a corrosion test as a function of time; normalising these results allows for comparison with other materials subject to the same test. The equation used for calculating NL_r of an element i present in the solid [185] is shown below (Equation 11):

$$NL_r = \frac{(C_i - C_0) * V}{f_i * SA * t} \quad (11)$$

Where "C_i" is the concentration of element "i" in solution (g/l), C_0 is the initial concentration of element i in solution however as doubly deionised water was used the value was zero (confirmed by ICP-OES). "V" is the volume of leachant used (l), "SA" is the reactive surface area of the sample (cm^2), and "t" is the time of the corrosion experiment (days).

In glass corrosion experiments, f_i is the mass fraction of element "i" in the material, typically calculated using the following formula:

$$f_i = \frac{w_i}{w_0} \quad (12)$$

Where w_i is the mass of element i in the wasteform (g), and w_o is the total mass of the sample used (g).

However, due to uneven partitioning of elements into different phases in a GCM, Equation 12 could not calculate the total mass fraction of element "i" in the wasteform, instead Equation 13 was used to determine the mass fraction of element "i" in the wasteform:

$$f_i = \sum_{i=1}^{n} \frac{w_i}{w_o} m_i \quad (13)$$

Where "n" is the total number of phases present in the wasteform, w_i/w_o is the mass fraction of element "i" in phase "n", and m_i is the volume fraction of phase "i" in the wasteform.

Averaged EDX wt% results were used to calculated the mass fraction of element "i" in each phase. The volume fraction of each phase was calculated from SEM images; a low magnification was used

to allow full view of the analysed sample (approximately 1 mm^2) and the surface area occupied by each phase was calculated, this was preformed 4-6 times to get as accurate a value as possible.

Error was calculated using the larger value from the maximum and minimum values determined from Equation 11, this involved maximising the values for C_i , whilst minimising the values for f_i and SA for calculating the total maximum value, and vice versa for determining the total minimum value.

4.0 Results

This chapter aims to present the results collected for each sample whilst chapter 5 will discuss the results presented here in more detail.

4.1 Joule Heated-In Container Vitrification Wasteform Characterisation

To help prediction of how each material will perform under repository conditions, identification of the phases present in them is needed. In addition, microstructural and phase characterisation will help further experiments using this technology by indicating which wastes need to be retreated to avoid the formation of harmful phases (if any). This chapter documents the various results collected from the characterisation techniques used before and after simple corrosion testing in aqueous environments (see section 3.2-3.4).

4.1.1 Joule Heated-Plutonium Contaminated Material

XRD results for this sample were split into two due to the “spots” that were visually observable on the sample. First, a sample was prepared for XRD without any segregation of these spots, the second XRD specimen was prepared by removing and segregating these “spots” so that none were believed to be present for the XRD analysis. Figure 31 displays the results for the non-segregated portion, revealing that the material is crystalline; the main phases suggested using the XRD database described in section 3.3.4 were clinoenstatite, enstatite, pigeonite, and augite. Substitution of various simulated waste elements would be enough to shift the peak locations and their associated intensities from those used to originally determine the XRD pattern for each specific crystal. The use of XRD to determine the exact phase present is well known, however a lesser known use of XRD for more difficult materials is the ability to use the peak locations and intensities, even if changed from a stoichiometric crystal, to assign a family of phases to the crystal in question. In this case, it can be said with a high degree of accuracy that the phase present is from the pyroxene family of phases.

A 2 g (±0.1 g) portion of the sample that was determined to have no crystalline phase was isolated using a combination of a copper saw and subsequent grinding until no more crystalline phases were visually observed. This was then analysed using XRD (figure 32) revealing it to be amorphous.

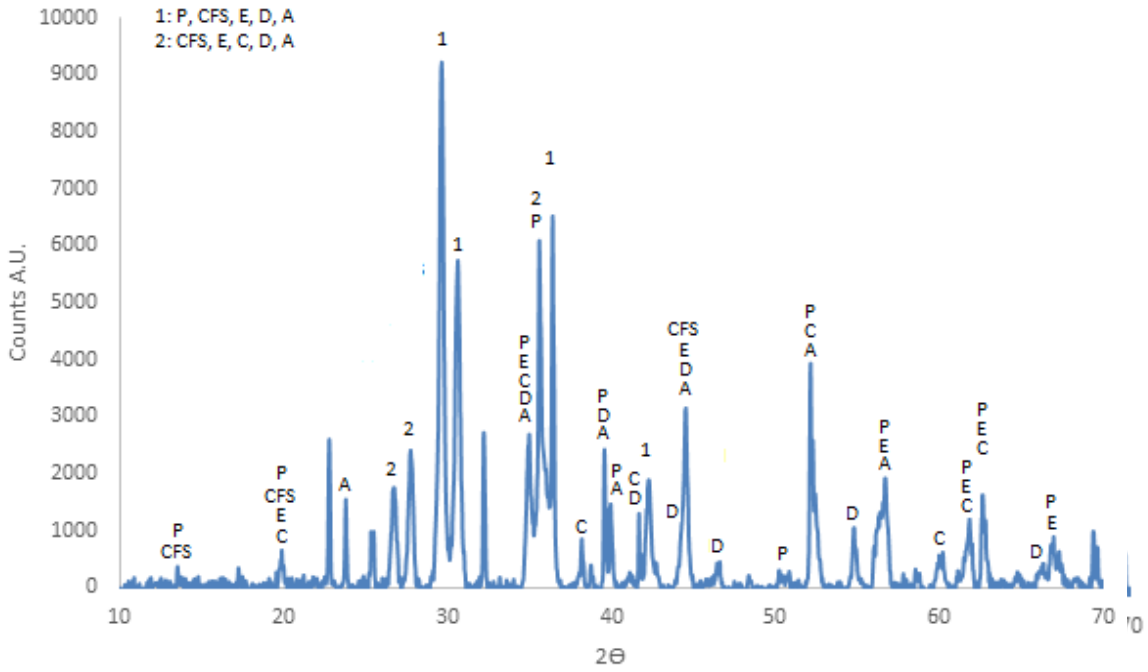

Figure 31: XRD trace of a powdered portion of JH-PCM without separation of the visibly crystalline phase(s). Peaks shown are pigeonite (P)[PDF 01-076-0543] , augite (A)[PDF 01-076-0544], enstatite (E) [PDF 01-076-0524], diopside (D)[PDF 01-071-0994] , clinoferrosite (CFS) [PDF 00-017-0548], and clinoenstatite (C) [PDF 00-019-0769]. Due to the large amount of pyroxene peaks, it is likely the main phase is from the pyroxene family of phases, with substitution causing shifts in peaks, leading to the convoluted XRD pattern.

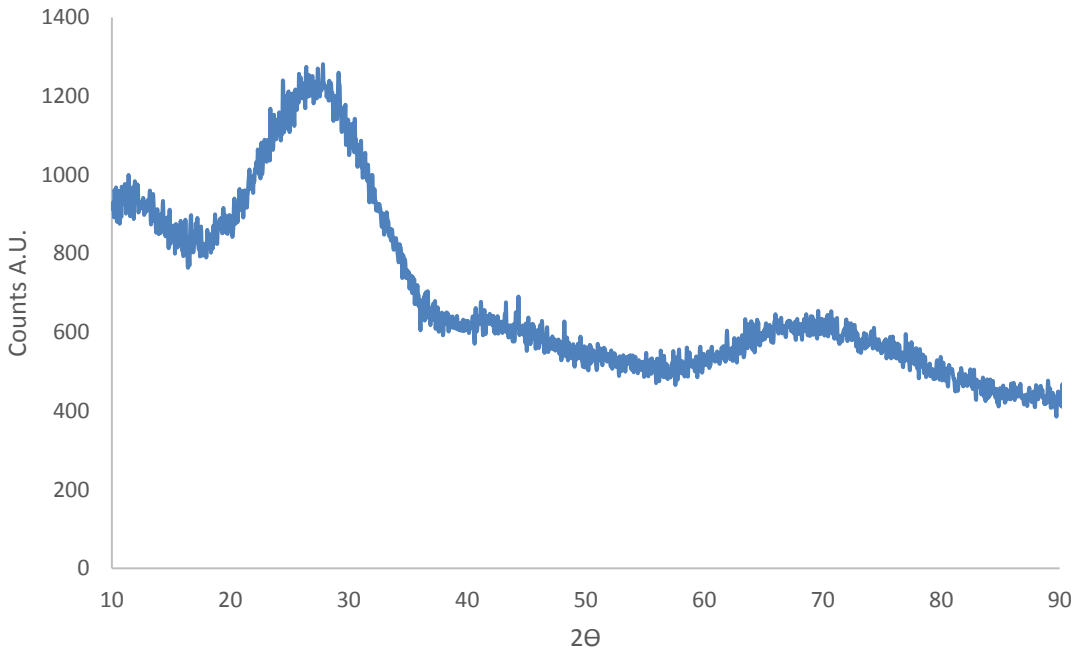

Figure 32: XRD trace of the powdered portion of sample JH-PCM which did not contain any of the visually identified crystalline phase. The XRD trace revealed a characteristic amorphous hump and absence of crystal peaks

BSE imaging suggests these spots were crystalline by morphology, due to the dendritic shape, as can be seen in Figure 33a). Not so readily seen is the presence of a second phase observed as the light phase surrounding, and intermixed, with the dendritic crystalline phase Figure 33b). A few areas were large enough (>2 μm^2) for EDX to be collected without a significant error associated with particles this small. The EDX maps displayed showed a relatively constant composition compared with the glass portion, with the exception of magnesium and calcium, shown in the EDX maps in Figure 33c) and d). The results obtained for the Ca-depleted phase (herein referred to as phase 1) are displayed in Table 20 but are not truly representative of the elements present; it is probable that small amounts of EDX signals from the surrounding glass and dendritic phase (herein referred to as phase 2) contaminated the results.

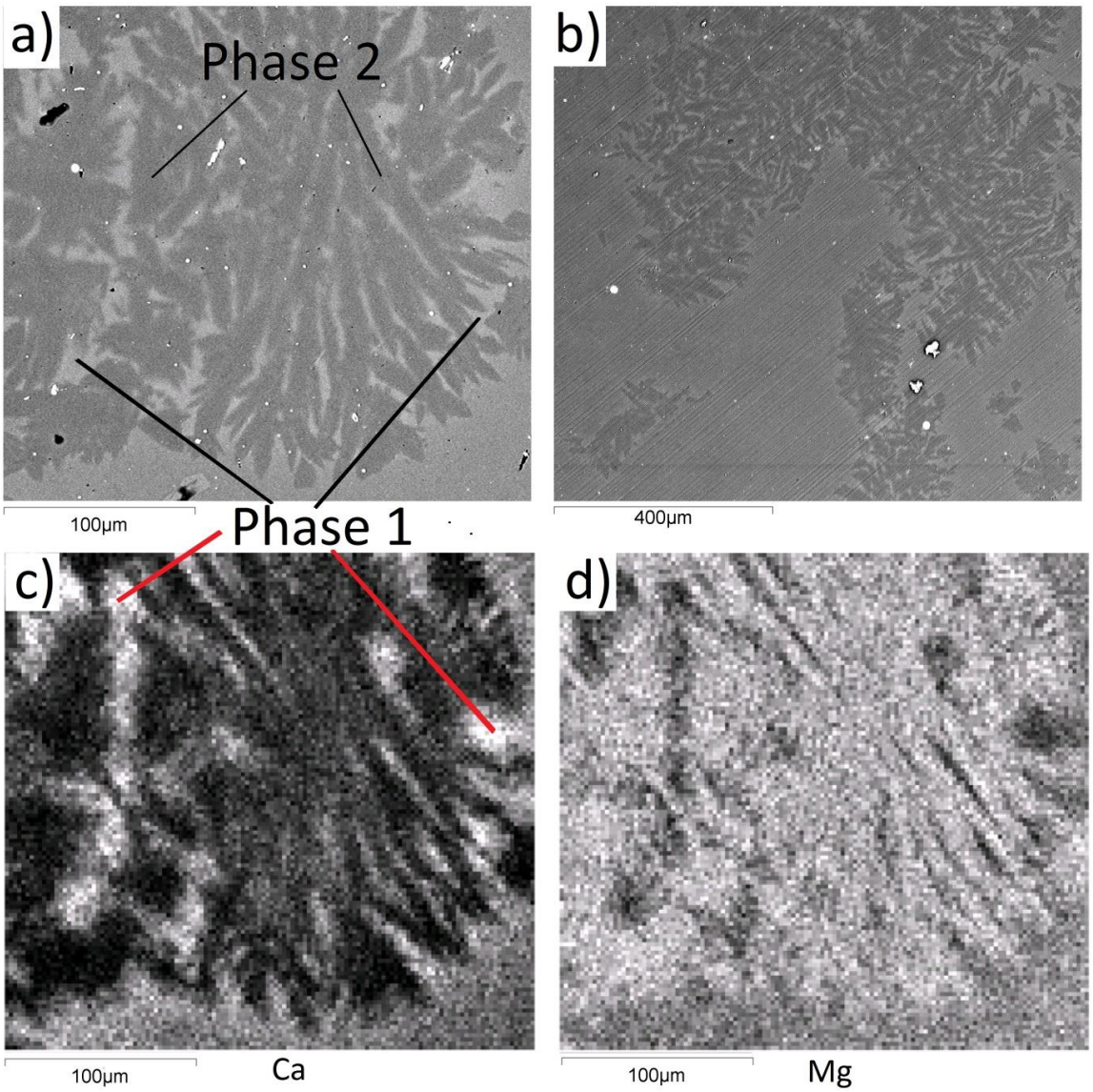

Figure 33: BSE images and EDX maps of the crystalline portion of sample JH-PCM. a) shows a smaller (100-200µm) more symmetrical version of this crystal, whilst b) illustrates the shape of the more larger (400µm) crystals.(c) Ca and (d) Mg EDX maps of image a) are shown to highlight the difference in these two phases i.e. Ca enriched and Mg depleted for phase 1 and vice versa for phase 2. Bright spots are artefacts of the gold coating.

Table 20: Composition of the phases present in the sample in oxide wt%. Results were obtained from the average of points taken where the lines indicate in figure 28. Error is displayed as either standard deviation from 10 different point scans, or the inherent error of EDX analysis (0.1 wt%), whichever was greater.

Phase 1	**Na_2O**	**MgO**	**Al_2O_3**	**SiO_2**	**K_2O**	**CaO**	**TiO_2**	**Fe_2O_3**
Compound %	2.2	3.5	11.4	62.0	1.3	17.5	1.2	0.4
Error ±	0.1	1.2	0.3	0.6	0.2	1.4	0.1	0.1
Phase 2								
Compound %	2.5	11.3	12.3	67.3	2.4	2.4	1.1	ND
Error ±	0.1	0.9	0.3	0.4	0.1	0.8	0.2	-

BSE-SEM showed the glass to be homogeneous (Figure 34). However, EDX evaluation of the glass yielded unusual findings; multiple point scans were performed in various locations revealing a large variation (±3 wt%, for Mg this is a 30% variation between the lowest and highest detected value, compared to the average) in the composition of certain elements (Table 21). High contrast backscattered imaging (Figure 35) reveals that the bulk glass is in fact made up of two amorphous phases.

Another phase was also seen in the form of spheroids, with bright contrast in BEI consistent with a metal oxide or metal. EDX of these spheroids determined they were an iron-chrome alloy or oxide (97.1 wt% Fe and 1.5 wt% Cr),carbon results were removed due to the inability of EDX to correctly identify carbon due to contamination (present for all SEM-EDX results).

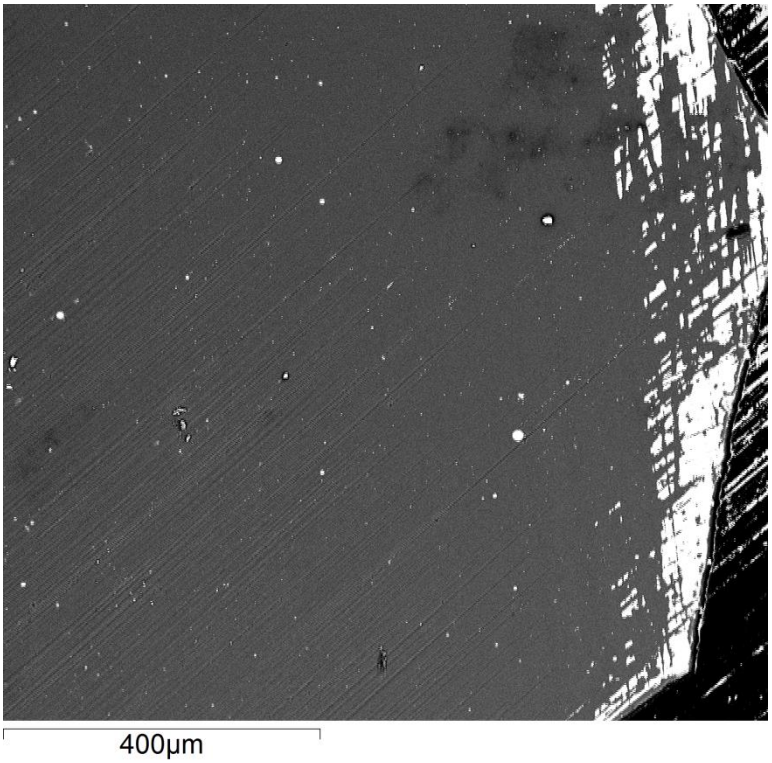

Figure 34: BEI taken of JH-PCM wasteform which had no observable crystalline phase. The white area on the right hand side is an artefact caused by uneven gold coating near the epoxy-glass boundary.

Table 21: The average, maximum, and minimum values found from analysing 20 random points in the glass taken from the image in Figure 34. A large difference can be seen in the values for certain elements, Na, Mg for example. Results given in oxide wt%.

	Na_2O	MgO	Al_2O_3	SiO_2	K_2O	CaO	TiO_2
Compound%	1.9	9.7	12.3	66.6	1.8	6.7	1.1
Max Value	4.4	13.4	13.2	67.5	2.1	10.8	1.3
Min Value	0.8	7.4	11.8	65.8	1.6	4.7	0.9

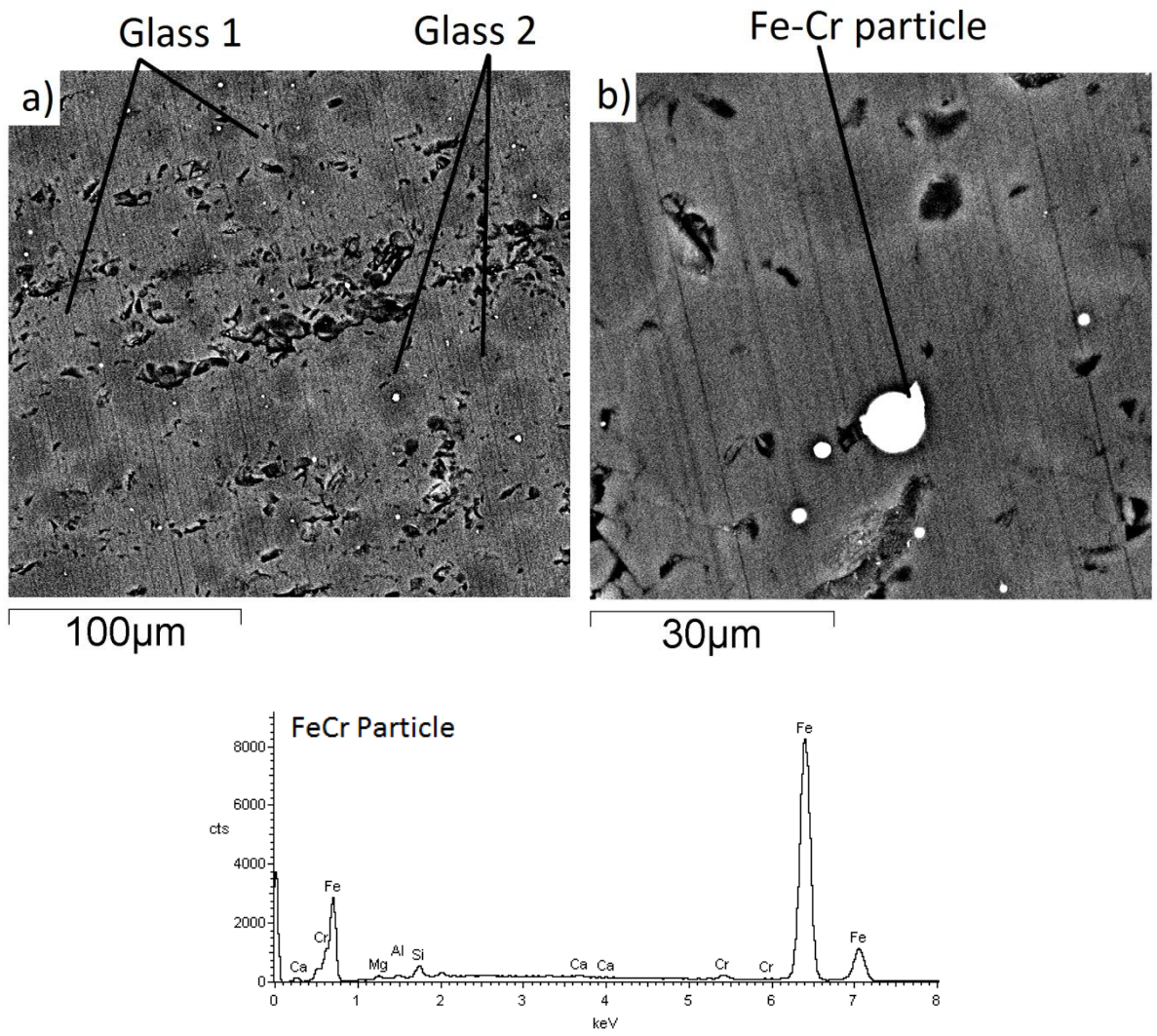

Figure 35: a) High contrast BEI mode showing areas of differing colour, indicative of an area of differing composition.b) high magnification (30 µm scale bar), high contrast BEI centred on an Fe-Cr particle, evident from the EDX graph of X-ray count (A.U) versus energy (keV) (c) taken from the labelled Fe-Cr particle in (b).

EDX from the two separate glass phases (Table 22) confirms the composition differences are small, with the major elements (aluminium and silicon) present in similar amounts. However changes in the remaining phases, while small by total wt% were large in comparison to each other, for instance sodium decreased from 3.9 wt% to 0.9 wt% (Table 22). It was also noticed that the second glassy phase was usually (but not always) associated with the small undissolved Fe metal spheres, little to no iron was detected in either glass and the amounts detected were within the error margin of EDX suggesting it is most likely not present, or if it is, in small amounts (<0.1 wt%).This suggests that the conditions during processing were not sufficient to fully melt the iron-containing wastes to allow incorporation into the glassy structure, or that the glass was saturated in this element.

Another possibility relates to the reducing conditions during processing. It is accepted that conditions during vitrification should be reducing to minimise melt foaming [186] and to prevent de-vitrification during the thermal treatment. However, should the conditions in the melter be too reducing, this will force metallic oxides to precipitate out of the melt [187,188]. Rather than having insufficient conditions to fully melt the waste, it appears that the conditions were in fact too reducing, causing the already melted iron components to precipitate out of the melt as small

metallic sphere of iron. Further, this theory is backed by the apparent dual glasses that formed in the material, the ionic strength of the different Fe cations results in changes in the viscosity of the melt and promotes glass immiscibility [189]. This conclusion could be established using Mossbauer spectroscopy or ion chromatography to establish the ratio of Fe^{2+}/Fe^{3+} which is generally considered to be a good indication of the conditions during the thermal processing; a ratio >0.6 is accepted as being to reducing [190]. Should this be the case, this would allow for the conditions of the melt to be altered to prevent the formation of both the dual glass and the Fe spheres, possibly enhancing the durability of the GCM dependant on the properties of the glass that forms.

Table 22: EDX composition of the two glasses found in sample JH-PCM displayed in oxide wt%, whilst differences were relatively small the result was two separate glasses. Spectra for each glass are shown below. Error is displayed as either standard deviation from 10 different point scans, or the inherent error of EDX analysis (0.1 wt%), whichever was greater.

Glass 1	**Na_2O**	**MgO**	**Al_2O_3**	**SiO_2**	**K_2O**	**CaO**	**TiO_2**
Average	0.9	12.3	12.3	65.5	2.0	5.9	1.1
Error ±	0.6	0.8	0.20	0.5	0.20	1.2	0.2
Glass 2							
Average	3.9	7.0	12.2	64.5	1.8	10.1	1.1
Error ±	1.0	0.7	0.2	0.3	0.10	0.8	0.2

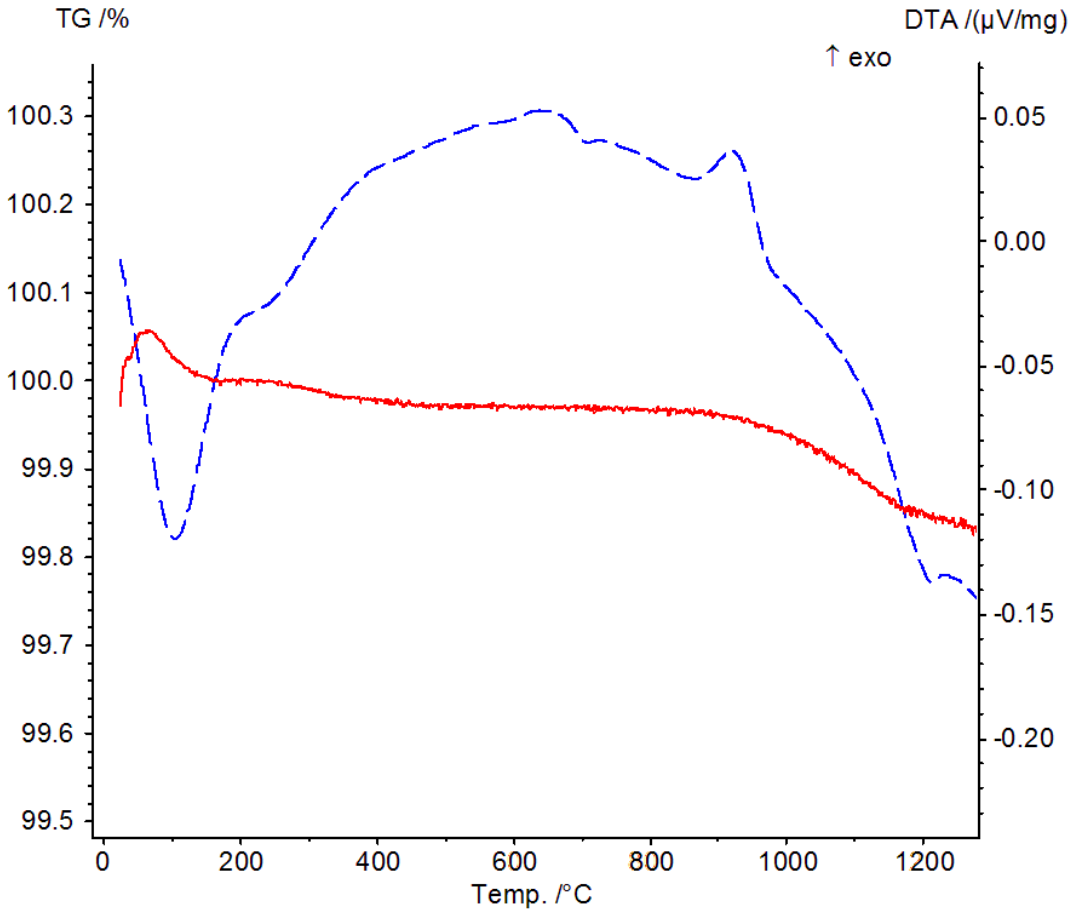

Figure 36: DTA curve (dotted blue line) and TGA curve (red line) of powdered sample JH-PCM in argon atmosphere at a heating rate of 20 °C per min (exothermic reactions are up). The irregular shape made distinguishing transition temperatures and crystallisation/melting temperatures difficult.

DTA data (Figure 36 blue line) reveals the wasteform to be thermally stable to a temperature of at least 900 °C. Whilst the curve itself might suggest exothermic reactions at 660 °C and 910 °C, the overall change in the values would suggest that these are statistical anomalies, rather than an exothermic reaction. Additionally, no change in the specimen following the DTA/TGA was observed (should any reaction occur, a change in colour and/or shape could have been observed).

TGA data (Figure 36 red line) revealed a small weight loss before 200 °C, attributable to moisture loss, and a second weight loss towards the end of the experiment (~1000 °C). The second weight loss could be attributable to the dehydroxylation of linked water in one or several phases contained within the GCM. This mass loss has also been observed in materials that utilise cerium as a surrogate, and was determined to be due to the reduction of cerium from 4+ to 3+, it was found to occur at approximately 800-1000 °C (becoming most noticeable at 1000 °C) and continue until 1300 °C in a helium atmosphere. Further, the reduction became less noticeable in an oxygenated atmosphere, as would be expected [169].

Whilst difficult to discern, a glass transition appears to be present at approximately 685 °C, evident from the step change in the TG% at that temperature, consistent with a glass transition. A crystallisation temperature is also present at 960 °C.

4.1.2 Joule Heated-High Metal Surrogate

Visual observation of the JH-HMS sample showed it to be a predominantly black (assumed) glassy phase with a second brown area which was present on about 20% of the total surface area (±10%), these areas were small, circular (>1 mm diameter) patches which often formed as clusters. The crystalline % was estimated using a series of low magnification SEM images (SEI and BSE images), and the result averaged. Similar to JH-PCM, the crystalline and presumed glassy, black phase were physically separated using a combination of a copper blade and grinding, XRD was performed separately on each portion. XRD on the crystalline portion (Figure 37) suggest the presence of a cerium oxide silicate ($Ce_{4.67}(SiO_4)_3O$), alumina III (rhombohedral), and fayalite (Fe_2SiO_4). Repeated XRD also showed that a complex calcium-magnesium-iron silicate ($Ca_{0.9}Mg_{0.71}Fe_{0.25}Si_2O_6$) phase is present. This is in agreement with the EDX results Table 24. XRD confirmed the black portion to be glassy, showing a typical amorphous hump, as seen in Figure 38, the composition of which can be seen in Table 23.

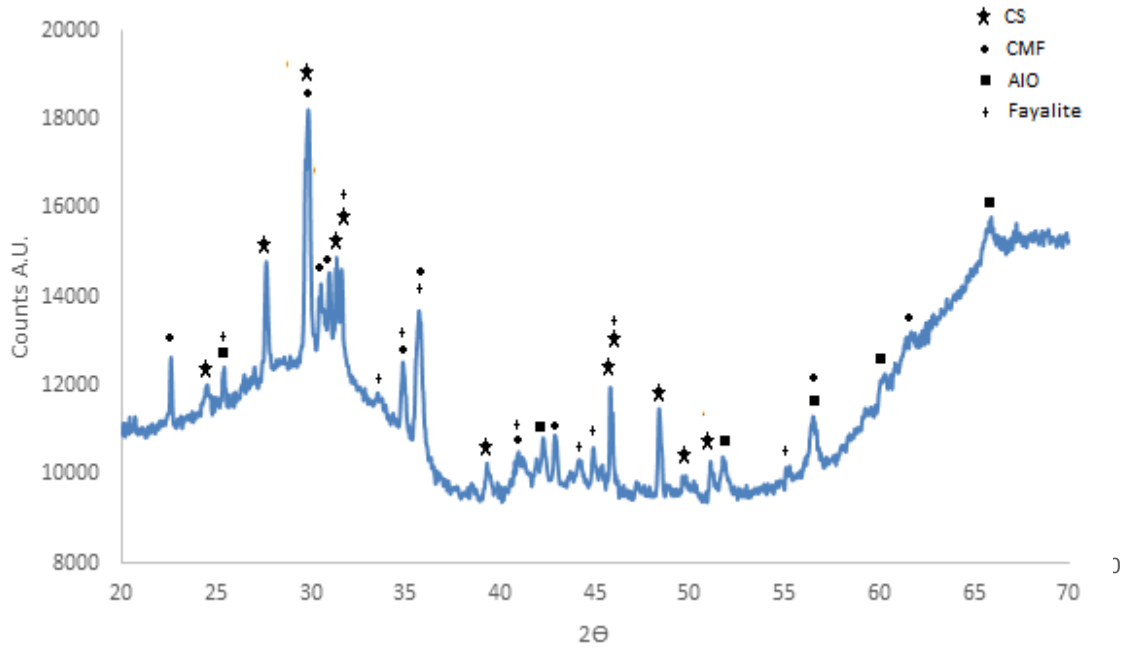

Figure 37: XRD trace of the powdered, and unaltered JH-HMS sample, showing the presence of cerium oxide silicate (CS)[PDF 00-022-0169], calcium magnesium iron silicate (CMF)[PDF 01-083-2015], aluminium oxide (shortened to AlO, phase is Al_2O_3) [PDF 01-088-0826], and fayalite (Fe_2SiO_4) [PDF 00-020-1139].CS and CMF accounted for the majority of the peaks present. Both fayalite and Al_2O_3 showed small peak intensities suggesting they were not present in large amounts compared to the other two.

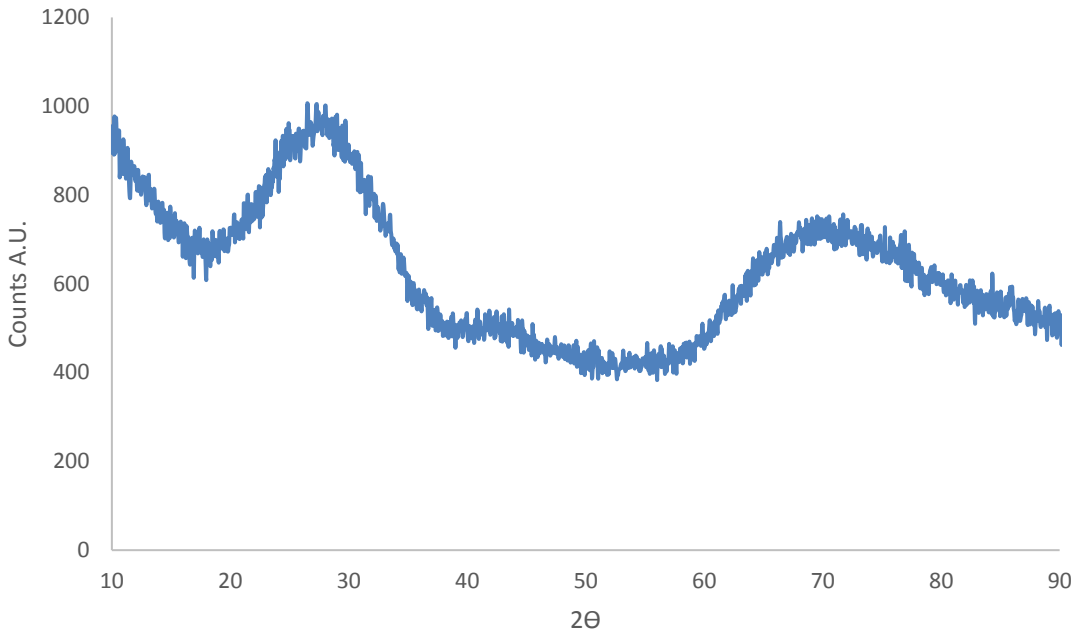

Figure 38: XRD of the powdered black phase (presumed to be glassy) separated from brown phase (shown to be crystalline) showing an amorphous hump and absence of crystal peaks confirming it to be glassy for the JH-HMS sample.

Table 23: Glass compositional analysis of sample JH-HMS, displayed in oxide wt%. Error is displayed as either standard deviation from 10 different point scans, or the inherent error of EDX analysis (0.1 wt%), whichever was greater.

Glass	MgO	Al_2O_3	SiO_2	CaO	Fe_2O_3	La_2O_3	Ce_2O_3
Compound %	2.5	7.0	49.7	7.5	12.7	5.7	15.0
Error ±	0.1	0.3	1.6	0.2	0.6	1.0	1.2

SEM-BSE imaging of the sample (Figure 39) revealed the brown phase was in fact a complex mixture of several, possibly including crystalline, phases as can be seen from the EDX maps in Figure 40. Figure 39, reveals the two brightest phases, along with the dendritic structure surrounding these phases. EDX analysis shown in Table 24 indicated the bright phases in both pictures in Figure 39to be of the same composition thus confirming that they are the same phase. The difference in shape is likely due to a difference in viewing angle; one is simply a cross section of the other. This relation was seen throughout the sample, i.e. where the bright phase was observed, so too were the dendrites. It was unclear if these were the only phases present, as a possible third phase can be observed in Figure 39b), as a darker phase in between the dendrites. To assess whether more than the observed phases were present EDX-mapping was employed (Figure 40).

Four phases were thus identified. The phase which appears the brightest under BSE imaging was composed of mainly Ce and La, and thus was termed the Ce-La phase, and was nearly always at the centre of the groups of crystalline phases. The biggest phase (termed phase 1), accounting for

roughly 75% (±10%, varies depending on overal size of crystal) of the total crystalline portion was slightly depleted in La and Ce compared to the glass. Phase 2 immediately surrounded the Ce-La phase, and was characterised by a greater depletion of Ce and La than in phase 1. Phase 3 showed the greatest depletion of Ce and La, and was found inbetween the Ce-La dentrites, rather than phase 2 which encompased it like a shell. The EDX data and location of these various phases are illustrated in Table 24 and Figure 41.

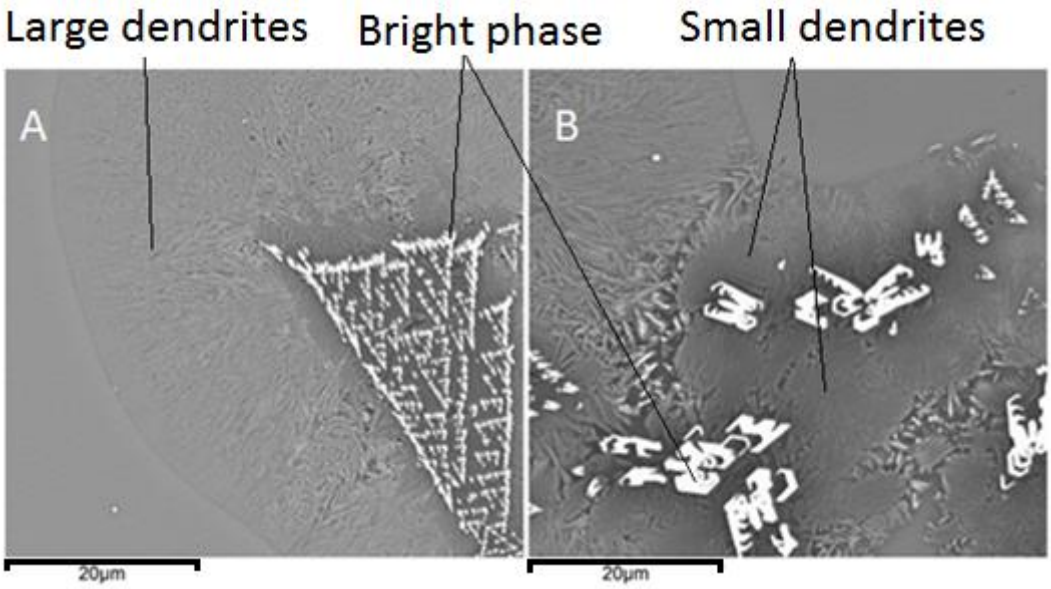

Figure 39: BSE images of the crystalline portion of the JH-HMS sample. a) At least three individual phases can be seen, the glass (surrounding the large dendrites), the bright phase in the centre of the picture in a triangular arrangement, and the large grey structure surrounding it. b) A darker, smaller (1-5 µm diameter) dendritic phase can be seen.

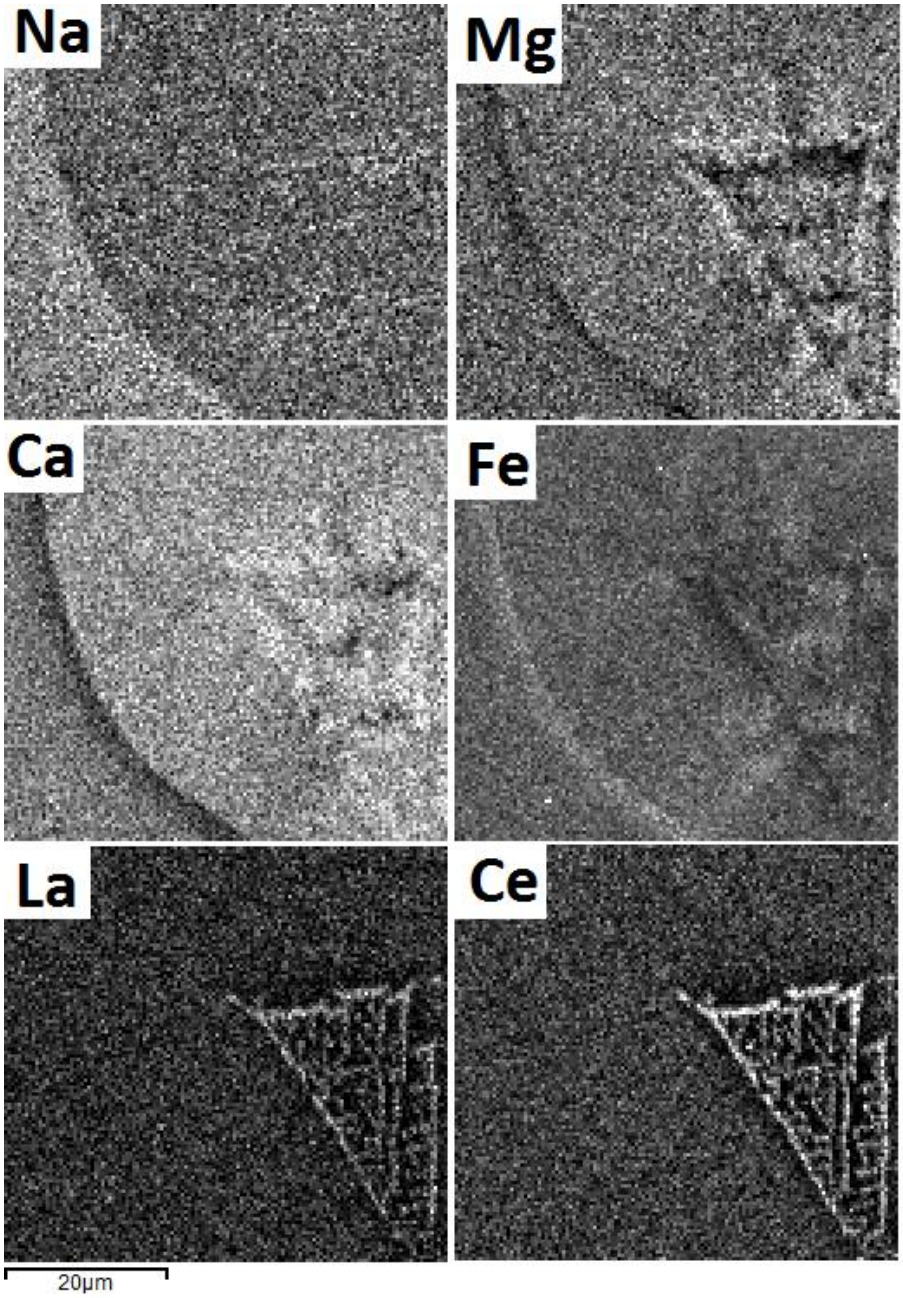

*Figure 40: EDX mapping of Na, Mg, Ca, Fe, La, and Ce of the area shown in **Figure** 39a)for sample JH-HMS. It is clearer that in area encompassing the Ce-La enriched phases, that both Ca and Mg saw an increase relative to the rest of the area analysed. Slightly more difficult to make out, is the decrease in Ce and La in the same area.*

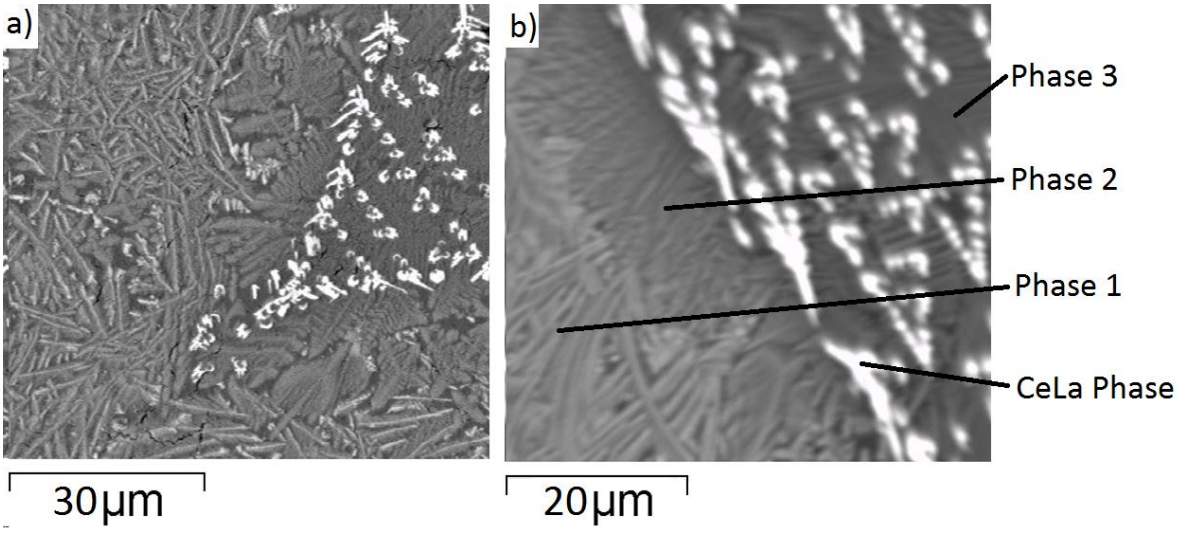

Figure 41: SEM-BSE of the crystalline portion of sample JH-HMS. a) shows the complicated morphology surrounding the Ce-La phase, whilst b) reveals the different phases identified and where subsequent EDX points were taken from.

Table 24: Composition in oxide wt% of the 4 phases found in sample JH-HMS. Typical EDX spectra for each phase are shown below. Error is displayed as either standard deviation from 10 different point scans, or the inherent error of EDX analysis (0.1 wt%), whichever was greater.

CeLa Phase	**MgO**	**Al_2O_3**	**SiO_2**	**CaO**	**Fe_2O_3**	**La_2O_3**	**Ce_2O_3**
Compound %	0.2	1.1	16.5	6.5	0.8	25.1	49.7
Error ±	0.2	0.8	2.3	0.3	0.4	1.2	2.5
Phase 1							
Compound %	3.3	7.2	48.9	9.6	11.6	7.9	11.6
Error ±	0.2	0.5	0.7	0.3	0.7	0.4	0.7
Phase 2							
Compound %	5.6	7.9	54.6	13.4	7.8	4.6	6.1
Error ±	0.1	0.4	1.1	0.2	0.6	0.4	0.6
Phase 3							
Compound %	5.7	8.8	59.2	12.4	11.2	1.6	1.2
Error ±	0.2	0.2	0.8	0.4	0.4	0.3	0.9

4.1.3 Joule Heated-SIXEP

Macroscopically, JH-SIXEP material was highly porous with the average pore size being 0.5 mm ±0.1 mm in diameter but these were not always spherical pores, rather they were generally elliptical. The pore density was difficult to assess as it varied over 5 separate analysed surfaces, but on average accounted for approximately 30% (±15%) of any surface after grinding and polishing. This is extremely undesirable in a wasteform as it increases the surface area of the sample leading to faster corrosion than a similarly sized non-porous waste and unnecessarily increases the volume of the wasteform [191].

XRD analysis revealed the sample was heterogeneous with two representative traces shown Figure 42 and Figure 43. Clinoenstatite ($MgSiO_3$), enstatite ($Mg_{0.944}Ca_{0.056}SiO_3$), periclase (MgO, cubic), magnesioferrite ($MgFe_{2\ 3+}O_4$), clinoferrosilite ($FeSiO_3$), and various other iron oxide phases such as magnetite (Fe_3O_4), wustite ($Fe_{0.902}O$), and hematite (Fe_2O_3) were likely present. As EDX found no phase comprising of just magnesium, periclase can be ruled out.

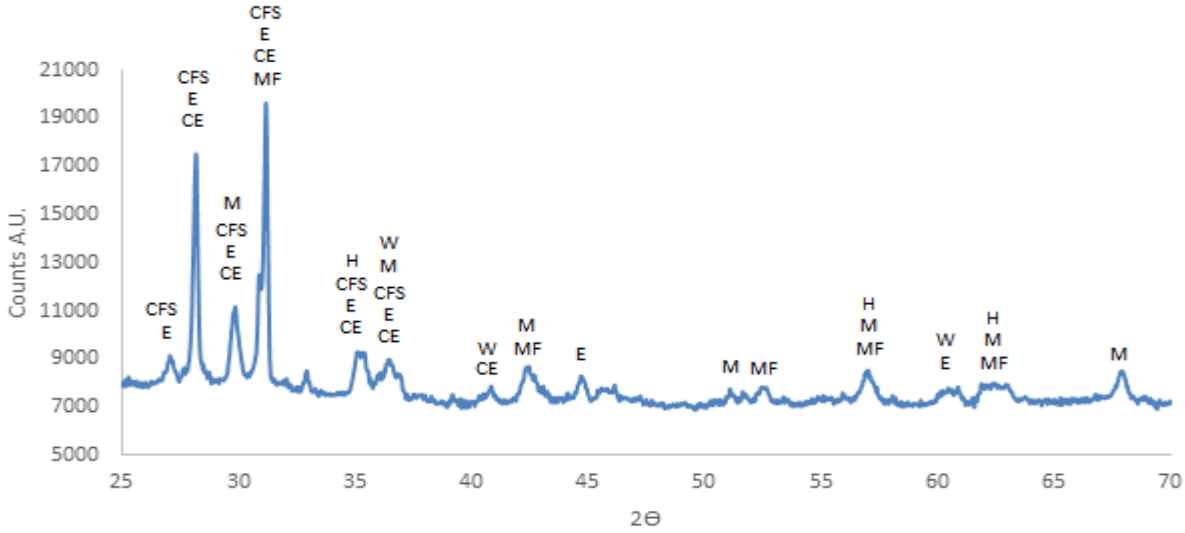

Figure 42: XRD of the powdered JH-SIXEP sample showing the possible presence of ClinoFerroSilite (CFS) [PDF 00-017-0548], Enstatite (E)[PDF 01-076-0525], ClinoEnstatite (CE) [PDF 00-013-0415], MagnesioFerrite (MF)[PDF 00-001-1120], Hematite (H)[PDF 01-073-0603], Wustite (W)[PDF 01-079-1971], and Magnetite (M)[PDF 01-072-2303]. It is most likely that hematite wustite or magnetite are present (but not all) as minor phases, based on further results only two of the remaining named phases are possible as a major phase. The large number of suggested peaks are most likely due to heavy element substitution causing peak shifts.

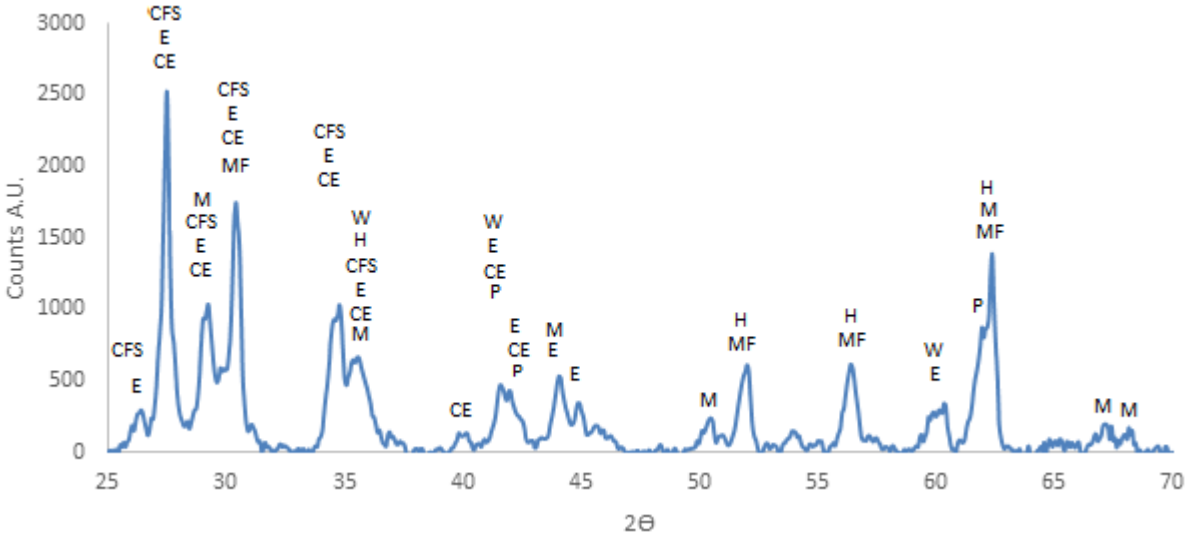

Figure 43: XRD of the powdered JH-SIXEP sample showing the possible presence of ClinoFerroSilite (CFS) [PDF 00-017-0548], Enstatite (E) [PDF 01-076-0524], ClinoEnstatite (CE) [PDF 00-013-0415], MagnesioFerrite (MF) [PDF 00-001-1120], Hematite (H), Wustite (W), and Magnetite (M). The same phases are present but in differing amounts leading to the difference in peak heights from Figure 42*.Further to figure 42, it is clear there is a minor iron phase (Wusitite/hematite/magnetite) followed by up two of the remaining named phases.*

SEI and BSE imaging (Figure 44) revealed a highly crystalline material. Four points were chosen to be analysed further determined by shape and size; the crystal approximately 100 µm long, 40 µm wide (on average, +/- 10 µm), in Figure 44awas termed “thick crystal 1”. A 50 µm by 50 µm (on average, +/- 10 µm) angular phase was termed “thick crystal 2”, however it was assumed at this point that these were in fact the same crystals but orientated differently. The third is the long small thin crystals termed “thin crystal”, seen in Figure 44, which varied in length from over 100 µm to smaller than 5 µm, the width was 3 µm +/- 1 µm. The last phase was the glass matrix. The EDX results obtained are shown in Table 25, it was confirmed that the two large phases, the thick crystal 1 and thick crystal 2 were of a similar composition. Based on the XRD and EDX data the crystalline phases are not the iron phases due to the low concentration of iron, and high concentration of other elements ruling out hematite, wustite, magnesioferrite, or magnetite, leaving only the pyroxene phases (enstatite and ferrosilite) and their polymorphs. Based on these results it can be concluded that both thick crystals and the thin crystal are a pyroxene phase (CFS,E, and CE).

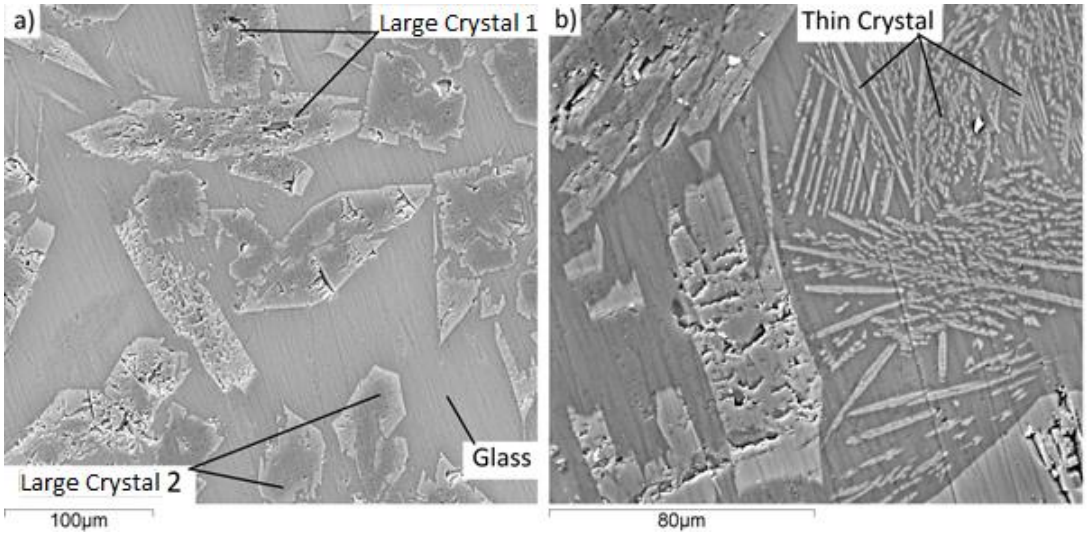

Figure 44: BEI of the two types of crystal observed in JH-SIXEP sample, a) containing broader crystals than the long and thinr crystalss seen in b).

Table 25: EDX results for the analysed phases. 5 points were taken for each phase analysed and averaged. Error is displayed as either standard deviation from 10 different point scans, or the inherent error of EDX analysis (0.1 wt%), whichever was greater.

Glass	**Na_2O**	**MgO**	**Al_2O_3**	**SiO_2**	**K_2O**	**CaO**	**Fe_2O_3**
Compound %	2.2	0.8	13.1	65.4	1.9	4.9	11.8
Error ±	0.2	0.2	0.5	0.1	0.2	0.4	1.3
Thick Crystal 1							
Compound %	0.2	24.8	1.6	57.8	0.2	0.6	15.0
Error ±	0.2	2.2	1.2	1.1	0.3	0.2	1.4
Thick Crystal 2							
Compound %	0.1	24.0	2.0	57.2	0.2	0.7	15.8
Error ±	0.4	2.3	1.2	1.5	0.2	0.2	1.3
Thin crystal							
Compound %	1.0	7.3	7.5	58.4	1.1	3.3	21.6
Error ±	0.2	1.0	1.0	1.1	0.1	0.2	1.3

4.2 Joule Heated Wasteform Corrosion Studies

Corrosion studies consisting of surface SEM-EDX analysis and depth profiling were used to determine corrosion progression after 2, 4, 6, 10, and 14 weeks. As samples JH-PCM and JH-HMS contained crystals embedded in a matrix homogeneously, but with differing sizes, it was assumed that the interfaces between these could be the least corrosion resistant. For this reason, analysis was centred on the changes, if any at the interfaces, between the glass and the crystalline phases present. The depth profiles were also aimed at looking how the crystals fared during corrosion testing. However, their small (~1-5 µm wide) size coupled with their relative scarcity in the wasteform made locating these phases in cross sections difficult; in some cases, a cross section through a crystal could not be found. For this reason, only depth profiles for 10 and 14 weeks are shown. This situation was made worse by the sample size (0.5 mm^3 dependant on sample density) used in the corrosion experiments, which lowered the chances of finding crystals which had intersected the cross section more difficult.

4.2.1 Joule Heated-Plutonium Contaminated Material

The analysis of this sample was split into two; the sample corrosion resistance and differences between glass 1 and glass 2, and the corrosion progression of the crystal. Whilst both had similar objectives, the main difference is that the corrosion progression of both glasses was expected to adhere to current glass corrosion models [192].

Observation of the surface after 6 weeks showed that a layer had developed over the entire surface, including the crystal. This layer was not seen before 6 weeks. This layer made direct observation of the crystal using SEM difficult as the layer appeared homogeneous in composition, shown in Figure 45. BSE was somewhat effective in determining its location, however EDX mapping allowed for better resolution providing useful information on the thickness of the layer as EDX has a larger interaction volume than that of BSE mode for the particular SEM settings in use, putting the thickness of the layer at somewhere between 1-3 µm. More accurate measurements are shown in subsequent cross sectional analysis. EDX maps showed little change in the crystal from pre-corroded samples (see Figure 33).

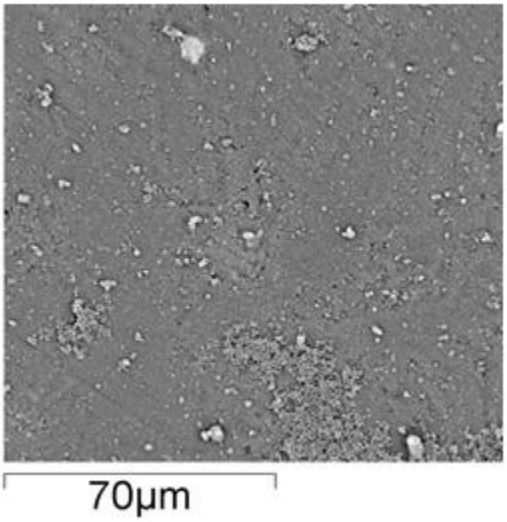

Figure 45: BSE image of a crystalline area from JH-PCM samples after 6 weeks of corrosion, the inability to distinguish the crystal is evidence that a layer has developed on top of the crystal (shown pre-corrosion in Figure 33a)..

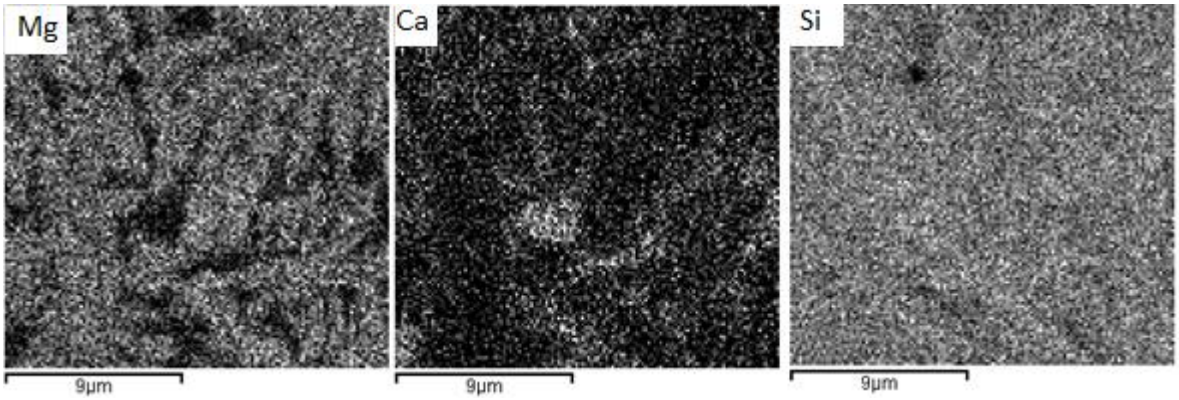

Figure 46: EDX maps of JH-PCM area shown in Figure 45 for magnesium, calcium, and silicon after 6 weeks corrosion, the deeper interaction volume of EDX allows for a clearer image of the underlying crystalline phase.

Retrieval of depth profiles for the crystal could only be obtained for 6,10, and 14 weeks due to the lack of a crystalline phase in the 2 and 4 week corrosion samples. In addition, the size of phase 1 made getting depth profiles impossible as the line scan was often interrupted by the bigger, phase 2 causing unreliable results. The depth profiles for phase 2 from these 6-14 week corrosion are shown in Figure 47-49. Depth scans revealed that if a leached zone was present it was small (<1µm) for 6 and 10 week corrosion. No corrosion layer was evident from depth profiles at these times, most layers present themselves from a spike in the silicon profile and none were seen. After 14 week corrosion time, the profile showed signs of a leached zone, approximately 2-3 µm deep, depleted in Na and Al. Mg concentrations did not decline in this zone, but remained constant until the end of the leached zone where concentrations declined along with all other elements. No spike in the silicon profile was observed, signifying that a corrosion layer was not present; however, the layer could have spalled of during sample preparation.

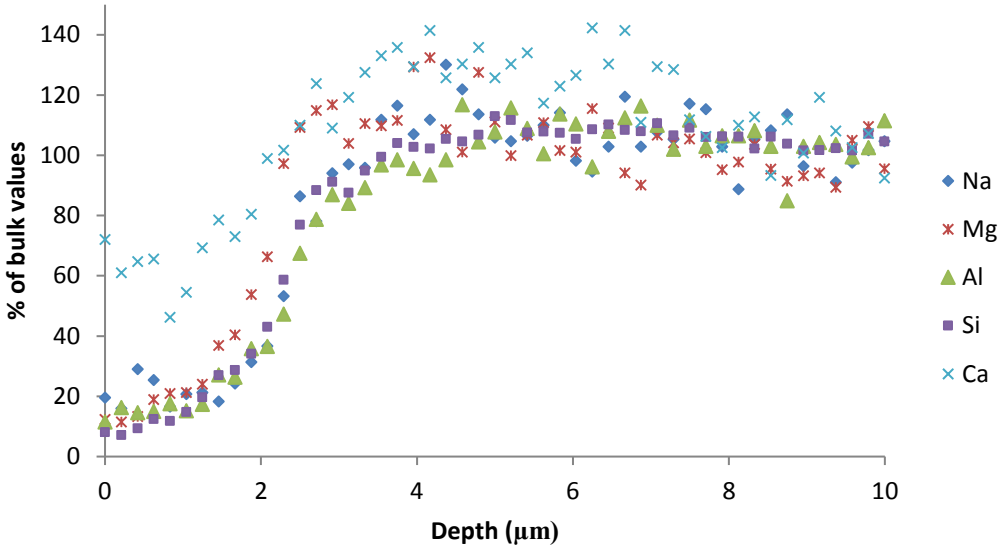

Figure 47: Graph of depth (µm) as a function of bulk values (as a %) for the crystal in JH-PCM (phase 2,Figure 33a) after 6 weeks of corrosion time.

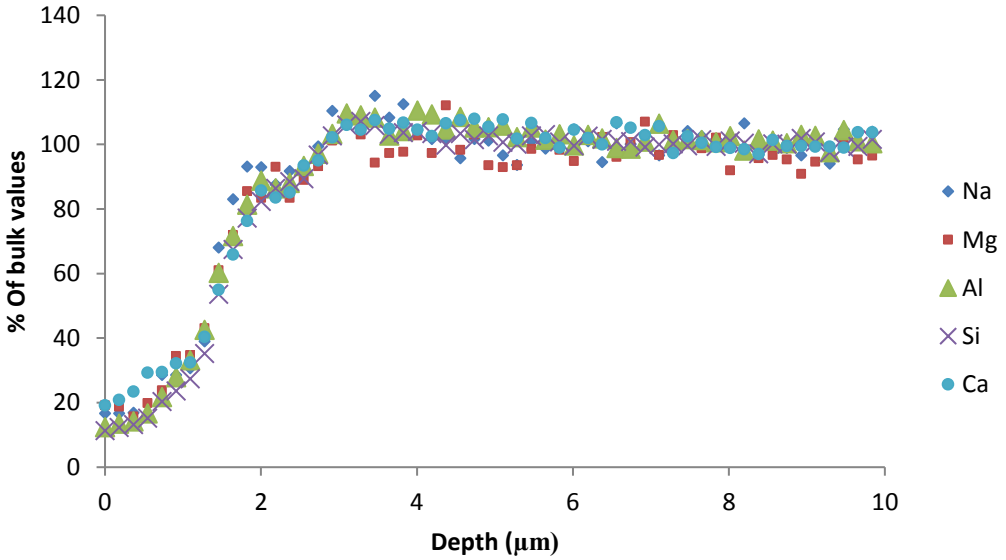

Figure 48: Graph of depth (µm) as a function of bulk values (as a %) for the crystal in JH-PCM (phase 2, Figure 33a) after 10 weeks of corrosion time.

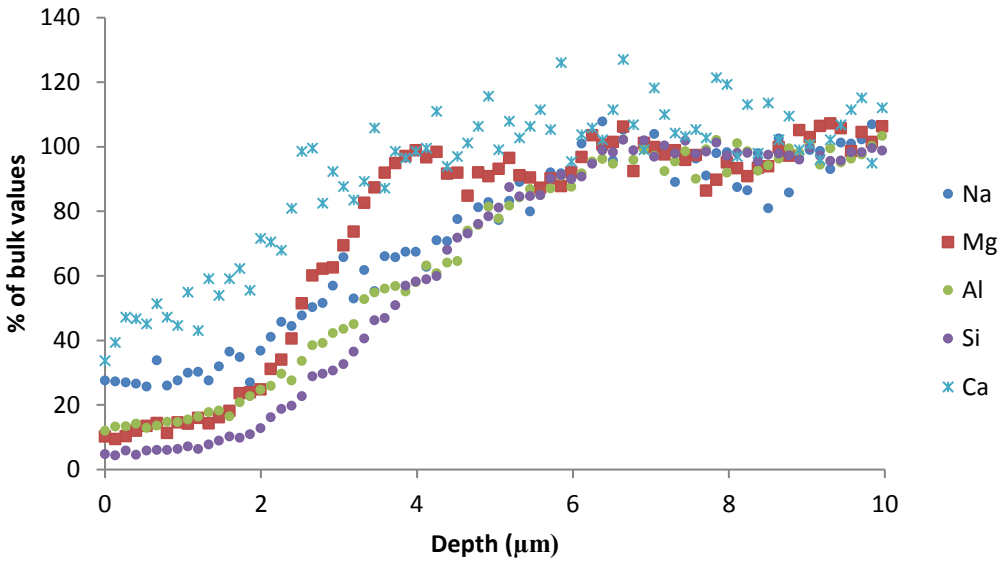

Figure 49: Graph of depth (µm) as a function of bulk values (as a %) for the crystal in JH-PCM (phase 2,Figure 33a) after 14 weeks of corrosion time.

The surface of the glass matrix was analysed using SEM-EDX which indicated that a gel layer had developed after 6 weeks, although this was not continuous showing areas where it had either flaked off during transport and investigation of the sample, or the environment had caused it to be removed, through water movement during handling. These areas were often characterised by “pits” in the centre of the less degraded glass (Figure 50), however these are not thought to occur due to pitting corrosion, and rather they are the result of the removal of the iron chrome particle discussed in section 4.1.1. The two glasses present also behaved differently during corrosion, glass 1 showed a non-continuous gel layer (Figure 50a), whilst glass 2, associated with the iron particles, displayed a continuous, gel layer (Figure 50b) centre island). In fact, only a few particles are observable on glass 2 whilst glass 1 was corroded more as the new surface was lower than that of glass 2. This was evident from the presence of the fine scratches produced during grinding still being observable (Figure 50b)Close inspection of the gel layer suggested that it could be precipitation initiated; Figure 51shows that the gel layer consisted of merged spherical particles indicative of such a layer.

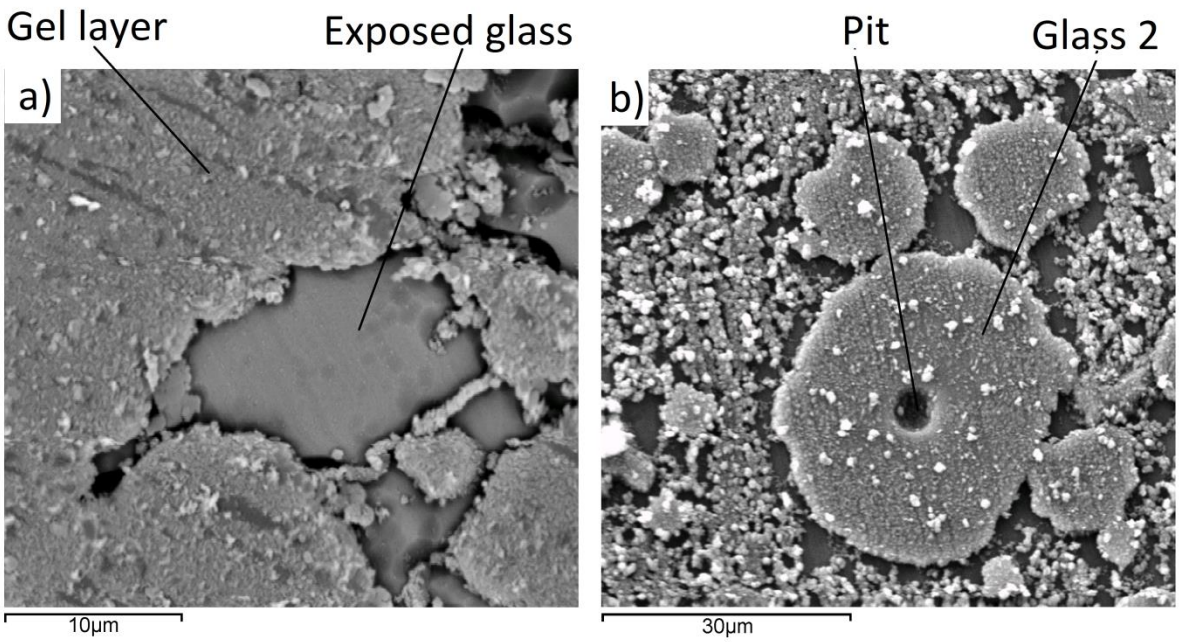

Figure 50: BSE images of the glassy portion of sample JH-PCM after 6 weeks of corrosion. a) Shows only glass 1, and displayed a non-continuous layer, b) reveals the pit in the glass thought to occur due to removal of an Fe particle, leaving a "hole". Also, visible on glass 2 in b) are scratches produced from preparation before corrosion showing little to no removal of the surface had occurred. The surrounding glass (glass 1) showed no such scratches on the exposed portions, indicating destruction and removal of the silica network.

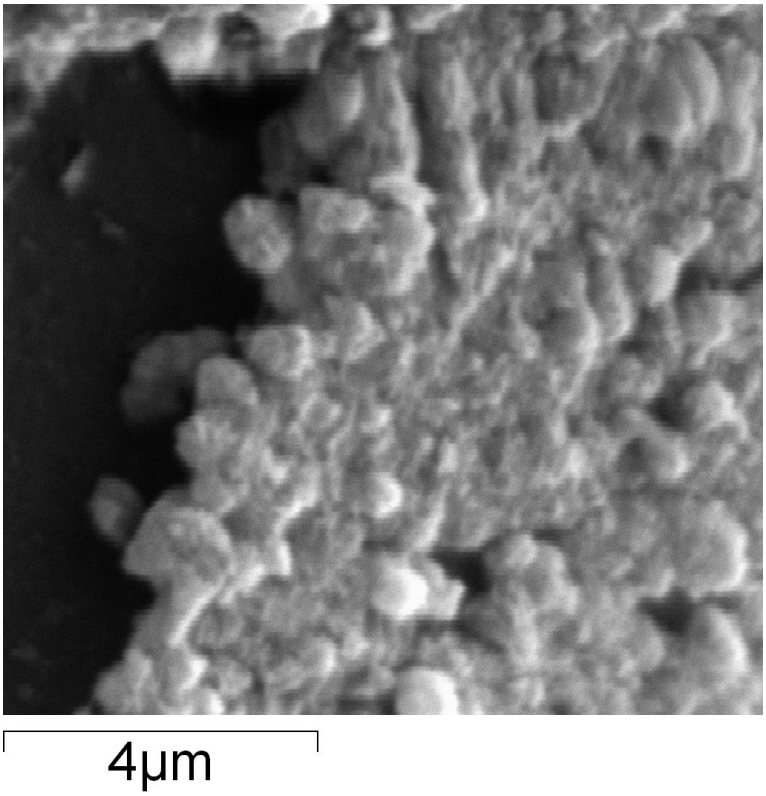

Figure 51: High magnification SEI of the corrosion layer present over glass 1 in JH-PCM clearly showing particles rather than a smooth gel layer as would be expected from current glass corrosion theory (see section 2.4 on glass corrosion).

Easily observable in the gel layer using EDX (Table 26), is the increase in magnesium in both the exposed glass and gel layer; calcium also saw a slight depletion. Unexpected was the increase in sodium (0.9 wt% pre-corrosion, 1.7 wt% post) in the exposed corroded glass surface for glass 1, as Na (and other mobile alkaline ions) is usually the first element to become depleted during leaching [64]. Therefore, the gel layer acted as a barrier to transport of this ion from the glass to the gel layer, building up at the pristine glass/gel layer interface, however the gel layer itself was depleted in Na.

Table 26: EDX of the corroded surface of glass 1 after 6 weeks of corrosion, from the gel layer, the exposed glass, and the uncorroded glass for comparison. Spectra for the gel layer and exposed glass are displayed below. Error is displayed as either standard deviation from 16 different point scans, or the inherent error of EDX analysis (0.1 wt%), whichever was greater

Glass 1 (gel layer)	**Na_2O**	**MgO**	**Al_2O_3**	**SiO_2**	**K_2O**	**CaO**	**TiO_2**
Compound %	0.5	14.5	12.9	62.8	1.2	8.0	0.3
Error ±	0.3	0.9	0.4	1.5	0.2	1.5	0.2
Glass 1 (no layer)							
Compound %	1.7	6.7	11.6	69.3	1.7	8.5	0.5
Error ±	0.4	0.3	0.5	0.7	0.1	0.8	0.3
Glass 2							
Compound %	0.5	14.4	14.0	63.6	1.0	5.3	1.1
Error ±	0.1	0.4	0.1	0.5	0.2	0.4	0.9
Glass 1 (pre-corrosion)	0.9	11.1	12.5	67.2	2.0	5.0	1.2

At 10 weeks, the corrosion layer from glass 1 had progressed to encompass both glasses in a continuous manner, showing less exposed areas than that at 6 weeks although the layer did crack. The difference between the two glasses is still visible, albeit harder to discern (Figure 52). Table 27 shows the change in composition for this layer, which had a similar composition for the layer on both glass 1 and glass 2, this could mean that the layer itself was due to spreading of the glass 1 layer onto glass 2, rather than glass 2 forming its own corrosion layer.

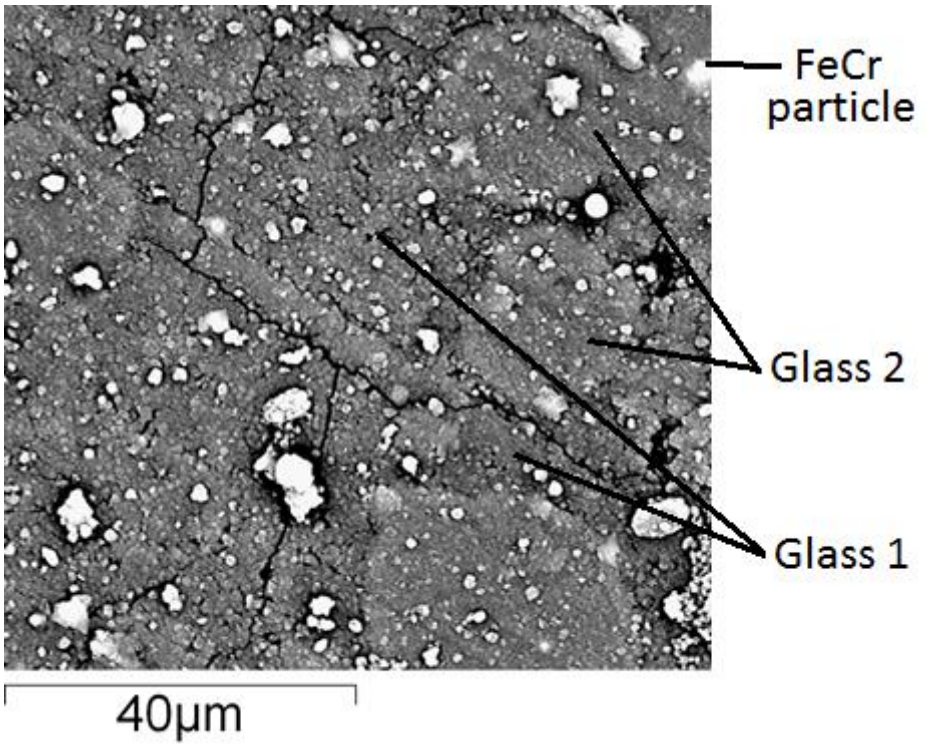

Figure 52: BSE image of surface of glassy area (both glass 1 and glass 2) in JH-PCM after 10 weeks of corrosion.

Table 27: EDX from Figure 52 showing the composition of the continuous gel layer on glass 1, and glass 2 in oxide wt% after 10 weeks. Error is displayed as either standard deviation from 10 different point scans, or the inherent error of EDX analysis (0.1 wt%), whichever was greater. The continuous gel layer that formed on glass 1 had similar amounts of magnesium compared to the non-continuous gel layer that formed after 6 weeks of corrosion time.

Glass 2	**Na_2O**	**MgO**	**Al_2O_3**	**SiO_2**	**K_2O**	**CaO**	**TiO_2**
Compound %	0.2	16.3	13.7	59.6	1.3	8.8	0.2
Error ±	0.1	2.4	1.3	1.7	0.4	2.2	0.1
Glass 1 (gel layer)							
Compound %	0.3	15.7	19.9	55.5	0.7	7.0	0.8
Error ±	0.3	2.4	1.8	2.4	0.1	0.8	0.7

Depth profiling was again performed to analyse change in composition of the glass/gel layer as a function of time, and BSE imaging was used to better assess the depth and nature of the corrosion layer present at various corrosion times (Figure 53). The 6 week scans show the variability in gel layer thickness (Figure 53a) and b)), whilst the 10 week scan (Figure 53c)) shows the areas where glass was not corroded, in contrast with the glassy area that formed a gel layer. Figure 53d) and e) show areas that formed gel layers with adjacent gel free areas after 14 weeks of corrosion. As the depth profiles were the same for all times investigated; only the 14 week samples profile are shown for each glass where a gel layer was present.

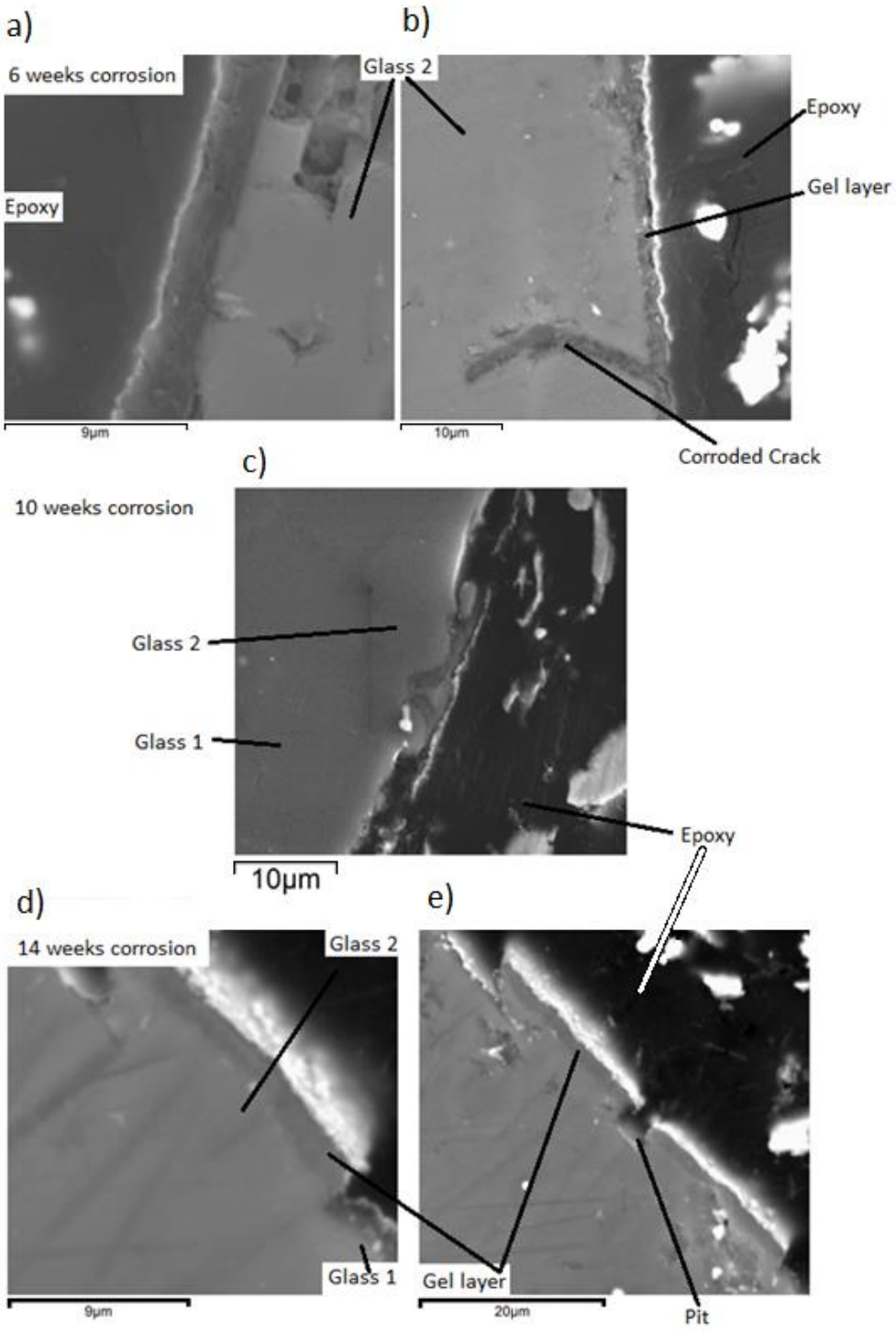

Figure 53: BSE cross section of JH-PCM at 6 weeks (a and b), 10 weeks (c), and 14 weeks (d and e). a) A gel layer is visible, b) The gel layer has ingressed into the sample, most likely via a crack. c) The gel layer is present on glass 2 only, glass 1 has corroded more than glass 2, evident by the difference in "height" of 2-3µm, this can be seen in d) and e). e) Corrosion has resulted in pits, most likely due to removal of the FeCr particles, no gel layer formed in these pits.

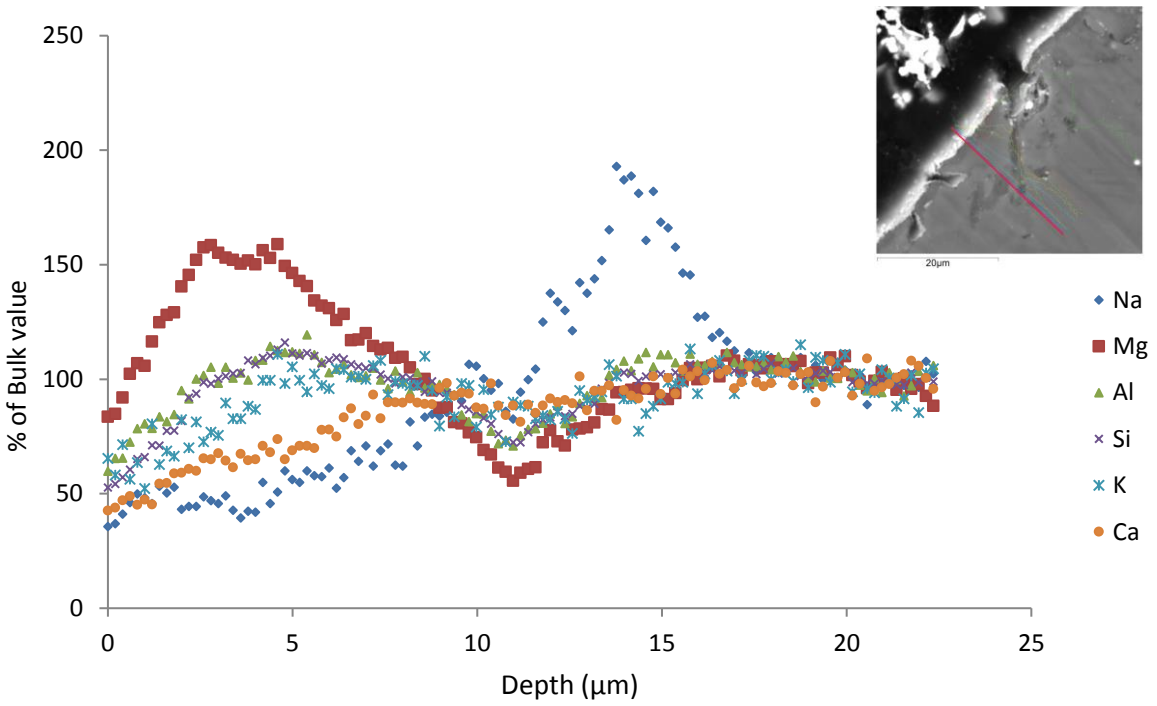

Figure 54: % of bulk values as a function of depth for "glass 1" in JH-PCM after 14 weeks of corrosion.Also shown is the BSE image where the linescan was taken.

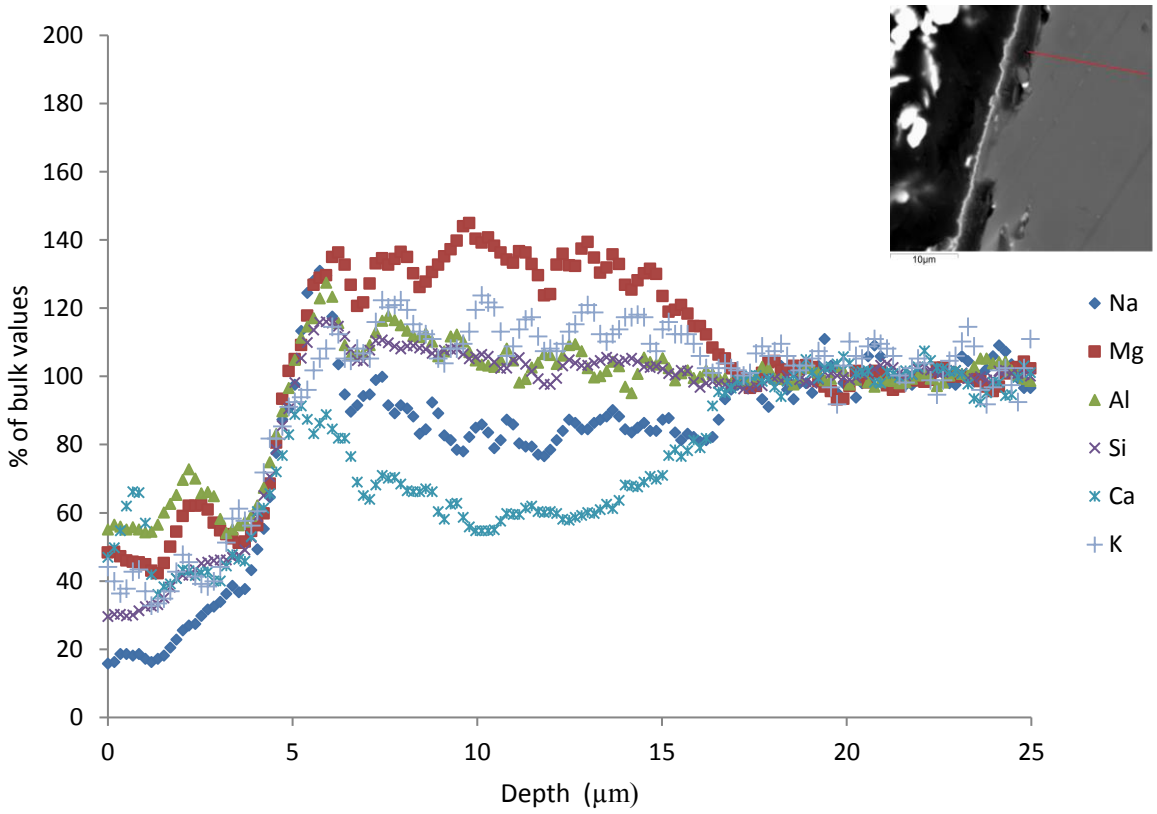

Figure 55: % of bulk values as a function of depth for "glass 2" in JH-PCM after 14 weeks of corrosion. Also shown is the BSE image where the linescan was taken.

Elemental depth profiles for glass 1 and glass 2 remained unchanged at all corrosion times (2-14 weeks) thus Figure 54and Figure 55are representative of elemental depth profiles at all corrosion times as no secondary corrosion mechanisms were observed, such as reactions with the gel layer with other species/ions [193]. Each glass developed its own separate corrosion profile; glass 1 showed an increase in the amount of magnesium from a depth of 10 µm but started to decrease from a depth of 3 µm until reaching the surface. All other elements displayed a steady decrease in concentration from a depth of 10 µm to the surface with Ca and Mg showing the highest rate of decrease. Glass 2 in contrast displayed a "zone" where Mg showed a rapid increase at a depth of ~17 µm, plateauing at this increased concentration until a depth of 3µm, after which it decreased steadily until the original glass surface was reached. Ca and K showed the opposite of this, although they displayed the same profile (plateau from 17-3 µm) the concentration was lower than bulk concentrations. In Figure 55, a spike in Na is observed at a depth of 11-17 µm, however this is not due to corrosion occurring near the surface, but indicated the EDX line scan intersected a corroded crack protruding in to the glass.

Cross sectional images also revealed a peculiar mode of corrosion for glass 2, where it was attacked from the side, at the interface between glass 2 and glass 1 (Figure 56). It is unknown why this occurred as glass 2 was seen to form a continuous, protective gel layer; why it did not form on the exposed sides is unclear. Whilst this was not observed for all instances at the glass 1-glass 2 interface, it was not an isolated incident. It was thought that this might be due to the morphology of glass 2; as this glass was mainly present as spherical particles the shape was merely the corrosion of the bottom part of a particle. However, this was not the case.

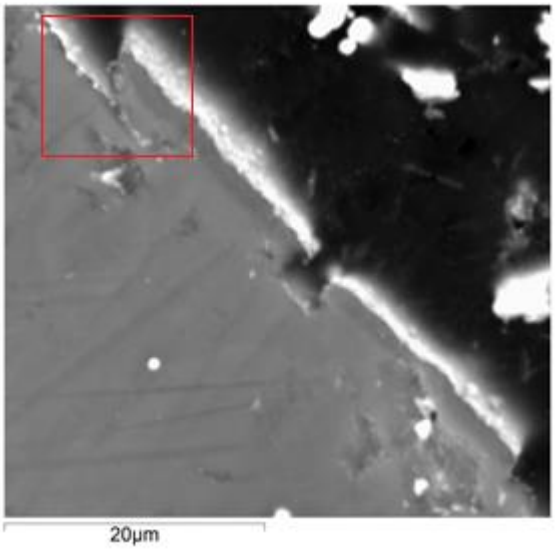

Figure 56: Cross section SEI of the two separate glasses in sample JH-PCM, and their attacked surface (black is epoxy). The area in red illustrates the attack on the Na-Glass from the side.

Figure 57 reveals the progression of solution pH during corrosion with time, measured as described in section 3.5.2 which followed the expected trend for a glass as predicted by current glass theory (see section 2.4), rising to over 10 in the first few weeks, before levelling off around pH 9.5 and rising again after 14 weeks. This pH regime will follow the standard glass corrosion model; during the rise to pH 9 leaching of weakly bound elements will occur, those that cause NBO, to be replaced by H_3O^+ once a steady state of pH ~9 is reached silicon dissolution will occur causing destruction of the silica

network. The presence of a corrosion layer in this sample may mitigate this network dissolution acting as a boundary between the attacking alkaline water and the pristine glass. How the crystals will react to the conditions is uncertain, however the collected results displayed a corrosion layer which may act in a protective manner similar to the glass corrosion layer.

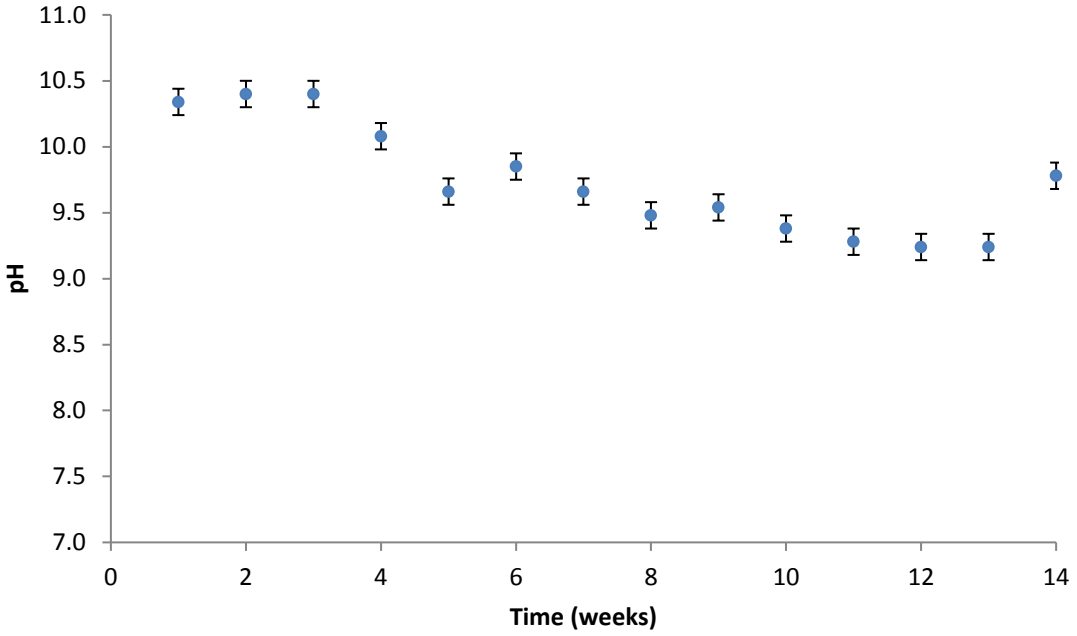

Figure 57: pH versus corrosion time (weeks) for JH-PCM sample (including both glass 1 and 2, and the crystalline components). Error bars reported are either the reported error of the pH machine (0.1 pH value), or the difference between the maximum and minimum values found from repeat tests, whichever was the larger.

ICP results (Table 28) revealed that leaching increased for all elements with the exception of iron up to 6 weeks. The error for the 10-week solution makes it unclear whether the values dropped (indicating precipitation) or remained steady (indicating no further leaching had occurred) as the upper end of the error places their values close to the results at 6 weeks. Previous results revealed that a semi-continuous gel layer (with minor cracking) had developed over the entire material which would tend to suggest that the latter of these is true; leaching was either slowed or stopped after 10 weeks. This is confirmed by pH results which revealed that the solution had achieved a steady state; a change in pH would be expected if precipitation had occurred.

Table 28: ICP results (in ppm) from 2-10 weeks from sample JH-PCM. Error is based on an average of 3 aliquots from the same solution using standard deviation. Result for potassium and iron after 4 weeks were unreliable with an estimated error approximating the average. Error is displayed as standard deviation only as these were larger than the systematic error of ICP-OES.

(ppm)	Al	Ca	Fe	K	Mg	Na	Si
2 Weeks	2.91	2.69	0.04	0.48	1.10	2.88	15.50
4 Weeks	2.79	3.25	0.00	-	0.22	3.46	19.49
6 Weeks	3.12	4.15	0.01	-	0.33	7.02	22.96
10 Weeks	2.71	4.06	0.00	-	2.75	6.84	20.51
Error (Std Dev.)							
2 Weeks	0.4544	0.0893	0.1025	0.1121	0.0145	0.4535	0.1143
4 Weeks	1.0948	0.3471	0.1421	-	0.0075	0.6261	0.5521
6 Weeks	0.8538	0.1415	0.1443	-	0.0057	0.2623	0.4365
10 Weeks	0.7234	0.1602	0.1811	-	0.0801	0.3795	1.2457

Normalised leach results for silicon (Figure 58) reveal a steady decrease for the duration of the experiment (10 weeks). Due to silicon's role in the glass and silicate crystals, this result is promising, indicating that the main structural component is retained in the crystalline/glass phase. The main element leached out of glasses is Na, the NL_r for which are displayed in Figure 59. As would be expected the release rate was higher than silicon due to the ease from which it is leached from the glass, however Figure 59reveals that the release rate decreases with time.

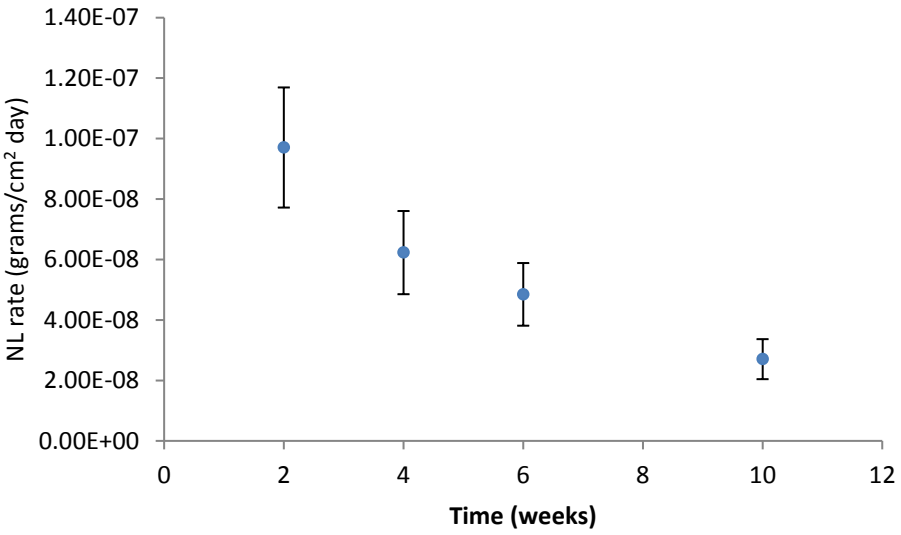

Figure 58: Normalised leach rates versus time for sample JH-PCM, for silicon. A continual decrease in the normalised leach rates is easily observable.

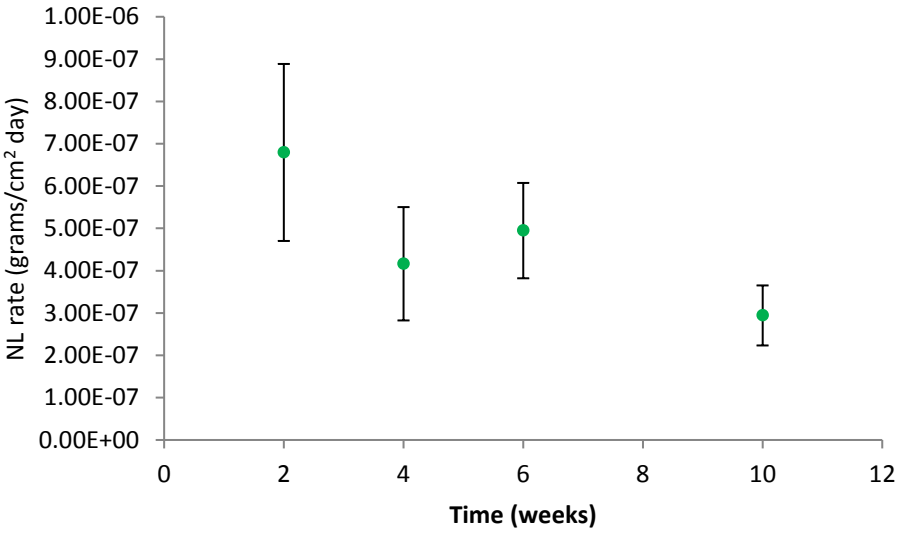

Figure 59: Normalised leach rates for sample JH-PCM for sodium.

4.2.2 Joule Heated-High Metal Surrogate

The complex nature of the crystalline portion of JH-HMS made the retrieval of repeatable corrosion results difficult; the CeLa phase, and various CaMgSi phases adjacent to it had complex morphologies displaying variable width, shape, and size all of which contributed to difficulty in location of those that intersected the surface. This was only exacerbated by the inability of the depth profiles to achieve an uninterrupted line scan; these scans were often interrupted by a second phase such as the darker dendritic phase or the Ce-La phase. The darker dendritic phase and Ce-La phase were also difficult to isolate and analyse for similar reasons.

SEM analysis of the surface after 2 weeks yielded no drastic change aside from a small etching effect that allowed for easier observation of the crystalline phase, no corrosion layer was observed. Undetected in uncorroded samples were Ce-La phases completely isolated from a dendritic phase,

dark or light, however at this corrosion time several such examples were seen. It is unknown whether this is due to complete removal of these phases or if this arrangement existed before corrosion and was not detected. The greatest difference at this time was in the small phase (0.5-2 µm) located in between the Ce-La phase, phase 3. It was seen to be almost completely removed from the sample (Figure 60b) showing this phase to be the least corrosion resistant of the phases. The glass was relatively unaffected by the environment until after 6 weeks, where it displayed a non-continuous layer which continued to some extent onto the grouped crystals (Figure 61). Interestingly this layer followed lines, most likely a relic from the grinding. The fact this layer continued onto the crystalline phase showed it was most likely precipitated rather than the more conventional hydration formation of the gel layer.

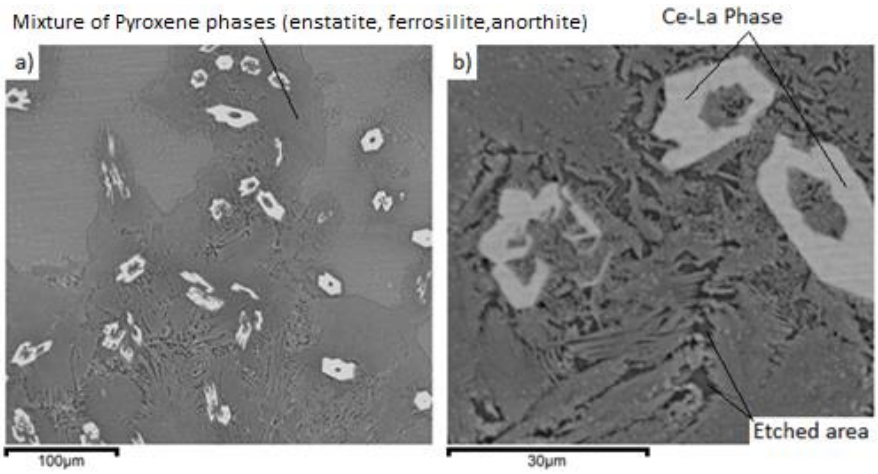

Figure 60: Surface BSE images of sample JH-HMS after 2 weeks of corrosion. a) Shows the larger crystal (pyroxene phases) arrangement, which showed no corrosion layers, or other indicators of corrosion. b) shows a higher magnification image of a), revealing a previously unseen (pre-corrosion) darker portion giving the area an etched appearance. It is unclear if this is due to corrosion or if it was present before corrosion.

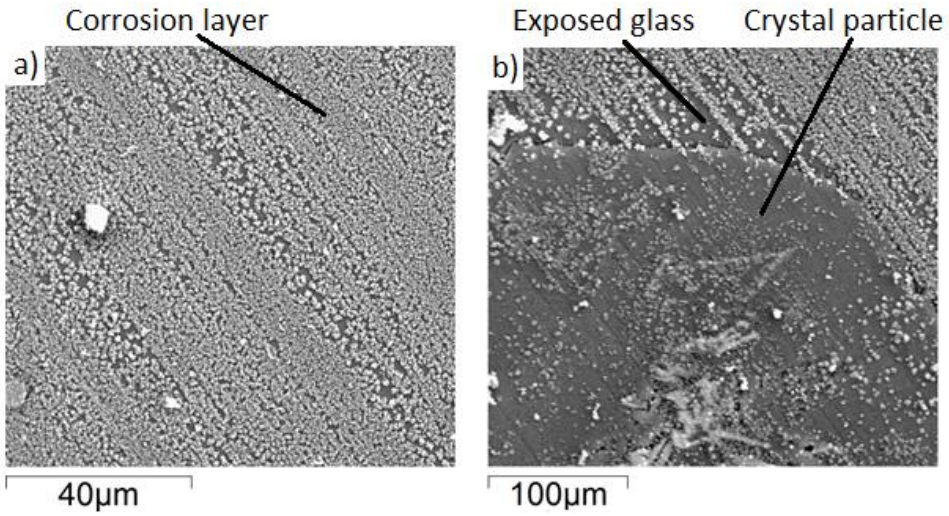

Figure 61: Surface BSE images of the glassy portion of JH-HMS (a) following 6 weeks of corrosion displaying a clear corrosion layer. b) shows a portion containing both the crystal portion and glass illustrating an exposed area in the glass corrosion layer approaching the crystal.

As can be seen in Figure 62and Table 29, a significant change occurs in the surface glass composition after 6 weeks of corrosion, specifically in the concentrations of Al, Si, Fe, La, and Ce. No observable change from this composition occurred on the surface past 6 weeks, displaying the same micrographs. No additional compositional changes were observed. Cross sectional analysis confirmed this observation, no layer was seen before 6 weeks, but at 6 weeks, and all subsequent corrosion times a thin gel layer along with a leached layer, visible as a white surface layer followed by a darkened region below it (Figure 62). Whilst SEI/BEI showed that this layer was approximately 2.16 µm thick (±1 µm) depth profiling revealed a leached layer below the gel layer, which extended an additional 2 µm into the sample. The profile displayed two trends dependant on the elements. Firstly, Mg, Na, Si, and Al steadily decreased over the leached layer whereas in contrast, La, Ce, and Fe concentrations remained constant through both the leached layer and partially through the gel layer (Figure 63and Figure 64), following this a steep decline in these elements was seen. Changes in the crystalline portion were more easily distinguished through cross sectional scans rather than surface ones.

Table 29: EDX results for the glass surface after 6 weeks of corrosion for sample JH-HMS, results displayed in oxide wt%. Error is displayed as either standard deviation from 20 different point scans, or the inherent error of EDX analysis (0.1 wt%), whichever was greater.

Glass Post Corrosion	MgO	Al_2O_3	SiO_2	CaO	Fe_2O_3	La_2O_3	Ce_2O_3
Compound %	2.3	4.4	33.5	7.3	18.0	11.3	23.1
Error ±	0.1	0.2	0.7	0.5	0.4	0.6	0.9

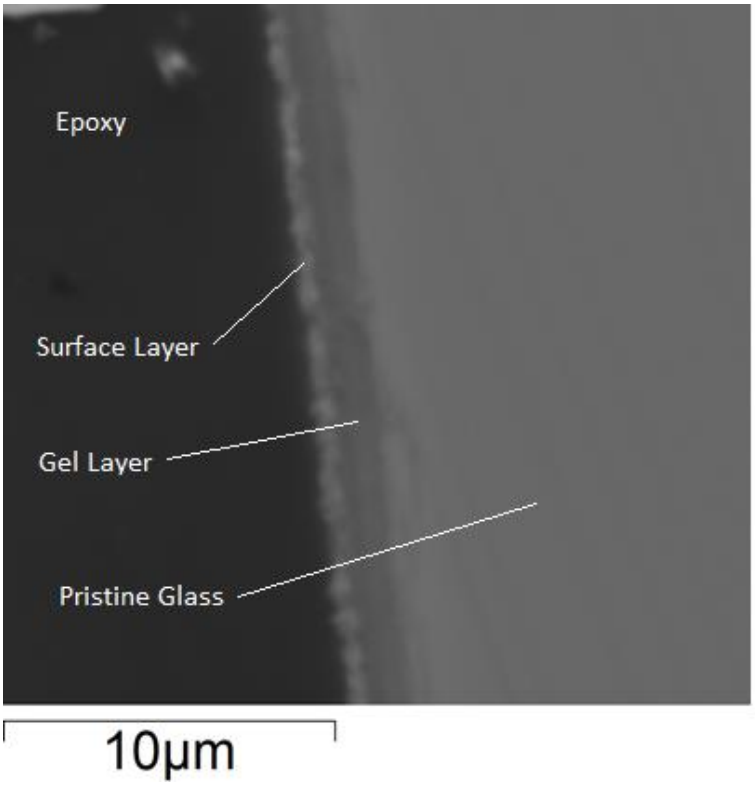

Figure 62: BEI cross section image of a 6-week corroded sample of JH-HMS showing a surface layer on top of the glass comprised of that observed on the surface (figure 55, partially covering corrosion layer), with an underlying layer of a differing composition.

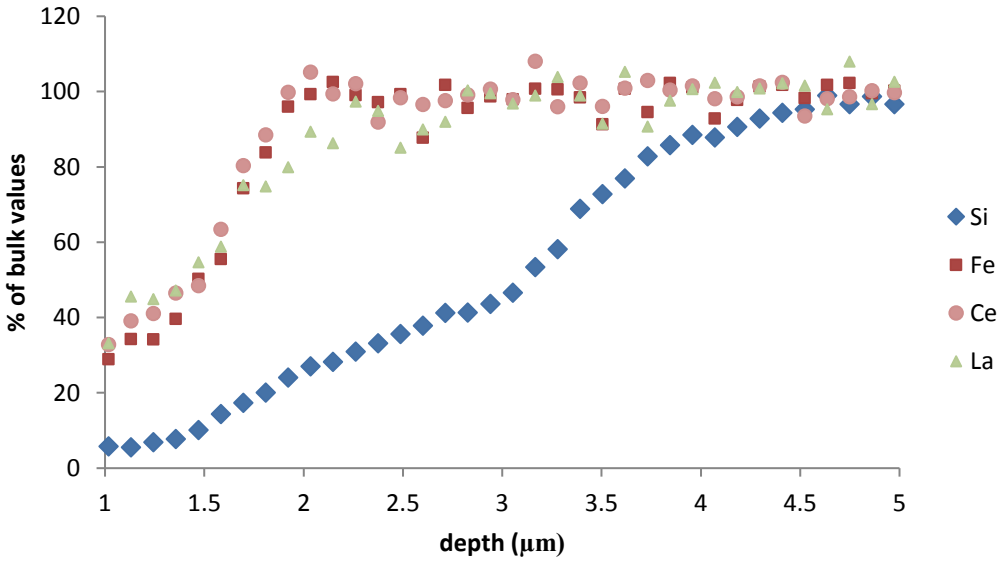

Figure 63: Graph displaying the depth profile of the glass portion of JH-HMS. This profile was seen for all times investigated where a gel layer was present; results are averaged from results for these times (2-14 weeks).

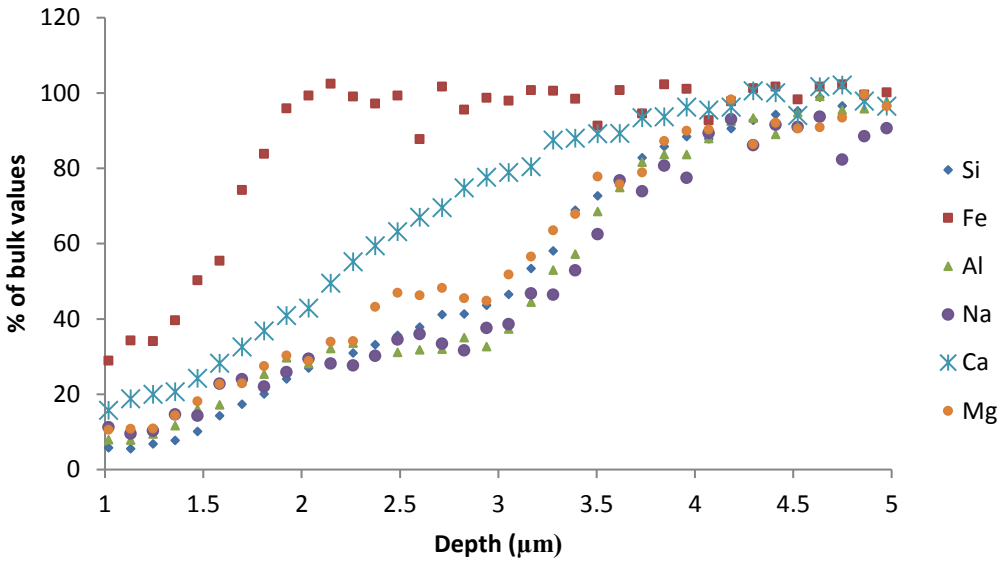

Figure 64: Graph displaying the depth profile of the glassy portion of JH-HMS for the elements shown. This profile was seen for all times investigated where a layer was present; results are averaged from results for these times (2-14 weeks). Silicon and iron are shown in both as a reference.

With the exception of Ca, the other elements showed a "shelf" 2 µm into the layer, evident in Figure 64 in the depth region of 1.5-3.5 µm. This trend was confirmed by several other scans performed at various locations around the glassy portion of the sample. When including EDX results into the total leached depth, it increases to 4 µm excepting both Ce and La which form a separate leached layer of 1 µm.

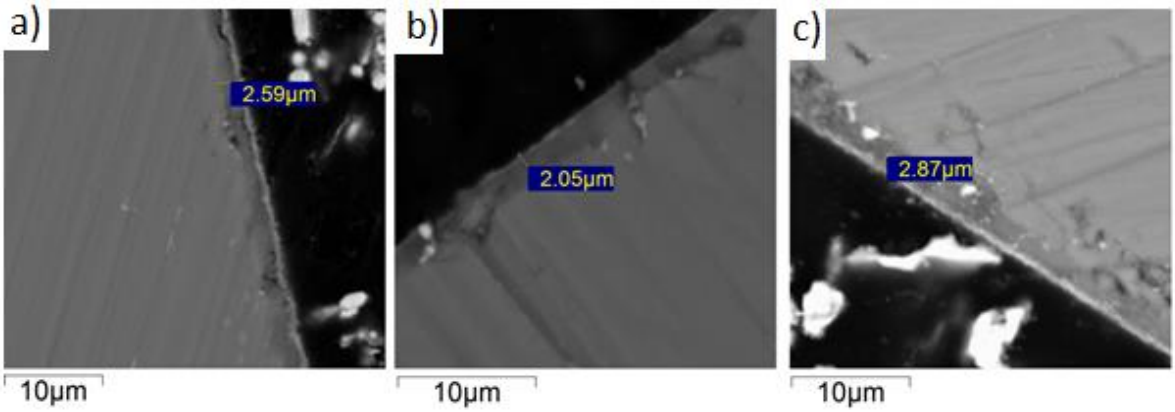

Figure 65: Cross section using BSE imaging of the glass and its gel layer in sample JH-HMS at a) 6 weeks, b) 10 weeks, c) and 14 weeks. Gel layer had an uneven depth producing a variable size gel layer (2-3 µm).

Figure 65 shows the corrosion layers over the glass for 6,10, and 14 weeks along with the calculated depth of the leached layer. The gel layer formed in an uneven manner, at its deepest it was calculated to be close to 3 µm and at its lowest around 2 µm. This was true for 6,10, and 14 weeks showing that no noticeable growth of the layers occurred as a function of time, up to 14 weeks. The associated EDX line scans also did not change.

Whilst the pyroxene phases did not display a definitive gel layer, it showed a layer where the concentration of elements did drop, as can be seen in Figure 66. After 4 weeks Na, Al, and Si all dropped off steadily whilst Ca, La, and Ce continued at close to bulk values until around 1 µm from the surface where they tapered off to approximately 50% bulk values. This trend was not the same for both iron and magnesium which displayed two unique profiles. Iron gradually increased until reaching 1 µm deep wherein it decreased. Magnesium initially showed a profile similar to that of calcium, a gradual decrease until 2 µm into the sample when it started to increase again, building up the closer to the surface.

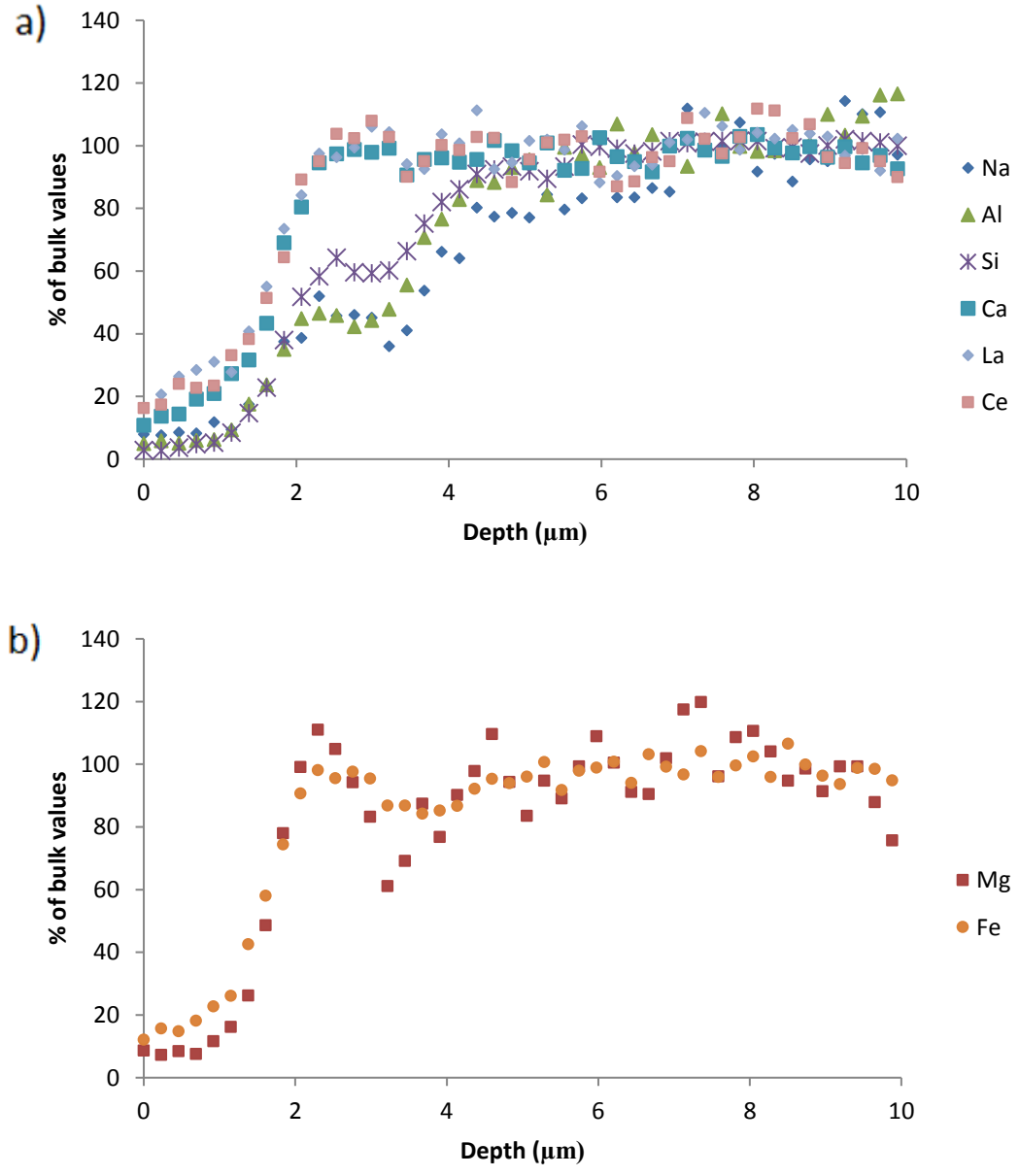

Figure 66: Depth profiles for the crystal at 6 week in JH-HMS. The graphs are split into two, Fe and Mg in b), with the remaining elements in a), for clarity.

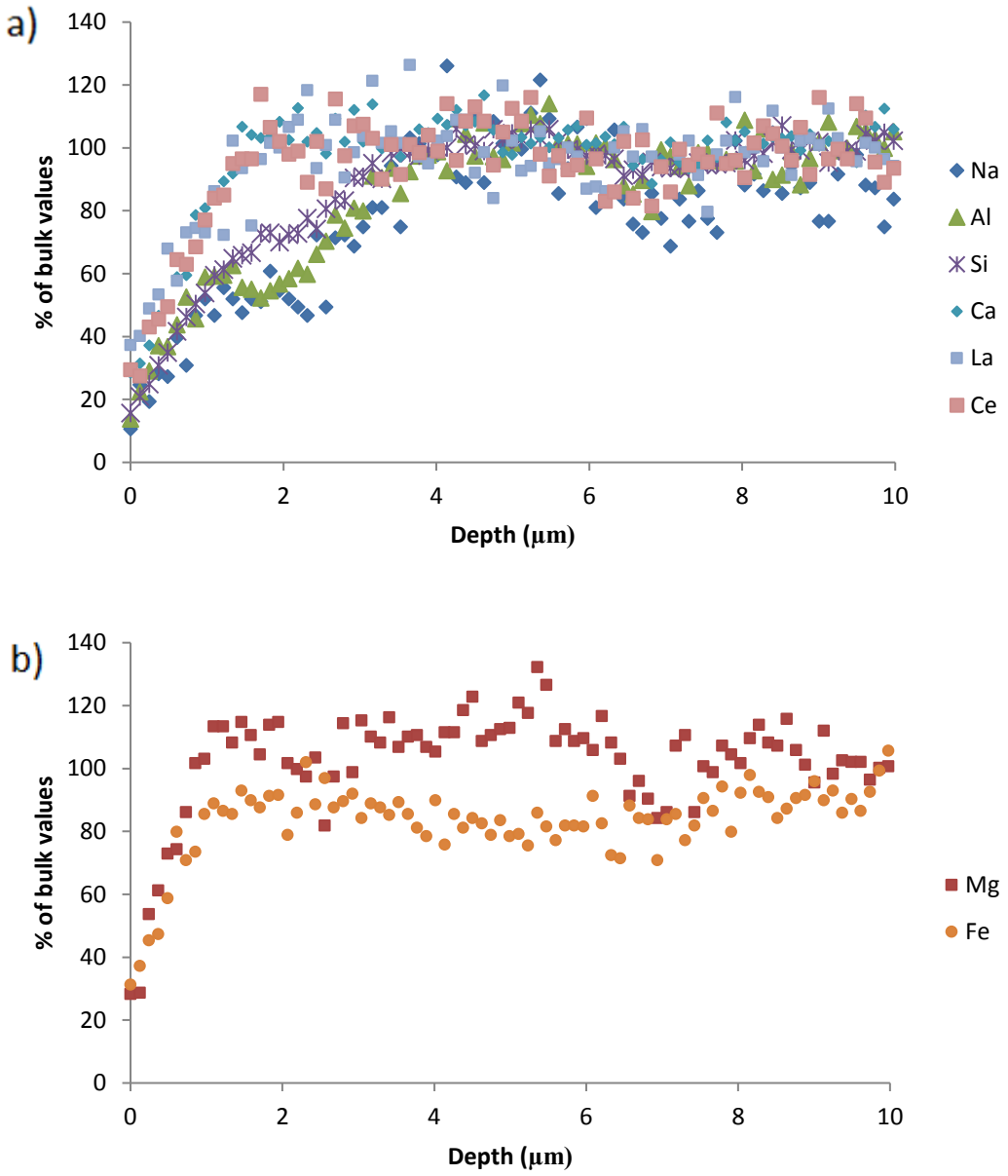

Figure 67: Depth profiles for the main crystal (largest pyroxene phase, originally phase 1) at 14 weeks in sample JH-MHS. The graphs are split into two, Fe and Mg in b), with the remaining elements in a), for clarity.

pH results for JH-HMS samples over 14 weeks (Figure 68) reveal that pH levels quickly rose to above pH 11, one of the highest recorded for all wasteforms investigated. Interestingly ICP-OES results from the solution corroding the specimens (Table 30) did not fully reflect such a high pH; for such an alkaline solution, considerable structural corrosion would be expected. In the glass this would destroy the silicate network resulting in a high concentration of silicon in solution (>50 ppm), with correspondingly high concentration of the waste elements contained in its structure, which would be released as the glass network dissolved. In the absence of secondary phases forming from precipitation, the low concentration of silicon would suggest that little corrosion of the glass network was occurring. This result whilst unexpected is encouraging as it suggests that the glass will retain its waste elements for significantly higher periods of time than the other glasses, and GCMs studied which had higher Si release in a less alkaline solution.

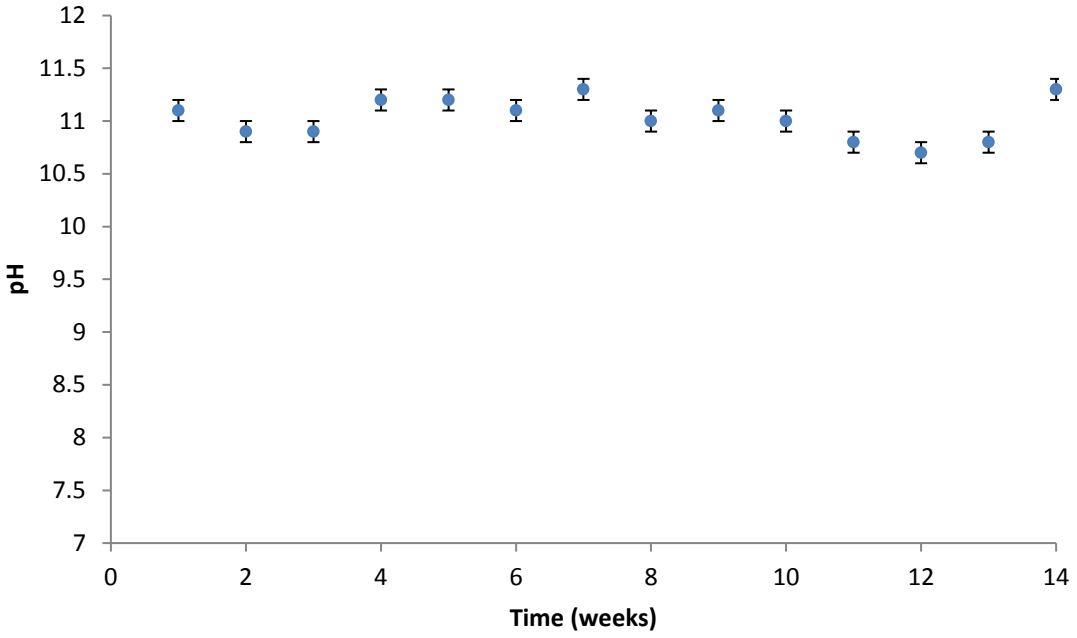

Figure 68: pH versus corrosion time (weeks) for sample JH-HMS up to 14 weeks. Error bars reported are either the reported error of the pH machine (0.1 pH value), or the difference between the maximum and minimum values found from repeat tests, whichever was the larger.

Table 30: ICP results (in ppm) for JH-HMS for 2,4,6, and 14 weeks. 10 week results were omitted due to faults with the machine. Error is based on the average of 3 aliquots from the same solution. Error is displayed as standard deviation only, as these were larger than the systematic error of ICP-OES.

(ppm)	Al	Ca	Fe	K	Mg	Na	Si
2 weeks	2.648	1.745	0.015	0.000	1.035	3.202	9.090
4 weeks	3.643	1.969	0.060	0.050	0.490	3.745	11.973
6 weeks	3.578	1.807	0.000	0.273	0.379	9.041	13.509
14 weeks	2.143	3.490	0.001	0.607	0.794	10.443	12.710
Error (Std Dev.)							
2 weeks	0.554	0.129	0.125	0.023	0.028	0.783	0.314
4 weeks	1.488	0.227	0.208	0.017	0.018	0.558	0.454
6 weeks	1.092	0.083	0.127	0.044	0.007	0.510	0.509
14 weeks	0.612	0.201	0.094	0.222	0.032	0.209	0.787

NL_r revealed a decrease in the release rate of aluminium and silicon (Figure69) for the duration of the experiment (14 weeks) a good indicator for how destruction of the glass network/crystalline network progresses due to their structural role. Mg and Ca release rates (Figure70) reflect this with a large decrease in release rate after 4 weeks, after which the release rates continued to decrease at a lesser rate.

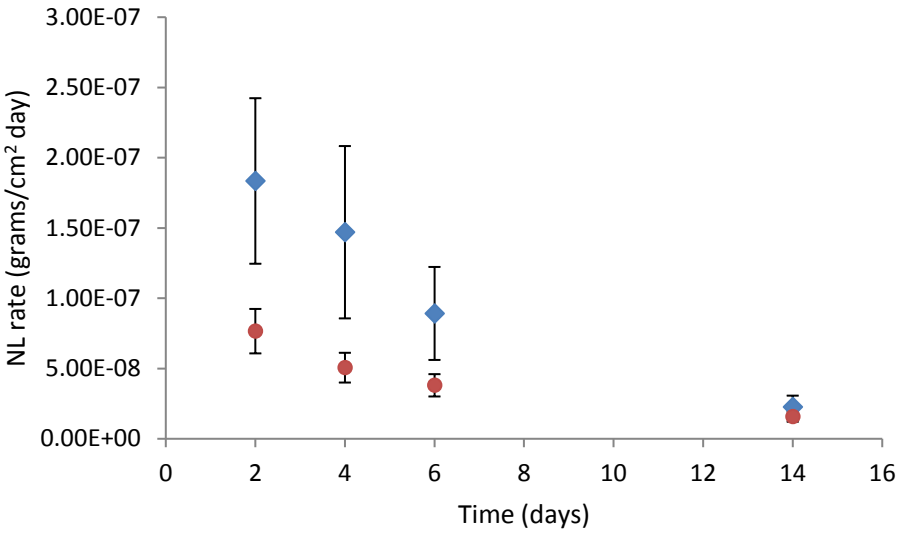

Figure 69: Normalised leach rates of silicon (red) and aluminium (blue) for sample JH-HMS.

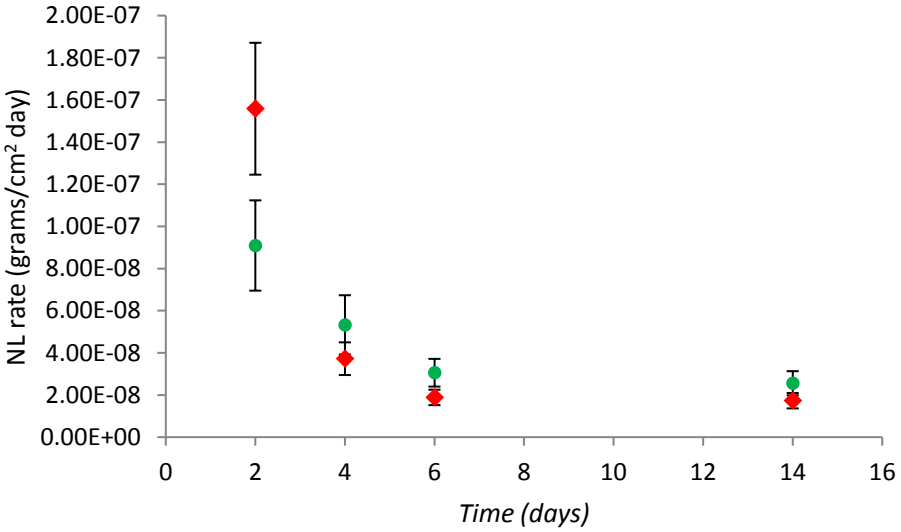

Figure 70: Normalised leach rates of magnesium (red) and calcium (green) for sample JH-HMS.

4.2.3 Joule Heated-SIXEP

Following 4 weeks of corrosion, a layer had developed on the glassy portion of the sample (Figure71b) and partially on the thin pyroxene phase but not on the thick pyroxene. A surface layer on the thinner crystal cannot be ruled out as some degree of corrosion/layer can be seen on top of it (Figureb). EDX was used to help identify compositional changes in the surface layer on all phases, (Table 31).

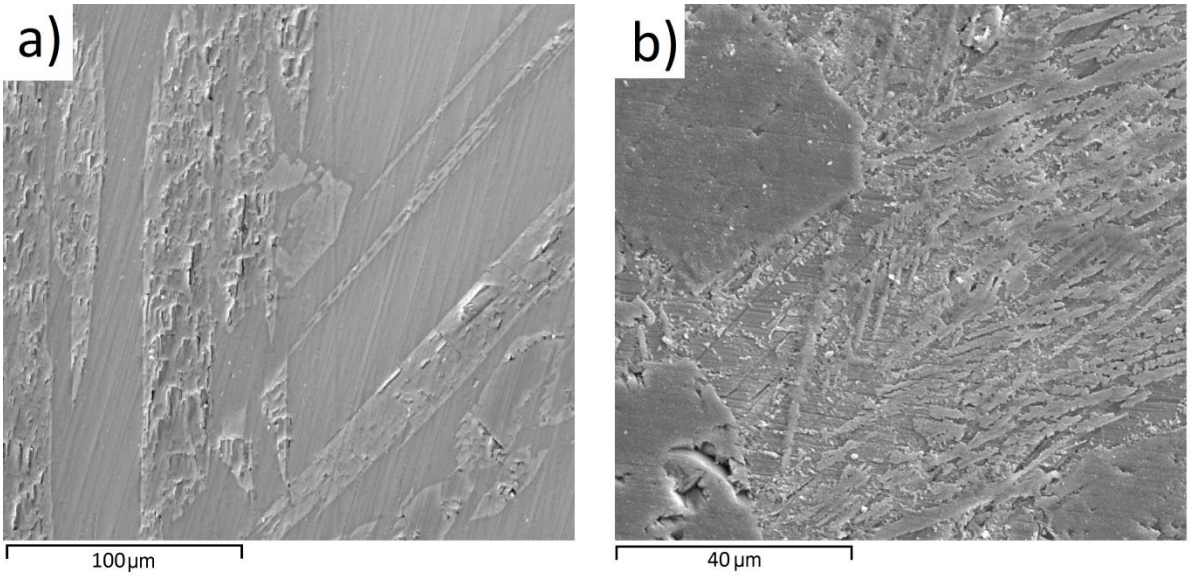

Figure 71: BSE images of JH-SIXEP sample a) pre-corrosion, b) surface after 4 weeks of corrosion showing an etching effect, surface debris, and a roughened appearance; sharp sides and points pre-corrosion in a) versus uneven sides in b) to the thin crystals that was previously absent.

Table 31: EDX results of the surface of JH-SIXEP sample after 4 weeks of corrosion, taken from the three different phases shown. Results in oxide wt%. Error is displayed as either standard deviation from 10 (5 for the thin crystal) different point scans, or the inherent error of EDX analysis (0.1 wt%), whichever was greater.

Thick Pyroxene	**MgO**	**Al_2O_3**	**SiO_2**	**CaO**	**Fe_2O_3**
Compound %	17.0	1.3	59.0	0.9	21.7
Error ±	0.9	0.3	1.00	0.3	1.5
Glass					
Compound %	0.8	12.0	67.7	6.2	13.4
Error ±	0.1	0.3	1.00	0.2	1.0
Thin pyroxene					
Compound %	2.1	1.5	30.6	2.5	63.3
Error ±	0.2	0.6	0.9	0.1	0.2

By week 6 this corrosion layer had progressed to cover the entire sample surface (Figure 72) including areas where this layer had spalled off revealing the pristine/leached glass underneath, this is obvious by the change in colour in these areas signalling a change in composition difference relative to the layer on top. Further results from 6 weeks onwards did not show any change in surface appearance, or in surface composition and so are not included.

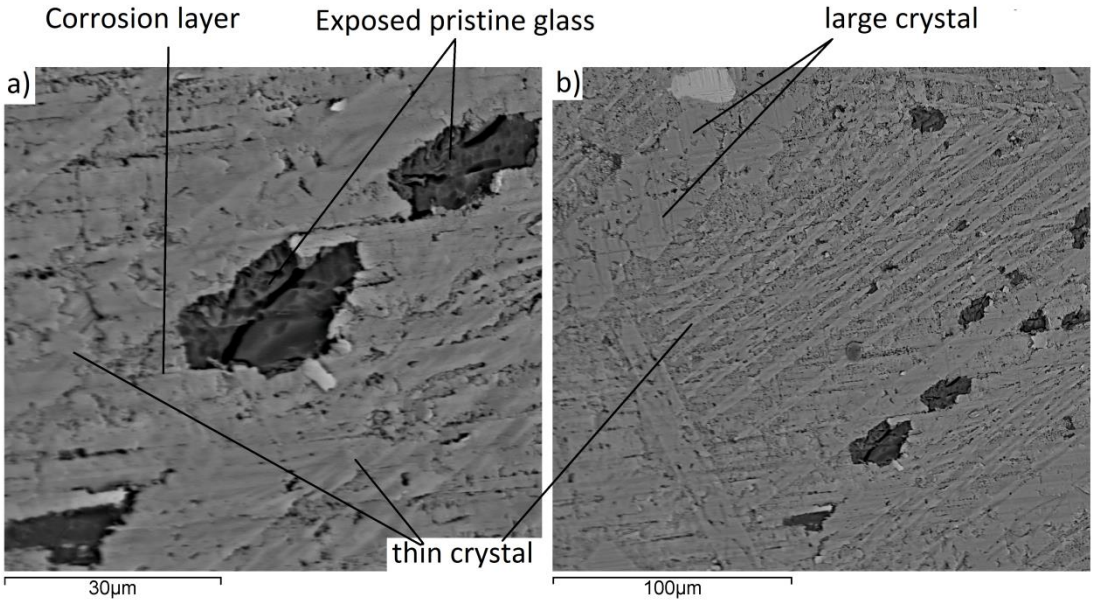

Figure 72: BSE image of the of JH-SIXEP surface after 6 weeksof corrosion. (a) focuses on the areas were the corrosion layer had spalled off revealing the phase underneath, the glass matrix. (b) Shows how the sample appeared after 6 weeks of corrosion; the corrosion layer is hard to discern without the areas where it is has spalled off, these were isolated to only the glass phase.

Table 32: EDX results from surface analysis on sample JH-SIXEP after 6 weeks of corrosion, for the various identified phases. Results in oxide wt%. Error is displayed as either standard deviation from 10 different point scans, or the inherent error of EDX analysis (0.1 wt%), whichever was greater. The high error for the uncovered glass and thin crystal is due to the small size (on the order of µm's) which approaches the spatial resolution of EDX. Typical spectra for each phase is shown below.

Large pyroxene	***MgO***	***Al_2O_3***	***SiO_2***	***CaO***	***Fe_2O_3***
Compound %	17.0	1.3	59.1	0.9	21.7
Error ±	0.9	0.3	1.0	0.3	1.5
Glass (covered)					
Compound %	1.0	11.4	67.5	6.0	14.1
Error ±	0.3	0.9	1.0	0.5	1.8
Glass (uncovered)					
Compound %	0.4	7.5	51.5	8.2	32.3
Error ±	0.1	1.8	6.9	0.9	7.9
Thin pyroxene					
Compound %	3.3	3.1	38.9	2.3	52.4
Error ±	1.8	2.4	11.0	0.4	14.1

The depth profiles for the elements shown after 4 weeks are displayed in Figure 73and Figure74. Iron was separated as it displayed a distinctly different profile. Although the depth profiles for the elements shown in Figure 73would suggest a lack of corrosion layer due to the gradual decrease in all elements (typical of leached layer rather than a gel layer), a gel layer was observed none the less (Figure75a). Figure 74 reveals that iron displayed an even composition until a depth of 1 µm where it observed a steady increased composition for approximately 0.4 µm (0.8-1.2 µm region) before displaying a rapid decline. Comparing this with the depth profiles in Figure 73, in the 0.8-1.2 µm range, Na and Mg were seen to slightly increase, whilst Al was revealed to have reached a plateau, neither increasing nor decreasing in concentration; before this region it was observing a steady decline. This is evidence that the corrosion layer tends to retain these elements, and due to the complete lack of change in the silicon profile, is not a primarily a silica gel layer.

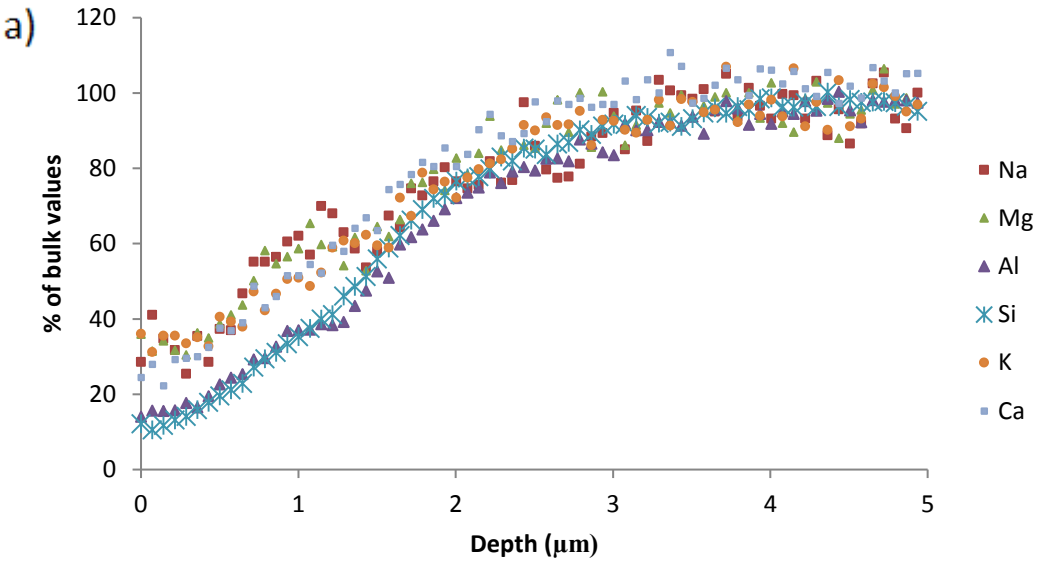

Figure 73: Depth profile for various elements in the glass in sample JH-SIXEP after 4 weeks.

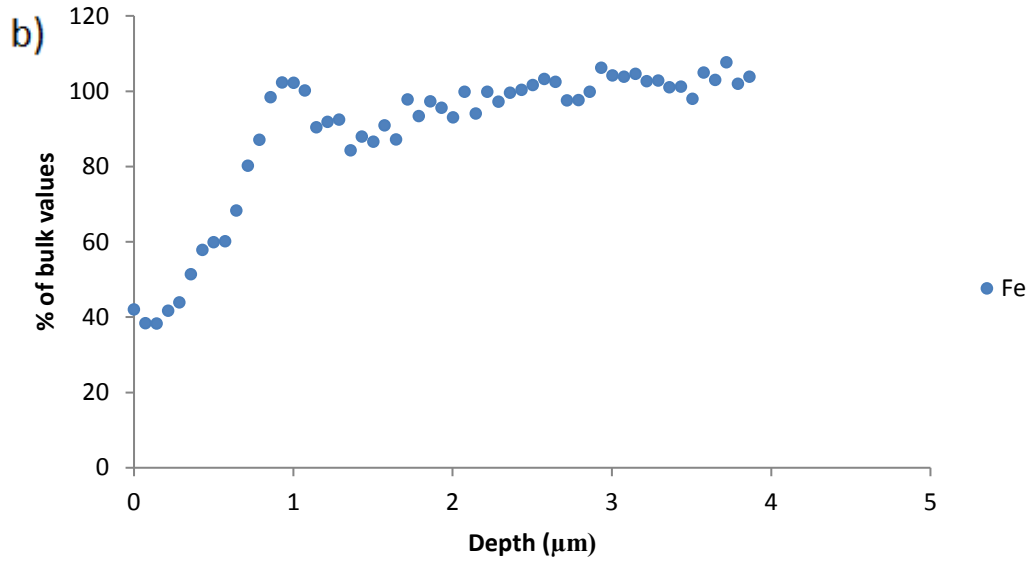

Figure 74: Depth profile for the glass in JH-SIXEP sample after 4 weeks in b) displaying only iron for clarity.

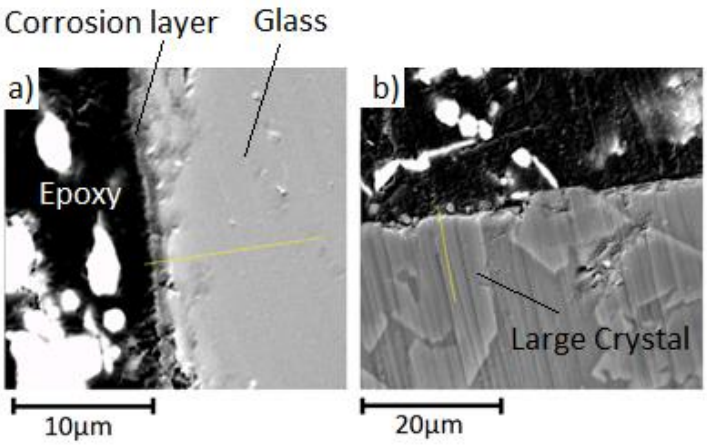

Figure 75: BSE image of JH-SIXEP sample after 4 weeks of corrosion, depth profile lines are shown. The presence of a corrosion layer on top of the glass is obserable in a), whilst b) shows a slight protrusion of the large crystal from the glass matrix, no corrosion layer on top of the crystal was observed,

Shown in Figure 76is the depth profile for the large pyroxene crystal at 4 weeks, other elements were detected (Ca,Al, and Na) however these results are not displayed due to the low X-ray counts associated with these elements, along with the accompanying error (±200%). This error arises when the number of detected X-ray energies associated with a certain element, approach the background X-ray energy making accurate concentration identification difficult, and can lead to erroneous results. Whilst these elements will most likely be present, the low concentration (<1 wt% region) will allow for identification only, but not quantitative information.

Depth profiles for the 4, 6, and 10-week corrosion times are displayed in Figure 76-78for the large pyroxene, taken from samples similar to the depth profile line shown in Figure 75b. Whilst no corrosion layer was observed for all corrosion times for the thick crystal, depth profiling revealed that the pyroxene was significantly affected by the conditions. At 4 weeks Mg and Si displayed an increase in concentration approaching the surface (10-20% increase relative to bulk), whilst Fe appeared to be removed showing a decrease to 70% bulk concentrations (Figure 76) over a 4 µm range. After 6 weeks (Figure 77) the corrosion affected zone had increased to 10 µm, with iron displaying an increase to 120% bulk value concentrations from 6-14 µm (peaking at 6-8 µm), Mg and Si showing a steady decrease from 14-8 µm and a steep decrease from 8-4 µm. No surface change was observed for this corrosion time; no layer had developed and no noticeable change had occurred that would explain this change from the 4-week depth profile. At 10 weeks (Figure 78), the profile changed again, showing a shrinkage in the corrosion zone to 5 µm. Mg concentrations dropped steeply to 10% bulk values over a 1 µm range, whilst Fe similar showed a steep decline in concentration to 40% over 1 µm followed by a steady decline from 40%-20% over a 4 µm range not observed in the Mg profile. The Si profile saw a slight decrease in concentration (100-80%) over the same 1 µm range that Fe and Mg observed a drop, however the concentration started to increase again from 80% back to 100%. Overall the profile at 10 weeks suggests the presence of a thin (2-4 µm) Si corrosion layer depleted in Mg but with some limited retention for Fe. Whilst this layer was not observed from surface images, it is possible it was missed due to the interaction zone that BSE images give, typically the image received is not that at the surface but that 0.5-2 µm below the surface (see sections 3.3.1-3.3.3).

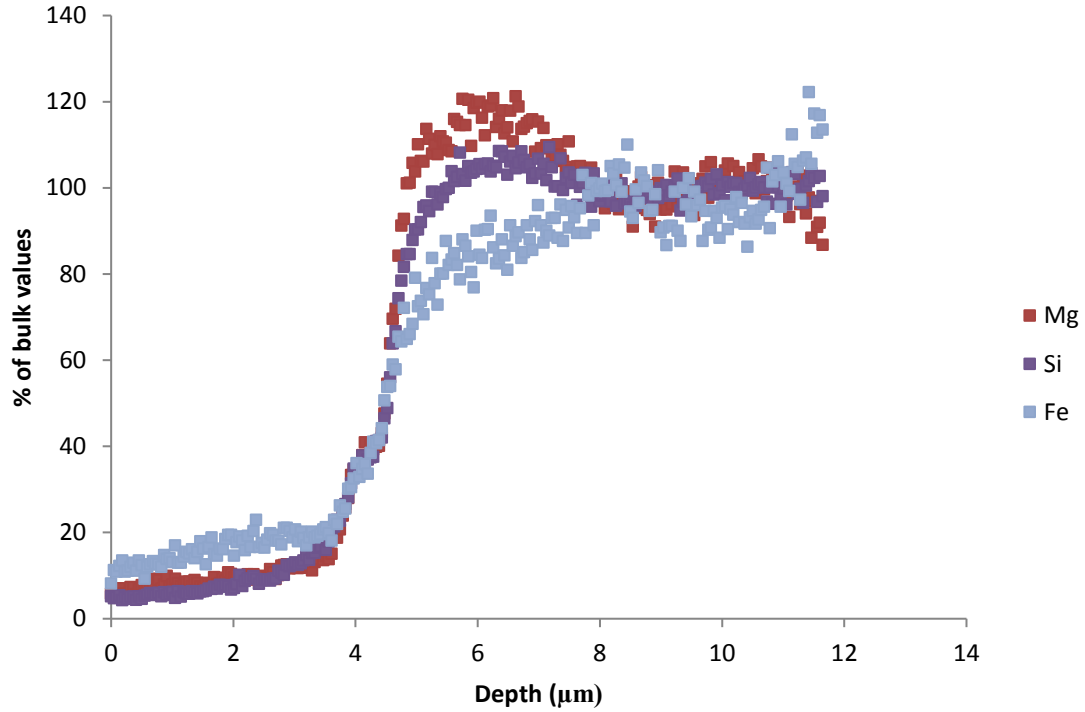

Figure 76: Depth profile for the large pyroxene in JH-SIXEP sample after 4 weeks of corrosion.

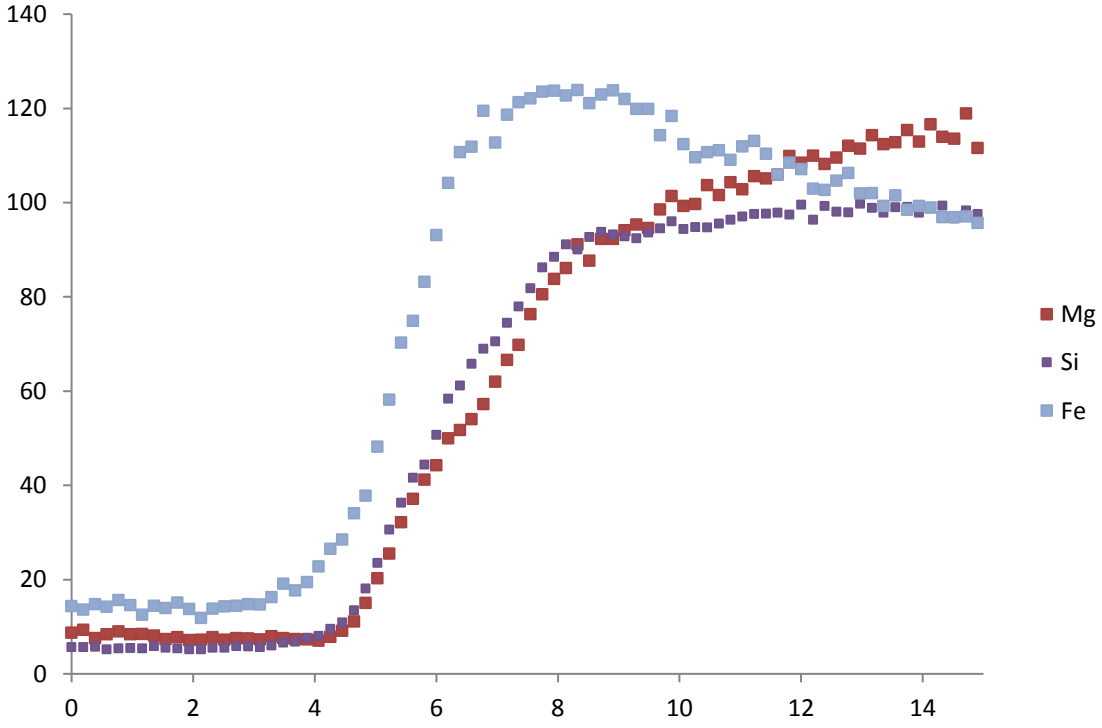

Figure 77: Depth profile for the large pyroxene in the JH-SIXEP sample after 6 weeks of corrosion.

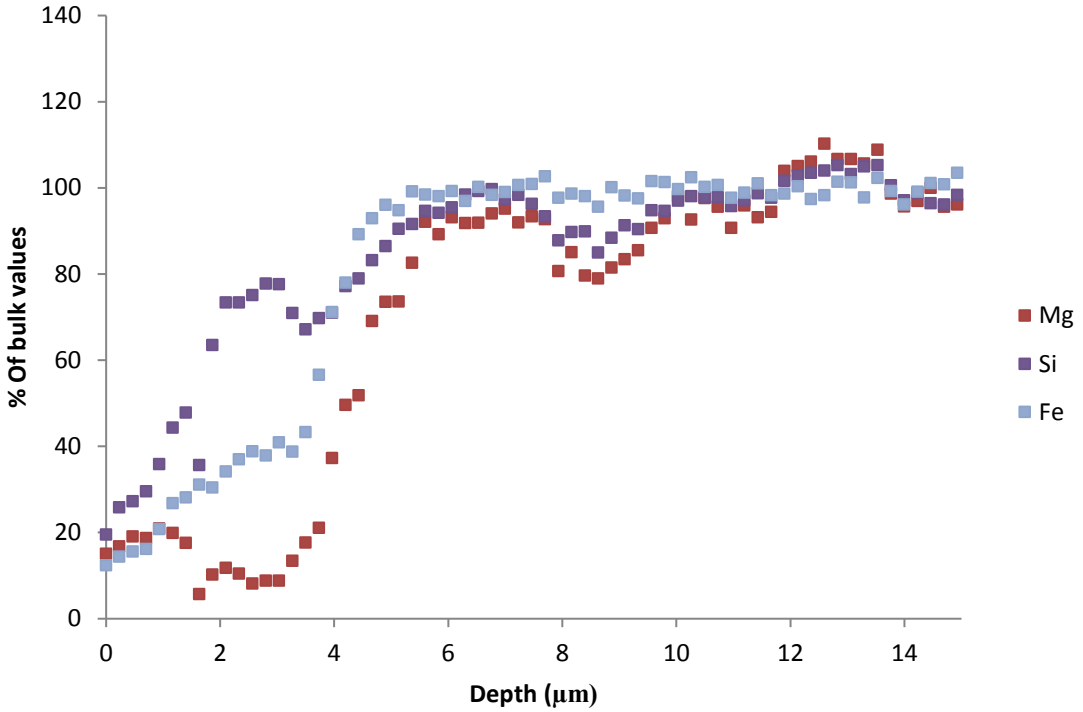

Figure 78: Depth profile for the large pyroxene in the JH-SIXEP sample after 10 weeks of corrosion.

Depth profiles for the thin pyroxene crystals were more difficult to collect due to many of the crystals that intersected the surface being broken, i.e. less than 5 µm long, or were less than 3-4 µm, this length is the minimum spatial resolution of EDX line scans at the parameters used. Due to this only results for 10 and 14 weeks of corrosion time were recorded, in Figure 79and Figure 80respectively. The 10-week depth profile (Figure 79) was similar to that seen for the large pyroxene at 10 weeks (Figure 78) in that 3 distinct profiles are observed, a slight drop occurs followed by a 3 µm plateau (Ca and Fe), a drop to ~50% bulk concentration with a slight recovery over 5 µm (Al and Si) and finally a significant drop (down to 20%) with a slight recovery to 40% over 5 µm. Similarly, to the thick crystal, this implies the presence of a corrosion layer and/or a leached layer. This profile was similarly seen at 14 weeks of corrosion (Figure 80), with a slight increase (~0.5 µm) to the region affected.

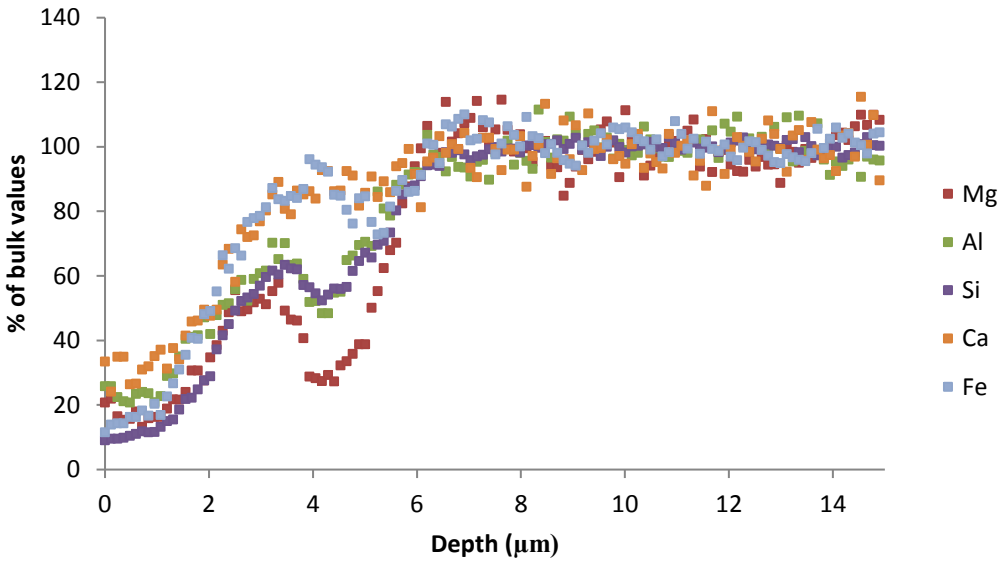

Figure 79: Depth profile for the thin pyroxene in JH-SIXEP after 10 weeks.

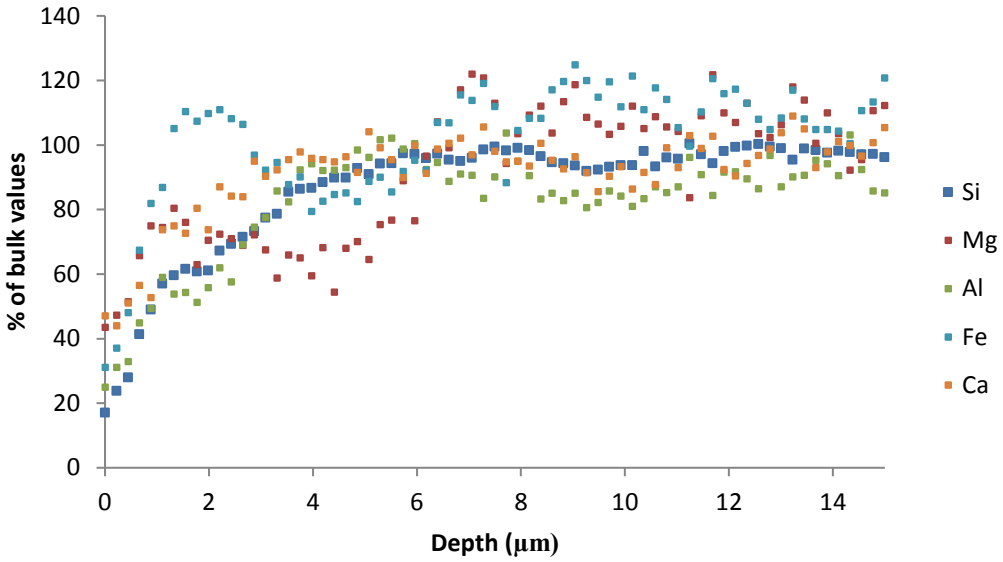

Figure 80: Depth profile for the thin pyroxene in JH-SIXEP after 14 weeks.

ICP-OES results and pH results (Table 33 and Figure 81) revealed the sample to have the lowest initial (0-6 weeks) pH of all the samples investigated, and a similarly low pH for the remainder of the experiment where it had the second lowest average (8.95, lowest was 8.91) over weeks 6-14. However, ICP-OES results did not reflect this low pH, showing a comparable release to other samples studied (Table 28, Table 30, and Table 46), current glass corrosion theory suggests (see section 2.4) that the further the pH is above 9, the more destructive the solution is to the glass network. Thus, it would be expected to have lower elemental release than samples where the pH rose above 10, which was not seen.

Table 33: ICP (in ppm) *results for JH-SIXEP for 2,4,6, and 14 weeks. 10 week results were omitted due to faults with the machine. Error is based on the average of 3 aliquots from the same solution. Error is displayed as standard deviation only, as these were larger than the systematic error of ICP-OES.*

(ppm)	Al	Ca	Fe	K	Mg	Na	Si
2 weeks	3.257	3.286	0.666	1.232	0.580	1.239	14.018
4 weeks	3.934	3.727	0.650	1.794	0.552	0.141	15.540
6 weeks	4.129	4.369	0.632	2.233	0.620	3.063	18.325
14 weeks	1.886	3.867	0.301	2.533	0.610	3.676	15.656
Error (Std Dev.)							
2 weeks	0.740	0.345	0.089	0.087	0.007	0.612	0.819
4 weeks	1.644	0.485	0.071	0.087	0.020	0.684	0.781
6 weeks	1.235	0.239	0.106	0.068	0.009	0.426	0.764
14 weeks	0.525	0.273	0.107	0.054	0.030	0.146	1.199

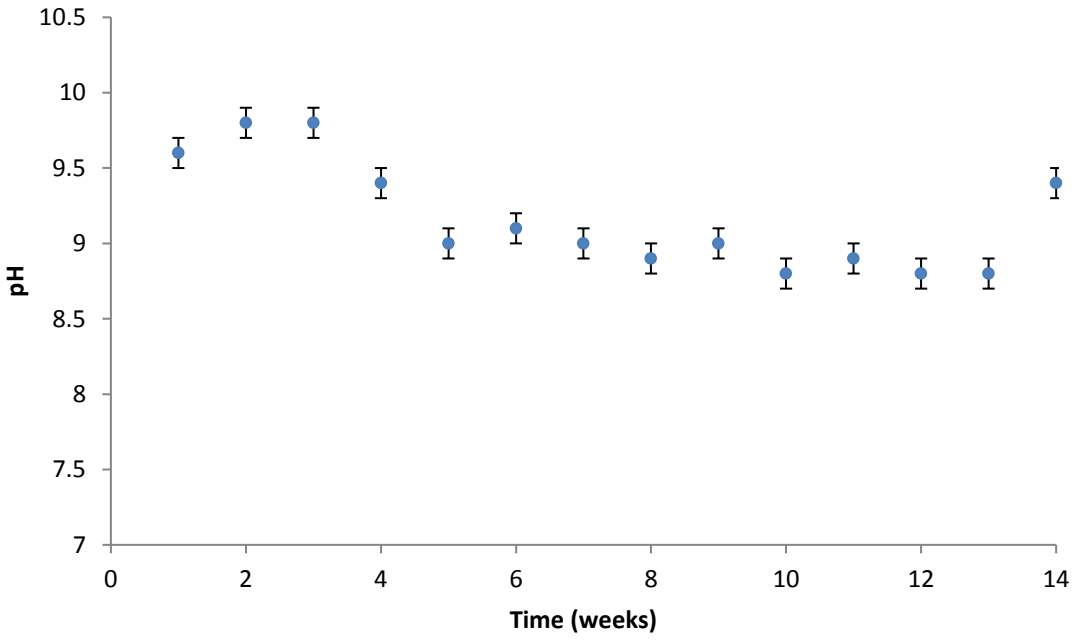

Figure 81:pH versus corrosion time (weeks) for sample JH-SIXEP up to 14 weeks. Error bars reported are either the reported error of the pH machine (0.1 pH value), or the difference between the maximum and minimum values found from repeat tests, whichever was the larger.

NL_r revealed a generally good resistance to corrosion due to the decreasing release rate of the structural element Si (Figure 82), and also Mg (Figure 83) which is easy to remove during the leaching stage. Fe also demonstrated a steady decrease in release rate (Figure 83), in agreement with the corrosion resistance of the material due to the large amount of Fe present in the GCM.

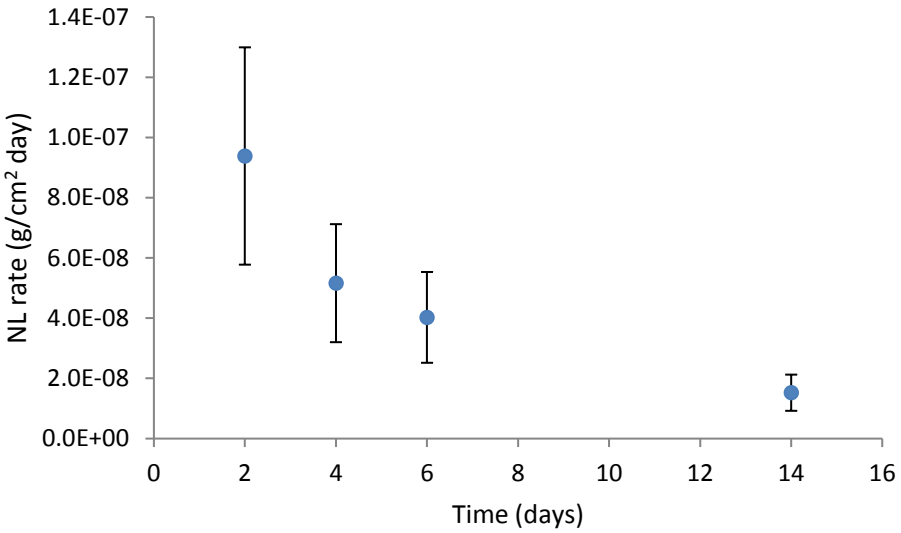

Figure 82: Normalised leach rates for silicon

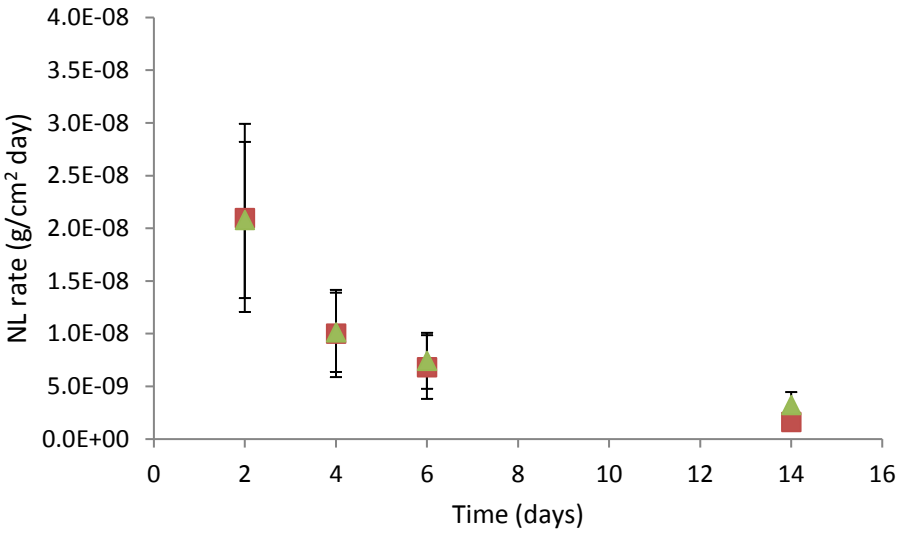

Figure 83: Normalised leaching rates for magnesium (green) and iron (red) for sample JH-SIXEP.

4.3 Plasma Furnace Wasteform Characterisation

4.3.1Plasma Furnace-High Metal Surrogate

The as-received PF-HMS sample was comprised of two visually different portions, a predominantly blue phase with some streaks of green, and a black portion which when polished was lustrous and similar in appearance to polished metals. Due to this it was assumed this portion had unreacted metal waste and is thus referred to as the metallic portion. The two portions were easily separable and isolated as such to allow different tests to be performed independently of each other.

XRD analysis (Figure 84) confirmed the blue/green phase to be completely amorphous, and it is thus referred to as blue glass and green glass.

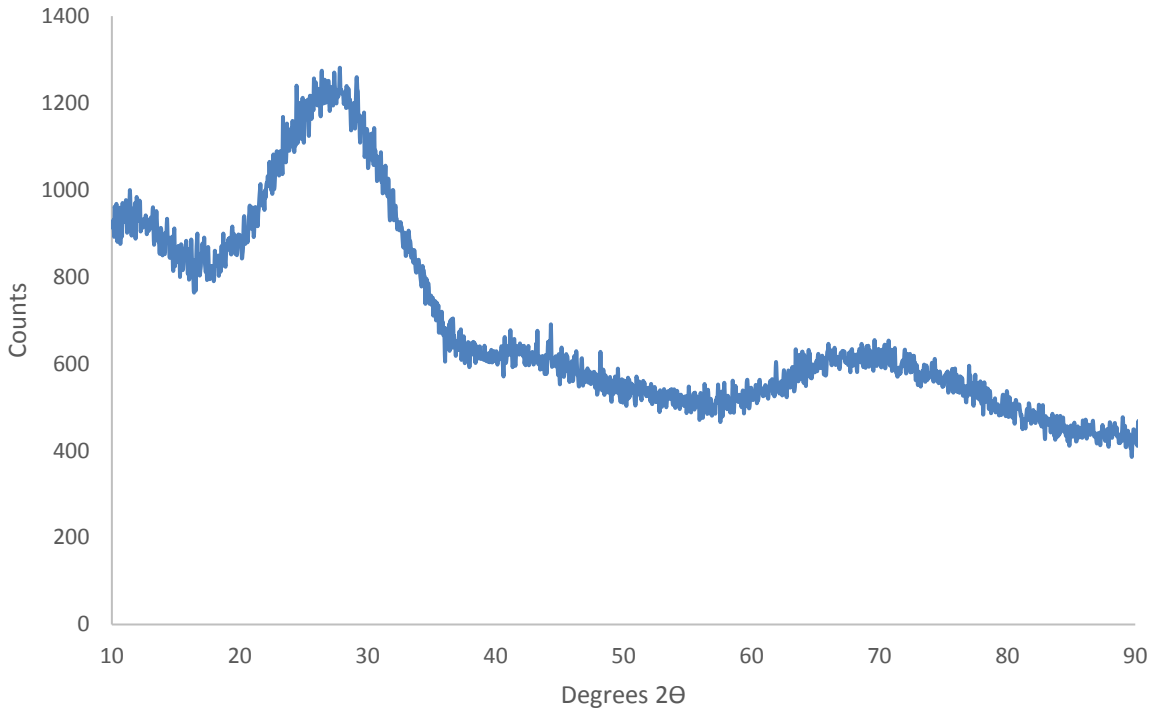

Figure 84: XRD trace for the blue/green phase for sample PF-HMS showing an amorphous trace and absence of crystalline peaks, revealing this to be purely glassy.

EDX analysis of the glasses, presented in Table 34, was chosen to analyse areas of different colours in the glass to observe any differences in composition arising from the colour difference. The compositions found for these different coloured areas were similar (Table 34) although these areas were found to be from portions of the glass where more ($3.48x10^8/m^2$ versus $2.7x10^7/m^2$), smaller pores (3-100 µm versus 50-200 µm diameter) had developed during treatment (Figure 85). Thus, it was concluded that the blue and green glass are the same glass but with different pore densities.

Table 34: Composition of the glass phases in oxide wt% for sample PF-HMS. Results are from 21 different point scans at various areas in the glass, the error represents either the standard deviation, the maximum/minimum of all the points, or the inherent error present in EDX (0.1 wt%) whichever of these was the largest.

Glass 1	**MgO**	**Al_2O_3**	**SiO_2**	**CaO**
Compound %	1.1	11.6	54.3	33.0
Error ±	0.1	0.1	1.4	1.5
Glass 2				
Compound %	1.3	11.0	54.2	33.5
Error ±	0.1	0.1	1.2	1.1

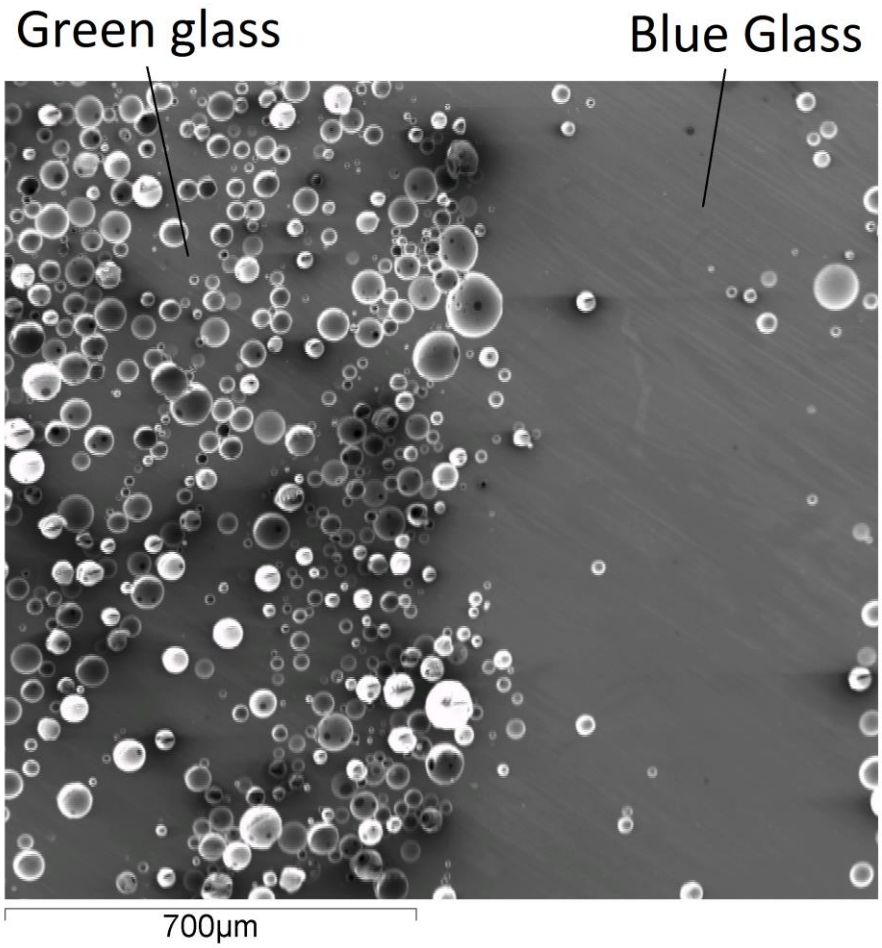

Figure 85: SEI of different glass regions. EDX analysis of the differences between the coloured areas for the glassy portion of sample PF-HMS was given in Table 34. Easily seen is the difference in pore density, with the green area displaying an increase in the number of pores compared to the blue portion. A distinct line between the two zones can be seen.

XRD traces for different regions of the metallic portion are shown in Figure 86and Figure 87. Figure 86revealed the possible presence of periclase, haematite, and an aluminium Iron alloy whilst Figure 87 suggests a magnesium-aluminium-iron alloy as the main phase with elemental nickel. Two XRD traces were necessary due to the large apparent inhomogeneity in the metallic portion of the sample, visual observation showed the entire metallic mass to be very different in colour and lustre.

As such several small portions were broken off and analysed using XRD, the traces shown are representative of the entire mass.

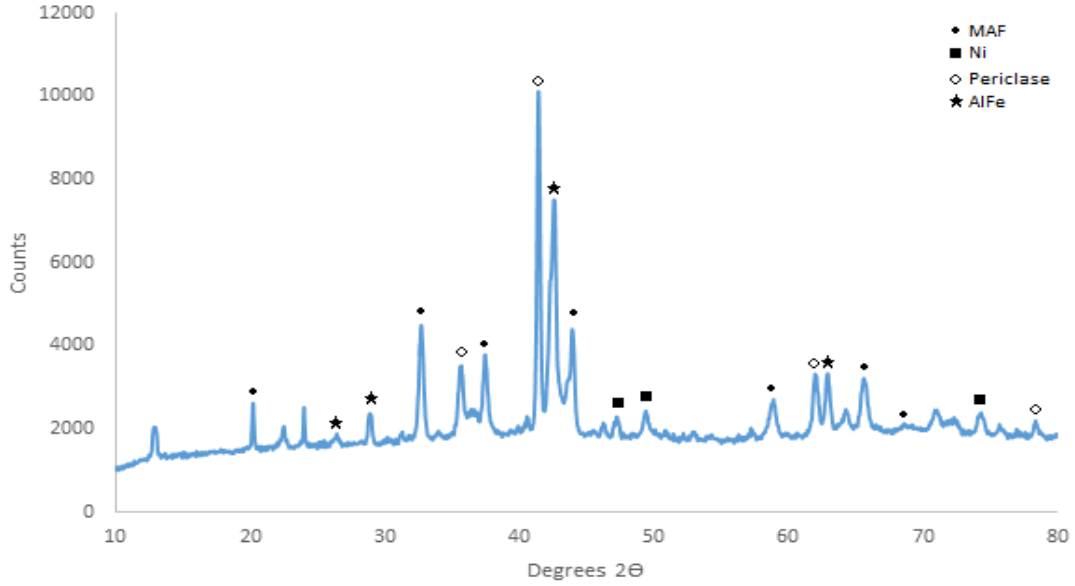

Figure 86: XRD for one part of the metallic portion of sample PF-HMS showing magnesium-aluminium-iron oxide (MAF)[PDF 01-074-1134], nickel (Ni)[PDF 00-001-1266], periclase [PDF 01-071-1176], and an aluminium iron intermetallic (AlFe) [PDF 00-050-0955].

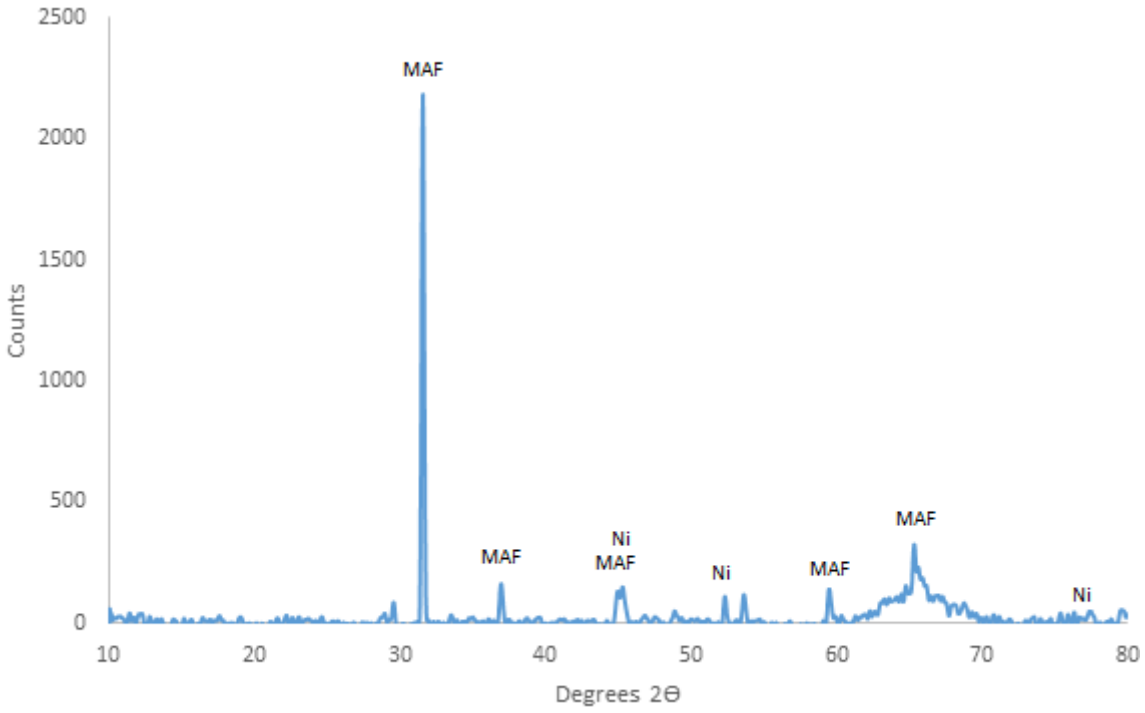

Figure 87: XRD for a second (different) part of the metallic portion for sample PF-HMS showing predominantly magnesium-aluminium-iron (MAF) with trace amounts of nickel [PDF shown in figure 74].

As would be expected from visual inspection and the XRD results, the metallic portion of the GCM was extremely varied in composition. EDX mapping (Figure 88and Figure 89) identified at least 10 different phases, mostly rich in iron. This is confirmed by the various EDX results shown in Tables 35-40, which are described below.

Initially the metallic portion was thought to contain a 3-4 unique phases, as such Figure 88was taken from a region thought to contain two phases due to BSE imaging (Figure 88a), however 4-5 phases could be observed based on the Mg, Fe, and Al distribution. This is easily visible in the Mg and Fe map (Figure 88b and d). Due to this result, a second map in a more complex area (by BSE imaging) was selected (Figure 89) showing that the metallic portion was made up of multiple phases, often with similar elemental components but differing ratios of each element (based on contrast), for instance an AlFe phase can be observed, however the contrast reveals that more than one type of AlFe phase is present. EDX mapping was favoured over SEI and BSE imaging for selecting EDX point scans to give more detailed information on the composition and is described further below.

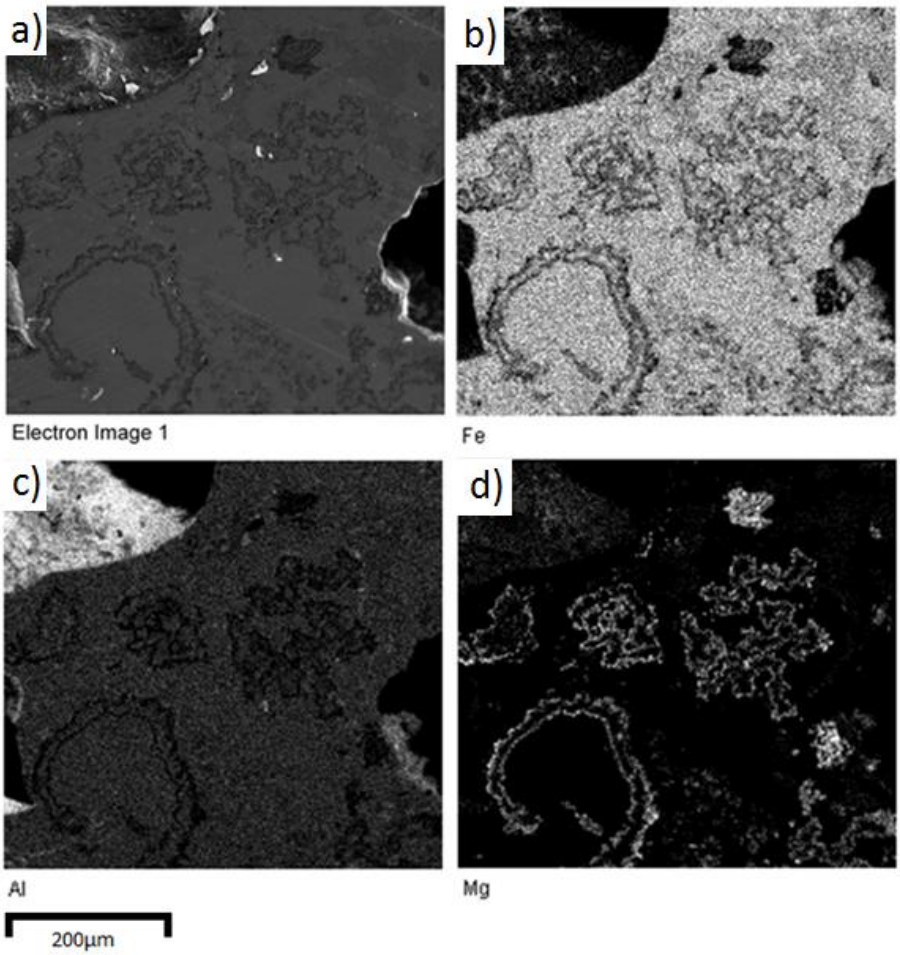

Figure 88: a) BSE image of the metallic sample with 3 EDX maps of the same area displaying the elemental distribution of Fe (b), Al (c), and Mg (d) for sample PF-HMS.

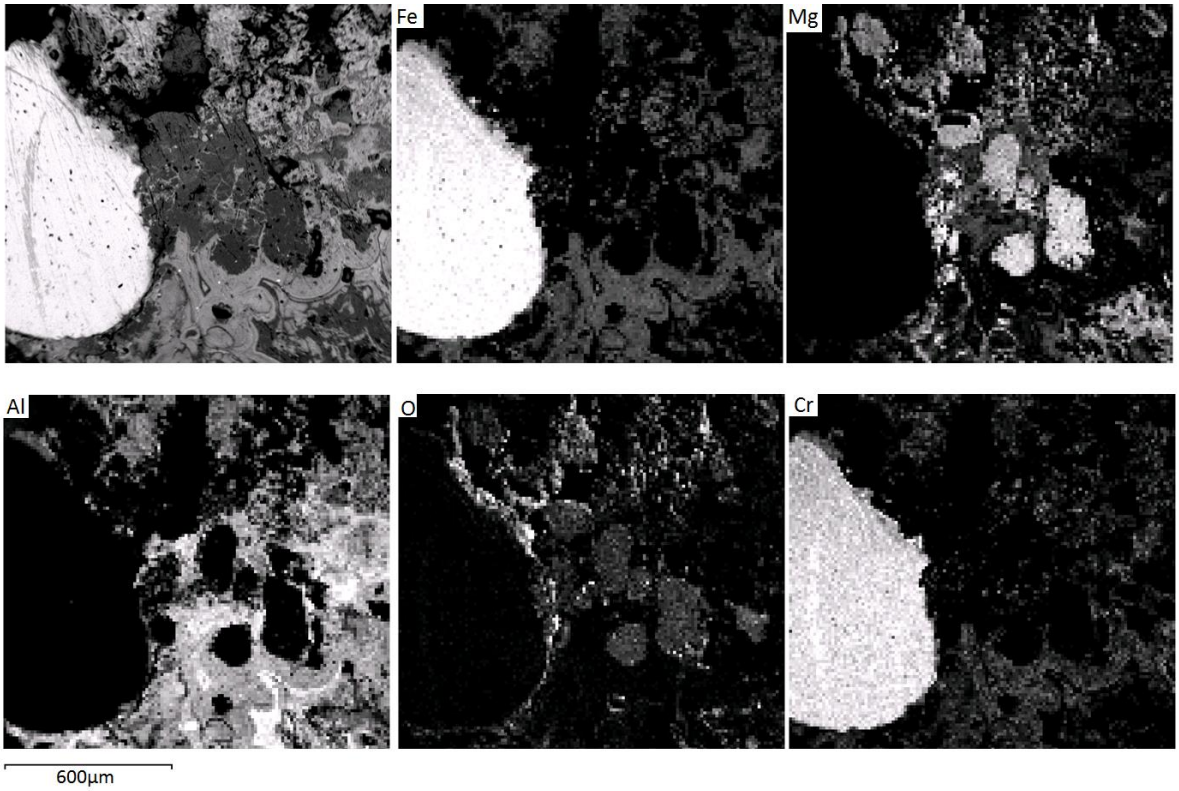

Figure 89: BSE image of another region of the metallic phase along with the distribution of Fe, Al, Mg, and O for sample PF-HMS.

A glassy phase existed between the bulk glass already discussed and the metallic portion. The composition of this glass varied depending on how close to the metallic portion it was. As a result of this it is not thought to be a different type of glass, rather it is likely to be the bulk glass enriched in waste elements due to its proximity to the metallic portion. This phase was approximately 10-50 µm wide and exhibits a large variation in composition depending on its distance from the metal/metal oxides along with the composition of those phases, as shown in Table 35. Due to the complex shape of the metallic areas, an accurate plot of how these elements decreased/increased as a function of distance from the metallic portion could not be established. However, in general, the glass closest to the metals had a larger concentration of magnesium, iron and chromium, with lower concentration of calcium and aluminium, as would be expected considering the large amount of Fe in the metal portion.

Table 35: EDX for sample PF-HMS showing the large composition differences in the glass nearby the glass/metal/metal oxide phases. The results are displayed in oxide wt%. BSE image from the EDX scan is shown in Figure 90.

	MgO	**Al_2O_3**	**SiO_2**	**CaO**	**Cr_2O_3**	**Fe_2O_3**
Mean (Oxide wt%)	2.7	10.4	54.3	30.9	0.9	0.9
Max.	10.4	13.6	59.9	33.4	1.7	3.0
Min.	1.2	9.2	45.3	23.8	0.0	0.0

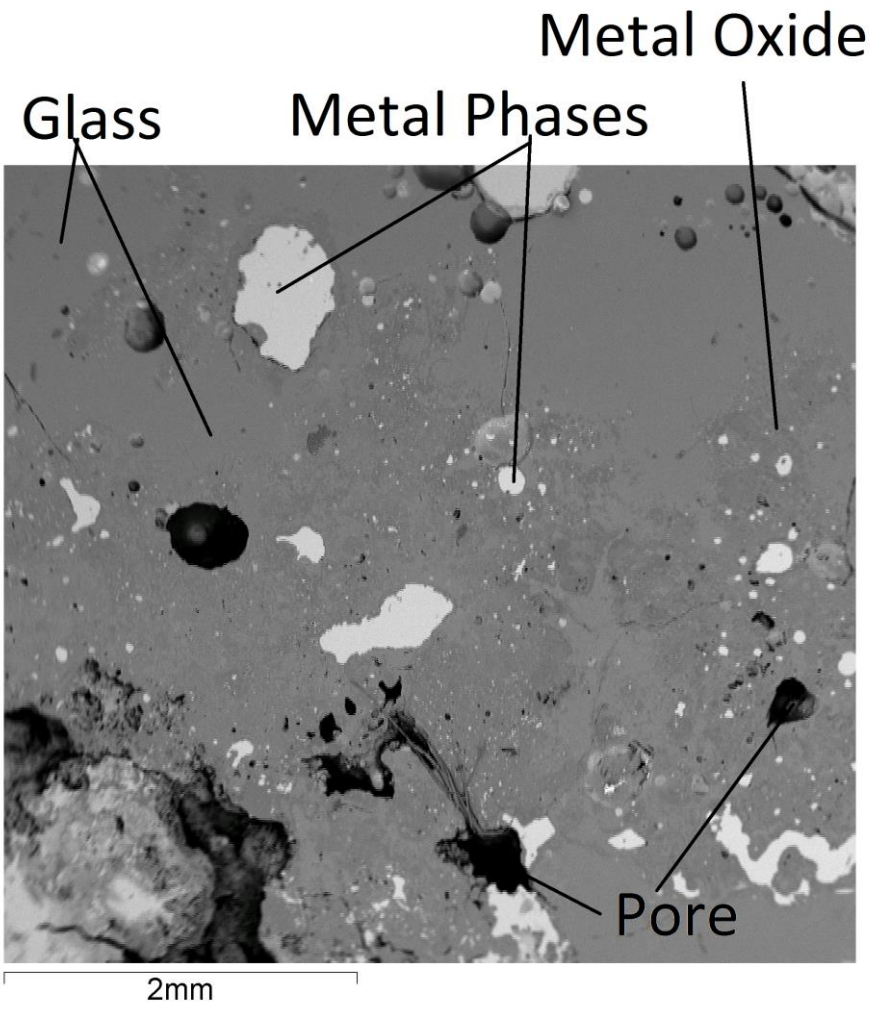

Figure 90: BSE image of the glass/metal/metal oxide boundaries for sample PF-HMS. The various phases were deduced using a combination of EDX results, specifically using oxygen content, and XRD data already shown. Bright spots on the BSE are metal phases, confirmed by low/zero concentrations of oxygen, the glass phase had a similar composition to that of the bulk glass already discussed, whilst the metal oxide phase was determined by a low silicon content such that glass formation was unfeasible.

Analysis of the metallic portion yielded many different phases and compositions, some showing limited oxygen implying they are metals, whilst others had significant amounts of oxygen showing either a metal oxide or glassy phase. A large distribution of these phases made complete characterisation difficult although the main phases discovered are discussed below by the major components present.

4.3.1.1 Al-Mg

At the metal-glass boundary an aluminium-magnesium oxide phases formed. Figure 91 shows the bulk glassy phase with various metallic phases (bright phase) surrounded by two unknown darker phases. EDX results (Table 36) confirm that the darker area is mainly composed of Mg and Al but in two different ratios, leading to two distinct variations.

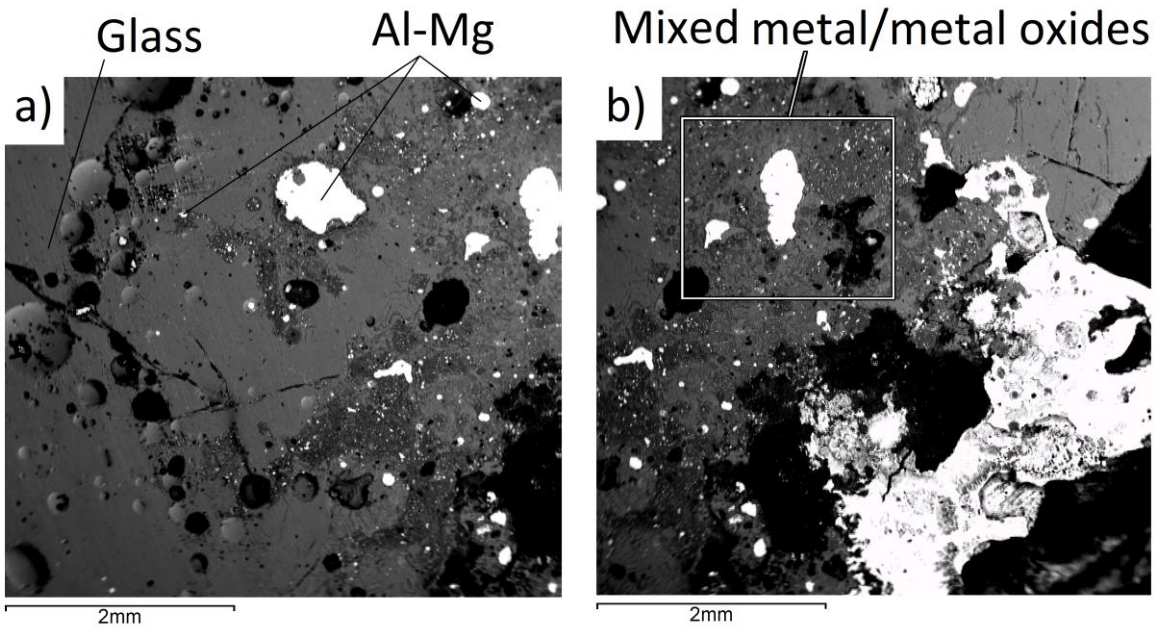

Figure 91: a) BSE image of the areas investigated for sample PF-HMS bordering the glass surrounding the metallic area. b) BSE image taken further into the mixed metal/metal oxide portion. The label "Al-Mg" identifies some of the areas identified by EDX as Al-Mg phases (Table 36).

Table 36: Composition of the two Al-Mg phases detected in oxide wt% for sample PF-HMS, EDX found the presence of oxygen indicating these were oxygen containing phases. Error is either the standard deviation over 20 similar points, or the inherent error present in EDX analysis (0.1 wt%), whichever was the greater.

	MgO	**Al_2O_3**	**SiO_2**	**CaO**	**Cr_2O_3**	**Fe_2O_3**
Al-Mg 1						
Compound %	25.9	71.7	0.8	0.6	0.1	0.9
Error ±	0.2	1.2	0.4	0.2	0.1	0.2
Al-Mg 2						
Compound %	42.8	50.4	2.0	1.5	1.0	2.3
Error ±	0.7	3.4	1.1	1.0	0.8	0.8

As has already been established, many phases were found to exist in the metallic portion with different morphologies, and a large variation in the minor elements content. Many of these phases were present as small spherical particles ranging from 5-100 µm in diameter, however some were present in more complex shapes. Several phases were consistent in composition when analysing only the major element(s) which usually appeared as either a two or one component system with minor elements. Discussed below are those that were the most common, and thought to make up most of the entire metallic waste-form as non-oxides, but should not be considered to be the remainder of phases present in the sample.

4.3.1.2 Al-Fe

EDX revealed that Al-Fe phases with small amounts (1-7 wt%) of other elements (Si, Mg, Ca, and Cr) were widespread. These were mostly present as many small 5-10 µm diameter spheres but they also occurred as a mixture of varying amounts of Al and Fe shown in Figure 92. In addition, they had varied composition, both the ratio of Al-Fe and the content and concentration of minor elements varied, more easily seen in Table 37, as the Al and Fe distribution appears as either an Al enriched phase or an Fe enriched phase. Multiple EDX scans of the two apparent Al-Fe phases revealed a tendency for either a 3:2 or 3:7 ratio of Al:Fe, this ratio was consistent throughout the material. It was repeatedly seen (Table 37) that the 3:2 Al-Fe tended to have more magnesium than the 3:7 Al-Fe, however the 3:7 Al-Fe tended to have almost double the concentration of Cr by wt%.

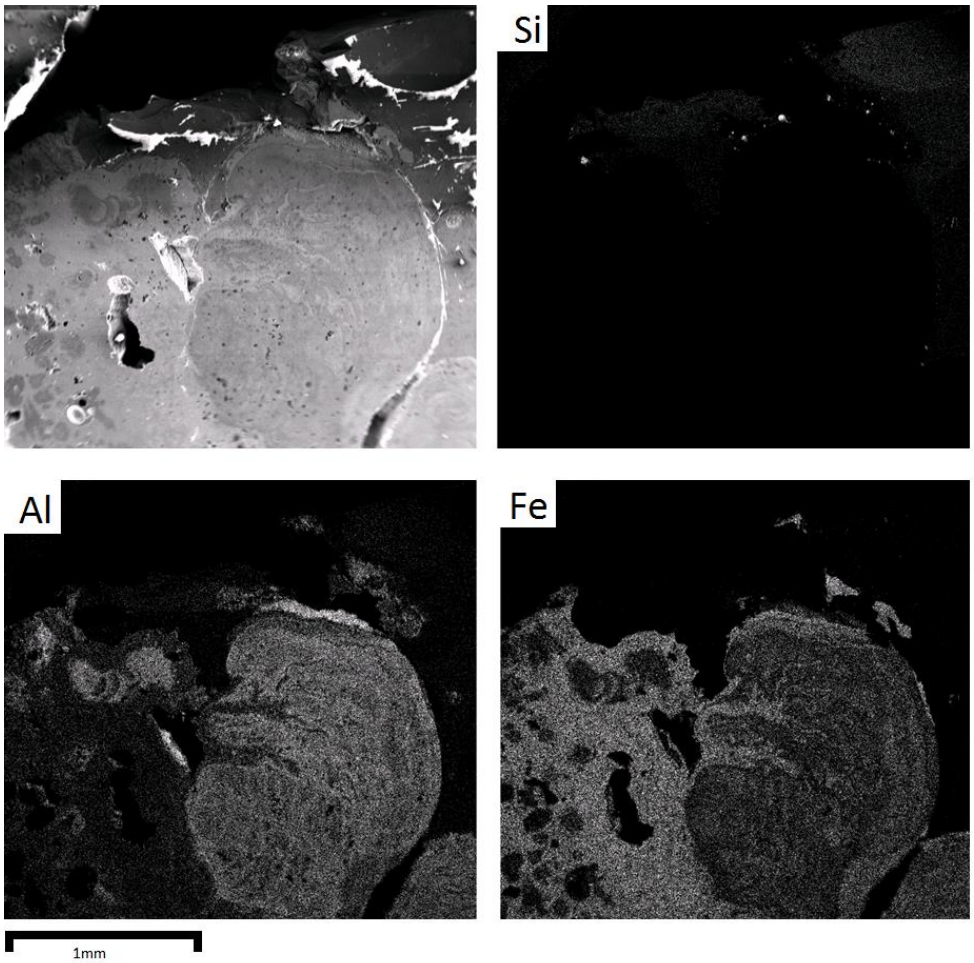

Figure 92: BSE image for sample PF-HMS with accompanying EDX maps for aluminium, iron, and silicon. The complexity of the composition of these phases is observed, although two Al-Fe phases can be clearly seen, small compositional fluctuations occur within each of these phases, most easily observed in the aluminium enriched particle.

Table 37: Composition of the two Al-Fe phases found for sample PF-HMS. All results are in wt%. Error is displayed as the standard deviation of 20 points, or the inherent error in EDX analysis (0.1 wt%), whichever was greater.

	Mg	Al	Si	Ca	Cr	Fe
Al-Fe 1						
Wt %	1.8	51.9	1.2	0.3	5.5	39.1
Error ±	0.6	2.0	0.3	0.1	0.2	1.3
Al-Fe 2						
Wt %	0.1	24.0	1.6	0.1	9.6	64.6
Error ±	0.1	5.3	0.1	0.1	0.3	5.0

4.3.1.3 Ca-Si

Whilst not as common across the entire material as the previous compositions discussed, portions of this phase existed as large particles with no definite shape, with a typical width of 0.5-1.5 mm (Figure 93), their composition is provided in Table 38. This phase was almost always embedded in a darker phase, identified as the Mg-Al oxide phase previously discussed.

Table 38: Composition of the Ca-Si oxide phase detected for sample PF-HMS, results in wt%. Error is either the standard deviation from 15 points for Ca-Si 1, 20 points for Ca-Si 2 or the inherent error present in EDX analysis (0.1 wt%) whichever was the greater.

	Na_2O	MgO	Al_2O_3	SiO_2	CaO	Cr_2O_3	Fe_2O_3
Ca-Si 1							
Wt%	0.0	6.0	6.8	20.6	65.1	0.6	0.9
Error ±	0.1	0.5	1.9	0.4	2.7	0.1	0.5
Ca-Si 2							
Wt%	0.1	1.8	10.2	39.6	46.3	1.1	1
Error ±	0.1	0.7	0.9	1.9	1.3	0.8	0.7

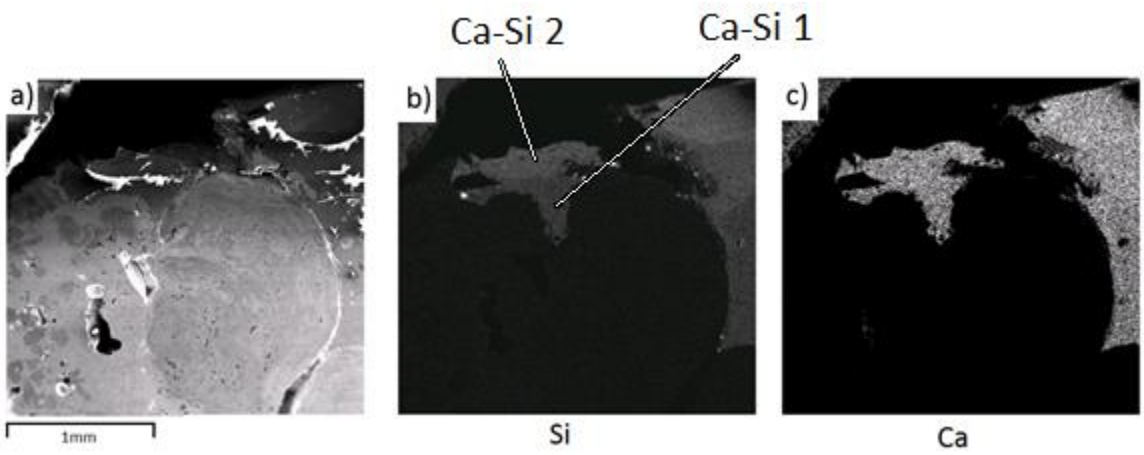

Figure 93: a) BSE image (extension to Figure 92) for sample PF-HMS, with the distribution of b) silicon, and c) calcium, showing the location of the Ca-Si phases, with composition reported in Table 38.

4.3.1.4 Fe based

Several metallic iron alloys were found, characterised by having a wt% of Fe greater than 70%, all were similar in appearance (Figure 94). However, little consistency was found in the concentration of the remaining elements. Over 50 different particles were analysed at various locations throughout the sample, with each new particle displaying a noticeable change in the concentrations of Mg, Ca, Al, and to some extent Si. Due to this, the results are given as an average, maximum and minimum, a 4th result has also been added, and represents the number of "groups" of particles with similar amounts of that element. This result is from the number. of unique averages, for instance calcium displayed 5 recurring averages, 1 wt%, 7 wt%, 12 wt%, 17 wt%, and 24 wt% (±1.5 wt% for each average) over the 50 points analysed, no points outside this range were present.

Table 39: Composition of the various Fe phases detected for sample PF-HMS. Results in wt%. Elements below 1 wt% are not included due to intensities below instrument error for this set of results.

	Mg	**Al**	**Si**	**Ca**	**Cr**	**Fe**	**Ni**
Average (wt %)	3.7	7.8	2.4	0.6	11.2	70.5	3.8
Maximum	17.9	10.5	9.1	5.7	16.9	80.0	4.7
Minimum	0.0	0.5	1.6	0.0	8.1	60.5	3.0
Groups	5	2	3	3	N/A	N/A	N/A

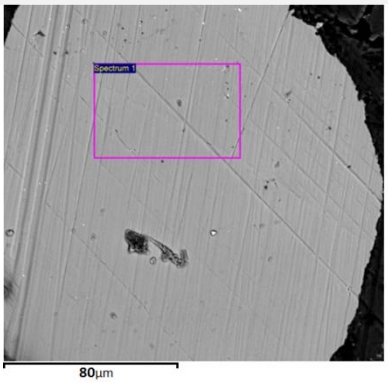

Figure 94: SEI showing the typical Fe phase in the metallic portion of sample PF-HMS, the composition of which is shown in Table 39.

One consistent Fe phase was detected, comprising of mostly iron and chromium, with low levels of other elements, shown in Table 40.

Table 40: EDX analysis of a mainly Iron-Chrome phase for sample PF-HMS. Error is given as standard deviation or the inherent error in EDX analysis (0.1 wt%), which ever was the greater.

	Al	Si	Ca	Cr	Fe
Wt%	3.0	2.4	0.3	7.9	86.5
Error ±	1.1	0.7	0.1	0.9	2.6

4.3.2 Plasma Furnace-Asbestos

XRD (Figure 95) from the PF-Asb sample suggests the existence of crystalline diopside ($MgCaSi_2O_6$), while a small amorphous hump was also observed. The peaks however, did not fully match the suggested phase due to slight shifts in peak locations (±1, 2Θ) and in intensities (±10%) which suggest that this phase is more complex then pure diopside, with some degree of substitution of magnesium and calcium with iron and aluminium, as can be seen in the EDX results presented in Table 41. This is discussed in more detail in the discussion section on this sample (section 5.5).

Three phases were identified using BEI (Figure 96), a crystalline phase made apparent by its morphology, small spherical particles (typically 2-5 µm diameter) which appeared bright under BEI suggesting these are either metallic or atomically denser than the surrounding material. As XRD showed a glassy phase was present, it can be reasonably assumed the matrix was amorphous.

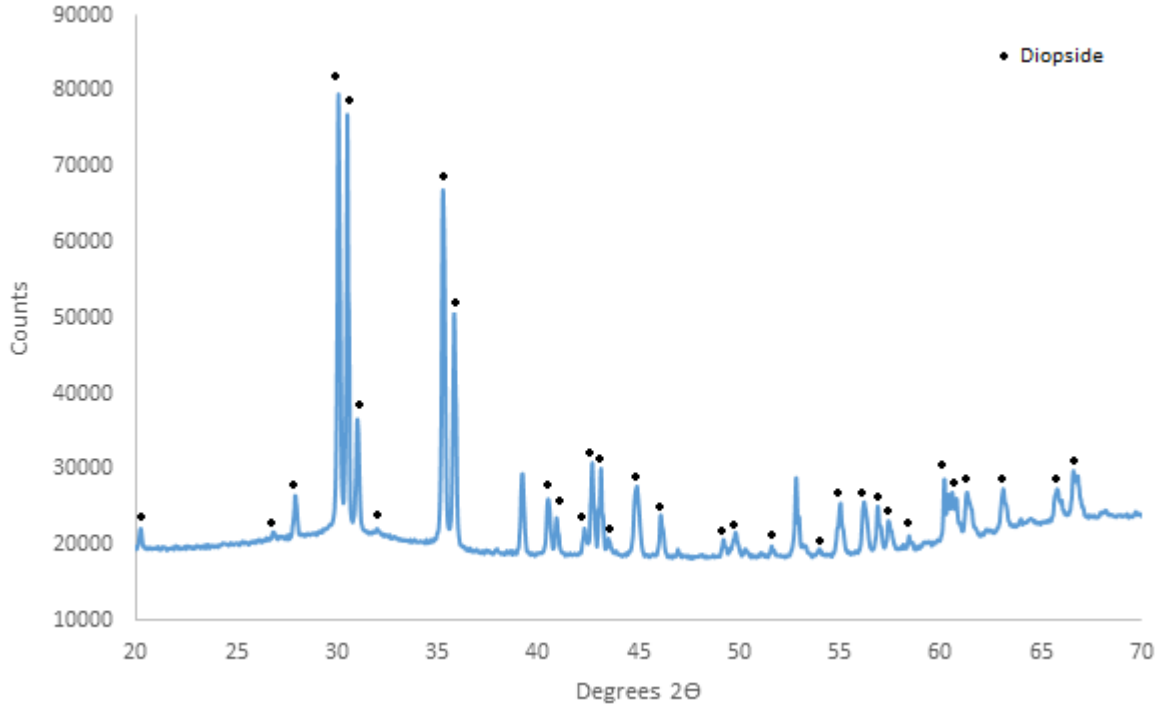

Figure 95: XRD for sample PF-Asb showing the peaks observed for a powdered sample. All the Fe-diopside [PDF 00-025-1217] peaks were present with the missing peaks attributed to the bright phase. The small amounts of this phase would be enough to mitigate the any major peaks from the iron phase as there was some degree of overlap. Unmarked peaks at 39.1 and 52.8 2Θ were not attributable to any phase (with the elements present in the sample).

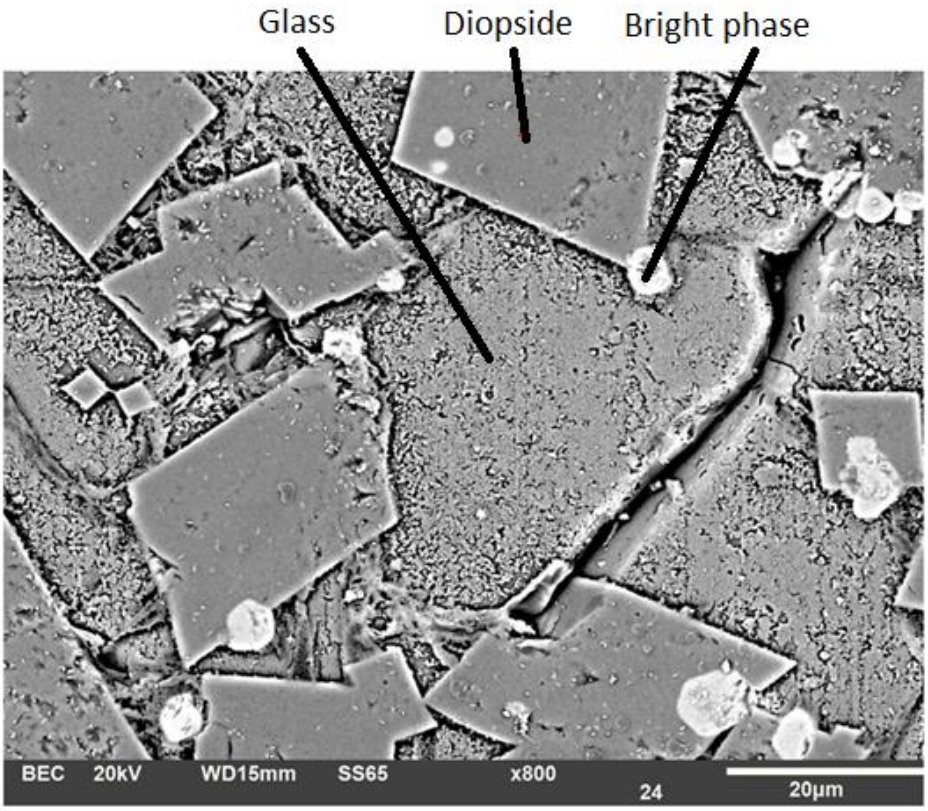

Figure 96: BSE image of sample PF-Asb, representative of the entire sample and showing three different phases.1) the main crystalline phase diopside. 2) Glassy matrix. 3) the bright phase,suspected to be metallic in nature, often forming at the edge of the diopside, evident in this figure.

EDX measurements of the glass, bright phase, and crystalline phases composition are presented in Table 41. EDX found that the bright phase was mainly composed of iron (66 wt%) with large amounts of chromium (13 wt%), the rest consisting of small amounts of magnesium and aluminium (1.5 and 4.3 wt% respectively). Due to the complete lack of oxygen detected, this is most likely unreacted metal waste.

Table 41: Composition of the diopside and glassy phase, as determined by EDX for sample PF-Asb. results for the glass are displayed as Oxide wt%, whilst results for diopside and the bright phase are shown in wt%, no oxygen content was provided for diopside as it varies from sample to sample due to contamination from dust particles and biological contamination from handling.

	Na_2O	MgO	Al_2O_3	SiO_2	CaO	Fe_2O_3
Glass						
Compound %	1.4	0.7	11.2	43.5	35.5	7.6
Error ±	0.1	0.1	0.1	0.3	0.2	0.2
Diopside	**Na**	**Mg**	**Al**	**Si**	**Ca**	**Fe**
Wt %	0.1	3.4	9.6	26.9	36.4	23.6
Error ±	0.1	0.1	0.3	0.3	0.2	0.4
Bright phase	**Cr**	**Mg**	**Al**	**Si**	**Ca**	**Fe**
Wt %	13.4	1.5	4.3	6.0	8.2	66.6
Error ±	1.2	0.7	1.0	0.5	1.3	2.8

4.3.3 Plasma Furnace-High Metal Surrogate 2

Visual inspection of the PF-HMS2 wasteform showed two portions of differing composition, one that consisted of various undissolved metals/metal oxides, and one that appeared glassy due to its green translucency similar to PF-HMS described in section 4.3.1. The metallic portion made up less than circa 5% by volume of the total wasteform received. For this reason, the metallic portion results are not included.

SEI (Figure 97) showed the wasteform to be composed of only one phase, which had a translucent green appearance and was thus presumed to be glassy. XRD analysis of the bulk (Figure 98) confirmed it to be completely amorphous. Compositional analysis carried out by EDX is presented in Table 42 revealing the glass to have a low silica content (35 wt% SiO_2), a surprising result as low silica glasses tend to devitrify during processing unless a quick quench time is applied [194]. However, Higby et al. [195] found that the combination of Al and Ca with similar amounts of Si resulted in a stable glass due to compensating nature of the Ca^{2+} and AlO_4^- .

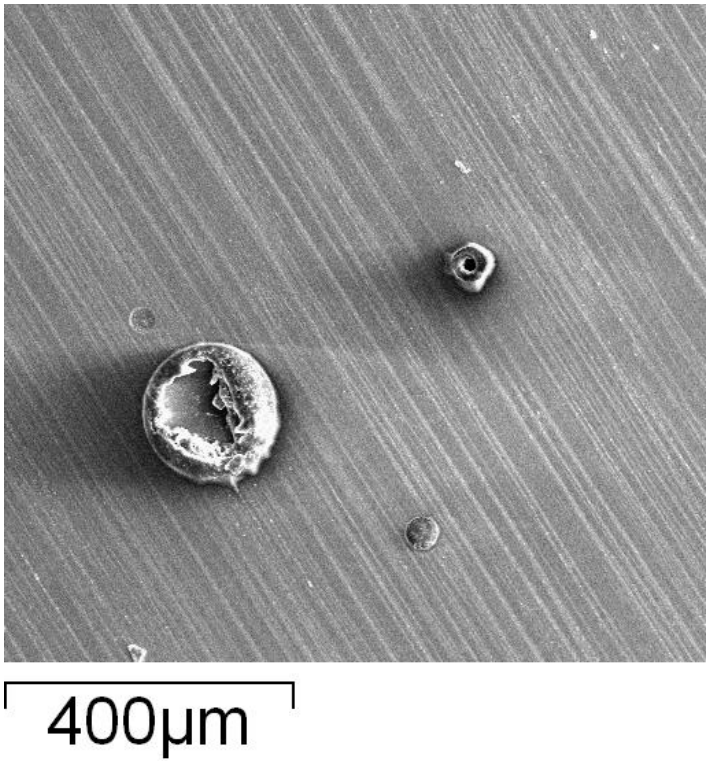

Figure 97: SEI of sample PF-HMS2 showing a homogenous sample without any phases present some contamination was present collecting in pores on the sample.

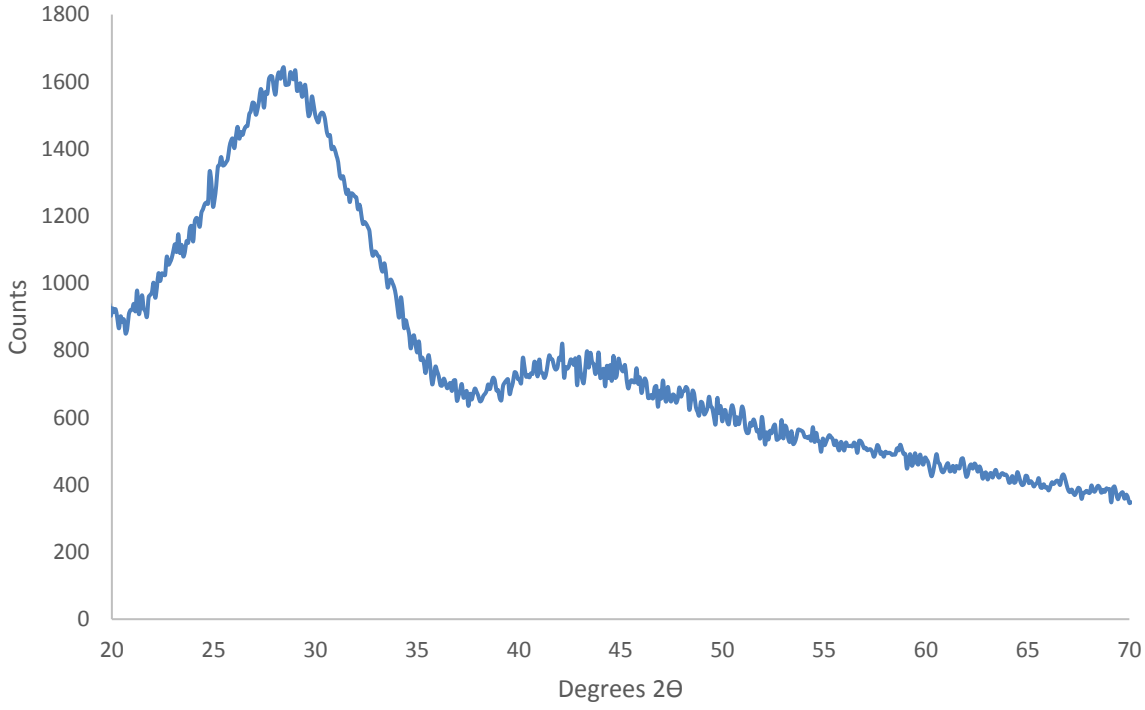

Figure 98: XRD trace of the powdered sample PF-HMS2, showing a characteristic amorphous hump and no crystal peaks showing the portion received was purely glassy

Table 42: Composition of the glass in compound wt% for sample PF-HMS2.Error is either the standard deviation over 20 points, or the inherent error of EDX (0.1 wt%) whichever was the largest.

	MgO	Al_2O_3	SiO_2	CaO	La_2O_3	Ce_2O_3
Compound %	1.9	12.3	35.6	29.2	8.3	12.8
Error ±	0.1	0.2	0.4	0.3	0.3	0.3

4.4 Plasma Furnace Corrosion Study

Corrosion analysis of the ILW wasteforms is vital to assessing their potential for surface storage, or sub surface disposal and multiple tests are performed on new matrices for wastes before they can be implemented as a wasteform. To help with this assessment detailed SEM/SEM-EDX analysis of both the surface and of cross sections were performed on the corroded samples after 2,4,6,10, and 14 weeks of corrosion. Results from all these corrosion times are not displayed where no new developments in the corrosion progression were found.

4.4.1 Plasma Furnace-High Metal Surrogate

The purely glassy portion and the second crystalline portion of the PF-HMS sample were treated separately during corrosion experiments. Glass surface scans showed little change to the surface until a high magnification of around 100,000 at which point the surface displayed the image seen in Figure 99. This image was seen for all times in corrosion past 6 weeks (up until the maximum of 14 weeks), whilst these were not seen before 6 weeks this is thought to be due to lack of high magnification images performed at these corrosion times. As no surface effect was observed pre-corrosion, and due to the high magnification necessary to view this surface effect, the corrosion layer that formed must be extremely thin (much less than 1 µm) as other corrosion layers on other glassy samples (see section 4.2.3) at much lower magnification (500-1000x) were clearly visible. Further, the corrosion layer that formed is different than those observed on other glassy portions of other GCMs where the corrosion layer and glass were separate entities, easily distinguished using BSE imaging (e.g. Figure 72). The PF-HMS glass appears to have been selectively etched, whereby portions of the glass dissolved into solution, rather than having a compositional unique surface layer form.

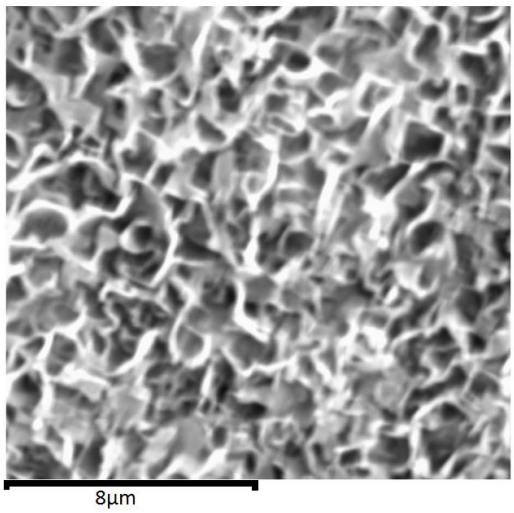

Figure 99:High magnification SEI of the surface of the glassy portion of PF-HMS after 6 weeks of corrosion showing the surface has a (non-spherical) porous appearance with sharp edges.

EDX of the surface (Table 43) showed little change to the uncorroded composition, with only a slight decrease in the minor elements; Mg, Cr, and Fe, this decrease is not unexpected although a noticeable decrease in calcium should have been observed due to the relative ease at which Ca (all alkali metals, and alkali earths) is likely to be removed during the leaching phase of glass corrosion (see section 2.4). This result is most likely due to the AlO_4^-/Ca^{2+} pairing that occurs in Al containing glasses which provides charge compensation up to charge neutrality (CaO/Al_2O_3=1) at which point the calcium begins to act as a modifier, causing NBO [195].

Table 43: Composition of the glass surface after 6 weeks of corrosion for sample PF-HMS. Error is either the standard deviation over 20 points, or the inherent error of EDX (0.1 wt%) whichever was the largest.

Glass surface	**MgO**	**Al_2O_3**	**SiO_2**	**CaO**	**Cr_2O_3**	**Fe_2O_3**
Compound %	0.8	10.3	56.8	31.0	0.8	0.7
Error ±	0.3	1.0	1.0	1.4	0.3	0.3

Depth profiling (Figure 100) confirmed that little change occurred to the main elements present in the glass i.e. calcia, silica, and alumina over all times investigated:

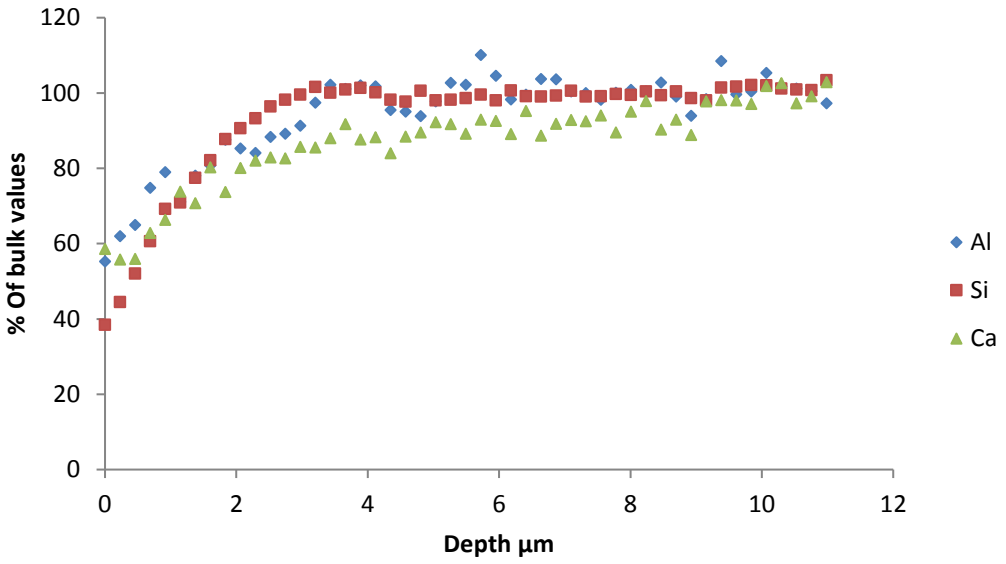

Figure 100: Average depth profile over all times investigated for sample the glassy portion of sample PF-HMS. Y axis represents the percentage of the value detected in the bulk of the specimen i.e. unaffected by corrosion.

All of the metallic portion of the sample suffered from severe corrosion, and after 2 weeks was reduced to a brown powder, making depth profiling impossible. This behaviour was seen for all corrosion times, and for all the metallic samples used regardless of differences in composition (due to the large inhomogeneity in the sample compositional differences were common). SEM analysis of the resulting powder is shown in Figure 101and was taken at high magnification to identify the morphology. EDX analysis (Table 44) found the composition varied greatly, however this was not reflected in the images found, only those such as shown in Figure 101were observed.

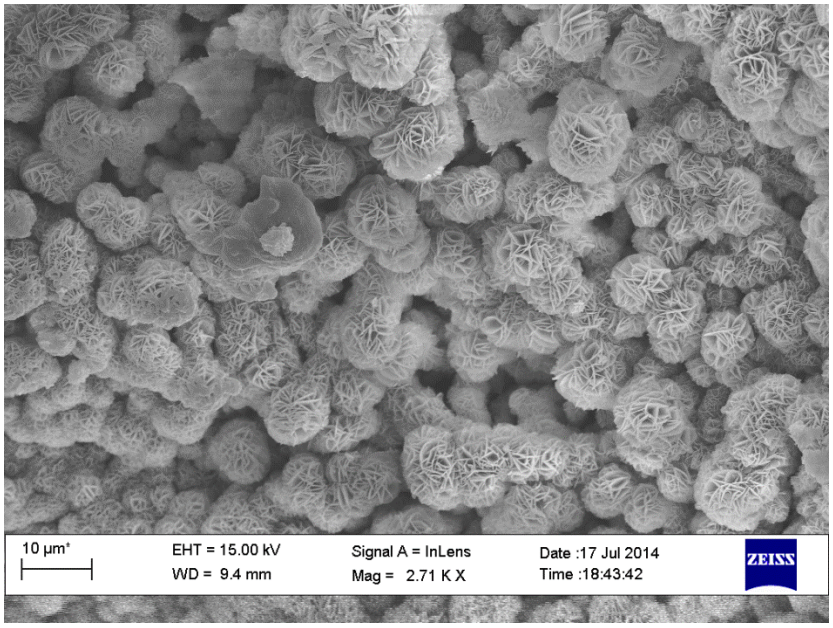

Figure 101: High magnification SEI of sample the metallic portion of PF-HMS after two weeks of corrosion showing how platelets had agglomerated into spheres whilst retaining a distinct platelet morphology giving an unual "coral" like structure.

Table 44: EDX of the remains of the crystalline portion of sample PF-HMS. Clearly seen is the variety in compositions from the maximum and minimum vales obtained over 30 different points. All results in wt%, Oxygen was present for all the samples but excluded as the exact amount was dismissible (see chapter 2.2.1).

	Fe	K	Na	Mg	Al	Si	Ca	Ti	Cr	Mn	Ni
Average (Wt%)	22.0	0.1	0.1	5.7	14.4	30.0	24.7	0.1	3.0	1.2	0.9
Maximum	84.2	0.2	0.2	10.7	26.0	50.0	49.0	0.7	9.5	4.8	2.8
Minimum	0.0	0.0	0.0	0.1	0.2	3.6	0.1	0.0	0.0	0.0	0.0

SEM-EDX of the small spheres (5-15 µm diameter, Figure 101) was not reliable due to the size, however a large amount (>60 wt%) of calcium and (30 wt%) oxygen was detected (remainder was made up of Al, Mg, Si, and Fe), and whilst the values cannot be used due to the error, it is clear that calcium makes up the bulk of these particles. This flower like morphology as small spheres has been observed in magnesium oxide [196] and calcium carbonate crystals [197], whilst no literature on a similar morphology for calcium oxide could be found. EDX cannot reliably determine the presence of carbon (see sections 3.3.1-3.3.3) thus it is possible that the calcium reacted with an as yet unseen carbon containing phase during corrosion producing a calcium carbonate microsphere.

Initial ICP-OES analysis of these samples found that all elements reached the upper limit for the standards used of 50ppm, a second round of tests using a larger concentration of standards were also found to reach the maximum of 100ppm. ICP-OES results are not displayed for this reason, whilst this result reveals that the concentrations of Al, Ca, Fe , Mg, Na, and Si all exceeded 100ppm (the highest standard concentration) after 2 weeks corrosion, calibration does not allow for meaningful values past the highest standard used (100ppm). This result was found for all corrosion times, and reveals that this portion of the waste is unsuitable for disposal.

4.4.2 Plasma Furnace-Asbestos

To assess the durability of the monolithic samples, MCC-2 tests as described in section 3.4, were performed every two weeks up to 10weeks. Surface scans (Figure 102) showed that precipitation had occurred, resulting in microcrystals distributed over the entire sample, as can be seen in Figure 102b). These crystals were usually associated with the diopside, providing a better template on which to crystallise than that of the amorphous structure present in the glass. EDX analysis of the microcrystal, diopside surface, and glass surface are shown in Table 45. The glass surface showed an increase in the concentration of Fe, but otherwise no noticeable change from pre-corrosion concentrations was observed, however diopside showed a decrease in the Fe content.

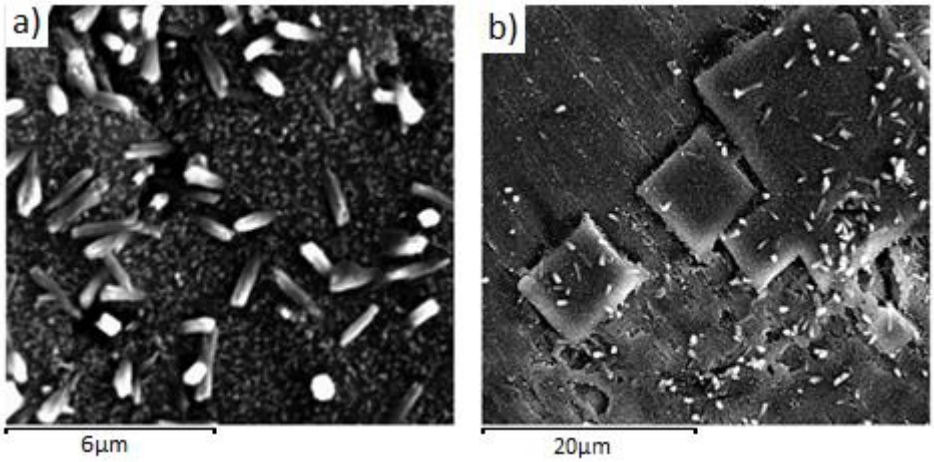

Figure 102: SEI of the corroded surface following 4 weeks of corrosion for sample PF-Asb. (a) High magnification image of corroded diopside crystal with microcrystals forming on top. (b) Distribution of microcrystals over diopside and glass.

Table 45: EDX of the corroded surface of the glass and diopside, along with the EDX of the small crystals shown on the surface. The size of these crystals approached the spatial resolution of EDX for this reason results have a large error; this could not be calculated instead the standard deviation of 30 point scans is given. Note, results for diopside surface are given in elemental wt% rather than oxide wt%.

Micro crystal	**MgO**	**Al_2O_3**	**SiO_2**	**CaO**	**Fe_2O_3**	**Na_2O**
Compound %	3.1	11.2	36.0	32.9	16.8	-
Error ±	1.2	3.2	6.7	2.4	1.7	-
Diopside surface	**Mg**	**Al**	**Si**	**Ca**	**Fe**	**Na**
Compound %	3.3	10.2	36.7	32.1	17.8	-
Error ±	0.6	1.3	2.9	2.3	2.1	-
Glass Surface	**MgO**	**Al_2O_3**	**SiO_2**	**CaO**	**Fe_2O_3**	**Na_2O**
Compound %	0.9	10.6	43.1	35.4	9.1	1.8
Error ±	0.1	0.3	0.7	0.7	0.4	0.8

SEM images from the surface (Figure 102 a), and cross sections (Figure 103), revealed the glass and diopside were at different heights, the diopside protruding from the glassy matrix. This indicates that the glass has been corroded more than the diopside leading to the difference in “height” between the two.

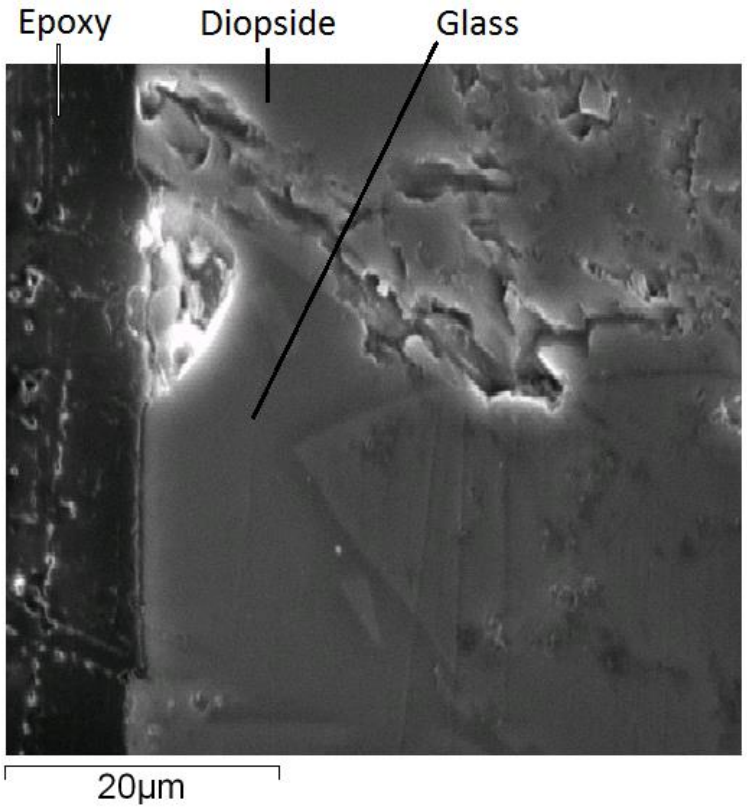

Figure 103: BSE image of sample PF-Asb after 4 weeks of corrosion. Diopside is observed to protrude from the glass this confirms that the diopside had higher corrosion resistance due to the difference in height.Also obserable is a thin corrosion layer.

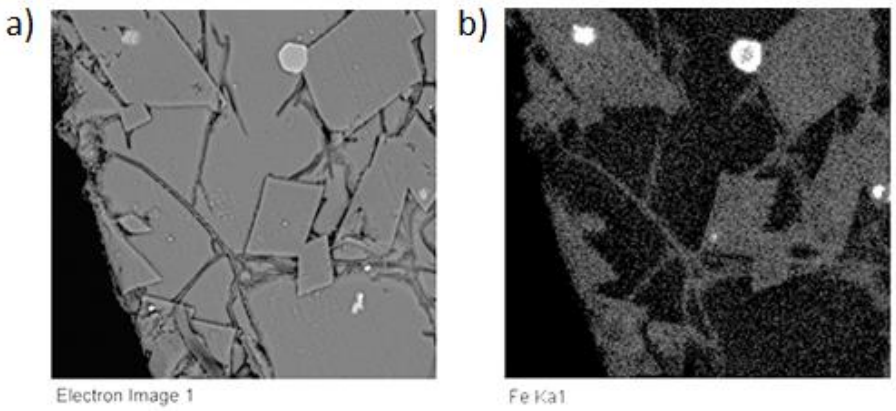

Figure 104: BEI of PF-Asb sample (a) along with the EDX map of iron (b). Cracks occur in the glass, extending from the diopside which contains an iron phase.

Figure 104shows that the glass has cracked during leaching and EDX mapping shows the presence of iron in these cracks, no other elements were found. This cracking was seen to originate from the diopside extending outwards until it intersected another crack or diopside crystal. This was repeatedly seen throughout the sample i.e. it was not isolated to one particular area in the sample, and repeated tests showed the same result. The crack tips were generally blunt; however, some sharp cracks were observed, both of these can be seen in Figure 104.

EDX depth profiles (Figure 105 and Figure 106) of the glass revealed an iron enriched surface layer becoming increasingly enriched with the length of time of the experiment. At week 4 (Figure 105a) iron concentrations had reached 160% bulk values (±20%) over 1.5 μm with all other elements showing a decrease in concentration to approximately 40% (±10%) over 1.5 μm. No indicators of a gel layer were present, such as a "shelf" of silicon, or rise in other elements (Al, Ca, O). By week 6 (Figure 105b) the concentration of iron at the surface was 120% bulk concentrations over 2 μm, however in areas this value was ~800%, this result is where the depth profile intersected an iron filled crack. The concentration of other elements at week 6 had not changed from week 4. Week 10 (Figure 106) revealed that iron surface concentrations were 160% bulk concentrations, similar to week 4, however the effected depth had increased from 1.5 μm to 3 μm. The other elements effected depth had extended to 3 μm, however it could be separated into two zones, from 0.5-3 μm a constant decrease from 100-80% bulk values was observed, whilst from 0.5-0 μm the concentration decreased to 40%. The profile at 10 weeks is indication that a corrosion layer had developed (0-0.5 μm) followed by a leached layer (0.5-3 μm).

ICP results (Table 46) showed that after 2 weeks, elements no longer increased in concentration, whether this is due to the iron enriched layer acting in a protective manner, or because crystallisation is occurring at a similar rate to leaching is unclear.

Diopside displayed an almost constant leached depth with no layers forming (Figure 107).

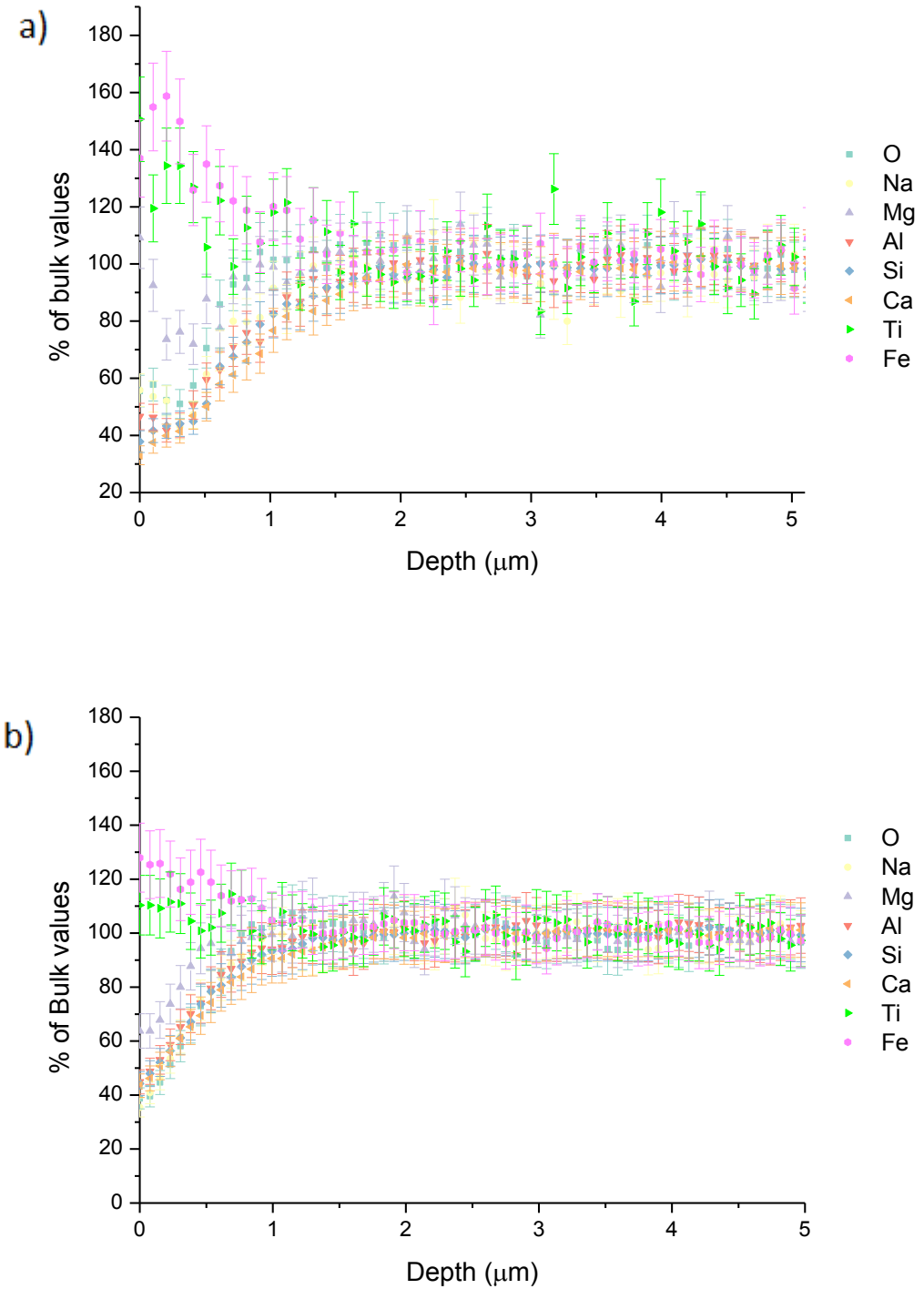

Figure 105: Depth profiles of PF-Asb after a) 4 weeks and b) 6 weeks of corrosion.

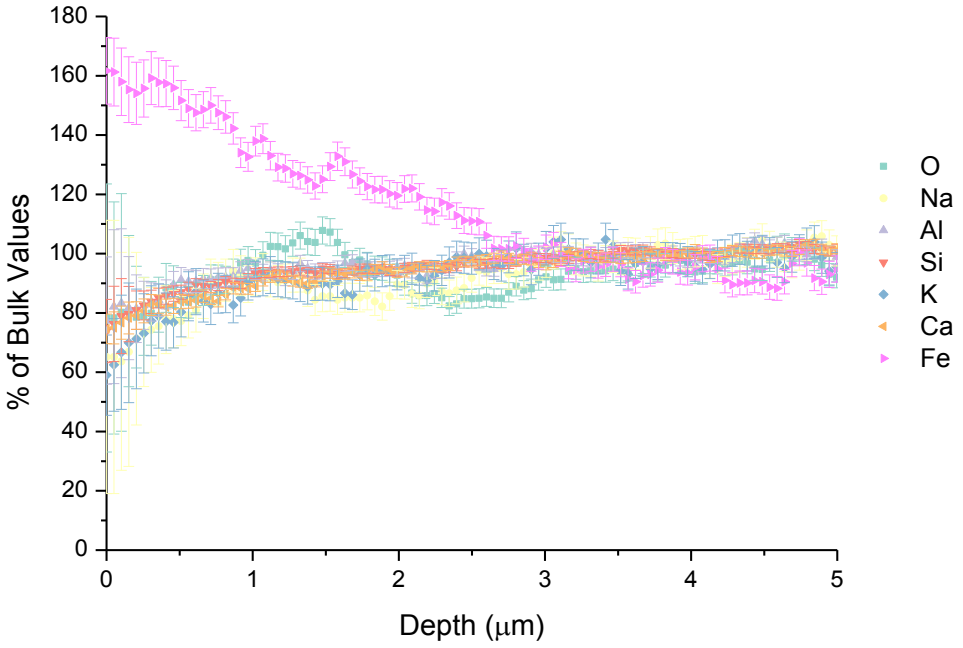

Figure 106:EDX line scan of glass in PF-Asb after 10 weeks of corrosion.

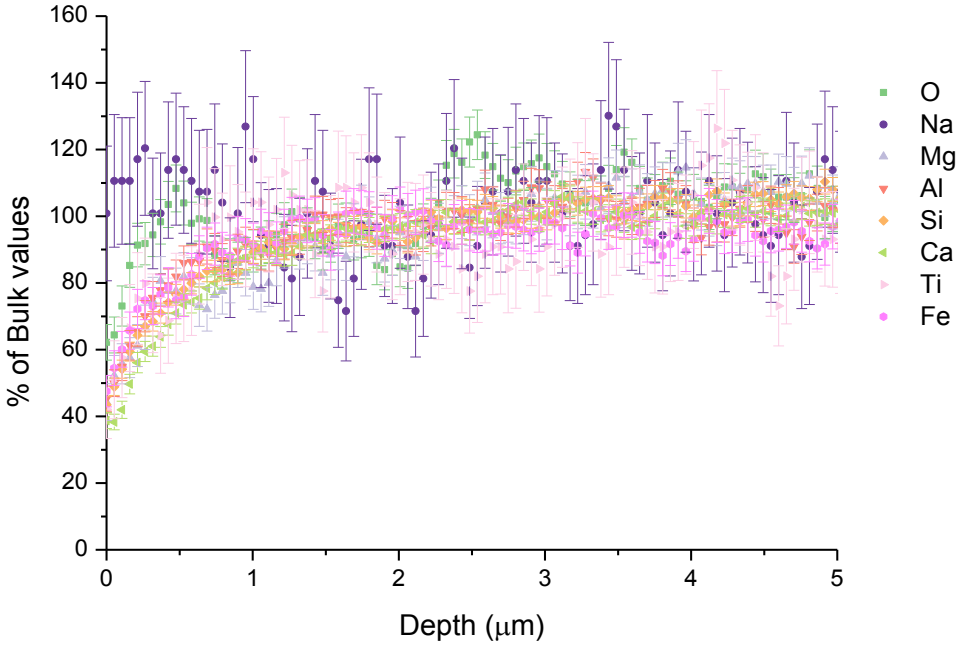

Figure 107: Diopside EDX line scan in PF-Asb at 4 weeks, this same profile was observed for all subsequent corrosion times.

Whilst images showed some sort of layer, EDX depth profiles gave no indication of such a layer, as can be seen from Figure 107.

The pH results (Figure 108) showed a typical profile for a glass with an immediate rise in pH as a result of leaching, followed by a drop due to the formation of protective layers reducing the number of leached ions in solution. ICP-OES results (Table 46) reflected this to some extent with a rise in ion concentration in solution for the first 6 weeks, as a result from stage 1 corrosion in glasses whereby leaching of elements is predominant (see section 2.4), followed by a drop. Calcium experienced the largest leaching, this result was not expected as sodium is typically released into solution in much greater quantities than calcium, however, the relatively low amounts of sodium in the wasteform accounts for this.

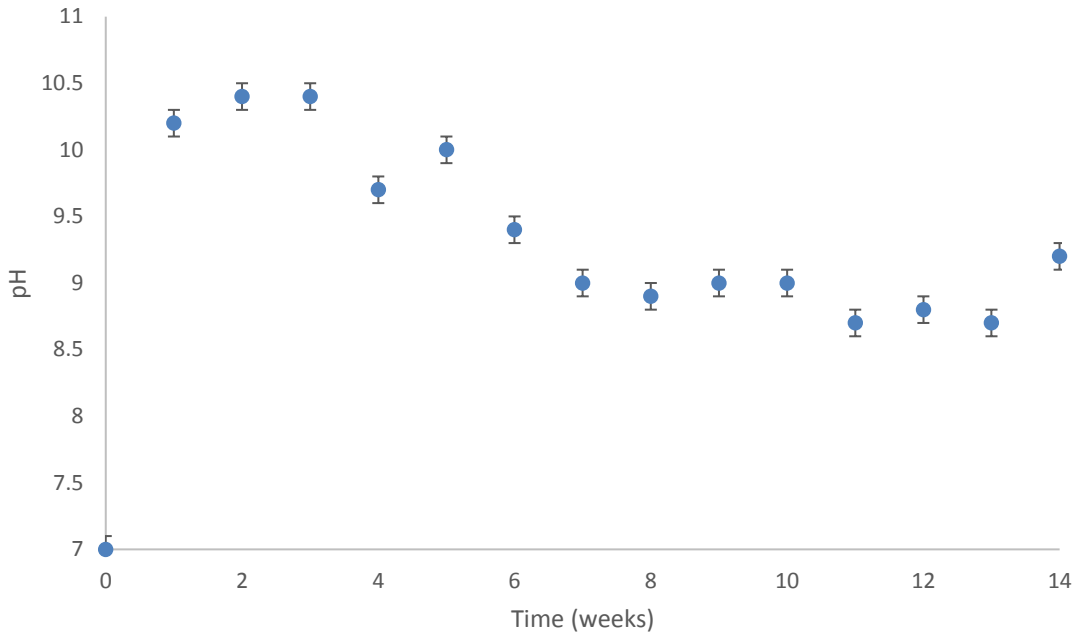

Figure 108: pH versus corrosion time (weeks) for sample PF-Asb up to 14 weeks. Error bars reported are either the reported error of the pH machine (0.1 pH value), or the difference between the maximum and minimum values found from repeat tests, whichever was the larger.

Table 46: ICP-OES (in ppm) results for various elements in solution over the corrosion time periods shown. Error is displayed as standard deviation of 9 aliquots over 3 samples only as these were larger than the systematic error of ICP-OES.

(ppm)	**Al**	**Ca**	**Fe**	**K**	**Mg**	**Na**	**Si**
2 Weeks	2.591	18.343	0.006	2.687	0.023	6.834	8.249
4 Weeks	5.132	17.343	0.045	2.358	0.060	3.884	12.996
6 Weeks	6.387	14.356	ND	ND	0.132	0.431	14.923
10 Weeks	5.514	19.907	ND	ND	0.070	7.286	10.625
14 Weeks	2.336	19.140	ND	ND	1.143	14.893	18.550
Error (Std Dev.)							
2 Weeks	0.061	0.105	0.129	1.572	0.002	0.168	0.052
4 Weeks	0.120	0.099	0.924	1.380	0.006	0.095	0.082
6 Weeks	0.149	0.082	0.004	-	0.014	0.011	0.095
10 Weeks	0.129	0.113	-	-	0.007	0.179	0.067
14 Weeks	0.055	0.109	-	-	0.119	0.365	0.118

NL_r rates for silicon and aluminium (Figure 109) revealed a steady decrease in the release rate for Al over 14 weeks and a decrease for Si up to 10 weeks, after which it rose slightly, most likely due to the increase in pH that occurred in the 14-week sample (Figure 108). This result generally indicates a good corrosion resistance, however, NL_r for Mg (Figure 110) indicated the opposite, a large increase was observed at 14 weeks. Mg was mainly found in the diopside phase, thus indicating a possible decrease in the corrosion resistance of this phase after 14 weeks. This coincides with the slight increase in Si release rates, now most likely attributable to the diopside phase rather than the glass. No increased corrosion of the diopside phase was observed in other analysis techniques.

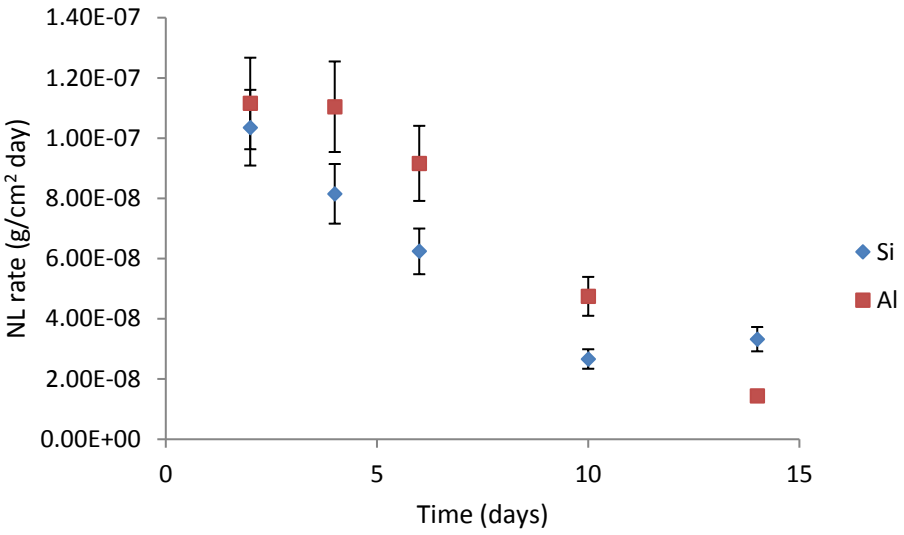

Figure 109: Normalised leach rate results for silicon (blue) and aluminium (orange). Both elements saw a decrease to the rate over time.Error is calculated based on the maximum/minimum value calulcated for that point.

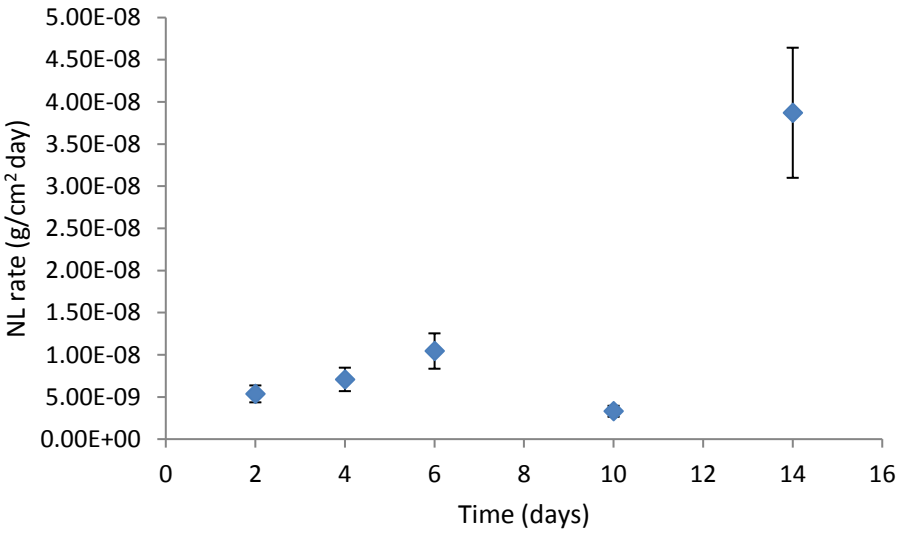

Figure 110: Normalised leach rate results for magnesium. Error is calculated based on the maximum/minimum value calulcated for that point.

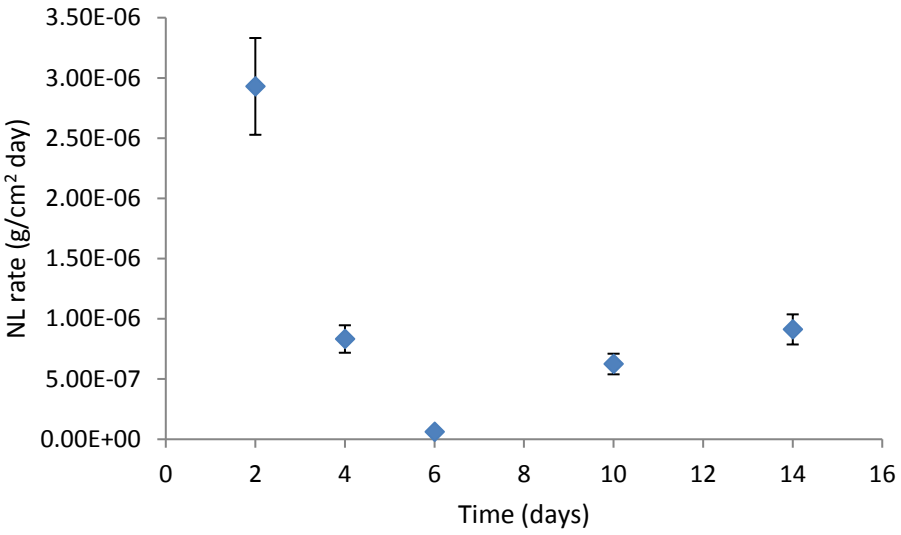

Figure 111: Normalised leach rate results for sodium. Error is calculated based on the maximum/minimum value calulcated for that point.

4.4.3 Plasma Furnace-High Metal Surrogate 2

No change to the PF-HMS2 sample was observed after 2 weeks' corrosion, however after four weeks some change had occurred to the attacked surface of the sample, displaying a "rough" layer (Figure 112) that easily came off. EDX analysis (Table 47) showed this layer to be depleted in calcium.

Table 47: EDX surface scans of the corroded surface of sample PF-HMS2 after 4 weeks, the pre-corrosion results are displayed for comparison. Results are shown as oxide wt%. Error is either the standard deviation over 20 points, or the inherent error of EDX (0.1 wt%) whichever was the largest.

	MgO	**Al_2O_3**	**SiO_2**	**CaO**	**La_2O_3**	**CeO_2**
Compound %	2.20	9.05	25.47	11.90	20.43	30.63
Error ±	0.33	0.67	2.34	1.06	2.15	1.66
Pre-Corrosion	1.92	12.25	35.62	29.18	8.26	12.77

After 6 weeks, the surface layer was fully developed and showed cracking, most likely from the procedures for SEM preparation. A low magnification image of the cracked surface layer and a similar image of an area where the surface layer had completely spalled off are shown in Figure 112a and b respectively. They reveal that underneath the gel layer, grinding marks remain from the original glass' surface. It is unclear whether the layer is not a typical gel layer and is a precipitated layer instead, or whether corrosion progressed such that the underlying glass retained the grinding relics; if all the glasses surface was attacked evenly the surface topography before corrosion (compare with Figure 97) would remain after.

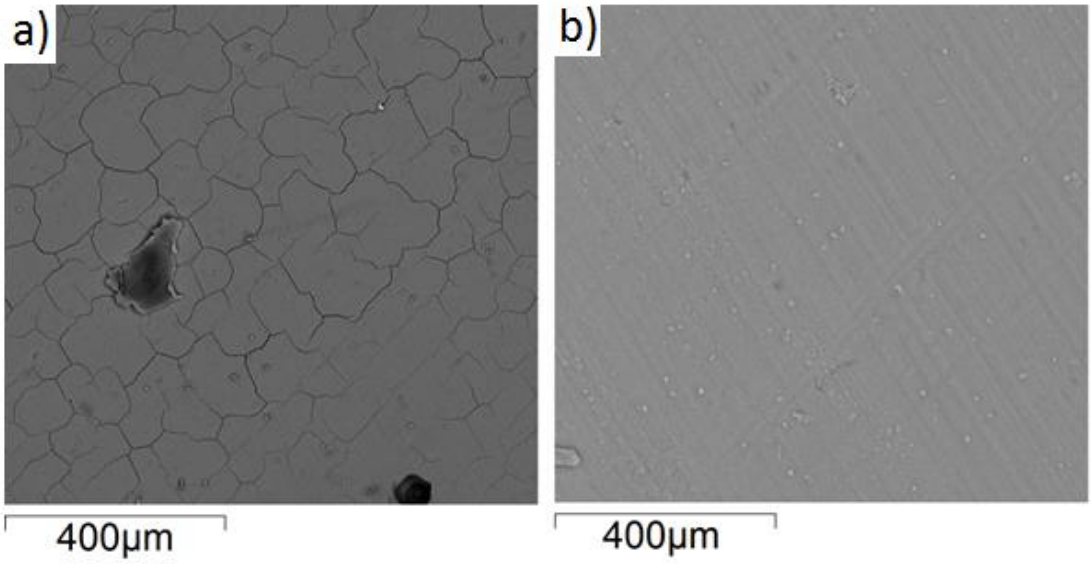

Figure 112: a) BSE image of the 6 weeks corroded surface layer in sample PF-HMS2 and b) areas where the surface layer had developed but later spalled off .

Further variation in the surface composition arose, depletion in calcium still occurred but not to the same extent as at 4 weeks. Other elemental changes were not as drastic as those at 4 weeks. The composition of the exposed glass was similar to that of the original composition, showing that the gel layer was in fact fully covering and so protecting the glass.

Table 48: EDX results for the surface layer and the glass seen in exposed areas, where the layer had spalled off, at 10 weeks of corrosion time for sample PF-HMS2. Error is either the standard deviation over 20 points, or the inherent error of EDX (0.1 wt%) whichever was the largest.

	MgO	**Al_2O_3**	**SiO_2**	**CaO**	**La_2O_3**	**CeO_2**
Surface layer						
Compound %	1.2	9.9	29.7	16.4	16.8	26.0
Error ±	0.2	0.4	1.1	2.1	1.4	1.9
Pristine glass						
Compound %	2.3	13.3	37.0	25.3	8.6	13.6
Error ±	0.1	0.2	0.7	0.4	0.5	0.6

From 10 weeks of corrosion onwards, no change was observed in composition or surface features.

Depth profiling revealed that the glass underwent several drastic changes over 14 weeks of corrosion. After 4 weeks both cerium and lanthanum (Figure 113 and Figure 114) showed a drop from 100% to 40-60% bulk concentrations where they remained for approximately 2 µm after which profiles sharply raised to 100% over 0.5 µm. The profile then dropped from 100% to 20% over 2 µm. This behaviour suggests the presence of a 2 µm thick cerium and lanthanum enriched layer at the surface followed by a cerium and lanthanum depleted zone 2-3 µm thick below. Both magnesium and calcium (Figure 115 and Figure 116) showed a continuous decrease over both the leached layer

and corrosion layer to 20-40% bulk values. The profile of aluminium (Figure 117) supports a gel layer hypothesis with a 2 µm shelf where the cerium and lanthanum profiles peaked, Al would act similarly to Si; a continuous decrease in Al content would point towards two leached zones, a shelf supports a surface layer.

Cerium and lanthanum profiles changed at 6 and 10 weeks of corrosion, exhibiting profiles typical of no surface layer, and a 2 µm leached layer. Aluminium also adopted a similar profile with no change until a depth of 2 µm where it decreased steadily to 20-40%bulk values. Calcium and magnesium both had similar profiles at these times, a decrease from a depth of 4-2 µm to 50% (±5%), followed by a second decrease at a different rate, from 50% to 20% over the course of 1 µm. By 14 weeks the profiles changed again, cerium and lanthanum displayed an increase in concentration of 100-170% (±10%) from a depth of 6-2 µm, followed by a decrease of 160-20% (±10%) from 2 µm to the surface. This profile indicates a gel layer with a high retention for cerium and lanthanum, and no leached layer at all. The other elements displayed a constant decrease over the same depth (6 µm to the surface) of 100-20% (±10%). These profiles suggest that the nature of the surface layer changed during the experiment, at first a layer formed with some capability to retain cerium and lanthanum but not protecting the glass from further leaching, then changing to a protective layer with little capability to retain these elements. Finally, the layer that formed had a very high retention capability for cerium and lanthanum, and stopped further leaching of these elements from the glass leading to the gradual increase in concentration of these elements up to the surface (with no decrease).

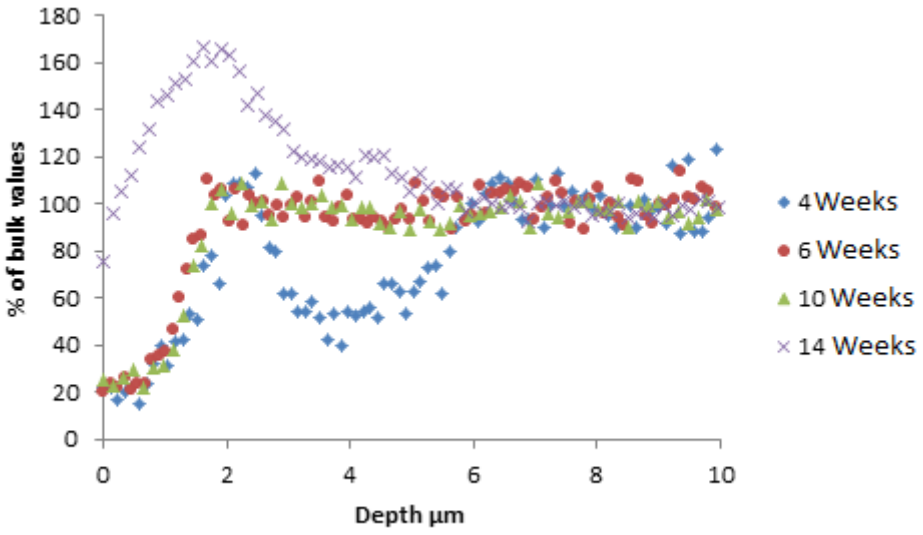

Figure 113: Depth profile of lanthanum from 4-14 weeks of corrosion for sample PF-HMS2.

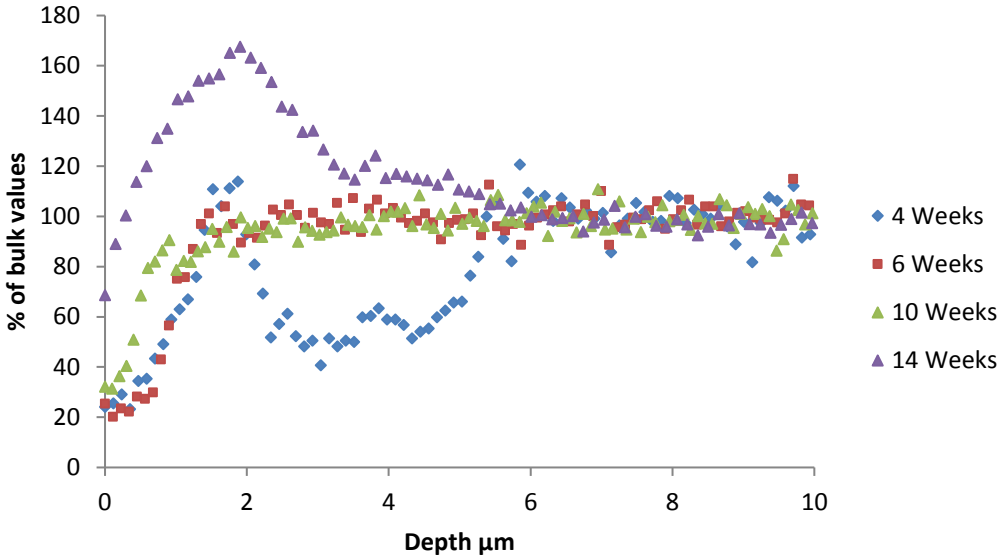

Figure 114: Depth profile of Cerium from 4-14 weeks of corrosion for sample PF-HMS2.

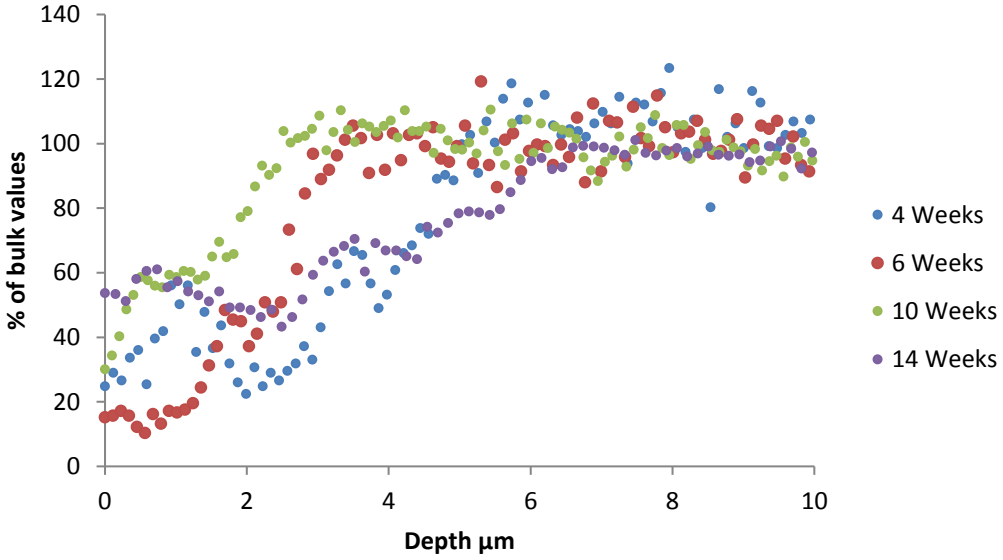

Figure 115: Depth profile of magnesium from 4-14 weeks of corrosion for sample PF-HMS2.

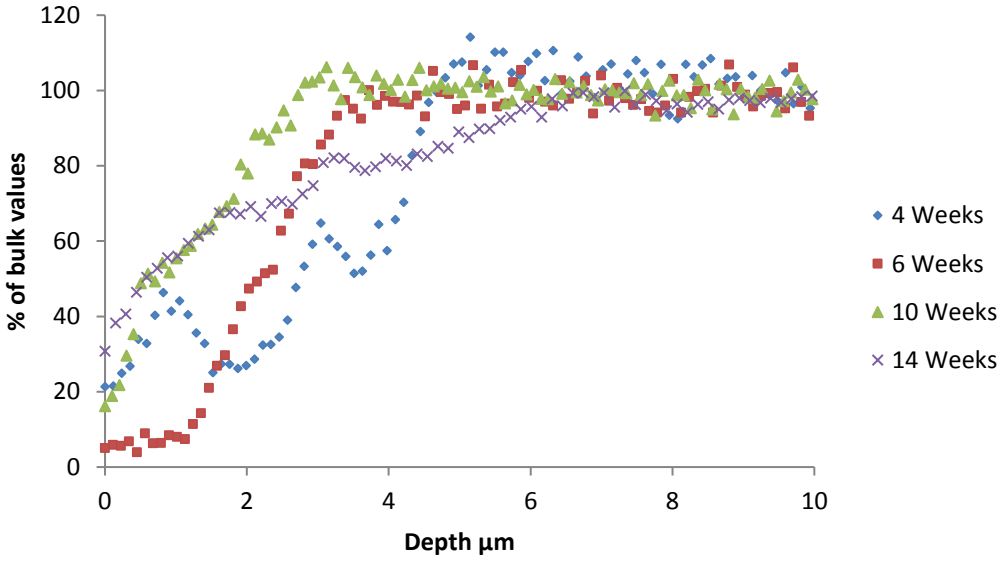

Figure 116: Depth profile of calcium from 4-14 weeks of corrosion for sample PF-HMS2.

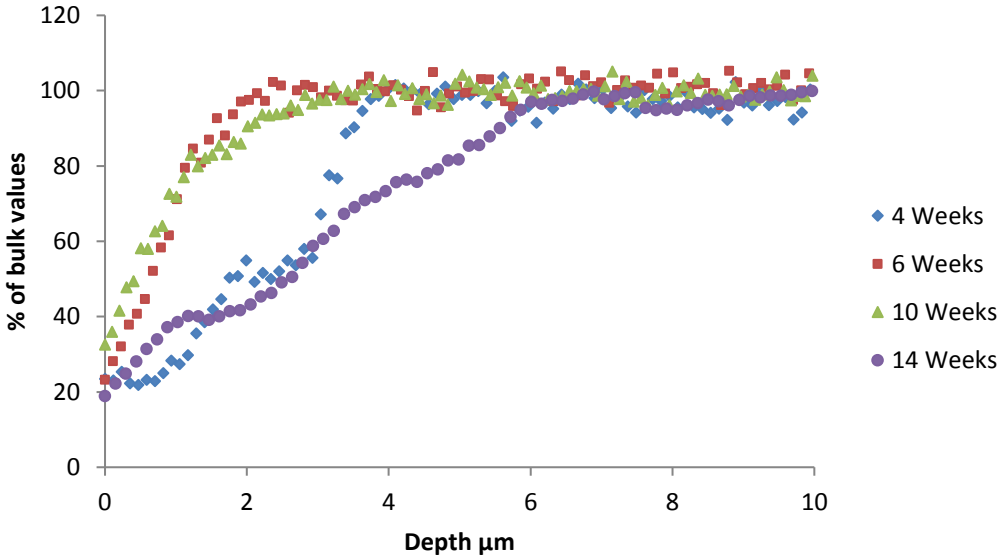

Figure 117: Depth profile of aluminium from 4-14 weeks of corrosion for sample PF-HMS2.

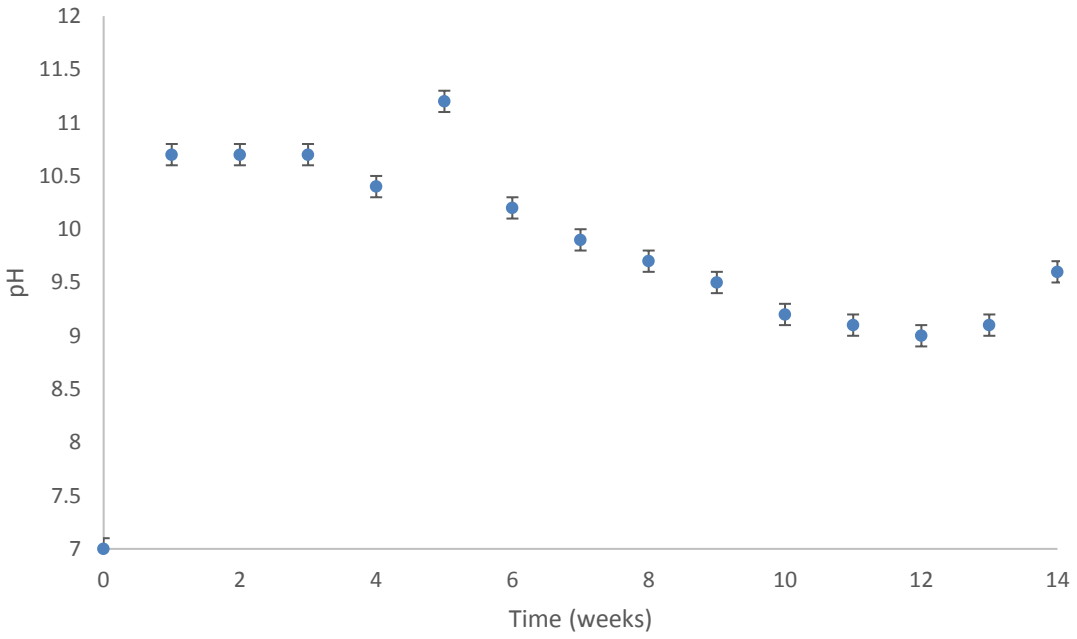

Figure 118: pH versus corrosion time (weeks) for sample PF-HMS2*. Error bars reported are either the reported error of the pH machine (0.1 pH value), or the difference between the maximum and minimum values found from repeat tests, whichever was the larger.*

Examination of pH versus time (Figure 118) revealed that pH increased drastically in the first week, but soon tapered off from 10.5 to almost 9, explained by the formation of a protective gel layer which inhibits leaching and hinders ion release from the solid into the solution. One anomalous result was found at 5 weeks of corrosion; however no explanation for this result could be offered other than contamination of the 5 week sample.

ICP-OES results (Table 49) reveal a steady increase in the leached elements in solution up to 10 weeks, at which point elemental release is drastically reduced, with the exception of calcium which

is reduced. However, the amount released in comparison to previous weeks (2 ppm) was not large and this is regarded as an anomalous result. Lanthanum and cerium standards could not be used due to machine and standard limitations.

Table 49: ICP-OES results (in ppm) from 4-14 weeks of corrosion time for sample PF-HMS2. Error is displayed as standard deviation from 9 samples over 3 aliquots of solution only as these were larger than the systematic error of ICP-OES.

(ppm)	**Al**	**Ca**	**Fe**	**K**	**Mg**	**Na**	**Si**
4 weeks	4.281	12.475	0.00	0.00	0.099	0.00	8.918
6 weeks	5.062	14.282	0.00	0.684	0.104	0.00	10.609
10 weeks	5.112	17.458	0.00	0.703	0.108	0.962	10.474
14 weeks	1.467	15.283	0.00	0.826	1.038	1.246	1.445
Error (Std Dev.)							
4 weeks	0.701	0.782	0.11	0.013	0.011	0.962	0.224
6 weeks	1.862	1.558	0.10	0.112	0.00	0.684	0.312
10 weeks	1.408	0.783	0.071	0.048	0.00	0.623	0.291
14 weeks	0.442	0.756	0.071	0.044	0.045	0.228	2.538

NL_r for Si and Al (Figure 119), structural components for the glass, showed a decrease over the duration of the experiment (14 weeks), further, the release rates were lower than previously analysed samples. As this looked at only the glass phase, this reveals the glass to be highly resistant to corrosion in the conditions (see section 3.4). Paradoxically, the Mg NL_r (Figure 120) show the opposite at after 14 weeks, but were in good agreement before. Whilst a large increase in the NL_r occurred, the Si and Al NL_r did not mirror this; this release was not due to depolymerisation of the silica network, but an increase in leaching.

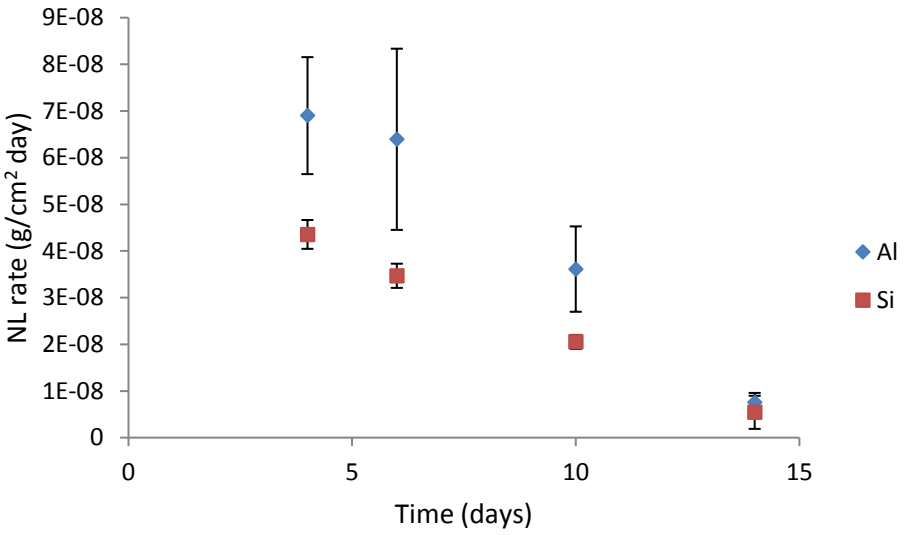

Figure 119: Normalised leaching rate (g/cm²day) versus time (days) for aluminium and silicon, for sample PF-HMS2.

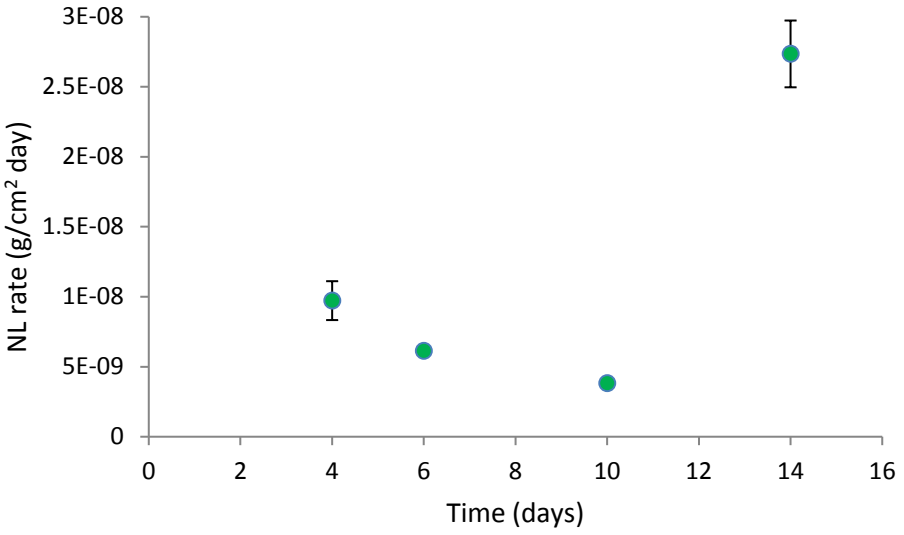

Figure 120: Normalised leach rate (g/cm² day) versus time (days) for magnesium.

5.0 Discussion

5.1 Joule Heated-Plutonium Contaminated Material

This sample contained 3 separate major phases; two glassy phases and the pyroxene phase along with 2 minor phases; iron-chromium metal alloy particles and an as yet unidentified phase surrounding the pyroxene. The minor phases are not expected to have a significant impact on the corrosion resistance of the material due to the small amounts present (~1-5%) and their isolated nature.

XRD results matched diopside ($MgCaSi_2O_6$) , augite (Ca, Na)(Mg, Fe, Al, Ti)(Si, Al)$_2O_6$, pigeonite (Ca, Mg, Fe)(Mg, Fe)Si_2O_6, enstatite ($MgSiO_3$)and ferrosilite all phases from pyroxene family, the composition boundaries for which are outlined in the ternary phase diagram shown in Figure 121. EDX results revealed a complete lack of iron in the sample removing (clino) ferrosilite and the hedenbergite ($CaFeSi_2O_6$) series as matches. The small amount of calcium and large amount of magnesium in the main crystal would place the phase in the pigeonite region of the phase diagram making it the foremost candidate. The formation of pigeonite is most likely due to the liquid-liquid phase separation, producing a glass which is more prone to crystallisation, as has been documented previously [198]. Little literature exists on the corrosion properties of pigeonite, with most research into pigeonite originating from mineralogy where it forms naturally in volcanic magmas [199,200,201] and in extra-terrestrial magmas [202,203]. However, the results from this study show it to have an equal if not better resistance to aqueous corrosion than that of the bulk glass (Figure 49 versus Figure 54 and 55) where leach depths were greater for the glassy phases.

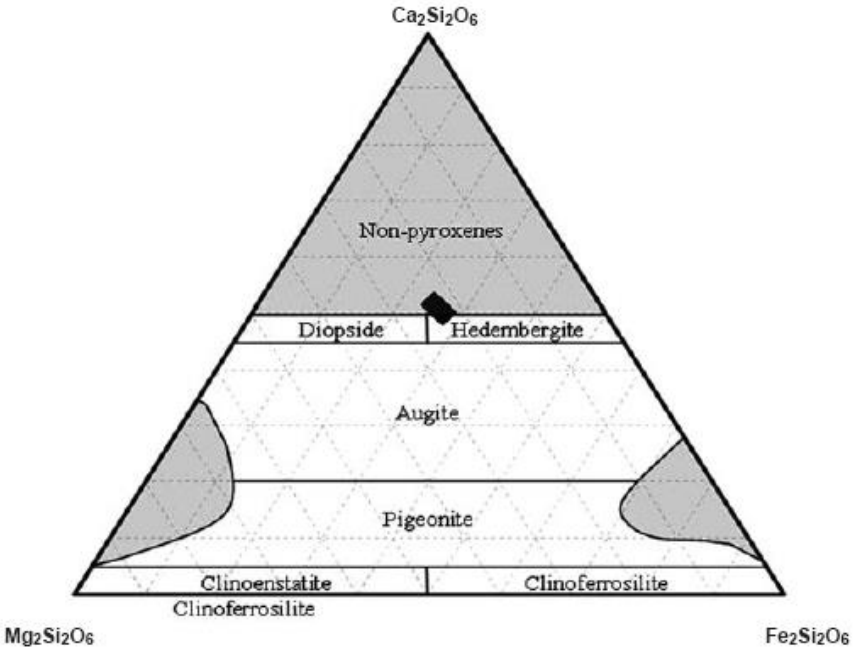

Figure 121: Rough ternary phase diagram for the pyroxene family of phases [204].

The second phase likely formed from the rejection of elements from the main crystalline phase (phase 1) giving a crystal enriched in aluminium, calcium, and magnesium thus ruling out all pyroxenes as candidates; the calcium alone places it in the non-pyroxene region of the phase diagram. Barbieri et al. showed that in CMAS glass, diopside and anorthite formed at 900-1100 ^{o}C and are the most likely crystals to form [205]. However, Barbieri et al. also found the phase distribution using quantitative Rietveld analysis as being 60% diopside, 20% anorthite with the remainder being glassy. Whilst the ratio of glass to crystal does not match these results, diopside always formed the major phase, with a maximum of 95/5 diopside to anorthite at 1000 ^{o}C with a 4h hold at this temperature, not dissimilar from the ratio of the crystalline phases seen in this wasteform. It is interesting that the phases in this GCM were a pyroxene and a calcium-aluminium-silicate (with some elemental substitution), a phase that has a similar composition to that of anorthite. Comparison of XRD data on anorthite shows a correlation on the major peaks, although some of the smaller ones are either absent or overshadowed by the more prominent pyroxene. The SiO_2-CaO-Al_2O_3 phase diagram (Figure 122) does show that by composition, the ratio of these 3 elements puts this phase on the boundary between anorthite and tridymite, however the comparison between tridymite XRD peaks and the XRD results shows that tridymite formation is unlikely. Additionally, the composition of the slag maker was chosen to specifically form anorthite, although it was uncertain whether this would actually occur due to the additional waste input. For these reasons, it can be reasonably concluded that anorthite is the second crystalline phase present.

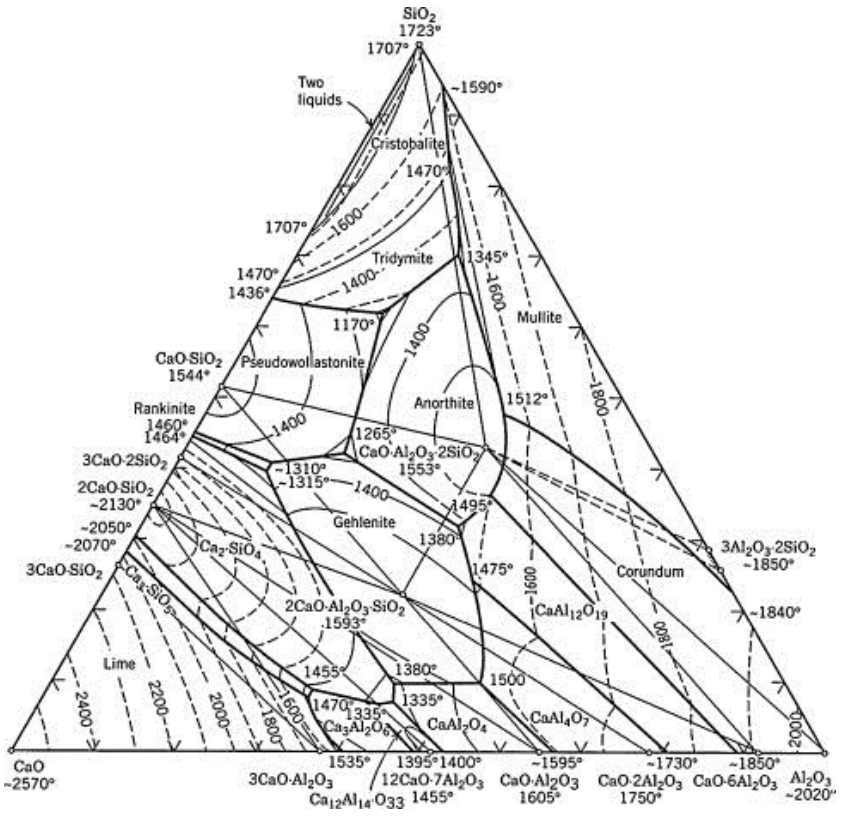

Figure 122: Al_2O_3-CaO-SiO_2 phase diagram [206].

Corrosion of the crystalline phase resulted in a continuous, thin, and homogeneous layer on the surface, as evident from the lines scans, calcium build-up occurred however this is assumed to be a

result of the anorthite interfering with the EDX scans and not due to any corrosion process. This result coupled with the surface images, cross sections, and depth scans suggests that the crystal is relatively unaffected (in comparison to the glassy phases) by the environment. This is also in agreement with literature involving the aqueous corrosion resistance of anorthite which was found to perform well in both acidic and alkaline regime [138,207]. Toya et al. [207] found weight losses in a glass ceramic containing both anorthite and diopside varying from 1.4-2.3mg/cm^3 over 24h (90 ^{o}C) in alkaline media dependant on the proportion of the material which was ceramic; the more crystalline the GCM was the higher the weight loss. Due to the lack of discrimination on the corrosion of each crystal, it cannot be shown which one performed better. Corrosion of diopside is discussed elsewhere in this report (section 5.5), but was found to be highly resistant to aqueous corrosion in several fields in comparison to glasses of similar composition. Fröberg et al. [135] showed that little to no changes occurred when anorthite glass ceramics were exposed to hydrochloric acid containing solution after 4 days, with negligible release of Ca, Si, and Mg ions. Although Toya et al. did show that the rate loss was large for this material, the losses described did not match what was seen here; it is possible that the gel layer that formed was a result of the nearby glass and that it extended over the crystal offering similar protection. Observation of the surface of the glass did show the layer that formed was likely to have formed via precipitation rather than by depolymerisation giving credence to the layer extension theory. If the topmost layer of the glass gel layer was precipitated, then it is easy to see how this layer would extend over the entire surface, covering not just the glass but the crystal as well. The results found by Toyal et al. [207] would suggest after 14 weeks in alkaline solution that at least 14 µm of material would be removed from the pigeonite/anorthite mix. As no such loss was observed the layer that formed is protective.

The glass-crystal interface is a very common weak point in the corrosion resistance of glass-ceramics and glass composites [68] due to thermal mismatches allowing a gap and/or cracking to separate the two leading to ingress of water and a higher surface area of attack. No evidence of attack on the wasteform by this method could be found by the analysis techniques used, attributed to the barrier phase between the main crystal and the glass, longer trials would be necessary to establish that this does not occur.

Liquid-liquid phase separation of glasses in the quaternary system CaO-MgO-Al_2O_3-SiO_2 has been documented before by several authors [204,208,209] and has been noted to occur due to segregation of the calcium and magnesium ions at high temperatures (in excess of 800 ^{o}C). EDX results confirm the difference in the two glasses is between the composition of calcium and magnesium in each respective glass. Interestingly, sodium was also affected to a large extent, with one glass demonstrating only trace amounts whilst the other had close to 4 wt%, for this reason the sodium enriched glass will be referred to as such; Na-Glass (glass 2), whilst the second one is referred to as “Na depleted glass” (glass 1).

The morphology of the Na glass would suggest that it formed first due to the spheroidal shape, and possibly formed around the Fe-Cr particles as BSE images revealed none of these particles existed in the Na depleted glass. Interestingly, it appears that the Na glass rejected excess Mg into the surrounding melt, allowing the formation of the Na-depleted glass which was enriched in Mg. This behaviour is often associated with crystalline materials (e.g. eutectic melts), and not (to the authors knowledge) with glasses. It is possible that the Na glass formed from the depolymerisation of crystalline phases which formed around the Fe-Cr particles, which explains the presence of the two

glasses, the morphology they took, and the relation to the Fe-Cr particles as they would act as nucleation sites. It is not entirely clear if there is some association between the glass-glass separation and these particles as no literature involving the effects of such an iron particle's effect on liquid-liquid phase separation could be found. However, the consistent location of these particles across the entire sample would suggest that they are linked in some way.

The difference in composition between these two glasses, whilst small, was enough to produce glasses with two very different properties in regards to corrosion resistance to aqueous media as described in section 4.2.1. BSE is no longer needed to discern the two glasses after 4 weeks of corrosion due to the faster corrosion rate resulting in a height difference between the two. Further, it is clear that a gel layer developed on both glasses following corrosion; however, the gel layer that formed on the Na depleted glass was non-uniform and did not fully cover the glass resulting in a non-protective layer, evident from the higher corrosion rate on that glass. In contrast the Na-glass showed a homogeneous, fully covering gel layer. However, the thickness of this layer varied for similar corrosion times, displaying a typical minimum of 2 μm and a maximum of 5 μm. No large difference in composition was present, nor was the presence of additional phases in these regions detected as a reason to explain the large difference in gel layer thickness. Interestingly, the morphology of the gel layer on the Na depleted glass suggests that it is not a gel layer in a conventional sense; rather, it appears to be a precipitation type layer; the layer is an agglomeration of spheres not indicative of a gel layer. The current model for glass corrosion [210] states that a gel layer forms from hydrolysis of loose silicon bonds at the surface. An alternate model describes a corrosion layer that results from precipitation, rather than hydrolysis, from a locally ion enriched solution at the water-glass interface [192], or that conversion of the gel layer to a crystalline phase occurs [211]. However, the latter model is often used in conjunction with the former, that instead of one occurring preferentially, both mechanisms occur at the same time [212,213,214]. Whilst it is not within the scope of this work to debate which model more accurately describes corrosion in glasses, all models must be considered to determine the long-term corrosion properties of the GCMs studied.

The precipitation theory is more suitably used here, evident by the lack of a protective gel layer on the sides of the Na-glass, more easily seen in Figure 56, and by the particle nature of the corrosion layer observed (Figure 51), on the Na glass (Figure 50). If corrosion of this glass was by the standard model, a gel layer should have developed on any exposed surface regardless of orientation; this is not the case. Figure 56 shows not only a lack of gel layer on the Na depleted glass, but corrosion of the Na-glass from the side, this phenomenon was not widespread, but neither was it isolated, where the layer that formed on the Na depleted glass was present beside the Na glass, no corrosion into the side of the Na-glass was observed. This demonstrates that the non-continuous layer on the Na depleted glass was protective to some degree.

Figure 56 also shows a gap in the glass near the centre, this gap is thought to be where the iron-chromium particle was located, pre-corrosion. The lack of this particle suggests that it was either completely corroded and/or removed from the material; no gel layer is seen to form in this pit. It is not unreasonable to assume that this will have an effect similar to that of pitting corrosion in alloys, where by the enclosed nature of the pit will result in a local increase in the concentration of ions in solution, accelerating corrosion, resulting from the increase in surface area. Indeed, it was seen that

corroded cracks propagated from these nodules into the glass, some extending 20 µm into the material.

Depth scans of the Na-glass (Figure 54) revealed that it did have a reasonable corrosion resistance as although the leach depth penetrated into the sample by 10 µm, this leached depth was constant at all corrosion times. The presence of grinding marks on the corroded surface (Figure 50b) shows that type 3,4, and 5 dissolutions, whereby the original surface is removed completely, did not occur indicating a protective coating with selective leaching i.e. type 1 or type 2 (see section 2.4). However, corrosion of the glass via the sides and the pit left by the iron-chrome particle renders the resistance of this glass somewhat ineffective as the protective coating is circumvented (Figure 56).

The weakest point in this material was the Na-depleted glass, which was more easily corroded. After 14 weeks, between 4-5 µm had been removed from this glass leaving the Na-glass relatively untouched. Regardless of the waste content of the glass this poses a major problem due to the shape this glass retained; it acted as filler or matrix for the Na-glass which had a tendency to form in isolated discrete spheres, thus bonding the Na-glass and the crystals. The result over extended periods of time would be the complete removal of the Na-depleted glass, which after time would cause the isolated particles of Na-glass to become detached from the wasteform, for similar reasons the crystals would also detach. Based on the amount etched away after 14 weeks of corrosion, the Na-depleted glass would have an expected rate loss of 18 µm/year. A 1 m^3 block of this GCM would thus be expected to last around 30,000 years before total dissolution of the binding glass, resulting in the block degrading into particles of the more resistant glass and crystal. As this is measured from the weakest phase, and assumed constant removal rate, it can be seen as a worst-case scenario. Whilst this is not ideal, the time it would take for this to occur far exceeds its requirements as an ILW thus this waste appears, in the context of this present study, suitable for disposal as an ILW matrix.

5.2 Joule Heated-High Metal Surrogate

The main objective of the trial was to assess to ability of the JH-ICV process to cope with not only a large amount of metal waste, but also diverse waste in both composition and shape. The resulting GCM was an inhomogeneous glass encapsulated crystal containing wasteform, with little consistency in the shape and size of the crystalline portion of the sample. Whilst a calculated total crystal volume of 20% was determined using BSE images (see section 4.1.2), the large variation in different areas (~10-30%) revealed the wasteform will be difficult to assess for its durability.

EDX analysis of the glass (Table 23) showed its composition to be consistent. Based on the total amount of misch metal used (27 wt% of total material), the amount of ceria in the total wasteform is approximately 18 wt% and similarly 9 wt% lanthanum oxide. Whilst the composition of the misch metal was not documented, it is assumed to be of the same composition used in previous trials by Impact Services Inc. involving mischmetal with the composition shown in Table 50. EDX analysis showed the amount of these waste elements in the glass to be 5.7 wt% (La) and 15 wt% (Ce). Clearly, nearly 1/3 of these elements segregated into the crystalline portion of the waste with a much lower lanthanum concentration than the wasteform average (1:1 ratio rather than 1:3).

Table 50: Composition of commercially available mischmetal used in previous trials by Impact Services Inc [173].

Mischmetal	wt%
Lanthanum	33.68
Cerium	66.11
Praseodymium	0.11
Neodymium	0.11

The analysis of the crystalline portion using SEM revealed a myriad of phases, revealing the crystalline portion complexity; multiple phases in close proximity makes identification and subsequent prediction of corrosion properties difficult.

The crystalline phases were identified using EDX (Table 24) and XRD (Figure 37), the former confirming the existence of 4 discrete phases by composition, being CeLa phase, phase 1, phase 2, and phase 3 (section 4.1.2). For the most part, the lanthanum and cerium were in the brightest CeLa phase, both XRD and EDX showed this phase is most likely a cerium-lanthanum silicate with small amounts of aluminium and calcium totalling 15 wt%. No literature could be found that described such a phase with the elemental composition found here, and little literature exists on a La/Ce-silicate phase. Lopez et al. [215] found similar phase formation in their borosilicate glasses when working with cerium only, which separated from the glass to form cerium oxide silicate. The microstructure of these phases found by Miae et al. were similar to those found in this wasteform (Figure 39, Figure 41), as can be seen from Figure 123 (Miae et al.) which was found to have crystallised off of the zirconia crucible. Miae et al. [216] also found the formation of a non-stoichiometric calcium cerium oxide silicate ($Ca_2Ce_8(SiO_4)_6O_2$) with similar morphology to the crystals found here. The phase found by Miae et al. in their experiment is thought to be the “Ce-La phase” found here, with substitution of lanthanum onto the cerium site. The durability of this phase was found to be better than an equivalent borosilicate glass used to immobilise cerium. Indeed, the corrosion results found that this phase fared better than the surrounding crystalline phase, and the adjacent glass, evident by the way this phase “protruded” from the bulk. However, whilst this may inhibit leaching of cerium and lanthanum, the detached nature of the small crystals means that they can be easily removed entirely from the bulk when the surrounding crystal has corroded. With 1/3 of the Ce/La sequestered into this phase, after the surrounding phase has been corroded the crystals will simply fall out of the matrix, ultimately leading to a much higher elemental loss than the glass.

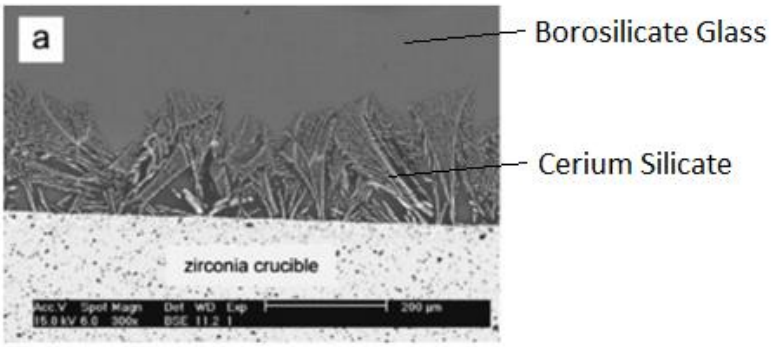

Figure 123: BSE image of dendrites of cerium silicate growing in a borosilicate glass [215]

The largest phase, identified by XRD (Figure 37) as being a calcium-magnesium-iron silicate, could not be accurately identified any further with XRD and EDX. The composition shows it to be a silicate, but not much more than this could be found due to the phase having 4 elements of roughly equal proportions in addition to the silicon. This issue was most likely due to the morphology of the phase, and the phase surrounding it; it is thought that it is composed of dendrites with a glassy phase surrounding it leading to EDX results contaminated with elements from the glass. Based on this, and results from the EDX maps, a theoretical composition was calculated assuming an overlap from the composition of the glass to give an adjusted, approximate composition of the crystal (Table 51) using Equation 14. A multiplication factor was added to the base values to allow for how much of the glass composition overlapped with the crystal.

$$C_X = \frac{C_a - a * C_g}{b} \tag{14}$$

where C_x is the composition of the crystal, C_a the composition of the crystal given by EDX, C_g the composition of the glass. “a” and “b” are factors deciding how much overlap is present, in this case a=0.775 and b=0.225, representing an glass overlap of 77.5%. “a” and “b” values were estimated from SEI and BSE images of the dendritic portion (phase 1).

Table 51: Composition of the glass, and calculated composition of the large crystalline phase in oxide wt% based on the theory of the initial EDX results having included the surrounding glass.

	MgO	Al_2O_3	SiO_2	CaO	Fe_2O_3	La_2O_3	Ce_2O_3
Glass from EDX	2.5	7.0	49.7	7.5	12.7	5.7	15.0
Crystal from EDX	3.3	7.2	48.9	9.6	11.6	7.9	11.6
Calculated Crystal	6.2	7.9	46.3	16.7	7.8	15.3	0.1

Lanthanum can be considered as a group 3 element for this calculation, as has been previously established [217], and thus plays a similar role to aluminium. This leads to a phase which has a similar composition to that of augite, a complex inosilicate with the chemical formula of $(Ca,Na)(Mg,Fe,Al,Ti)(Si,Al)_2O_6$. This matches one of the documented colours for augite (brown) along with the crystal structure (monoclinic) and composition determined by XRD. The exact chemical formula given by XRD (PDF 01-083-2015) was $Ca_{0.9}Mg_{0.71}Fe_{0.25}Si_2O_6$. A multitude of other phases

were analysed for compatibility with the results, and ruled out based on the crystal structure, known morphologies, colour, and composition. These include; forsterite, fayalite, Al_2SiO_5 group, humite group, mullite, all sorosilicates, all cyclosilicates, sodium pyroxenes, pyroxenoid group, double chain inosilicates, phyllosilicates, tectosilicates excepting anorthite. Alternative possibilities include; enstatite series (and polymorphs), pigeonite, hedenbergite series, anorthite, and the garnet group.

It is suggested that this phase is augite, but due to the feasibility of some alternatives such as the garnet group and anorthite in particular, more accurate techniques are required to confirm this.

The corrosion of the glass as described in section 4.2.2 was unusual in that the top layer that formed appeared to be precipitated rather than forming from the depolymerisation of the silica network; the spheroids that formed on top are associated with precipitation and not depolymerisation. Beneath this layer was a conventional gel layer, beneath which was a 1-3 μm leached zone. This structure did not change for all corrosion times, which reveals that the gel layer imparted significant corrosion protection to the glass. Furthermore, the lack of change to the Ce and La profiles suggests that these elements are difficult to remove from the glass. This behaviour is made better by the relatively low amount of crystalline material in the wasteform. A large amount of corrosion resistant glass will act to protect the crystalline components from aqueous corrosion acting as glass encapsulated crystalline GCM. This is an ideal arrangement, in particular due to the multicomponent crystal aspect to the GCM, rather than calculate the individual corrosion properties of the crystalline components, only the glass need be calculated as it will limit the corrosion of the wasteform due to its large volume.

The crystal formations had mixed response to the water, the phase closest to the Ce-La silicate appeared to suffer the worst having been etched away, whilst the augite dendrites encompassing the Ce-La silicate, had been corroded less than the bulk glass (more corrosion resistant). As was mentioned (see section 4.2.2), the depth profiles of the unidentified crystals closest to the Ce/La oxide silicate proved difficult to obtain as they often intersected each other making the depth profile include the elevated/depressed values from the intersecting crystal. This was especially true for the phase immediately surrounding the Ce-La silicate, and due to the intermittent nature of the Ce-La silicate, made depth profiling of either phase impossible.

One recurring theme with the augite was the possible formation of two corrosion layers. The subsurface layer occurs with a silicon shelf (where the profile remains constant) and where all elements, excepting Ce/La/Fe, saw a steady decrease. The surface layer saw a sudden spike in Na, Mg, and Fe profiles (small spike in Al) whilst all other elements experienced a steep drop in concentration.

The distribution of the waste elements into each phase coupled with the inhomogeneous distribution of each phase makes calculating normalised leaching rates impractical; calculating the mass fraction of an element in the wasteform produces an unacceptably large error for certain elements. Normalised leach rates (Figure 69 and Figure 70) for the sample revealed a steady decrease for all elements over the time of the experiment, this result will most likely reflect the glass as it made up the majority of the wasteform, and thus the corrosion layer(s) that formed were protective. The leaching rate for Si and Al reflect the structural damage of the glass, an increase would be representative of a non-protective corrosion layer, and clearly this was not the case. As no cracking or spalling was observed there is no reason to believe that this state will change with

increased corrosion time, as was seen in other GCM's in this experiment (sample PF-HMS2, section 4.4.3).

Whilst the corrosion resistance of the glass and Ce/La oxide silicate of the GCM was excellent, the corrosion properties of the augite and adjacent phases proved to be less than adequate. The corrosion resistance of the latter mitigated the corrosion resistant Ce phase, which after time would detach from the bulk wasteform. The results found here would at first glance show the GCM to be suitable for ILW disposal, further analysis of these results could suggest the opposite; having the Pu surrogate phase simply "fall out" is not ideal. That said, it is possible that this mechanism may occur at a rate that is acceptable for ILW due to the much lower timescales needed for safe isolation. Further work on longer corrosion times is required to assess if this is the case.

5.3 Joule Heated-SIXEP

The waste used in this specimen was that of clinoptilolite from SIXEP, pile fuel cladding, and silo waste. Clinoptilolite is a naturally occurring zeolite and used in nuclear processing for the decontamination of nuclear waste containing solutions, such as ^{134,137}caesium and ^{90}strontium, produced in nuclear reprocessing and decommissioning. The ability of this material to accept these ions into its structure comes from the arrangement of the aluminium and silicon tetrahedra, their positions leave large channels that allow for the absorption of these ions [162]. As noted by Juoi et al. [162], current methods for safe disposal of spent ion exchangers such as clinoptilolite is that of immobilisation in bitumen, cement, and more recently, glass.

The simulated PFC consisted primarily of aluminium [218,219] and as the temperatures involved in the wasteform processing were well above the melting temperature of pure aluminium, the PFC will have been destroyed during the treatment. Actual PFC, is of course, much different from that originally used, due to over 50 years of unimpeded corrosion, and possible chemical reactions with undocumented materials in the silo, such as organic wastes. This makes prediction of how these corroded fuel pile claddings will react during processing difficult, however prediction based on an idealistic sample of PFC will allow for a basis on which to build further work on corroded specimens of PFC. For the case of this experiment it is assumed to fully melt. In regards to the other waste added, the temperatures involved were sufficient to fully melt them, namely different types of steel, iron oxide, and magnesium rods introducing large amounts of these elements into the melt.

It proved difficult to identify the exact phases present in the JH-SIXEP sample described in section 4.1.3 (thick crystals 1 and 2, and thin crystal in Figure 44) due to the large amount of substitution present causing shifts in peak location from stoichiometric ones, along with changes in peak intensity. To summarise, the phases detected were clinoenstatite, enstatite, periclase, magnesioferrite, clinoferrosilite, and various other iron oxide phases (magnetite, wustite, hematite) although it is unlikely that all these phases are present. Clinoptilolite was the main waste used for this GCM, the general formula for clinoptilolite is $M_x\,[Al_xSi_yO_{2(x+y)}]\cdot pH_2O$ where M is (Na, K, Li) and/or (Ca, Mg, Ba, Sr), n is cation charge; y/x = 1–6, p/x = 1–4 [220]. It has been reported by Bosch et al. [142] that the thermal treatment of natural clinoptilolite (without Cs) resulted in the destruction of the zeolitic structure into a crystalline/amorphous material, heating at 1000 ^{o}C resulted in the formation of an alkali feldspar, plagioclase and large proportion of glass. Whilst it is has been

reported that substitution of magnesium and iron into the plagioclase structure is possible at the expense of calcium [221], the complete lack of calcium and sodium in what is a mixture of anorthite and albite ($NaAlSi_3O_8$) makes this phase formation unlikely, for similar reasons the alkali feldspars can be ruled out. In addition, EDX results showed no phase that contained only iron and magnesium ruling out the presence of magnesioferrite, $Mg(Fe^{3+})_2O_4$. A more likely scenario is the formation of a pyroxene, due to the wide variety of pyroxene phases that could be matched to the XRD (Figure 42 and Figure 43) along with the composition of the phase as detected by EDX (Table 25). The pyroxenes identified were enstatite ($MgSiO_3$) and ferrosilite ($Fe^{(2+)}SiO_3$) with their clino polymorphs. The $MgSiO_3$- $FeSiO_3$ system has been studied extensively by geologists [222] and has been documented to form from thermal decomposition of iron containing wastes [223]. Karamanov et al. studied the thermal properties of a clinoptilolite and iron containing waste (primarily blast furnace slag and zeolitic waste) for safe disposal. During processing of materials designed to form a glassy phase, high iron content has been known to cause liquid-liquid immiscibility [224], this has resulted in high-iron containing liquids during melting which promoted the formation of magnetite spinel's [224]. Further, extended times at temperatures above 1000 ^oC was shown to result in formation of a pyroxene phase from the initial magnetite spinel [224]. This hypothesis for the formation of a pyroxene in this sample is in good agreement with the results found here which showed the presence of an iron phase of which magnetite was a candidate, in addition to showing the presence of a pyroxene phase.

Based on the EDX results (Table 25, thick crystal 1 and 2), the candidates from XRD analysis (Figure 42 and 43), and the above information, it can be concluded that the main phase, is an enstatite-ferrosilite composition in the range of En^{60} – FS^{40}; this mixture of enstatite and ferrosilite has been referred to in the literature as hypersthene but is more commonly referred to by the ratio of the two. In this report, it is referred to the former for simplicity. Three polymorphs of enstatite and ferrosilite exist, proto-enstatite, ortho-enstatite, and clino-enstatite (similarly for ferrosilite). Work has been performed on the conditions necessary to form these polymorphs by Lee and Heuer [225] on the enstatite endmember. Work performed by Lee and Heuer [225] on the various stability fields on the polymorphs of enstatite can shed light on the identity of the thinner crystalline phase. The stability temperatures for the pyroxene groups are shown in Figure 124, however these are not truly representative of the forms that may appear, due to other factors not included in the graph. For example, clinopyroxene is the preferred phase at low temperatures, however Lee and Heuer showed that cooling rates of 5 ^oC per minfrom the proto stability temperature was enough to retain most of this structure at room temperature. Indeed, a rapid quench rate was required to fully retain the clinopyroxene structure. Based on the temperatures and times used in the formation of this material (>1000 ^oC for 24 h without a quench) proto would be the expected phase to form. However, it was shown by Lee and Heuer that even with careful temperature controls and no external force on the sample, clinoenstatite formed around protoenstatite crystals that were less than 7 μm in size due to internal stress resulting in a martensitic transition. Magnetite, clino/enstatite, and clino/ferrosilite account for all XRD peaks in Figure 42 and 43, however as enstatite and ferrosilite form a solid solution series only two phases should be expected from the XRD; hypersthene and magnetite. SEM images and EDX analysis proved that two crystalline phases existed in addition to a magnetite phase by morphology and composition. If the large pyroxene crystalline phase is indeed hypersthene by composition, then it stands to reason that a secondary large trace would be present for the large amount of the thin pyroxene. No such trace was observed. It is likely that the large pyroxene crystal

(thick crystal 1 in Figure 44) is the orthorhombic form of the crystal (proto-enstatite/ferrosilite) whilst the smaller crystalline phase (thin crystal in Figure 44b) is the monoclinic form (clino-enstatite/ferrosilite), which formed in the way described by Lee and Heuer. Whilst the Al and Ca content would make this unlikely due to the limited solubility of these elements [226], the spatial resolution of EDX may result in the inclusion of elements from the surrounding glass that may not be present in the thin crystal at all. Thus, it can be said with reasonably high accuracy that due to the small amount of these elements found (related to the small intensity of X-ray peaks detected associated with these elements) that they are from the surrounding glass and not the crystal itself. This results in a crystal with a similar composition to that of its larger cousin, but smaller in size. Lee and Heuer also observed the samples they investigated were also porous, but it was not said for what reason this occurred.

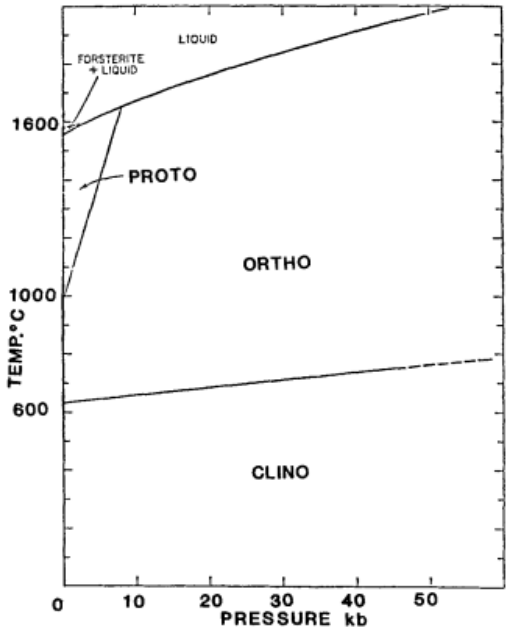

Figure 124: Stability field of the pyroxene family as a function of temperature and pressure [225].

The progression of the corrosion of the JH-SIXEP sample had 3 stages as described in section 4.2.3;

1. A partial gel layer developed, covering the glass and to some extent the thin proxene crystal. No gel layer was seen to develop on the hypersthene. This was seen on the 4 weeks corroded sample.
2. The layer had extended to cover the entire surface of the sample, but was not thick. Spalling of this layer was seen but not widespread over the sample and assumed to be a result of post corrosion sample handling. This occurred after 6 weeks.
3. The gel layer was not seen to increase in thickness for the remainder of the corrosion times (up to 14 weeks), leading to an apparent reduction in the corrosion rate, as found by ICP and pH tests, indicating little leaching had occurred from 6 weeks onwards.

The overall corrosion of the sample based on these stages is promising however a thin gel layer covering the entire sample is sometimes indicative of type 5 corrosion (see section 2.4), where a

layer develops, spalls off, and is replaced by a new one; a highly undesirable non-passivating corrosion mechanism. Normalised leaching rates were calculated from the ICP results and revealed that the release rate decreased as a function of time for all elements, at 14 weeks the release rate had been reduced by almost an order of magnitude for silicon (Figure 82). Similar release rate profiles were observed for Mg and Fe (Figure 83). This would suggest that the corrosion mechanism is type 1 and not type 5; a thin and protective layer had developed halting further leaching and inhibiting corrosion.

The EDX analysis of the entire surface (Figure 72) yielded surprising results; all elements decreased in concentration with the exception of iron which showed a large increase. In fact, the increase resulted in the surface of the hypersthene having a composition closer to that of almost pure ferrosilite. This result can be explained by the solubility of the elements in solution, mainly that of iron. The solubility of iron in solution approaches zero for iron oxides, typically it is in the ppb range, this would prohibit the migration of iron ions into deionised water, and those that did would quickly precipitate into iron oxide. The thin layer (0.6-1.3 μm) that was seen to develop in the cross-sectional analysis was found to in some cases, have a higher amount of iron relative to the other elements in the layer. This would account for any ions that were leached, having precipitated amongst the gel layer. It should be noted that the results are shown as ratios to each other; the EDX program automatically corrects concentrations to add up to 100%, thus whilst it appears that silicon had a large decrease in concentration, it is more likely that this occurred due to a large increase in the iron concentration.

Depth profiles for each phase (Figure 73, Figure 74 , and Figure 76-80) displayed a promising trend, the minimum elemental depth before the concentration of elements returns to those in bulk was quite low (5 μm ±1 μm) further signifying that the material is resistant to corrosion and leaching. The glass depth profile is consistent with current glass corrosion models, whereby a leached layer develops followed by a gel layer, in some cases a protective gel layer. Due to the images displaying a gel layer at all corrosion times, very little change in surface topography as a function of time of corrosion, consistent depth profile, and consistent leached depth it can be said that this layer is protective, and will inhibit corrosion. This is not an unexpected result considering the initial composition of the glass, it contained very little alkaline, and alkaline earth elements which are most susceptible to leaching. These elements are typically leached out first due to their small ionic radius and weak bonding within the glass structure. Additionally, the main waste element in the glass, iron; can act as a glass former integrating itself into the glassy structure making it difficult to remove.

The proto-pyroxene displayed a change in the depth profile over the course of the corrosion time (Figure 79 and Figure 80). After 4 weeks, an increase in magnesium and silicon concentrations approaching the surface occurred at a depth of 1-3 μm of approximately 20% greater than in bulk, whilst iron remained relatively constant in this region. Following this the concentration for all these elements dropped signifying the end of the crystal. After 6 weeks, this profile changed to show an increase in the iron content in the region of 30% ±5 between 1-7 μm range, whilst the magnesium and silicon showed a steady decrease in this region ending at 4 μm showing the end of the crystal. It is clear from that after 10 weeks of corrosion a layer had developed on top of the crystal which was depleted in magnesium, but enriched in iron. The magnesium concentrations were found to approach 0% in certain crystals distributed around the material; however, these were exceptions to the general trend of low levels rather than complete removal of magnesium. It is possible that with

further corrosion, that the proto-pyroxene phase would observe complete removal of magnesium to a depth of 5 µm ±1. This magnesium depletion was only seen in the layer that had formed, which remained constant in thickness, and no further depletion in any elements was observed beneath this layer. For this reason, even if complete removal of magnesium had occurred past 14 weeks of corrosion time, it is thought that unless the layer was removed, magnesium removal would be isolated to the corroded layer. Long term tests are needed on this waste material to fully assess the durability of this phase.

Depth profile observed for the clino-pyroxene (Figure 76-78) was identical to that seen in the proto-pyroxene after 10 weeks (Figure 79). Whilst SEM images (Figure 71b and Figure 75b) did not show a corroded layer, depth profiling showed that between 2-7 µm a change in composition occurred indicative of a corroded layer was present. As was seen in the proto-pyroxene (Table 32), the compositional changes were a decrease in magnesium, and an increase in iron, in addition calcium followed the same profile of iron, whilst aluminium showed the same profile of silicon. This is thought to be due to the role aluminium plays in the crystal, mainly substituting for silicon, similar to the role it plays in glass, thus removal would be at a similar rate. It is encouraging that this profile did not change from its formation to the end of the experiment. Interestingly, the profile of the proto-pyroxene at 10 weeks onwards was nearly identical (minus the extra elements) for the clino-pyroxene at 4 weeks onwards, both these profiles remained unchanged after they formed. Longer corrosion times are suggested for analysing the proto-pyroxene however due to the similarities between both phases it is thought that the proto-pyroxene will adopt a similar profile, importantly that no change will occur after formation of the layer.

Overall the wasteform was found to be more than adequate from a corrosion standpoint, the waste was fully incorporated into the material in either the glass or pyroxene phase(s) all of which showed a good resistance to aqueous corrosion. Due to the lack of weight loss, or changes in surface indicating consistent removal of corroded layers, and small ion release no time could be calculated for the wasteforms life time, but would be expected to surpass the requirements for an ILW. The only issue with this wasteform is the final volume, which could be considerably reduced if the pores were removed.

The clinoptilolite waste used in this study (Table 7) was found to contain concentrations of both Cs and Sr below EDX detection limits (0.1 wt%) which matches with the amount added (~0.1 wt%), the thermal decomposition of zeolites (specifically clinoptilolite) containing these elements has been well document [227, 228]. The phases found to form in other studies are considerably different from the ones that formed for the clinoptilolite used in this study. For instance Bogdanova et al. [228] found the main phases that formed above 1000 ^{o}C to be pollucite ($(Cs,Na)_2Al_2Si_4O_{12}\cdot 2H_2O$), whilst Bosch et al. [142] discovered plagioclase and feldspar formed, most likely a result of the Si/Al ratio. Due to this, future work should concentrate on the phases that form when large amounts of Cs are incorporated into the waste, as it may result in the formation of phases not found in this study, and thus change the corrosion properties.

5.4 Plasma Furnace-High Metal Surrogate

It is clear from visual inspection that with the amount of excess metal used the plasma furnace could not successfully convert all the waste elements and glass frit into a purely glassy sample, resulting in a glass encapsulated crystal type GCM, specifically, the crystalline portion was a metal/metal oxide (M/MO). As such the characterisation and corrosion aspects of each section are discussed separately before concluding on the resulting combined properties. This is an especially important method for determining the lifetime of such a wasteform due to the corrosion properties of each portion possibly being vastly different. The lifetime will ultimately be decided by the more vulnerable portion, if no interaction occurs between the two.

As described in section 4.3.1 the green and blue glassy portion was mainly silica, calcia and alumina, with little solubility for any other elements (3 wt% oxide total of minor elements). As the composition of the glass is similar to the ratio of elements contained in the glass frit it appears that few waste elements are contained in the bulk glass.

As was mentioned in the results, coloured sections of the glass were immediately evident from pictures; a light blue appearance and a light green (Figure 21), with other areas displaying a deep blue/black. It appears that with these colours the pore size and density changed considerably from relatively few large pores for the blue coloured glass (50-100 µm diameter, $2.7x10^{7}m^{-2}$) to small high density pores for the green (5-100 µm diameter, $3.48x10^{8}m^{-2}$). However, EDX analysis revealed little compositional differences for these regions.

Although not detected, iron in small amounts is well known to change the colour of glasses to a light green, indeed it is the reason that soda-lime glass used for bottles are of often green; iron impurities in silica sand causes the colour change and must be removed for clear window glass. Ferric and ferrous iron have different absorption spectra in silica glass, with ferric having maxima at 223, 378, 414, 442, and 470 nm, whilst ferrous having maxima at 190, 420, 1075 nm (results above visible spectrum omitted) [229]. The correlation of these wavelengths with that of the visible spectrum (350-780) would result in ferric iron absorbing violet, blue and green, with ferrous iron removing only blue. Further, the 1075 nm absorption band of ferrous iron is broad, and extends into the red/orange/yellow part of the visible spectrum removing or reducing these colours [229]. For a purely ferrous iron coloured glass, the result would be a blue-green glass, conversely, ferric iron would result in a green-yellow glass. In fact, both these colours existed in the glass shown in Figure 21 in the form of bands. The amount of ferric iron in the glass needed to produce a yellow colouring has been shown to be relatively high. Whilst no iron was detected by EDX, due to the small size of the yellow area and the lack of colour in SEM analysis, it is conceivable that that region was not analysed.

This hypothesis also explains the changes in pore size and density, during the thermal treatment, reduction of ferric iron to ferrous iron would cause the evolution of oxygen, illustrated in Equation 15. The viscosity of the melt would prohibit the evolved oxygen from fully escaping, thus when the glass solidified it would contain oxygen filled bubbles.

$$4Fe^{3+} + 2O^{2-} <> 4Fe^{2+} + O \qquad (15)$$

It has been previously shown [230], that changes in the melting point of sodium silicate glasses changes the Fe^{3+}:Fe^{2+} ratio, with the amount of ferrous iron increasing as the temperature increases, thus increasing the 1075 nm absorption band whilst simultaneous decreasing those associated with the ferric iron. It is unfortunate that the temperatures were not measured during the thermal processing of this glass, as it would allow comparison with Mirhadi and Mehdikhani who analysed the ratio as a function of temperature.

Further work to determine whether the above is true, would need to be performed, such as optical absorption spectroscopy ore extended X-ray absorption spectroscopy.

The crystalline portion was more complicated in comparison, displaying, multiple different phases (Figure 88-93). The various EDX maps collected demonstrate the complexity of the metal portion of the GCM in both composition and shape. Overall the number of different unique phases by composition was greater than 10, however some were in small enough amounts to go undetected by XRD. Within these phases several variations on them were found, displaying the same major elements but with slightly different amount of the minor elements, greater than the error of the machine. Given that small composition changes can lead to large differences in the properties of the resulting material, aluminium and steel for instance, the effect this has on the corrosion of individual phases and by extension the whole wasteform, is difficult to assess. The materials detected by XRD were periclase, haematite, nickel, aluminium-iron alloy, and magnesium-aluminium-iron alloy. In addition, the binary phases missed by XRD due to the amount present (<5 wt% ± 5%) but observable by SEM and EDX (Figure 88, 89, Figures 91-93 and Tables 36-40) were mainly based on iron-aluminium (metal), calcium-silicon (oxide), and magnesium-aluminium (oxide) with various trace elements such as silicon, magnesium, manganese, chromium, and nickel.

Identification of the exact Al-Fe phase present was performed using the ratio of the Al-Fe from EDX results (Table 37), and the Al-Fe binary phase diagram (Figure 125). As the operating temperatures of the furnace at least exceeded 1200 ^{o}C, with a maximum operating temperature of 1800 ^{o}C, it is possible that the initial waste metals could form all the phases present in this phase diagram. At the very least the phases from 60 at% aluminium up to 100% could theoretically form.

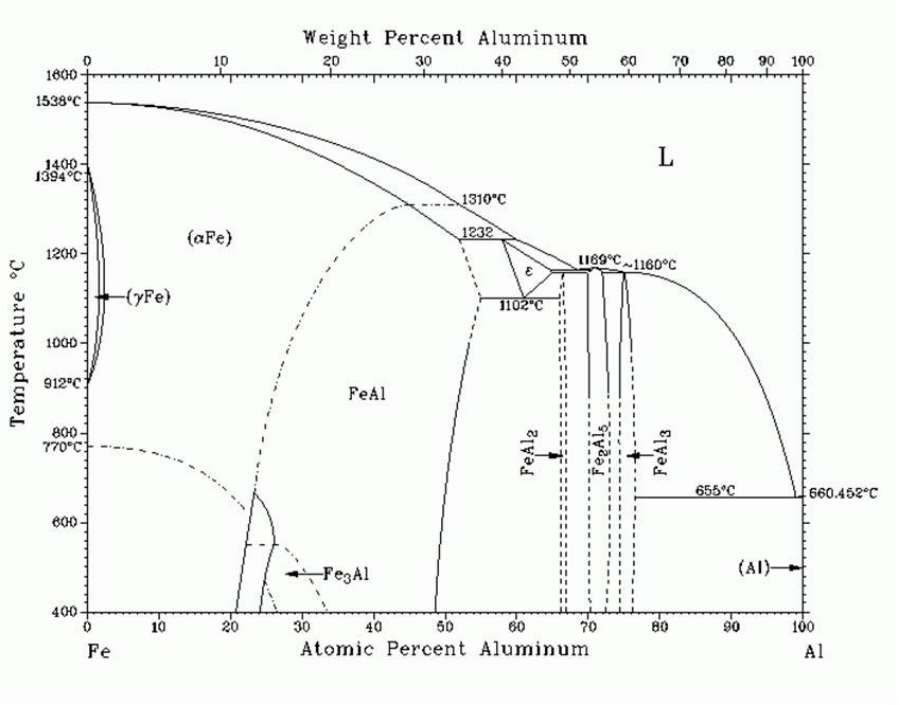

Figure 125: The Fe-Al binary phase diagram between 400 and 1600 °C [231].

Table 52: EDX results modified to show only the aluminium and iron content, giving a ratio of the two elements to allow identification. This calculation was performed on samples containing less than 7 wt% of other elements. Results are given in the original wt% and the at% for comparison with Figure 125.

Wt%	**Phase 1**	**Phase 2**	**Phase 3**	**Phase 4**	**Phase 5**	**Phase 6**
Al	63.4	41.7	36.3	54.2	38.8	61.9
Fe	36.6	58.4	63.7	45.8	61.2	38.1
At%						
Al	78.2	59.6	54.1	71.0	56.8	77.0
Fe	21.8	40.4	45.9	29.0	43.2	22.9

Whilst Fe-Al alloys have been studied for their low density, high strength, and oxidation resistance, little work has been performed on the Al rich end of the phase diagram (<50 at%) [232]. However, a thorough review was written by Xiaolin et al. specifically on the Al rich end. 5 different intermetallics have been identified, FeAl, Fe_5Al_8, $FeAl_2$, Fe_2Al_5, and Fe_4Al_{13}. Based on their review and the compositional analysis, the most likely phases present are $FeAl_2$, Fe_2Al_5, and FeAl.

Corrosion studies on such phases have been conducted in the context of how they affect the aluminium alloys when they are precipitated as intermetallic alloys during processing. As to the authors knowledge, no such study on a similar system to the one found exists due to its complexity, therefore only comparisons with simple systems can be used. Several authors [233,234] have found that the presence of iron intermetallic particles is detrimental to the corrosion resistance of the parent aluminium alloy. In the absence of iron intermetallics, corrosion of aluminium is simple in

that a protective layer develops halting further corrosion, however these inclusions will be sites for cathodic reactions and [234] found they can also act as pitting sites further enhancing corrosion at these particles. In addition, the corrosion of these particles has been found to cause localised increased in the pH acting as the cathode for the evolution of oxygen, in some cases Ph as high as 11 were documented [235]. Aluminium is unstable in this environment quickly degrading to aluminium hydroxide:

$$Al + 4OH^- = Al(OH)_4^- + 4e^- \quad (16)$$

The corrosive effect of the iron aluminide intermetallic's should be somewhat mitigated by the inclusion of silicon and nickel as minor elements (2.5 wt% and 3 wt% respectively) as has been found by Nis [236] however it is not completely removed. Overall the presence of these phases will most likely cause accelerated corrosion to occur to the aluminium phases often surrounding the particles.

Certain phases were present in large amounts but as thin films surrounding another phase, thus not readily detected by EDX. One such phase is the magnesium-iron alloy, a material used in the aerospace industry for lightweight applications. Compositions of these materials usually involve trace compositions of one element or the other, thus the phase observed which was 50 Mg, 50 Fe by weight with the addition of silicon, nickel and aluminium totalling less than 7 wt% could not be found in the literature.

The majority of the rest of the metal phases were all iron based (< 70 wt% Fe) containing various amounts of manganese, silicon, magnesium, aluminium, calcium, and chromium representative of the amount of iron used in the processing. From the compositions, it seems that a substantial amount of steel did not fully melt, as would be expected from the operating temperatures, however this did have an effect on the homogeneity of the metal as EDX revealed (Table 40) that chromium had been reduced to 6.5-14 wt% and pockets of chromium enriched areas had developed. This will have a detrimental effect on the metal as this amount of chromium present is insufficient for a protective layer to develop, although does offer some protection.

One of the main concerns with the wasteform was the rapid physical degradation of the metallic portion, following 2 weeks of corrosion the sample had disintegrated into a powder with some large remains. ICP results were not displayed as they had reached the maximum range for the standards used (50 ppm-100 ppm) for all the elements. The mechanism for this is thought to be due to the difference in densities between the hydroxides and oxides, and also the oxides and metals which would develop when in contact with water. This difference would lead to volume expansion putting strain on the entire material resulting in cracking; this would be made worse as the surrounding material was glassy. This phenomenon has been well documented in the process of cementation where alumina, magnesia, and lime all undergo this process. Pecqueur et al. [237] found when the pH is in excess of 10 aluminium corrodes via the following reaction:

$$Al + 4OH^- + 4H_2O \rightarrow 4AlO_2^- + 6H_2 \quad (17)$$

When the pH drops below 10, and remains in the 9-10 region (conditions this material was subject to) this then degrades further to aluminium oxide:

$$AlO_2^- + 2H_2O \rightarrow Al(OH)_3 + OH^- \quad (18)$$

These reactions result in a calculated expansion of around 2%. Indeed, Pecqueur et al. were documenting swelling caused by municipal solid waste incinerator bottom ash when encapsulated in bitumen for road/pavement usage. This corrosion progression of aluminium was documented as being one of the causes for the final wasteform cracking.

The reaction process for magnesia and calcia follows a similar progression:

$$CaO + H_2O \rightarrow Ca(OH)_2 \quad (19)$$

$$MgO + H_2O \rightarrow Mg(OH)_2 \quad (20)$$

As is found from studies on this reaction during the hardening of cement, the expansion of CaO to $Ca(OH)_2$ resulted in a molar solid volume expansion of around 90% [238], whilst MgO to $Mg(OH)_2$ resulted in a molar solid volume expansion of 117% [238].

Overall, the expansion of these phases explains why the short corrosion time resulted in a catastrophic failure in the structure of the specimen. ICP results exceeded the maximum standard used (100 ppm) after 2 weeks, and in all subsequent weeks. This makes this part (containing no glass) of the wasteform unsuitable for disposal for any lengths of time. It is safe to assume from the results collected, that rapid deterioration of the wasteform and subsequent collapse of the monolithic nature would result in large amounts of waste being released into the biosphere due to the large increase in surface area from monolith to powder.

Whilst this is indeed a poor result for a wasteform designed to last for 100s of years, this experiment only looked at the corrosion result of the portion where the waste elements segregated. As mentioned a blue glass developed with an approximate composition of the glass frit. The corrosion resistance of this phase was outstanding (Figure 100) showing no gel layer, or if a gel layer was present it would be smaller than 0.1 µm (using the highest magnification SEM, Figure 99), and an exceedingly small leached layer consistent at less than 2 µm for all times investigated (Table 43). If the susceptible portion of the waste was encapsulated in the more corrosion resistant glass the wasteform would be expected to contain waste elements from the biosphere for much longer than designed. This may prove difficult to accomplish due to the processing route, the design envisaged was a one-step treatment only, whereas this would require at least 2 treatments and modification to the furnace to ensure the waste was successfully encapsulated. At the very least, less metallic waste should be used in the heating process to ensure a homogeneous mix into a pure glass.

5.5 Plasma Furnace-Asbestos

The main objective of this trial as described in section 4.3.2 was to successfully render two species of asbestos based nuclear waste inert and therefore safe for disposal in a landfill site as LLW under normal conditions for asbestos waste, specifically this looked at destroying the fibrous nature of the asbestos used; where the harmful aspect of asbestos originates from.

Asbestos is the general name for several amphibole and serpentine minerals occurring naturally as fibres; the specific amphibole's classified as asbestos are anthophyllite ($Mg_7Si_8O_{22}(OH)_2$); riebeckite

($Na_2[Mg,Fe]_5Si_8O_{22}(OH)_2$); cummingtonite/grunerite series ($[Mg,Fe]_7Si_8O_{22}(OH)_2$)the asbestos in this series are known by the trade name amosite ; tremolite ($Ca_2[Mg_{4.5\text{-}5.0},Fe_{0.5\text{-}0.0}]Si_8O_{22}(OH)_2$); and actinolite ($Ca_2[Mg_{2.5\text{-}4.5},Fe_{1.5\text{-}0.5}]Si_8O_{22}(OH)_2$). Only one asbestos is found in the serpentine group, namely chrysotile with the general formula of $Mg_3(OH)_4Si_2O_5$. Originally these minerals were used due to their thermal properties as they provided a cheap method for insulation thus nuclear sites constructed/renovated before 1997 often contain such insulation. In addition to the problems associated with safe disposal of asbestos under normal conditions, any asbestos insulation that was present on a nuclear site will have the added hazard of possible contamination and thus will have to meet both criteria for safe disposal.

The dangers of these minerals are well known, and found to cause diseases such as mesothelioma, lung cancer, asbestosis, and pleural thickening; diseases which are long term and often fatal [239] thus any Asbestos Contaminated Materials (ACM) must be removed from the environment, through either destruction or immobilisation. To this end, characterisation of the final wasteform was used not only to help determine the phases present for corrosion assessment, but also to exclude the presence of any asbestos minerals.

XRD determined that the main phase was in fact an iron bearing form of diopside; no main peaks from chrysotile or amosite were found in this trace showing that the thermal destruction of the asbestos was successful, the traces for both these minerals are shown in Figure 126and Figure 127, the important peak is that at 11 2Θ, which was absent in the trace preformed on the final wasteform.

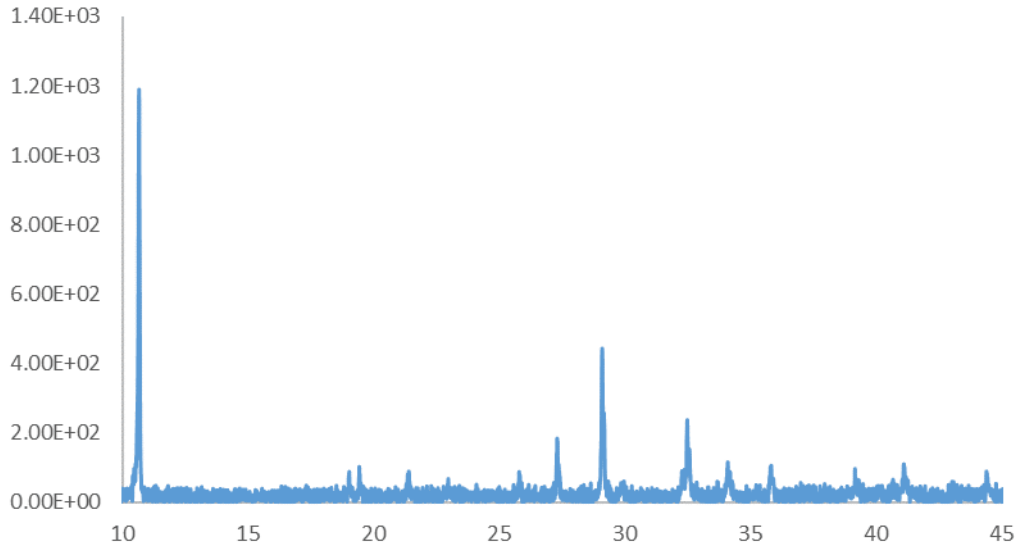

Figure 126: XRD data for amosite [PDF 44-1401].

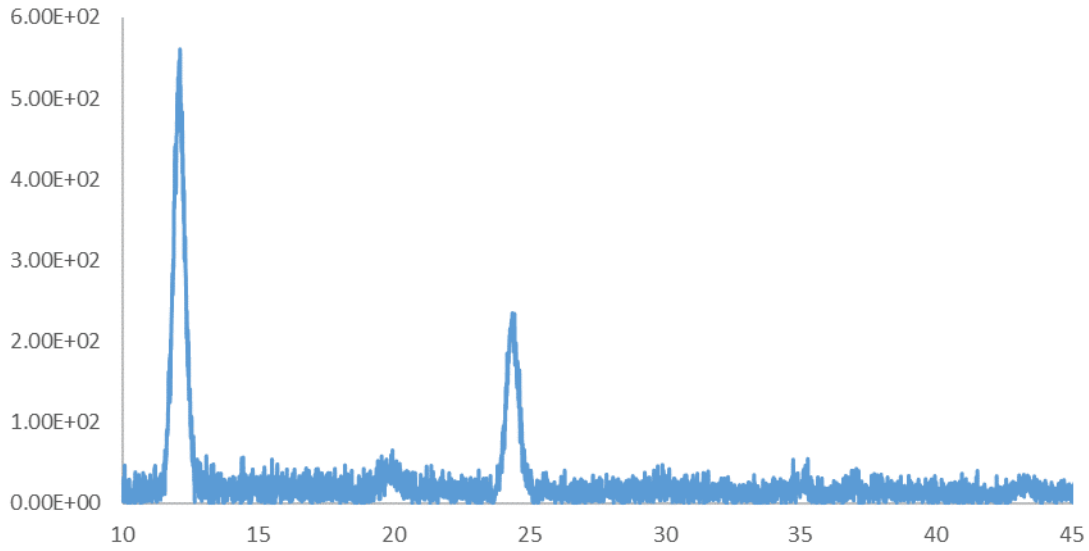

Figure 127: XRD data for chrysotile [RRUFF ID:R070088.1].

The operating temperature of the plasma furnace was sufficient to thermally destroy both the amosite and chrysotile with the decomposed phases posing no asbestos related health hazard. SEM-BSE confirmed the absence of fibrous material characteristic of asbestos, these fibres are usually 5 µm in width, 3 µm in breadth and have an aspect ratio of 3:1 for length, as a minimum [240] comparative SEM-SEI pictures are shown in Figure 128. Looking at the final waste-form using SEM (Figure 96), no such fibres could be seen, only the parallelepiped crystals already identified as diopside which were several times bigger in each dimension (20-80 µm).

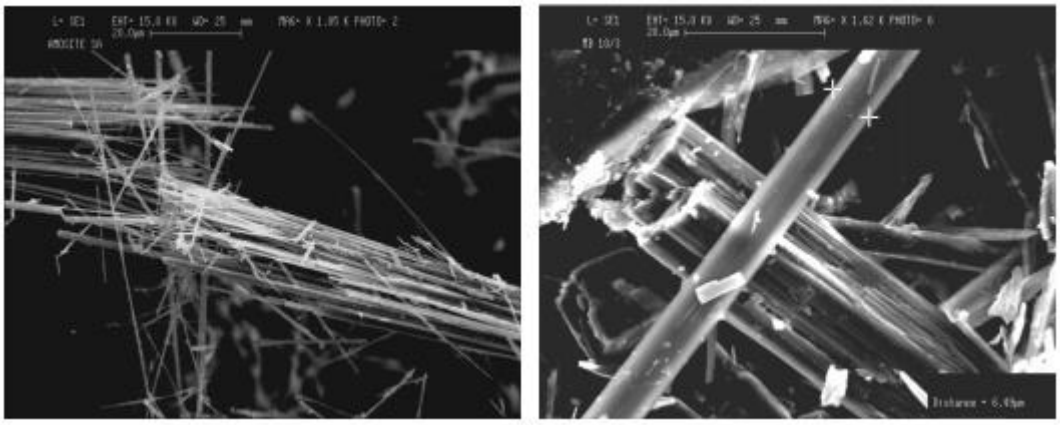

Figure 128: SEM-SEI of fibrous asbestos typical of both chrysotile and amosite [241].

Diopside containing GCM's are commonly used as glazes in ceramics for table ware and china, and more recently as a possible replacement in dental ceramics due to their promising properties such as hardness and corrosion resistance [135,138, and 242]. However, most literature on diopside containing GCM's reported that during processing it was often accompanied by a secondary crystalline phase such as enstatite and/or anorthite [243], and (pseudo) wollastonite [244], due to its tendency to form a solid solution with them. No evidence for either of these phases was found in XRD and EDX analysis (Figure 95and Table 41).

For non-nuclear based ACM only destruction of the asbestos is of concern after which safe disposal in a landfill site or similar is preformed, however when such waste is used in a nuclear environment further precaution is needed. For this reason, corrosion resistance of the GCM is still a concern due to the possibility that radioactive elements or toxic heavy metals (cobalt, nickel, copper, manganese, titanium, and chromium) present in the waste leaching into the biosphere through complete dissolution of the GCM or extensive leaching.

Most of studies on diopside corrosion and formation are concerned with stoichiometric diopside ($MgCaSi_2O_6$) whilst the diopside was found by EDX (Table 41) to contain both iron and aluminium replacement on the calcium and magnesium sites in relatively large amounts. This complicates comparison between results from this study with previously performed studies, to the authors knowledge no literature on the corrosion resistance of the substituted diopside exists.

Results from the corrosion of the GCM described in section 4.4.2 showed the diopside to have a higher resistance to chemical attack in alkaline solutions than its glassy counterpart, evident from both the depth profiles and surface analysis (Figure 102,and Figures 105-107). The originally polished surface resulted in a flat surface whereby the diopside crystals could only be identified using BSE (Figure 96), however following corrosion the crystals can be easily identified using SEI (Figure 102b). This result can be explained by a difference in relative height between the two phases allowing SEI, which shows contrast due to topographical differences, to identify the two phases as separate; further images of the cross section (Figure 103) confirmed the glass to be the more corroded phase. Depth profiles of the diopside also showed only a small leached layer of approximately 2 µm (Figure 107), which did not change over the entirety of the experiment duration (14 weeks). The corrosion resistance of diopside has been studied mainly in the fields of matt glazes and for disposal of incinerator waste, municipal waste, and industrial waste, where immobilisation of heavy metals is of primary concern [245].

Cracks developed in the glass from one diopside crystal to another (Figure 104). The amount of cracking was extensive, with most observed diopside crystals having multiple cracks leading from them however it was not extensive enough to cause fragmentation of the glass. The cracks themselves appeared localised to the surface only, cross sections exhibited no cracking past a depth of 10-50 µm and in addition, crack tips were nearly always blunt. This would suggest the cracking was most likely chemically induced similar to stress corrosion cracking, rather than thermal expansion mismatches from the 90 ^{o}C test which would be expected to cause cracking throughout the entirety of the sample, and not just at the surface. All the cracks observed contained thin lines of an iron containing phase, due to the oxygen content this was most likely an iron hydroxide and due to a very low solubility limit for iron in solution will probably have formed by precipitation.

This mechanism is likely due to a combination of the crystalline diopside acting as a good base from which to precipitate other crystalline phases, the increased surface area that arises due to the crack and the inability of iron to dissolve into solution in any significant amount. Additionally, the enclosed volume that these cracks create could act in a similar fashion to how pits cause accelerated corrosion in metals, a greater surface area and enclosed space results in a localised increase in ion concentration and pH, ideal conditions for corrosion and precipitation. The overall role these cracks played in the corrosion performance of the wasteform as a whole was increased concentrations of iron at the surface, but due to the localisation of these cracks to the surface, little structural

compromise is anticipated. This is supported by a lack of evidence for splintering of glass fragments, the handling of the samples post corrosion would have resulted in observable areas of pristine glass, where the corroded and cracked glass would've detached from the bulk; no such areas were found.

The expected life time of the sample is difficult to calculate, the glass will corrode faster than the diopside but its corrosion will eventually lead to exposed crystals of diopside, which would be vulnerable to being removed, by moving water for example. For these reasons, the normalised leach rates were calculated from the ICP and EDX results to better see how the corrosion progressed. The structural elements were first observed (Figure 109), the NL_r for Al and Si revealed a progressively downward trend, however silicon NL_r did increase slightly after 14 weeks, although it was unclear if this was a statistical anomaly or due to a yet unseen corrosion mechanism that started after 14 weeks. In general, this trend is promising, showing that the dissolution of the network is decreasing with time. However, it should be noted that these results reflect the combined Si and Al leach rates from both the diopside and glass and that the individual leach rates for each phase could be different. This could be an explanation for the increase in Si at 14 weeks; if one phase was releasing more Si as time progressed, and the other phase was releasing less, the combined Si release would appear as shown in Figure 109.

The theory that the Si release rate increase was due to two different release rates occurring for each phase is supported by the release rate of the remaining elements, in particular Mg and Na (Figure 110 and 111), which both showed increases after 10 and 6 weeks respectively. This can shed further light on how each phase is behaving as the majority of the Mg was in the diopside, and the majority of the Na in the glass. The large release rate of Mg at 14 weeks suggests an enhanced corrosion of the diopside; however, no indication of enhanced corrosion was found. Depth profiling for the glass did reveal an increasing leach depth with time, when compared to the pH progression, no accompanying increase in the gel layer was found. This result is further confirmed by the increase in pH at 14 weeks (Figure 108). Overall these results suggest that the glass leaching increased after 14 weeks, explaining the increase in Na and Si leach rates, and possibly explaining the increase in Mg. Whilst the glass contained an order of magnitude less Mg than the diopside, if the release rate was large enough it would explain the increased NL_r. A possible explanation for this result is the increase in iron filled cracks that occurred with time; it is possible the increase in surface area accelerated leaching of elements. For the first 10 weeks, glass leaching through the surface was greater than leaching through the increased surface area of the cracks. When leaching through the un-cracked surface reached a minimum (10-14 weeks), leaching through the cracks which ingressed into the sample would exceed the first, allowing observable results.

The decomposition of chrysotile results in forsterite, silica, and water:

$$2Mg_3Si_2O_5(OH)_4 > 3Mg_2SiO_4 + SiO_2 + 4H_2O \quad (21)$$

Similarly, amosite experiences a mass loss from dehydration at in the 500-700 ^oC region, decomposing by the following the below means:

$$([Mg], [Fe])_7Si_8O_{22}(OH)_2 > ([Mg],[Fe])_7Si_7O_{21} + SiO_2 + H_2O \quad (22)$$

All results point towards the diopside having a good retention for the waste elements and good corrosion resistance in general. The glass in comparison suffered from surface cracking, and a

leached layer up to 10 μm deep by 14 weeks. This cracking effect is thought to lead to enhanced leaching of waste elements in the glass (primarily Na and Mg), the effect increasing over time as more cracking of the glass occurs. Due to the increase in leaching occurring in the last week of the experiment, it is unclear if the leaching stabilises or worsens making a definitive life time of the wasteform uncertain.

5.6 Plasma Furnace-High Metal Surrogate 2

Simulated fuel cladding, pond solids, and plutonium contaminated material immobilisation using plasma thermal techniques was the objective of this part of the study as described in section 3.1.6 with all of the above posing difficulties for safe disposal, in particular pond solids. Inspection of the material received showed it to be made up of a mostly translucent green glass, with a small Metallic/Metal Oxide portion (M/MO). Overall the glass accounted for 95% (±3 wt%) by weight of the total material received. Experimentation on the M/MO potion could not be performed due to the small amount received.

The use of a plasma furnace with argon or nitrogen used for the plasma gas is the standard procedure and many similar trials (specifically PF-HMS) have been done, creating a reducing environment of carbon monoxide and hydrogen [246]. However, air was pumped into the furnace chamber for processing this sample having the opposite effect, leading to oxidation during the melt process. Indeed, this was the reason for the choice of air over argon/nitrogen; it was thought that oxidation of metal into their oxide counterparts would be preferable to the metallic form. Air was chosen to help oxidise the metallic waste leading to a homogeneous wasteform, and to some extent this was successful as it was clear a small amount of these wastes did not fully incorporate into the final wasteform. The metals involved would have different melting points, their oxides even more so, differences in specific gravity would result in these wastes sinking during the melting process, a common occurrence in treatment involving these sorts of wastes [247]. It is suggested that this can be mitigated by using a more aggressive stirring technique, other than the thermal convection which was used and thought to be effective enough to avoid such an outcome. Colour changes in the glass were due to the inhomogeneity of trace elements, no significant variation in composition was found for the major elements analysed.

Excluding the small M/MO portion, the glass was able to incorporate a large portion (~70 %) of the simulant mischmetal waste, however, none of the iron based waste had gone into the glassy phase, as no iron was detected. Based on the results from PF-HMS which displayed a similar glass + M/MO combination, along with the small metal portion received, it can only be concluded that the iron has sequestered into a M/MO phase as seen in PF-HMS, a mismatch in the amount of mischmetal used, and the amounts present in the glass suggests that some of these elements also sequestered into a separate phase. Calculations were performed to assess how much of the waste had been incorporated into the glassy phase (Table 53), as all the metal waste was placed together (Al and Mg rods, and various steel waste) 3 calculations were done; no waste was excluded, Fe only wastes were excluded, the Mg and Al rods (but not Mg/Al from other sources) and the Fe wastes were excluded. The calculation was made using the data from section 3.1.6, Table 17, and Table 18; each waste element was broken down into its constituent elements, further, it was assumed that all these elements went into a one, homogeneous phase thus allowing the composition of such a phase to be

calculated. Comparison of these results with the actual composition of the glass revealed the most likely waste element(s) that did not incorporate into the glass, for example, no Fe was detected in the glass thus no Fe based waste elements contributed to the final composition of the glass. With this knowledge the calculation was run again with the absence of this waste element and an additional waste element (e.g. Mg rods), which was again compared with the glass composition. This process was repeated until a composition close to the actual glass composition was achieved thus revealing the most likely waste elements that did not go into the glass, and therefore formed a separate phase(s).

This revealed that 20% of the lanthanum was not in the glass, and similarly, almost 20% of the calcium was present in another phase. The rest of the elements are in good agreement with the theoretical prediction of the glass composition.

Table 53: Theoretical calculations of the composition based on the removal of certain wastes from the initial setup. Predicted W/O fe shows the results if all iron based waste was not included in the processing giving the theoretical composition shown. Similar results were calculated for removal of all iron based waste + the removal of the aluminium and magnesium rods (but not those elements from the glass frit), shown as predicted W/O rods/Fe.

	Fe_2O_3	Al_2O_3	MgO	SiO_2	CaO	La_2O_3	Ce_2O_3
Predicted (all waste)	23.7	15.9	2.4	26.8	17.1	4.7	9.4
Predicted W/O Fe	0.00	20.4	5.3	34.4	21.9	6.0	12.0
Predicted W/O rods/Fe	0.00	15.2	2.5	38.1	24.3	6.7	13.3
Actual	0.00	12.3	1.9	35.6	29.2	8.3	12.8

The corrosion profiles of sample PF-HMS2 (Figures 113-117) exhibited odd behaviour in that they changed 3 times during the course of the experiment. Repeat experiments also yielded the same profile changes. The unusual profile is thought to be a result of how the corrosion layer behaves once formed. Once a gel layer forms, as was seen in this material, it is expected to act in a protective manner reducing the elemental leach rate and preventing further depolymerisation of the silica network. Normalised leach rates of silicon and aluminium, which form part of the glass structural network, show that this occurred with leach rates of these elements dropping steadily with time (Figure 119). However, normalised leach rates for magnesium (Figure 120) revealed a more erratic trend, at first sowing a decrease but at 14 weeks a large increase to the leach rate occurred. The NL_r for magnesium, along with the depth profiles is thought to come from removal of the surface layer during corrosion, and not as a result of any post corrosion handling. Removal of the gel layer would result in the exposed glass being re-attacked by the leachant, causing an increase in the leaching of elements at that time (and thus NL_r). This would also explain the drastic depth profile changes, the portion of the glass that had been re-attacked will have an extended leach zone when compared to the portions of the glass that had not had the surface layer removed.

If corrosion does follow the trend of gel layer forming, then removal, then at the conditions present in the experiment (90 ^{o}C, deionised water, no stirring etc.) a loss of 2 µm (±0.1 µm) of the glass surface every six weeks can be expected, as a worst-case scenario. For a 1 m^3 block of this glass to be fully corroded would take approximately 28,770 years. Considering this figure was calculated based

on a fully submerged block in water at 90 °C, it can be expected that this number will be much larger in surface repository conditions, resulting in a slower corrosion rate thus exceeding the requirement for ILW.

Whilst this review is limited to just the glassy component, it is suggested that further tests be done on the M/MO portion, should a larger portion than that provided here exist. However, based on corrosion results from JH-HMS, PF-HMS and PF-HMS2 (sections 4.2.2, 4.4.1 and 4.4.3 respectively) as they all had aspects of the M/MO (PF-HMS had a M/MO portion, JH-HMS had a Ce/La enriched phase), a reasonable prediction of the properties can be made. Due to the same heating regime, and technique (plasma furnace) used for PF-HMS, it can be assumed that all the metallic species with limited solubility in the glass (iron in this case) formed as oxides, mixed metal oxides, and unreacted metal. The results of JH-HMS showed that cerium, lanthanum, and silicon formed a phase when exposed to temperatures similar to those used for this wasteform. As was found in PF-HMS, the corrosion resistance of this M/MO wasteform was extremely poor, whilst JH-HMS found a reasonable corrosion resistance for the Ce-La silicate phase.

One of the main issues is the metal portion which went untested in this experiment, should it follow the same corrosion progression outlined in section 4.3.1, and summarised here, the release of the iron and the remaining cerium and lanthanum would be instantaneous relative to the timescales involved. This is highly undesirable, however using a theoretical scenario whereby a 1 m^3 block of glass/metal i.e. glass encapsulated metal, where the metal portion is located at the centre of the block, surrounded by glass. This issue would be vastly diminished in this case as it would take the previously determined time to reach the metal phase, which would be hoped by this time to be rendered inert.

5.7 General issues

Several issues arose that were common, or were applicable, to all the samples investigated and are discussed here.

5.7.1 Partitioning of plutonium simulants

The sequestration of the actinide simulants (Ce/La) into a single phase, or in this case partial sequestration, could pose an issue from a criticality point of view. Whilst the two elements were in both the glass and the CeLa silicate, the increased amount of these elements in the silicate phase could theoretically result in a criticality incident, an extremely undesirable event. However, the shape and size of the CeLa silicate should mitigate this extreme, most fissionable materials critical mass is determined based on the material having the shape of a sphere (the most efficient shape for this process); clearly this is not the case here. The small particle size, and spacing between particles should be enough to prevent any sort of criticality incident. Consistent with current safety measures in the field of nuclear and nuclear waste, a further precaution would be necessary, as a failsafe in the unlikely event that crystallisation did produces a phase that was both big enough and dense enough to produce a criticality event. It is suggested that the addition of a neutron poison be added to the GCM recipe, in particular, boron. The behaviour of boron as a neuron posion, and glass additive is already well known [248], with most HLW glasses containing boron for this reason. An additional neutron poison such as gadolinium could also be added, aimed at partitioning into the CeLa silicate

itself, further reducing a criticality event, however it is unclear if gadolinium would partition into this phase and should this course of action be taken, further research would be required.

With the addition of just boron to the recipe, coupled with the unfavourable microstructure of the CeLa silicate, this should reduce if not eliminate any criticality issues.

5.7.2 Anomalous pH at 14 weeks

At 14 weeks' corrosion time an increase in the pH was observed across all samples where pH was analysed, of approximately 0.5. It is unclear whether this was a statistical anomaly, or the beginning of a renewed corrosive attack on the samples. SEM images of both the cross sections and surface showed no evidence that a secondary corrosion mechanism was occurring; the images indicated that corrosion was reduced, in line with the relatively unchanged size of the leached layer, where one was present. Indeed, ICP-OES results confirm that a reduction in Si concentrations (a good indicator of network dissolution) occurred in all samples except PF-Asb. Further, only the PF-Asb sample showed any noticeable increase in other elements that could be responsible for an increased pH. Indeed, all other samples showed a decrease in the element concentration. Overall, the evidence would suggest that the increased pH at 14 weeks was either due to contamination, or due to the solution analysed being the last of solution in the digestion vessel; for all other aliquots, only a portion of the solution was removed (see section 3.4). There is evidence that this is conclusion may not apply to sample PF-Asb, where other analysis techniques suggested an increase in corrosion, more easily seen in the normalised leach rates for magnesium, and to some extent sodium. Further corrosion time experiments are necessary to establish the nature of the Ph increase, to assess whether it is a secondary corrosion mechanism, or an artefact of the experimentation setup.

The results from pH analysis revealed a sudden increase of approximately 0.5 at 14 weeks' corrosion time. Corresponding ICP-OES results also revealed an increase in the concentration of Si, Mg, and Na good indicators that network attack was occurring at an increased rate relative to previous times. This is clearly observed in the normalised leach rate results for these elements at that time. However, no corresponding change in either leach depth or SEM surface/cross sectional images were observed.

5.7.3 Normalised leach rate comparisons

Normalised leach rates for elements of importance from the materials analysed here are displayed in Table 54. In addition, comparative normalised leach rates for other materials are displayed in Table 55 note the comparative NL_R are often averaged over the experiment time and where this is the case the experiment duration is noted. Little literature exists on leach rates of cemented nuclear waste, as during experimentation on cement as a HLW encapsulate it was found to have an unacceptably high leach rate, relegating it to LLW/ILW encapsulation [249]. This is reflected in the release rate for sodium shown in Table 54, it has been reported that a generic (no elements quoted) intrinsic leach rate of cementitious wastes to be $100x10^{-6}$ g cm^{-2} day^{-1} [250].

The values shown are to allow for an approximate average NL_r for the materials shown.

Table 54 results from a generic ILW cement [251] (1 year), HLW borosilicate glass [252] (28 days), and yellow phase contaminated glass composite material (28 days), along with the noted normalised released rates for the elements shown.

Table 54: Comparison of cement, borosilicate glass, and yellow phase GCM normalised leach rates for Cs, Na, Sr, and combined actinides.

	NR_R (10^{-6} g/cm^2 day)			
Elements	**^{137}Cs**	**Na**	**Sr**	**Actinides**
Cement[1]	4.8	7300	-	-
Borosilicate glass[2]	0.3	0.9	0.3	-
Yellow phase gcm[2]	1-10	1-10	1-0.1	0.001

Table 55 summarises the important NL_R for the materials analysed here, and shows the highest NL_r found for that element over the course of the experiment. It is clear from these results that the GCMs analysed here outperform cement encapsulation by several orders of magnitude, not an unexpected result considering the general performance of cement versus glasses and ceramics for leach rates. Unexpectedly, they had lower NL_r for Na compared to typical HLW borosilicate glass. Considering the dual and sometimes multi-component facet to GCMs this value was expected to be much higher, clearly this is not the case, and is a promising indicator towards the durability of the wasteforms. However, these results cannot be taken as an absolute indicator of how well the GCMs will fair in the long term, as has already been discussed.

Table 55: Summarised leach rates for Na, Mg, Si, and Ca (where available) for all the wasteforms investigated here, with the exception of PF-HMS (due to ICP-OES data surpassing the maximum limit) for comparison with table 54. It is clear these wasteforms are on par with borosilicate glasses, and significantly better than cementation.

	NR_r (10^{-6} g/cm^2 day)			
Elements	**Na**	**Mg**	**Si**	**Ca**
JH-PCM	0.68	0.02	0.10	0.14
JH-HMS		0.16	0.08	0.09
JH-SIXEP	0.58	0.02	0.09	0.47
PF-Asb	2.93	0.04	0.10	0.23
PF-HM2		0.03	0.04	0.08

5.8 Summary

Table 56 is a tabled summary of all 6 wasteforms quickly showing the major/minor phases present, the corrosion products, and the corrosion behaviour of each wasteform. This allows for quick comparison between the two different thermal techniques used, the different wasteforms within each thermal technique, and for GCM's with similar phases. Finally, based on the results presented here, a recommendation on each wasteforms suitability for immediate disposal as an ILW is given.

Table 56: Summary of each wasteform showing the major phases, minor phases, the corrosion products, and the corrosion behaviour. A recommendation on the wasteforms suitability for ILW disposal is given.

Joule heated	**JH-PCM**	**JH-HMS**	**JH-SIXEP**
Major Phases	pigeonite, anorthite, and dual glasses	CeLa Silicate, Augite[a], CaMgFe Silicate, glass	Clino and proto Hypersthene, glass
Minor Phases	FeCr particles, diopside[b]	none	Magnetite
Corrosion products	Corrosion layer on crystals, and one glass	Corrosion layer on glass only	Corrosion layer over all phases
Corrosion Behaviour	Attack via second, unprotected glass. Pitting, attack on glass 1 via exposed sides	Attack via CaMgFeSi causing detachment of CeLa silicate from GCM	glass corrosion layer expanded over crystals
Suitable as ILW	Yes	Undetermined	Yes

Plasma Furnace	**PF-HMS**	**PF-Asb**	**PF-HMS2**
Major Phases	Glass, M/MO	Diopside, Glass	Glass (studied)
Minor Phases	n/a	FeCr particle	MMO (not studied)
Corrosion products	Not identified (multiple)	Corrosion layer, microcrystals	Corrosion layer
Corrosion Behaviour	Catastrophic failure of M/MO portion	Protective corrosion layer, Iron filled cracks formation of microcrystals on diopside	fully protective
Suitable as ILW	No	Yes	Undetermined[c]

a) Several other phases were possible, augite was chosen as the most likely. b) It could not be accurately established if this phase was present. c) Should the material contain an M/MO portion similar to that in sample PF-HMS, it would be unsuitable.

6.0 Future Work

The experimental work performed here forms a basis from which to remove unsuitable GCMs without the need of expensive, and lengthy experimental techniques such as ToF-SIMS. The GCMs with potential have been established, the poor ones discarded and these techniques should be used to further our understanding of them. More advanced techniques should be used to definitively characterise the phases present, as the techniques used here were insufficient to precisely determine their identity. The phases present, and any literature on their corrosion properties will be paramount in predicting how these GCMs may behave in the future; past the corrosion times used here.

One of the issues found here was the comparison of Joule heated technology versus plasma furnace technology. The plasma furnace was found to be inadequate for the successful vitrification/encapsulation of high metal content waste, most readily apparent in sample PF-HMS, and somewhat apparent in PF-HM2. As discussed on the glassy portion of sample PF-HMS, it is possible that the reason for this inability to cope with high metal content waste was due to the conditions on the melter being too reducing, allowing for the precipitation of metals into metallic and metal oxide phases, most evident from the colouration effect in the glass portion of PF-HMS. Should this be the case, changes in the temperatures and other conditions could allow for the successful incorporation of these wastes into a more stable wasteform, without sacrificing the benefits that plasma furnaces provide. This can be established using Mössbauer spectroscopy, fine X-ray absorption spectroscopy, and ion chromatography; further work should try to identify the ferric to ferrous ratio to this end. It is suspected the reason for the overly reducing conditions is excessive temperatures; this could be compensated for by altering the atmosphere of the melter itself.

Conversely to the failure of PF to treat high metal content waste, the success of the technology to process asbestos based waste was absolute; the asbestos was rendered completely inert by converting to an entirely different phase. Whilst more expensive than conventional asbestos disposal (cementation), “nuclear” asbestos requires special consideration. Based on the results found, this waste stream and thermal route are ready for next stage testing, using possibly radioactive versions of asbestos, and longer leach times. However, it is likely that this waste will be labelled as a LLW and so very little further work would be required; the main issue for this waste stream was the destruction of the asbestos.

Joule heated technology demonstrated a more than reasonable ability to immobilise and encapsulate difficult wastes, that are often problematic and cannot be dealt with using conventional means. Considering the dangers of these wastes, and the success demonstrated here, further trials are warranted in an effort to develop a wasteform that can deal with these wastes now. Too often progress is slowed by the reluctance to change from the tried and tested technique, to a new one, evident by the lack of a new wasteform to cope with these difficult wastes. For the wastes examined it is proven that the “tried and tested” is not suitable, whereas the materials investigated here are far more suitable than those we have available. The next stage in this process is to analyse how

these wasteforms cope using the actual wastes that were only simulated here. Should those tests also be a success, it is suggested that we begin using these wastes and thermal technique to begin disposal.

Additionally, longer corrosion times for several GCMs analysed here are required, such as in sample PF-Asb where NL_r increased near the end of the experiment, possible signifying a secondary corrosion mechanism. Regardless, any ILW will require extended time periods of corrosion tests to ensure that these wasteforms will immobilise/encapsulate their waste elements for thousands of years.

This thesis demonstrates that contrary to the current ideology that crystallisation in glasses should be kept to a minimum, sometimes the crystal phase(s) that form are better than the parent material, forming a material that overall has a longer lifetime. This is not a new development in this field, as has been discussed, much literature exists in many fields that have already come to this conclusion. Nuclear waste requires not one disposal route for each waste level as is the current method, but an array, to have several matrices from which to choose from. It is the authors opinion that further work should investigate the potential for GCMs to go past the research stage, and progress to large scale trials.

7.0 Conclusions

Six GCMs (3 using Joule heating and 3 using plasma technology) containing a variety of wastes were received from Sellafield and first characterised to identify the phases present, and then corroded using MCC-2 corrosion method. The wastes used were chosen to simulate ILW; high metal content, SIXEP waste containing plutonium contaminated material, Magnox sludge, pile fuel cladding, clinoptilolite, and asbestos, produced from various nuclear activities and legacy waste silos.

The wastes were characterised using XRD, and SEM-EDX to establish the composition of the various phases that formed, allowing for identification of the crystalline phases where possible. This in turn allowed for comparison with known literature on these phases and the corrosion results found here. Leaching tests using de-ionised water at 90 ^{o}C were performed from 2-14 weeks, both the samples and the solution were analysed using SEM-EDX, ICP-OES, and pH. The use of EDX line scans on cross sections of the sample was employed to acquire the elemental profile as a function of depth, revealing the presence of leached layers and/or corrosion/gel layers. This was used with EDX surface analysis to better understand how each sample had corroded, and more specifically, to see how each phase had corroded. ICP-OES analysis of the sample was used to calculate normalised leach rates for each GCM to further understand the overall corrosion resistance of the GCMs, and to establish whether these wastes were suitable for ILW on a surface repository.

The Joule heating thermal processing of the PCM waste, HMS, and SIXEP waste streams resulted in the formation of three crystal containing glasses from processing. All 3 samples had formed a non-stoichiometric pyroxene as the main crystalline component, (clinoenstatite/clinoferrosilite, pigeonite and augite, respectively). The clinoenstatite/ferrosilite and the pigeonite demonstrated a high corrosion resistance; more so than the bulk glass, showing a maximum leached depth of 2-5 μm compared to the glass which whilst showed a similar leach depth, had several microns of glass completely removed. The HMS waste which contained the augite, had simulated Pu material (Ce and La), which had sequestered into a highly durable dendritic Cerium/lanthanum oxide silicate. This was mitigated by the surrounding augite as it was the least durable phase of the GCM and resulted in the detachment of fragments of the Ce/La phase from the bulk. Interestingly, the PCM GCM had formed two CMAS glasses, with similar but differing composition. The corrosion properties of each glass were vastly different; demonstrating that even small composition changes to the glass can result in different corrosion properties. The predictions of the lifetime for these GCMs exceeded that required for surface disposal of ILW.

The plasma furnace samples consisted of two high metal surrogate waste GCMs, where the furnace intentionally had more metal waste added than the process was designed for, and an asbestos waste GCM. The HMS GCMs had resulted in a metal encapsulated glass, with a pure glassy component containing few waste elements, and a metal/metal oxide portion. Whilst the corrosion results of the glass in both samples were more than adequate for ILW disposal, the metal portion in one of the samples resulted in disintegration from a monolith into a powder like substance after 2 weeks of corrosion. The second HMS GCM did not have sufficient amount of the metal/metal oxide for experimental study. This result demonstrated that whilst the glass had an extremely good corrosion resistance for the wasteform to be suitable for disposal, the GCM would have to be engineered so as the glass fully encapsulated the metal portion to meet ILW disposal requirements. Practically this

would not be the case as the heavier metal portion would sink during thermal processing as no stirring was employed resulting in one face of the block containing all the metal/metal oxide. The asbestos containing GCM proved to be 100% effective in destroying the asbestos fibres, thus rendering them inert. The resulting phase was a durable diopside phase, with a leached depth of 3 μm. The diopside formed homogeneously making up almost 50% of the final wasteform.

One of the primary goals of this thesis was to not to only assess the durability of 6 GCMs produced using joule heating and plasma technology, but also to assess whether potential wasteforms could be reasonably analysed using mainly EDX and ICP-OES. The motivation behind this is to develop a quick method for determining whether a wasteform is suitable and warrants further research, and to eliminate wasteforms that are clearly unsuitable without the need for techniques such as SIMS or TEM which can often take months, and require an experienced operator; the techniques used here require little training to be proficient. In addition, it was shown that whilst NL_r might show the material to be suitable for disposal, effects unique to GCMs can occur which result in an unsuitable wasteform. In particular, importance should be placed on the corrosion properties of the weakest phase, as although the waste elements might be in a durable phase, the surrounding material may corrode at a rate which results in reactive surface increase of the waste-bearing phase and eventually release of this phase into the biosphere, in a method seen for the JH-HMS sample. Based on the results collected, further work is warranted on several of these samples, plasma furnace for disposal of asbestos seems to be a highly successful method for allowing disposal of these wastes as it removes the need for compliance with government requirements for asbestos containing waste; the final wasteform does not contain any. It is clear that plasma technology is unsuitable for large amounts of metallic waste, without the need for further heat treatments or stirring of the melt, other than that provided by convection. Overall, joule heating thermal techniques resulted in a wasteform that would exceed the requirements for ILW disposal and shows promise for making durable GCMs.

8.0 References

1 Mason, D. and Buchan, A. "Sellafield legacy wastes update." NuSAC (2007) P5 Open Paper; http://citeseerx.ist.psu.edu/viewdoc/download?doi=10.1.1.434.5563&rep=rep1&type=pdf.

2 Gregson, C. R., D. T. Goddard, M. J. Sarsfield, and R. J. Taylor. "Combined electron microscopy and vibrational spectroscopy study of corroded magnox sludge from a legacy spent nuclear fuel storage pond." Journal of Nuclear Materials 412, no. 1 (2011): 145-156.

3 Salama, S. N., and S. M. Salman. "Characterization of glass-ceramic corrosion and durability." Journal of the European Ceramic Society 13, no. 6 (1994): 521-528.

4 Hrma, P. "Crystallization during processing of nuclear waste glass." Journal of Non-Crystalline Solids 356, no. 52 (2010): 3019-3025.

5 Lee, W. E., M. I. Ojovan, M. C. Stennett, and N. C. Hyatt. "Immobilisation of radioactive waste in glasses, glass composite materials and ceramics." Advances in Applied Ceramics 105, no. 1 (2006): 3-12.

6 Lutze, W., in Radioactive Wasteforms for the Future, edited by Lutze, W., Ewing, R.C. (North Holland, Amsterdam, 1988), p. 31

7 Donald, I. W., B. L. Metcalfe, and RN J. Taylor. "The immobilization of high level radioactive wastes using ceramics and glasses." Journal of Materials Science 32, no. 22 (1997): 5851-5887.

8 Loiseau, P., D. Caurant, N. Baffier, L. Mazerolles, and C. Fillet. "Glass-ceramic nuclear waste forms obtained from SiO_2-Al_2O_3-CaO-ZrO_2-TiO_2 glasses containing lanthanides (Ce, Nd, Eu, Gd, Yb) and actinides (Th): study of internal crystallization." Journal of Nuclear Materials 335, no. 1 (2004): 14-32.

9 Loiseau, P., and D. Caurant. "Glass—ceramic nuclear waste forms obtained by crystallization of SiO_2-Al_2O_3-CaO-ZrO_2-TiO_2 glasses containing lanthanides (Ce, Nd, Eu, Gd, Yb) and actinides (Th): study of the crystallization from the surface." Journal of Nuclear Materials 402, no. 1 (2010): 38-54.

10 Ojovan, M. I., J. Juoi, O. K. Karlina, and W. E. Lee. "Processing ceramics for radioactive waste immobilisation." Advances in Science and Technology 45 (2006): 1986-1995.

11 J.M. Juoi, M.I. Ojovan, W.E. Lee. “Development of glass-composite materials for radioactive waste immobilisation.” Proc. ICEM’05, September 4-8, Glasgow, Scotland, ICEM05-1069, ASME (2005).

12 Ojovan, M. I., J. M. Juoi, and W. E. Lee. "Application of glass composite materials for nuclear waste immobilisation." J Pak Mater Soc 2, no. 2 (2008): 72-76.

13 Beall, G. H. "Design and properties of glass-ceramics." Annual Review of Materials Science 22, no. 1 (1992): 91-119.

14 Inaba T, Nagano M, Endo M. Investigation of plasma treatment for hazardous wastes such as fly ash and asbestos. Electrical Engineering in Japan. 1999 Feb 1;126(3):73-82.

15 Dellisanti F, Rossi PL, Valdrè G. Remediation of asbestos containing materials by Joule heating vitrification performed in a pre-pilot apparatus. International Journal of Mineral Processing. 2009 May 16;91(3):61-7.

16 Chapman CC, Buelt JL, Slate SC, Katayama YB, Bunnell LR. Vitrification of Hanford wastes in a joule-heated ceramic melter and evaluation of resultant canisterized product. Battelle Pacific Northwest Labs., Richland, WA (USA); 1979 Aug 1.

17 Tzeng CC, Kuo YY, Huang TF, Lin DL, Yu YJ. Treatment of radioactive wastes by plasma incineration and vitrification for final disposal. Journal of Hazardous Materials. 1998 Feb 28;58(1):207-20.

18 Sobolev IA, Dmitriev SA, Lifanov FA, Kobelev AP, Stefanovsky SV, Ojovan MI. Vitrification processes for low, intermediate radioactive and mixed wastes. Glass Technology. 2005 Feb 1;46(1):28-35.

19 McMillan, P. W., and C. E. Matthews. "Microporous glasses for reverse osmosis." Journal of Materials Science 11.7 (1976): 1187-1199.

20 Weber, W. J. , and Roberts, F. P. "A review of radiation effects in solid nuclear waste forms." Nuclear Technology 60.2 (1983): 178-198.

21 Frugier P, Martin C, Ribet I, Advocat T, Gin S. “The effect of composition on the leaching of three nuclear waste glasses: R7T7, AVM and VRZ.” Journal of Nuclear Materials. 2005 Nov 15;346(2):194-207.

22 Ernsberger, F. M. "Mechanical properties of glass." Journal of Non-Crystalline Solids 25.1 (1977): 293-321.

23 Matzke, Hj., and Vernaz, E. "Thermal and physicochemical properties important for the long term behavior of nuclear waste glasses." Journal of Nuclear Materials 201 (1993): 295-309.

24 Mysen, Bjorn, and Pascal Richet. “Silicate glasses and melts: properties and structure.” Book, Vol. 10. Elsevier, 2005. Chapter 4.

25 Zachariasen, W. H. "The atomic arrangement in glass." Journal of the American Chemical Society 54, no. 10 (1932): 3841-3851.

26 Stanworth, J. E. "Oxide glass formation from the melt." Journal of the American Ceramic Society 54, no. 1 (1971): 61-63.

27 Schilm, J., Herrmann, M. and Michael, G. "Corrosion of Si_3N_4 ceramics in aqueous solutions: Part 2. Corrosion mechanisms in acids as a function of concentration, temperature and composition." Journal of the European Ceramic Society 27, no. 12 (2007): 3573-3588.

28 Gieré, R., and Stille, P. "Energy, waste and the environment: a geochemical perspective." Geological Society of London, 2004. Page 41

29 Manara D, Grandjean A, Pinet O, Dussossoy JL, Neuville DR. Sulfur behavior in silicate glasses and melts: Implications for sulfate incorporation in nuclear waste glasses as a function of alkali cation and V 2 O 5 content. Journal of Non-Crystalline Solids. 2007 Jan 1;353(1):12-23.

30 Magnin M, Schuller S, Mercier C, Trebosc J, Caurant D, Majerus O, Angeli F, Charpentier T. Modification of molybdenum structural environment in borosilicate glasses with increasing content of boron and calcium oxide by 95Mo MAS NMR. Journal of the American Ceramic Society. 2011 Dec 1;94(12):4274-82.

31 Hrma P, Vienna JD, Wilson BK, Plaisted TJ, Heald SM. Chromium phase behavior in a multi-component borosilicate glass melt. Journal of non-crystalline solids. 2006 Jul 1;352(21):2114-22.

32 Li H, Darab JG, Smith PA, Schweiger MJ, Smith DE, Hrma PR. Effect of minor components on vitrification of low-level simulated nuclear waste glasses. Inst. of Nuclear Materials Management, Northbrook, IL (United States); 1995 Dec 31.

33 Stefanovsky SV, Ivanov IA, Gulin AN. Aluminophosphate glasses with high sulfate content. InMRS Proceedings 1994 (Vol. 353, p. 101). Cambridge University Press.

34 Bottinga, Y., and Weill, D. F. "The viscosity of magmatic silicate liquids; a model calculation." American Journal of Science 272.5 (1972): 438-475.

35 Risbud S.H., Kirkpatrick R.J., Taglialavore A.P., Montez B. “Solid-state NMR evidence of 4-, 5-, and 6-fold aluminum sites in roller-quenched SiO_2-Al_2O_3 glasses.” Journal of the American Ceramic Society. 1987 Jan 1;70(1).

36 Bunker B.C., Tallant D.R., Kirkpatrick R.J., Turner G.L. “Multinuclear nuclear magnetic resonance and Raman investigation of sodium borosilicate glass structures.” Physics and chemistry of glasses. 1990;31(1):30-41.

37 Bunker, B. C. "Molecular mechanisms for corrosion of silica and silicate glasses." Journal of Non-Crystalline Solids 179 (1994): 300-308.

38 Topping, J. A., and M. K. Murthy. "Effect of small additions of Al_2O_3 and Ga_2O_3 on the immiscibility temperature of Na_2O-SiO_2 glasses." Journal of the American Ceramic Society 56.5 (1973): 270-275.

39 Dunshi G, Zhiying H, Yuxia Y, Hanyi C, Zonghan L, Xianyu X, Ren H, Liqun Y. A study of alkali resistance of CaO · Al2O3 · SiO2 glasses. Journal of non-crystalline solids. 1986 Mar 1;80(1-3):341-50.

40 Shelby, J. E. "Formation and properties of calcium aluminosilicate glasses." Journal of the American Ceramic Society 68.3 (1985): 155-158.

41 Paul, A. "Chemical durability of glasses; a thermodynamic approach." Journal of Materials Science 12.11 (1977): 2246-2268.

42 Budd S.M. “The Mechanisms of chemical reaction between silicate glass and attacking agents: Part 1. Electrophilic and nucleophilic mechanisms of attack.” Physics and Chemistry of Glasses. 1961 Aug;2(4):111-4.

43 Clark D.E., Dilmore M.F., Ethridge E.C., Hench L.L. “Aqueous corrosion of soda-silica and soda-lime-silica glass.” Journal of the American Ceramic Society. 1976 Jan 1;59(1-2):62-5.

44 de Ligny D, Westrum E.F. “Entropy of calcium and magnesium aluminosilicate glasses.” Chemical Geology. 1996 Jun 7;128(1):113-28.

45 George AM, Stebbins JF. “Structure and dynamics of magnesium in silicate melts: A high-temperature 25Mg NMR study.” American Mineralogist. 1998 Sep 1;83(9-10):1022-9.

46 Cormier L, Neuville DR, Calas G. Structure and properties of low-silica calcium aluminosilicate glasses. Journal of Non-Crystalline Solids. 2000 Sep 30;274(1):110-4.

47 López-Delgado A, Tayibi H, Pérez C, Alguacil FJ, López FA. A hazardous waste from secondary aluminium metallurgy as a new raw material for calcium aluminate glasses. Journal of hazardous materials. 2009 Jun 15;165(1):180-6.

48 Toya T, Tamura Y, Kameshima Y, Okada K. Preparation and properties of CaO–MgO–Al 2 O 3–SiO 2 glass-ceramics from kaolin clay refining waste (Kira) and dolomite. Ceramics international. 2004 Dec 31;30(6):983-9.

49 Giordano D, Dingwell DB. Non-Arrhenian multicomponent melt viscosity: a model. Earth and Planetary Science Letters. 2003 Mar 30;208(3):337-49.

50 Thompson LM, Stebbins JF. Non-bridging oxygen and high-coordinated aluminum in metaluminous and peraluminous calcium and potassium aluminosilicate glasses: High-resolution 17O and 27Al MAS NMR results. American Mineralogist. 2011 May 1;96(5-6):841-53.

51 Mysen BO, Virgo D, Seifert FA. The structure of silicate melts: implications for chemical and physical properties of natural magma. Reviews of Geophysics. 1982 Aug 1;20(3):353-83.

52 Rossin R, Bersan J, Urbain G. Etude de la viscosité de laitiers liquides appartenant au système ternaire SiO 2-A1 2 O 3-CaO. Revue Internationale des Hautes Températures et Réfractaire. 1964;1:159-70.

53 Riebling EF. Structure of sodium aluminosilicate melts containing at least 50 mole% SiO2 at 1500 C. The Journal of Chemical Physics. 1966 Apr 15;44(8):2857-65.

54 Shannon RT, Prewitt CT. Effective ionic radii in oxides and fluorides. Acta Crystallographica Section B: Structural Crystallography and Crystal Chemistry. 1969 May 15;25(5):925-46.

55 Navrotsky A, Zimmermann HD, Hervig RL. Thermochemical study of glasses in the system $CaMgSi2O6\text{-}CaAl_2SiO_6$. Geochimica et Cosmochimica Acta. 1983 Aug 1;47(8):1535-8.

56 Holland, D., A. Mekki, I. A. Gee, C. F. McConville, J. A. Johnson, C. E. Johnson, P. Appleyard, and M. Thomas. "The structure of sodium iron silicate glass–a multi-technique approach." Journal of Non-Crystalline Solids 253, no. 1 (1999): 192-202.

57 Paul, A., and Zaman, M. S.. "The relative influences of Al_2O_3 and Fe_2O_3 on the chemical durability of silicate glasses at different pH values." Journal of Materials Science 13.7 (1978): 1499-1502.

58 Bishay, A., and Hayek, M. "Some physical properties of $CaO\text{-}Fe_2O$,-B-O, glasses in relation to structure." The Physics of Non-crystalline Solids: Fourth International Conference, Clausthal-Zellerfeld, 1976. Vol. 4. Trans Tech Publication, 1977.

59 Holland D, Mekki A, Gee IA, McConville CF, Johnson JA, Johnson CE, Appleyard P, Thomas M. The structure of sodium iron silicate glass–a multi-technique approach. Journal of non-crystalline solids. 1999 Aug 31;253(1):192-202.

60 Yu X, Day DE, Long GJ, Brow RK. Properties and structure of sodium-iron phosphate glasses. Journal of Non-Crystalline Solids. 1997 Jul 1;215(1):21-31.

61 Paul A, Zaman MS. The relative influences of Al_2O_3 and Fe_2O_3 on the chemical durability of silicate glasses at different pH values. Journal of Materials Science. 1978 Jul 21;13(7):1499-502.

62 Neuville DR, Cormier L, Massiot D. Al coordination and speciation in calcium aluminosilicate glasses: Effects of composition determined by 27 Al MQ-MAS NMR and Raman spectroscopy. Chemical geology. 2006 May 16;229(1):173-85.

63 Barbieri, L., Bonamartini, A. C. and Lancellotti, I. "Alkaline and alkaline-earth silicate glasses and glass-ceramics from municipal and industrial wastes." Journal of the European Ceramic Society 20.14 (2000): 2477-2483.

64 Adams, P. B. "Glass corrosion a record of the past? A predictor of the future?." Journal of Non-Crystalline Solids 67.1 (1984): 193-205.

65 Smets, Bruno M.J., and Tholen, M. G.W. "The absence of a mixed-alkali effect in the leaching of corrosion-resistant glasses." Journal of Materials Science 20.3 (1985): 1027-1032.

66 Hamilton, J. P., and Pantano, C. G. "Effects of glass structure on the corrosion behavior of sodium-aluminosilicate glasses." Journal Of Non-Crystalline Solids 222 (1997): 167-174.

67 Ojovan, M. I., and W. E. Lee. "Glassy wasteforms for nuclear waste immobilization." Metallurgical and Materials Transactions A 42, no. 4 (2011): 837-851.

68 Hench, L. L., D.E. Clark, and E. L. Yen-Bower. "Corrosion of glasses and glass-ceramics." Nuclear and Chemical Waste Management 1, no. 1 (1980): 59-75.

69 Doremus, R. H., and G. H. Sigel Jr. “Glass science.” New York: Wiley, 1994.

70 Ménard O., Advocat T., Ambrosi J.P., Michard A. “Behaviour of actinides (Th, U, Np And Pu) and rare earths (La, Ce And Nd) during aqueous leaching of a nuclear glass under geological disposal conditions.” Applied geochemistry. 1998 Jan 31;13(1):105-26.

71 Van Iseghem P, Aertsens M, Gin S, Deneele D, Grambow B, Strachan D, McGrail P, Wicks G. GLAMOR–or how we achieved a common understanding on the decrease of glass dissolution kinetics. Environmental Issues and Waste Management Technologies in the Materials and Nuclear Industries XII. 2009 Sep 21:115-26.

72 Frugier P, Gin S, Minet Y, Chave T, Bonin B, Godon N, Lartigue JE, Jollivet P, Ayral A, De Windt L, Santarini G. SON68 nuclear glass dissolution kinetics: Current state of knowledge and basis of the new GRAAL model. Journal of Nuclear Materials. 2008 Oct 15;380(1):8-21.

73 Doremus RH. Interdiffusion of hydrogen and alkali ions in a glass surface. Journal of Non-Crystalline Solids. 1975 Dec 1;19:137-44.

74 Frugier P, Gin S, Lartigue JE, Deloule E. SON68 glass dissolution kinetics at high reaction progress: mechanisms accounting for the residual alteration rate. InMRS Proceedings 2006 (Vol. 932, pp. 94-1). Cambridge University Press.

75 Geneste G, Bouyer F, Gin S. Hydrogen–sodium interdiffusion in borosilicate glasses investigated from first principles. Journal of Non-Crystalline Solids. 2006 Aug 15;352(28):3147-52.

76 Boksay Z, Bouquet G, Dobos S. Kinetics of formation of leached layers on glass surfaces. Physics and Chemistry of Glasses. 1968 Jan 1;9(2):69.

77 Tovena I, Advocat T, Ghaleb D, Vernaz E, Larche F. Thermodynamic and structural models compared with the initial dissolution rates of {open_quotes} SON {close_quotes} glass samples. Materials Research Society, Pittsburgh, PA (United States); 1994 Dec 31.

78 Feng X, Barkatt A. Structural Thermodynamic Model for the Durability and Viscosity of Nuclear Waste Glasses. InMRS Proceedings 1987 (Vol. 112, p. 543). Cambridge University Press.

79 Paul A. Chemical durability of glasses; a thermodynamic approach. Journal of materials science. 1977 Nov 1;12(11):2246-68.

80 Grambow, B., and Strachan, D. (1984) Leach testing of waste glasses under nearsaturation conditions. Materials Research Society Symposium Proceedings, 26, 623- 634

81 Vernaz ÉY. Estimating the lifetime of R7T7 glass in various media. Comptes Rendus Physique. 2002 Sep 1;3(7-8):813-25.

82 Gin S, Mestre JP. SON 68 nuclear glass alteration kinetics between pH 7 and pH 11.5. Journal of Nuclear Materials. 2001 May 31;295(1):83-96.

83 O'Neil JR, Taylor HP. The oxygen isotope and cation exchange chemistry of feldspars. American Mineralogist. 1967 Sep;52:1414-37.

84 Hellmann R, Cotte S, Cadel E, Malladi S, Karlsson LS, Lozano-Perez S, Cabié M, Seyeux A. Nanometre-scale evidence for interfacial dissolution–reprecipitation control of silicate glass corrosion. Nature materials. 2015 Mar 1;14(3):307-11.

85 Frankel G.S. “Pitting corrosion of metals a review of the critical factors.” Journal of the Electrochemical Society. 1998 Jun 1;145(6):2186-98.

86 Dueffer P.F. “Glass reactivity and its potential impact on coating processes.” In proceedings of the annual technical conference-society of vacuum coaters 1996 (pp. 174-186).

87 Hupa L., Bergman R., Fröberg L., Vane-Tempest S., Hupa M, Kronberg T., Pesonen-Leinonen E., Sjöberg A.M. “Chemical resistance and cleanability of glazed surfaces.” Surface Science. 2005 Jun 10;584(1):113-8.

88 Hench L.L, Clark D.E. “Physical chemistry of glass surfaces. “Journal of Non-Crystalline Solids. 1978 Apr 1;28(1):83-105.

89 Messiga B, Riccardi M.P. “Alteration behaviour of glass panes from the medieval Pavia Charterhouse (Italy).” Journal of Cultural Heritage. 2006 Dec 31;7(4):334-8.

90 King F, Padovani C. “Review of the corrosion performance of selected canister materials for disposal of UK HLW and/or spent fuel.” Corrosion Engineering, Science and Technology. 2011 Apr 1;46(2):82-90.

91 Williamson A.J., Morris K., Shaw S., Byrne J.M., Boothman C., Lloyd J.R. “Microbial reduction of Fe (III) under alkaline conditions relevant to geological disposal.” Applied and Environmental Microbiology. 2013 Jun 1;79(11):3320-6.

92 Biederman G., Schindler P.A. “On the solubility product of precipitated iron hydroxide.” Acta Chem. Scand. 1957;11(4).

93 Tang Z., Hong S., Xiao W., Taylor J. “Characteristics of iron corrosion scales established under blending of ground, surface, and saline waters and their impacts on iron release in the pipe distribution system.” Corrosion Science. 2006 Feb 28;48(2):322-42.

94 Buckwalter, C. Q., and L. R. Pederson. "Inhibition of nuclear waste glass leaching by chemisorption." Journal of the American Ceramic Society 65.9 (1982): 431-436.

95 McVay, G.L. Buckwalter C.Q."Effect of iron on waste-glass leaching." Journal of the American Ceramic Society 66.3 (1983): 170-174.

96 Donald, I. W., B. L. Metcalfe, and RN J. Taylor. "The Immobilization Of High Level Radioactive Wastes Using Ceramics And Glasses." Journal of Materials Science 32.22 (1997): 5851-5887.

97 Ewing, Rodney C., and Werner Lutze. "High-Level Nuclear Waste Immobilization With Ceramics." Ceramics International 17.5 (1991): 287-293.

98 Ringwood A.E., Oversby V.M., Kesson S.E., Sinclair W., Ware N., Hibberson W., Major A. “Immobilization of high-level nuclear reactor wastes in SYNROC: A current appraisal.” Nuclear and Chemical Waste Management. 1981 Jan 1;2(4):287-305.

99 Lumpkin G.R., Smith K.L., Gieré R., Williams C.T. “Geochemical behaviour of host phases for actinides and fission products in crystalline ceramic nuclear waste forms.” Geological Society, London, Special Publications. 2004 Jan 1;236(1):89-111.

100 Smith K.L, Lumpkin G.R., Blackford M.G., Day R.A., Hart .KP. “The durability of Synroc.” Journal of Nuclear Materials. 1992 Aug 2;190:287-94.

101 White, W. B. "Theory of Corrosion of Glass and Ceramics" Corrosion of Glass, Ceramics and Ceramic Superconductors (1992): 2-28.

102 Utton CA, Hand RJ, Bingham PA, Hyatt NC, Swanton SW, Williams SJ. Dissolution of vitrified wastes in a high-pH calcium-rich solution. Journal of Nuclear Materials. 2013 Apr 30;435(1):112-22.

103 Wang Q., Yan J., Tu X., Chi Y., Li X., Lu S., Cen K. “Thermal treatment of municipal solid waste incinerator fly ash using dc double arc argon plasma.” Fuel. 2009 May 31;88(5):955-8.

104 Chang J.S., Urashima K., Tong Y.X., Liu W.P., Wei H.Y., Yang F.M., Liu X.J. "Simultaneous removal of NO_x and SO_2 from coal boiler flue gases by DC corona discharge ammonia radical shower systems: pilot plant tests." Journal of Electrostatics 57.3 (2003): 313-323.

105 Sobiecka E., Cedzynska K., Smolinska B. “Vitrification as an alternative method of medical waste stabilization.” Fresenius Environmental Bulletin. 2010 Jan 1;19(12a):3045-8.

106 Heberlein, J., and Murphy, A. B.. "Thermal plasma waste treatment." Journal of Physics D: Applied Physics 41.5 (2008): 053001.

107 Morris, J. "Recycling versus incineration: an energy conservation analysis." Journal of Hazardous Materials 47.1 (1996): 277-293.

108 Boulos, M. I. "Thermal plasma processing." Plasma Science, IEEE Transactions on 19, no. 6 (1991): 1078-1089.

109 Gomez E., Rani D.A., Cheeseman C.R., Deegan D., Wise M., Boccaccini A.R.” Thermal plasma technology for the treatment of wastes: a critical review.” Journal of Hazardous Materials. 2009 Jan 30;161(2):614-26.

110 Reynolds, Q. G. "The dual-electrode DC arc furnace-modelling brush arc conditions." Journal of the Southern African Institute of Mining and Metallurgy 112.7 (2012): 605-611.

111 Buelt, J. L., and J. H. Westsik. “ In situ vitrification: Preliminary results from the first large-scale radioactive test. “ No. PNL-SA-15277; CONF-880354-5. Pacific Northwest Lab., Richland, WA (USA), 1988.

112 Thompson, L. E. “Mixed waste treatment cost analyses for a range of geomelt vitrification process configurations.” AMEC Earth and Environmental, Inc. 309 Bradley Blvd., Suite 115, Richland, WA (US), 2002.

113 Steiner, Herbert, Manfred Edlmann, and Rudolf Meierhofer. "Glass-ceramic cooktop." U.S. Patent No. 5,844,206. 1 Dec. 1998.

114 Döhring T., Jedamzik R., Thomas A., Hartmann P. “Forty years of ZERODUR mirror substrates for astronomy: review and outlook. “ In SPIE Astronomical Telescopes+ Instrumentation 2008 Jul 14 (pp. 70183B-70183B). International Society for Optics and Photonics.

115 Sengupta P. “A review on immobilization of phosphate containing high level nuclear wastes within glass matrix–Present status and future challenges.” Journal of Hazardous Materials. 2012 Oct 15;235:17-28.

116 Watson E.B. “Two-liquid partition coefficients: experimental data and geochemical implications.” Contributions to Mineralogy and Petrology. 1976 Jan 1;56(1):119-34.

117 Mahood G., Hildreth W. “Large partition coefficients for trace elements in high-silica rhyolites. Geochimica et Cosmochimica Acta. “ 1983 Jan 31;47(1):11-30.

118 Dingwell D.B., Hess K.U., Knoche R. “Granite and granitic pegmatite melts: volumes and viscosities.” Geological Society of America Special Papers. 1996 Jan 1;315:65-72.

119 Scheetz B.E., Agrawal .D.K, Breval E., Roy R. “Sodium zirconium phosphate (NZP) as a host structure for nuclear waste immobilization: A review. “ Waste Management. 1994 Jan 1;14(6):489-505.

120 O. Terra, N. Dacheux, F. Audubert, R. Podor, "Immobilization of tetravalent actinides in phosphate ceramics" J. Nucl. Mater. 352, 2006, 224-232

121 James, P. F. "Kinetics of crystal nucleation in silicate glasses." Journal of Non-Crystalline Solids 73.1 (1985): 517-540.

122 Loiseau P., Caurant D., Baffier N., Mazerolles L., Fillet C."Glass–ceramic nuclear waste forms obtained from SiO_2–Al_2O_3–CaO–ZrO_2–TiO_2 glasses containing lanthanides (Ce, Nd, Eu, Gd, Yb) and actinides (Th): Study of internal crystallization." Journal of nuclear materials 335.1 (2004): 14-32.

123 Wicks, George G., and Wayne A. Ross. "Nuclear waste management." Advances in ceramics, vol. 8; 1984; p. 1-5; American Ceramic Society; Columbus, OH (USA); 85. American Ceramic Society annual meeting; Chicago, IL (USA); 25-28 Apr 1983; CONF-830451--

124 Caurant D., Majérus O., Loiseau P., Bardez I., Baffier N., Dussossoy J.L. “Crystallization of neodymium-rich phases in silicate glasses developed for nuclear waste immobilization.” Journal of Nuclear Materials. 2006 Aug 1;354(1):143-62.

125 Dormuth K.W., Nuttall K. “The Canadian nuclear fuel waste management program.” Radioact. Waste Manage. Nucl. Fuel Cycle. 1987;8(2-3):93-104.

126 Bancroft G.M., Metson J.B., Kanetkar S.M., Brown J.D. “Surface studies on a leached sphene glass.” Nature. 1982 Oct;299:708-10.

127 Vance, E. R., and J. B. Metson. "Radiation damage in natural titanites." Physics and Chemistry of Minerals 12.5 (1985): 255-260.

128 Hayward P.J., Hocking W.H., Mitchell S.L., Stanchell M.A. "Leaching studies of sphene-based glass-ceramics."Nuclear and Chemical Waste Management 5.1 (1984): 27-37.

129 Digeos A.A., Valdez J.A., Sickafus K.E., Atiq S., Grimes R.W., Boccaccini A.R. "Glass matrix/pyrochlore phase composites for nuclear wastes encapsulation." Journal of Materials Science 38.8 (2003): 1597-1604.

130 Lee W.E., Ojovan M.I., Stennett M.C., Hyatt N.C. “Immobilisation of radioactive waste in glasses, glass composite materials and ceramics. “ Advances in Applied Ceramics. 2013 Jul 18.

131 Boccaccini A.R., Bernardo E., Blain L., Boccaccini D.N. “Borosilicate and lead silicate glass matrix composites containing pyrochlore phases for nuclear waste encapsulation.” Journal of Nuclear Materials. 2004 May 1;327(2):148-58.

132 Pace S., Cannillo V., Wu J., Boccaccini D.N., Seglem S., Boccaccini A.R. “Processing glass–pyrochlore composites for nuclear waste encapsulation.” Journal of Nuclear Materials. 2005 May 1;341(1):12-8.

133 Topp S.V. “Scientific basis for nuclear waste management.” Elsevier Science Publishing Company, Inc., New York; 1982 Jan 1. pp. 69-81.

134 Tulyaganov D.U., Agathopoulos S., Ventura J.M., Karakassides M.A., Fabrichnaya O., Ferreira J.M. “Synthesis of glass–ceramics in the CaO–MgO–SiO_2 system with B_2O_3, P_2O_5, Na_2O and CaF_2 additives.“ Journal of the European Ceramic Society. 2006 Dec 31;26(8):1463-71.

135 Fröberg L., Hupa L., Hupa M. “Corrosion of the crystalline phases of matte glazes in aqueous solutions.” Journal of the European Ceramic Society. 2009 Jan 31;29(1):7-14.

136 Leroy C., Ferro M.C., Monteiro R.C., Fernandes M.H. “Production of glass-ceramics from coal ashes.” Journal of the European Ceramic Society. 2001 Feb 28;21(2):195-202.

137 Manfredini, L. Barbieri’T. "Vitrification Of Fly Ash From Thermal Power Stations." Glass Technol 38.5 (1997): 165-70.

138 Toya T., Tamura Y., Kameshima Y., Okada K. "Preparation and properties of CaO–MgO–Al_2O_3–SiO_2 glass-ceramics from kaolin clay refining waste (kira) and dolomite." Ceramics International 30.6 (2004): 983-989.

139 Barbieri L., Bonamartini A.C., Lancellotti I. “Alkaline and alkaline-earth silicate glasses and glass-ceramics from municipal and industrial wastes.” Journal of the European Ceramic Society. 2000 Dec 31;20(14):2477-83.

140 Alizadeh, P., and Marghussian, V. K.. "Effect of nucleating agents on the crystallization behaviour and microstructure of SiO_2–CaO–MgO (Na_2O) glass-ceramics." Journal of the European Ceramic Society 20.6 (2000): 775-782.

141 Juoi, J. M., and M. I. Ojovan. "Characterisation and durability of glass composite waste forms immobilising spent clinoptilolite." Waste Management Conference Proceeding, Tucson, AZ, USA. 2007.

142 Bosch P., Caputo D., Liguori B., Colella C. “Safe trapping of Cs in heat-treated zeolite matrices.” Journal of Nuclear Materials. 2004 Jan 15;324(2):183-8.

143 Cappelletti P., Rapisardo G., De Gennaro B., Colella A., Langella A., Graziano S.F., Bish D.L., De Gennaro M. “Immobilization of Cs and Sr in aluminosilicate matrices derived from natural zeolites.” Journal of Nuclear Materials. 2011 Jul 31;414(3):451-7.

144 Henry N., Deniard P., Jobic S., Brec R., Fillet C., Bart F., Grandjean A., Pinet O. “Heat treatments versus microstructure in a molybdenum-rich borosilicate.” Journal of Non-Crystalline Solids. 2004 Feb 1;333(2):199-205.

145 Donald, I. W., and B. L. Metcalfe. "Thermal properties and crystallization kinetics of a sodium aluminophosphate based glass." Journal of Non-Crystalline Solids 348 (2004): 118-122.

146 Ringwood, A. E. "Disposal of high-level nuclear wastes: a geological perspective." Mineral. Mag. 49.2 (1985): 159

147 Corrosion-inhibited metal-glass." U.S. Patent 3,205,566, issued September 14, 1965.

148 Ahmad Z. “Principles of corrosion engineering and corrosion control.” Butterworth-Heinemann; 2006 Sep 18.

149 Schneider M., Kremmer K., Lämmel C., Sempf K., Herrmann M. “Galvanic corrosion of metal/ceramic coupling.” Corrosion Science. 2014 Mar 31;80:191-6.

150 Gouda, V. K. "Corrosion and corrosion inhibition of reinforcing steel: I. immersed in alkaline solutions." British Corrosion Journal 5.5 (1970): 198-203.

151 Almusallam A.A. “Effect of degree of corrosion on the properties of reinforcing steel bars.” Construction and Building Materials. 2001 Dec 31;15(8):361-8.

152 Chyung, C. K. "Secondary grain growth of Li_2O-Al_2O_3-SiO_2-TiO_2 glass-ceramics." Journal of the American Ceramic Society 52.5 (1969): 242-245.

153 Holand W., Beall G.H. “Glass ceramic technology.” John Wiley & Sons; 2012 Jun 8.

154 Wang X., Chen M., Zhu S., Wang F. "Interfacial reactions between a SiO_2 Al_2O_3 ZnO CaO based glass and alpha alumina." Surface and Coatings Technology 232 (2013): 6-12.

155 Trivedi, R., and V. Laorchan. "Crystallization from an amorphous matrix—I. Morphological studies." Acta metallurgica 36.8 (1988): 1941-1950.

156 Cocić M., Logar M., Matović B., Poharc-Logar V. “Glass-ceramics obtained by the crystallization of basalt. ” Science of Sintering. 2010;42:383-8.

157 Romero M., Rawlings R.D., Rincón J.M. “Development of a new glass–ceramic by means of controlled vitrification and crystallisation of inorganic wastes from urban incineration.” Journal of the European Ceramic Society. 1999 Oct 31;19(12):2049-58.

158 Shibayan, R., and Basu, B. "Hardness properties and microscopic investigation of crack–crystal interaction in SiO_2–MgO–Al_2O_3–K_2O–B_2O_3–F glass ceramic system." Journal of Materials Science: Materials in Medicine 21.1 (2010): 109-122.

159 Mehulić K. “Glass-Ceramics.” Acta Stomat Croat. 2005 Jan 1;483:486.

160 Tian Y., Zuo W., Chen D. “Crystallization evolution, microstructure and properties of sewage sludge-based glass–ceramics prepared by microwave heating.” Journal of Hazardous Materials. 2011 Nov 30;196:370-9.

161 Michie E.M., Grimes R.W., Boccaccini A.R. “Hot-pressed phosphate glass–ceramic matrix composites containing calcium phosphate particles for nuclear waste encapsulation.” Journal of Materials Science. 2008 Jun 1;43(12):4152-6.

162 Juoi J.M., Ojovan M..I, Lee W.E. “Microstructure and leaching durability of glass composite wasteforms for spent clinoptilolite immobilisation.” Journal of Nuclear Materials. 2008 Jan 31;372(2):358-66.

163 Pace S., Cannillo V., Wu J., Boccaccini D.N., Seglem S., Boccaccini A.R. “Processing glass–pyrochlore composites for nuclear waste encapsulation.” Journal of nuclear materials. 2005 May 1;341(1):12-8.

164 Ojovan M.I., Juoi J.M., Boccaccini A.R., Lee W.E. “Glass composite materials for nuclear and hazardous waste immobilisation.” In MRS Proceedings 2008 (Vol. 1107, p. 245). Cambridge University Press.

165 Rushton, M. J.D., Grimes, R. W. and Owens, S. L. "Predicted changes to alkali concentration adjacent to glass–crystal interfaces" Journal of the American Ceramic Society 91, no. 5 (2008): 1659-1664.

166 Litton D.A., Garofalini S.H. “Molecular dynamics simulations of calcium aluminosilicate intergranular films on (0001) Al_2O_3 facets.” Journal of the American Ceramic Society. 2000 Sep 1;83(9):2273-81.

167 Rushton M.J., Grimes R.W., Owens S.L. “Partial ordering of glass networks adjacent to simulated glass–crystal interfaces.” Journal of Non-Crystalline Solids. 2011 Aug 31;357(16):3278-87.

168 Pinet O., Grandjean A., Frugier P., Rabiller H., Poissonnet S. “Leaching behavior of a polyphase glass–ceramic containment matrix.” Journal of non-crystalline solids. 2006 Aug 15;352(28):3095-102.

169 Marra JC, Cozzi AD, Pierce RA, Pareizs JM, Jurgensen AR, Missimer DM. Cerium as a surrogate in the plutonium immobilized form. Environmental Issues and Waste Management Technologies in the Ceramic and Nuclear Industries VII. 2001 Apr:381-8.

170 Zamoryanskaya MV, Burakov BE. Feasibility limits in using cerium as a surrogate for plutonium incorporation in zircon, zirconia and pyrochlore. InMRS Proceedings 2000 (Vol. 663, p. 301). Cambridge University Press.

171 Kolman DG, Park Y, Stan M, Hanrahan Jr RJ, Butt DP. An assessment of the validity of cerium oxide as a surrogate for plutonium oxide gallium removal studies. LANL, US1999. 1999 Feb.

172 Stockdale JA, Bostick WD, Hoffmann DP, Lee HT. Surrogate formulations for thermal treatment of low-level mixed waste. Part 1: Radiological surrogates. Oak Ridge K-25 Site, TN (United States); Oak Ridge Associated Universities, Inc., TN (United States); 1994 Jan 1.

173 Private Communication with Sellafield Ltd.

174 Zipperian, D. “Silicon Carbide Abrasive Grinding”, Quality Matters Vol I, 2002 pg 1, Found at (16/01/2017); http://metallographic.com/Newsletters/SIC-newsletter2.PDF

175 P. J., Potts, “A handbook of silicate rock analysis.” Vol. 622. Glasgow; London: Blackie, 1987. Page 336

176 P. J., Potts, “A handbook of silicate rock analysis.” Vol. 622. Glasgow; London: Blackie, 1987. Page 37

177 Danilatos, G. D. "Review and outline of environmental SEM at present." Journal of Microscopy 162.3 (1991): 391-402.

178 C.,Travier,. "Review of electron guns." Proceedings of the Fourth European Particle Conference, World Scientific Published Co. Pte. Ltd. Vol. 1. 1994.

179 D. B.,Holt and Joy,D. C. eds. “SEM microcharacterization of semiconductors.” Vol. 12. Academic Press, 2013. Page 52

180 Goldstein J., Newbury D.E., Echlin P., Joy D.C., Romig Jr A.D., Lyman C.E., Fiori C., Lifshin E. “Scanning electron microscopy and X-ray microanalysis: a text for biologists, materials scientists, and geologists.” Springer Science & Business Media; 2012 Dec 6.

181 Robinson V.N. “Imaging with backscattered electrons in a scanning electron microscope scanning.” 1980 Jan, Scanning Vol.3; 15-26.

182 Meyers H.P., Myers H.P. “Introductory solid state physics.” CRC press; 1997 Apr 26.

183 Blazek, A. (Ed.). Thermal Analysis: proceedings of the 8th ICTA, Bratislava, Czechoslovakia, August 19-23, 1985. Page 77

184 Huang M., Hieftje G.M. “Simultaneous measurement of spatially resolved electron temperatures, electron number densities and gas temperatures by laser light scattering from the ICP.” Spectrochimica Acta Part B: Atomic Spectroscopy. 1989 Jan 1;44(8):739-49.

185 Ojovan M.I., Lee W.E. “Glassy wasteforms for nuclear waste immobilization.” Metallurgical and Materials Transactions A. 2011 Apr 1;42(4):837-51.

186 Zurer PS. US charts plans for nuclear waste disposal. Chem. Eng. News;(United States). 1983 Jul 18;61(29).

187 Bickford DF, Diemer RB. Redox control of electric melters with complex feed compositions I. Analytical methods and models. Journal of Non-Crystalline Solids. 1986 Jul 2;84(1-3):276-84.

188 Bickford DF, Diemer RB, Iverson DC. Redox control of electric melters with complex feed compositions II. Preliminary limits for radioactive waste melters. Journal of Non-Crystalline Solids. 1986 Jul 2;84(1):285-91.

189 Day DE, Wu Z, Ray CS, Hrma P. Chemically durable iron phosphate glass wasteforms. Journal of non-crystalline solids. 1998 Nov 1;241(1):1-2.

190 Hunter RT, Edge M, Kalivretenos A, Brewer KM, Brock NA, Hawkes AE, Fanning JC. Determination of the Fe2+/Fe3+ ratio in nuclear waste glasses. Journal of the American Ceramic Society. 1989 Jun 1;72(6):943-7.

191 Ojovan M.I., Hand R.J., Ojovan N.V., Lee W.E. “Corrosion of alkali–borosilicate waste glass K-26 in non-saturated conditions.” Journal of Nuclear Materials. 2005 Apr 1;340(1):12-24.

192 Vernaz, E. Y., and J. L. Dussossoy. "Current state of knowledge of nuclear waste glass corrosion mechanisms: the case of R7T7 Glass." Applied Geochemistry 7 (1992): 13-22.

193 Schmitz I, Schreiner M, Friedbacher G, Grasserbauer M. “Tapping-Mode AFM In Comparison To Contact-Mode AFM As A Tool For In Situ Investigations Of Surface Reactions With Reference To Glass Corrosion.” Analytical chemistry. 1997 Mar 15;69(6):1012-8.

194 MacDowell, J. F., and G. H. Beall. "Immiscibility and crystallization in Al_2O_3-SiO_2 glasses." Journal of the American Ceramic Society 52.1 (1969): 17-25.

195 Higby P.L., Ginther R.J., Aggarwal I.D., Friebele E.J. “Glass Formation and thermal properties of low-silica calcium aluminosilicate glasses.” Journal of Non-Crystalline Solids. 1990 Dec 2;126(3):209-15.

196 Alavi M.A., Morsali A. “Alkaline-earth metal carbonate, hydroxide and oxide nano-crystals synthesis methods, size and morphologies consideration.” INTECH Open Access Publisher; 2011.

197 http://2010.igem.org/wiki/index.php?title=Team:Newcastle/solution&oldid=198785. Secretion of calcium carbonate crystals using the genetically engineered bacterium “Bacillus subtilis” trade name: BacillaFilla. Newcastle University.

198 James, P. F. "Liquid-phase separation in glass-forming systems." Journal of Materials Science 10.10 (1975): 1802-1825.

199 Nakamura Y., Kushiro I. “Compositional relations of coexisting orthopyroxene, pigeonite and augite in a tholeiitic andesite from Hakone volcano.” Contributions to Mineralogy and Petrology. 1970 Dec 1;26(4):265-75.

200 Evans B.W., Moore J.G. “Mineralogy as a function of depth in the prehistoric Makaopuhi tholeiitic lava lake, Hawaii.” Contributions to Mineralogy and Petrology. 1968 Jan 1;17(2):85-115.

201 Pasqual D., Molin G., Tribaudino M. “Single-crystal thermometric calibration of Fe-Mg order-disorder in pigeonites.” American Mineralogist. 2000 Jul 1;85(7-8):953-62.

202 Ikeda Y. “Petrology and mineralogy of the Y-793605 Martian meteorite.” Antarctic Meteorite Research. 1997 Sep;10:13.

203 Goodrich C.A. “Olivine-phyric martian basalts: A new type of shergottite.” Meteoritics & Planetary Science. 2002 Dec 1;37(S12):B31-4.

204 Ríos C.A., Castellanos O.M., Gómez S.I., Ávila G.A. “Petrogenesis of the metacarbonate and related rocks of the silgará formation, central santander massif, colombian andes: an overview of a" reaction calcic exoscarn.” Earth Sciences Research Journal. 2008 Jun;12(1):72-106.

205 Bonamartini Corradi A., Bondioli F, Cannillo V., Maria Ferrari A., Lancellotti I, Montorsi M. “The Anorthite–Diopside System: Structural and Devitrification Study. Part I: Structural Characterization by Molecular Dynamic Simulations.” Journal of the American Ceramic Society. 2005 Mar 1;88(3):714-8.

206 Levin EM, McMurdie HF. Phase diagrams for ceramists, 1975 supplement.

207 Toya T., Nakamura A., Kameshima Y., Nakajima A., Okada K. “Glass-ceramics prepared from sludge generated by a water purification plant.” Ceramics international. 2007 May 31;33(4):573-7.

208 De Vekey R.C., Majumdar A.J. “The role of TiO_2 in the formation of cordierite glass-ceramics” Phys. Chem. Glasses, 16 (1975), pp. 36–43

209 Torres F.J., de Sola E.R., Alarcón J. “Effect of boron oxide on the microstructure of mullite-based glass-ceramic glazes for floor-tiles in the $CaO–MgO–Al_2O_3–SiO_2$ system.” Journal of the European Ceramic Society. 2006 Dec 31;26(12):2285-92.

210 Charles R.J. “Static fatigue of glass. I. ” Journal of Applied Physics. 1958 Nov 1;29(11):1549-53.

211 Andersson Ö.H, Karlsson K.H., Kangasniemi K. “Calcium phosphate formation at the surface of bioactive glass in vivo.” Journal of Non-Crystalline Solids. 1990 May 2;119(3):290-6.

212 Grambow B., Müller R. “First-order dissolution rate law and the role of surface layers in glass performance assessment.” Journal of Nuclear Materials. 2001 Sep 30;298(1):112-24.

213 Cailleteau C., Angeli F., Devreux F., Gin S., Jestin J., Jollivet P., Spalla O. “Insight into silicate-glass corrosion mechanisms.” Nature materials. 2008 Dec 1;7(12):978-83.

214 Frugier P., Gin S., Minet Y., Chave T., Bonin B., Godon N., Lartigue J.E., Jollivet P., Ayral A., De Windt L., Santarini G. “SON68 nuclear glass dissolution kinetics: Current state of knowledge and basis of the new GRAAL model.” Journal of Nuclear Materials. 2008 Oct 15;380(1):8-21.

215 Lopez C., Deschanels X., Bart J.M., Boubals J.M., Den Auwer C., Simoni E. “Solubility of actinide surrogates in nuclear glasses.” Journal of Nuclear Materials. 2003 Jan 31;312(1):76-80.

216 Miae, K.,and Jong H. "Calcium-borosilicate glass-ceramics wasteforms to immobilize rare-earth oxide wastes from pyro-processing." Journal of Nuclear Materials 467 (2015): 224-228.

217 Greenwood N.N., Earnshaw A. “Chemistry of the Elements.” (1984) Page 1104

218 Willey D.M. “Treatment and disposal of problematic and poorly characterized nuclear fuels in a post-irradiation examination facility.” Hot cell post-irradiation examination and poolside inspection of nuclear fuel. 2013:67.

219 Gray J., Jones S. R., and Smith A. D. "Discharges to the environment from the Sellafield site, 1951-1992." Journal of Radiological Protection 15.2 (1995): 99.

220 Wang S., Peng Y. "Natural zeolites as effective adsorbents in water and wastewater treatment." Chemical Engineering Journal 156.1 (2010): 11-24.

221 Bryan, W. B. "Fe-Mg relationships in sector-zoned submarine basalt plagioclase." Earth and Planetary Science Letters 24.2 (1974): 157-165.

222 Naney, M. T. "Phase equilibria of rock-forming ferromagnesian silicates in granitic systems." American Journal of Science 283.10 (1983): 993-1033.

223 Karamanov A., Aloisi M., Pelino M. “Vitrification of copper flotation waste.” Journal of Hazardous Materials. 2007 Feb 9;140(1):333-9.

224 Romero M., Rincon J.M. “Preparation and properties of high iron oxide content glasses obtained from industrial wastes.” Journal of the European Ceramic Society. 1998 Dec 31;18(2):153-60.

225 Lee W.E., Heuer A.H. “On the polymorphism of enstatite”. Journal of the American Ceramic Society. 1987 May 1;70(5):349-60.

226 Chinnam R.K.,Lee W.E. “Degradation of Partially Immersed Glass: A New Perspective,” In preparation.

227 Akdeniz Y, Ülkü S. “Thermal stability of Ag-exchanged clinoptilolite rich mineral.” Journal of thermal analysis and calorimetry. 2008 Dec 1;94(3):703-10.

228 Bogdanova V.I., Fursenko B.A., Galai G.I., Belitsky I.A., Predeina L.M., Pavlyuchenko V.S., Drobot I.V. “Caesium immobilization using zeolite-containing rocks and high temperature treatment. ” in defence nuclear waste disposal in Russia: International perspective 1998 (pp. 69-84). Springer Netherlands.

229 Glebov LB, Boulos EN. Absorption of iron and water in the Na_2O–CaO–MgO–SiO_2 glasses. II. Selection of intrinsic, ferric, and ferrous spectra in the visible and UV regions. Journal of non-crystalline solids. 1998 Dec 1;242(1):49-62.

230 Mirhadi B, Mehdikhani B. Effect of batch melting temperature and raw material on iron redox state in sodium silicate glasses. Journal of the Korean Ceramic Society. 2011;48(2):117-20.

231 Hansen M., Anderko K., Salzberg H.W. “Constitution of binary alloys.” Journal of the Electrochemical Society. 1958 Dec 1;105(12):260C-1C.

232 Li X., Scherf A., Heilmaier M., Stein F. “The Al-rich part of the Fe-Al phase diagram.” Journal of Phase Equilibria and Diffusion. 2016 Apr 1;37(2):162-73.

233 Aziz, P. M., and H. P. Godard. "Pitting corrosion characteristics of aluminum-The influence of iron and silicon." Corrosion 10.9 (1954): 269-272.

234 Aziz, P. M., and Hugh P. Godard. "Pitting corrosion characteristics of aluminum-Influence of magnesium and manganese." Industrial & Engineering Chemistry 44.8 (1952): 1791-1795.

235 Park J.O., Paik C.H., Huang Y.H., Alkire R.C. “Influence of Fe-Rich intermetallic inclusions on pit initiation on aluminum alloys in aerated NaCl.” Journal of the Electrochemical Society. 1999 Feb 1;146(2):517-23.

236 Nis K. “Electrochemical behavior of aluminum-base intermetallics containing iron.” Journal of the Electrochemical Society. 1990 Jan 1;137(1):69-77.

237 Pecqueur G., Crignon C., Quénée B. “Behaviour of cement-treated MSWI bottom ash.” Waste Management. 2001 Jun 30;21(3):229-33.

238 Chatterji S. “Mechanism of expansion of concrete due to the presence of dead-burnt CaO and MgO.” Cement and Concrete Research. 1995 Jan 31;25(1):51-6.

239 Murray R. “Asbestos: a chronology of its origins and health effects.” British journal of industrial medicine. 1990 Jun 1;47(6):361-5.

240 Kusiorowski R., Zaremba T., Piotrowski J., Adamek J. “Thermal decomposition of different types of asbestos.” Journal of Thermal Analysis and Calorimetry. 2012 Aug 1;109(2):693-704.

241 Rinaudo, C., E. Belluso, and D. Gastaldi. "Assessment of the use of raman spectroscopy for the determination of amphibole asbestos." Mineralogical Magazine 68.3 (2004): 455-465.

242 Cheng T.W. “Effect of additional materials on the properties of glass-ceramic produced from incinerator fly ashes.” Chemosphere. 2004 Jul 31;56(2):127-31.

243 Reinosa J.J., Rubio-Marcos F., Solera E., Bengochea M.A., Fernández J.F. “Sintering behaviour of nanostructured glass-ceramic glazes.” Ceramics International. 2010 Aug 31;36(6):1845-50.

244 Fröberg L., Kronberg T., Hupa L. “Effect of soaking time on phase composition and topography and surface microstructure in vitrocrystalline whiteware glazes.” Journal of the European Ceramic Society. 2009 Aug 31;29(11):2153-61.

245 Park, Young Jun, and Jong Heo. "Vitrification Of Fly Ash From Municipal Solid Waste Incinerator." Journal of Hazardous Materials 91.1 (2002): 83-93.

246 Katou K., Asou T., Kurauchi Y., Sameshima R.. Melting municipal solid waste incineration residue by plasma melting furnace with a graphite electrode. Thin Solid Films. 2001 May 15;386(2):183-8.

247 Katou K., Asou T., Kurauchi Y., Sameshima R. “Melting Municipal Solid Waste Incineration Residue By Plasma Melting Furnace With A Graphite Electrode.” Thin Solid Films. 2001 May 15;386(2):183-8.

248 Kash SW, Woods DC. Measurement of the Transport Mean Free Path of Thermal Neutrons in D 2 O by a Boron Poisoning Method. Physical Review. 1953 May 15;90(4):564.

249 Apted MJ, Ahn J, editors. Geological repository systems for safe disposal of spent nuclear fuels and radioactive waste. Elsevier; 2010 Jul 27. Chapter 9.4.1

250 VANCE E, BEGG B. Immobilisation of spent nuclear fuel and high-level radioactive waste for safe disposal in geological repository systems. Geological Repository Systems for Safe Disposal of Spent Nuclear Fuels and Radioactive Waste. 2010 Jul 27:261.

251 Ojovan MI, Varlackova GA, Golubeva ZI, Burlaka ON. Long-term field and laboratory leaching tests of cemented radioactive wastes. Journal of hazardous materials. 2011 Mar 15;187(1):296-302.

252 Lee WE, Ojovan MI, Stennett MC, Hyatt NC. Immobilisation of radioactive waste in glasses, glass composite materials and ceramics. Advances in Applied Ceramics. 2006 Feb 1;105(1):3-12.